ISSN: 0858-2114

# International Agricultural Engineering Journal

Published by Asian Association for Agricultural Engineering (AAAE)

September 2025, 34 (1-4)

# Asian Association for Agricultural Engineering
## International Agricultural Engineering Journal


### Aims and Scope

The aim of this journal is to share advancements in Agricultural Engineering, with specific focus on Asia, with professionals working in the field. The scope of the journal includes soil and water engineering, farm machinery, farm structures, post-harvest technology, bio technology, food processing and emerging technologies. Topics of interest to agricultural engineers such as ergonomics, energy, systems engineering, precision agriculture, protected cultivation, secondary agriculture, terra mechanics, instrumentation, environmental considerations in agriculture, Artificial Intelligence, sensors and related applications are also covered. The journal utilizes double-blind review process.

**International Agricultural Engineering Journal**
**ISSN 0858-2114**
***September 2025, 34 (1-4)***

# Contents

International Agricultural Engineering Journal ISSN 0858-2114

*September 2025, 34(1-4):1-16*

# Development of Turmeric Processing Machinery

**S.Ganapathy[1*], T. Pandiarajan[1], M.Balakrishnan[1], I.P. Sudagar[2], R.Arulmari[3], V. Arun Prasath[4]**

## ABSTRACT

Conventional practices of postharvest handling of turmeric do not yield high quality dried fingers. To address this challenge, a set of machinery namely, washer, boiler, dryer and polisher were designed and developed for postharvest operations of turmeric. All four pieces of equipment were integrated using conveyors so as to make a value chain. The washer was equipped with a jet spray of recirculated water on the turmeric rhizomes moving inside a rotating perforated drum kept at 13° inclination. The equipment capacity was about 300 kg/h and operational efficiency was 95%. The washed turmeric was filled into a boiler vessel of 150 kg capacity and the boiling operation was done in 10 min using steam at 196.1 kPa. This operation improved the quality of processing considerably as the rhizomes were gelatinized in hygienic enclosure and the boiling time was saved by a factor of 4. The boiled turmeric was transferred to a rotary dryer of 500 kg capacity, equipped with an electric coil heater of 4 kW and powered by a motor of 5 hp. Effective drying of rhizomes was completed in 36 h, yielding rhizomes at 10% moisture (d.b) from an initial moisture content of 145% (d.b). The dried rhizomes were finally conveyed to a polisher of 800 kg capacity equipped with a dust proof cover over the body of the polisher. The polisher applies friction on the rhizomes due to the perforations of the drum and the batch operation was done in 40 min. Using this machinery, a typical turmeric farmer of western Tamilnadu state of India will require only 2 days to complete the entire postharvest operations of 3 tonnes of fresh harvest compared to about 21-28 days for drying alone on farmyard with sun drying in a biologically unsafe environment.

***Keywords:*** *Boiling; Drying; Efficiencies; Turmeric; Value Chain; Washing.*

## 1. INTRODUCTION

Turmeric is an economically important spice crop grown in the Western zone of Tamil Nadu, primarily in the Erode, Karur, and Salem districts adjoining the Cauvery River. According to economical year 2017, 21,000 ha of land is under turmeric cultivation on a typical season and about 90,000 metric tonnes of dried turmeric rhizomes are produced annually in the state of Tamilnadu in India (Manjunatha *et al.*, 2017). As of 2024, Tamil Nadu has approximately 24,814 hectares under turmeric cultivation, producing about 111,665 metric tonnes of turmeric annually.

[1]Professor, Agricultural Engineering College and Research Institute, TNAU, Coimbatore.
[2]Professor, [3]Assistant Professor, Agrl. Engineering College and Research Institute, TNAU, Kumulur.
[4]Assistant Professor, National Institute of Technology, Rourkela.
**Corresponding author – email: ganapathy.s@tnau.ac.in*
Received: 22 January 2025; Revised: 23 April 2025; Accepted: 24 April 2025.

This marks a significant increase from the 2020–21 season, where the state cultivated around 20,894 hectares and produced approximately 86,513 metric tonnes (Jyotirmayee *et al.,* 2024). These figures highlight Tamil Nadu's substantial role in India's turmeric production, underscoring the importance of continued investment in post-harvest handling and processing technologies to enhance the turmeric value chain. Turmeric is also an essential spice crop in the neighbouring states of Andhra Pradesh and Karnataka and also in the North eastern states of India. It is a high moisture crop, highly perishable, and hence its processing and storage are important (Prasath *et al*., 2024).

Postharvest handling of turmeric plays a crucial role in producing quality finished product namely dried turmeric finger. Conventional practice of handling involves steam boiling in open barrels, sun drying and take at least 28 days for completion. The quality of dried turmeric is inferior as microbial load is in

the field, and polishing with a machine (Bhattacharya, 2014). These operations are labour intensive suspected and significant loss of curcumin is reported (Hirko *et al.,* 2020; Hailemariam *et al.,* 2023; Prasath *et al*., 2024). The existing practices of postharvest handling of turmeric render the crop suitable only as the main ingredient for curry powder. Turmeric utilization as curry powder is the least lucrative option for the farmers as there are other ways of adding value to turmeric.

Increasingly pharmaceutical industry is looking for high quality processed turmeric or its derivatives such as oleoresin, essential oils, and most importantly curcumin (El-Saadony *et al.,* 2023; Sharifi-Rad *et al.,* 2020). These high value products are now not manufactured from turmeric in Tamil Nadu to any significant extent, primarily due to the poor quality of the raw material resulting from conventional practices of turmeric processing. However, multiple uses for turmeric and accordingly the demand for high quality turmeric is increasing from the manufacturing industries. The increasing demand for organic food additive makes turmeric an ideal natural food colorant. Additionally, anti-cancer and anti-viral properties of turmeric also contribute to its increasing demand from pharmaceutical industries.

Currently the farmers do not practice washing of rhizomes after postharvest and as a result dirt and foreign matter from the field enter the processing operations. Consequently, significant loss of quality occurs when the rhizomes are subjected to boiling, drying and polishing. The turmeric was boiled in 25 kg batches and processed. The boiling temperature used in the developed turmeric boiling system, as mentioned in the uploaded document, corresponds to steam at a pressure of 196.1 kPa (2 kg/cm²). At this pressure, the boiling (steam) temperature is approximately 120°C in 25 kg batches and is done on the field within 3-4 days after harvest. A convectional boiling-based turmeric boiling system was developed, featuring a mobile steam blanching vessel designed to retain maximum curcumin content and reduce cooking time. The system achieved a reduced cooking time of 10 minutes, with improved color values compared to traditional methods (Farzana *et al.,* 2018). In another study, three drying methods (sun, hot air oven, and fluidized bed) with turmeric pretreatments (boiled/un-boiled, whole/sliced) were compared for quality retention, showing that sliced boiled rhizomes sun-dried achieved uniform drying and highest oleoresin content (8.10%). Despite longer drying time, sun drying is recommended for post-harvest operations as it yielded turmeric with maximum curcumin content (5.82%) and better overall quality (Saha *et al.,* 2022).

Steam boiling was also more efficient than traditional water boiling in terms of fuel use, batch size, and labor requirements (Viswanathan *et al.,* 2002). Arora *et al.* (2007) observed that turmeric was dried using sun, hot air oven, and fluidized bed methods with different pretreatments to assess quality retention. Sun drying, though slower,

resulted in the highest curcumin (5.82%) and oleoresin (8.10%) content, making it the most effective method for producing quality turmeric powder. The equipment involved are water tube boilers for steam source and open pushcart type barrels for steam application on batches of turmeric. The carts are covered with gunny bag sacks on the top of the cart and the operation is done on less desirable hygienic environment. The boiled turmeric rhizomes are then spread on the farmyard drying floor for about 21-28 days for sun drying. The drying floor is mostly unpaved and the turmeric is kept in contact with the earth during this period. During drying there is greater likelihood of contamination of rhizomes. Also, sun drying leaves no controls on the part of farmers to ensure the quality of drying operation. Vagaries of weather and intermittent rains very often result in the loss of value of finished product. Finally, the dried rhizomes are polished using a machine introduced during 2005-06 which relies on abrasive removal of outer skin from the fingers. The drawback with the existing polishing machine is that all the fine particles are released into air causing environmental pollution and posing a human health hazard.

Thus, the present state of turmeric processing has many challenges and needs improvements on the various unit operations. Therefore, this study was undertaken to improve the existing practices of turmeric processing and also introduce a washing operation prior to the rest of the operations. A set of turmeric value chain machinery was designed and developed to enable turmeric farmers to enhance the quality of processed fingers, reduce overall processing time, and access high-value markets in pharmaceutical and other food processing industries. This work summarizes the developments towards the design and development of four primary processing equipment for turmeric, namely washer, boiler, dryer and polisher.The machinery was designed for a scale suitable for laboratory trials and small farmer holding 2-5 ha. However, scaling up of this machinery to cater to larger processing units is feasible and imperative for a cluster-based approach in a turmeric production zone.

## 2. MATERIALS AND METHODS

### 2.1. Turmeric Washer

Washing of harvested turmeric rhizomes is expected to improve the efficiency of operations like boiling, drying, and polishing. Farmers currently do not consider washing important, which is related to the water shortage in turmeric growing regions. Therefore, a water recirculating batch type washing machine for turmeric was designed and developed (Susendran, 2018; Susendran, *et al*., 2019). The machine was designed to handle about 300 kg/h output and was made mobile by means of towed wheels. The schematic of the turmeric washer is illustrated in Fig. 1. The washer consists of a rotating stainless-steel drum with perforations and is mounted at an inclination of 9-13° on frames and provided with accessories such as water jets axially at the top of the drum. The turmeric is fed to the top of the drum through a bucket elevator. The turmeric slides down the rotating drum and follows a helical path towards the outlet end while being subjected to high - velocity water jets from the top, ensuring thorough washing of the fingers.

The main components of the turmeric washer are feeding mechanism, cylindrical rotary drum, water spray assembly, washed turmeric outlet, motor, pump, and water collection tank. The washing drum is of 180 cm long and 60 cm in diameter and is made of stainless sheet punched with rectangular holes of size 6 x 25 mm, with 60% perforation of the total surface area. The feed hopper was made of mild steel of size 0.5 m x 0.5 m at the top end and 0.12 m x 0.21 m at the bottom end and was 10 cm deep. An inclined bucket elevator with 20 buckets spaced at 0.19 m on an endless belt was fitted with the washer. The total length of the belt was 2 m. The bucket elevator was driven by a 1 hp motor. Freshly harvested turmeric rhizomes were loaded in the elevator and

were conveyed into the mechanical washer for washing. A water spray assembly with a high-velocity jet spray system is installed in the washer. The pipe was 2.10 m long and 3 cm in diameter, with 17 holes of 4 mm diameter drilled at a spacing of 10 cm. A gate valve controls the water flow rate into the drum, and a collection tank directly underneath the rotating drum collects waste water for filtration and re-circulation by a pump. A one hp single-phase variable speed motor rotates the washing drum, supported on a separate frame attached to the main structure of the machine. The motor powers the rotating drum through a set of pulleys and helical gear drives for smooth operation under load. Initially, a pair of rotors were used to transfer power through friction to the drum, but due to slippage, a helical gear drive was later substituted.

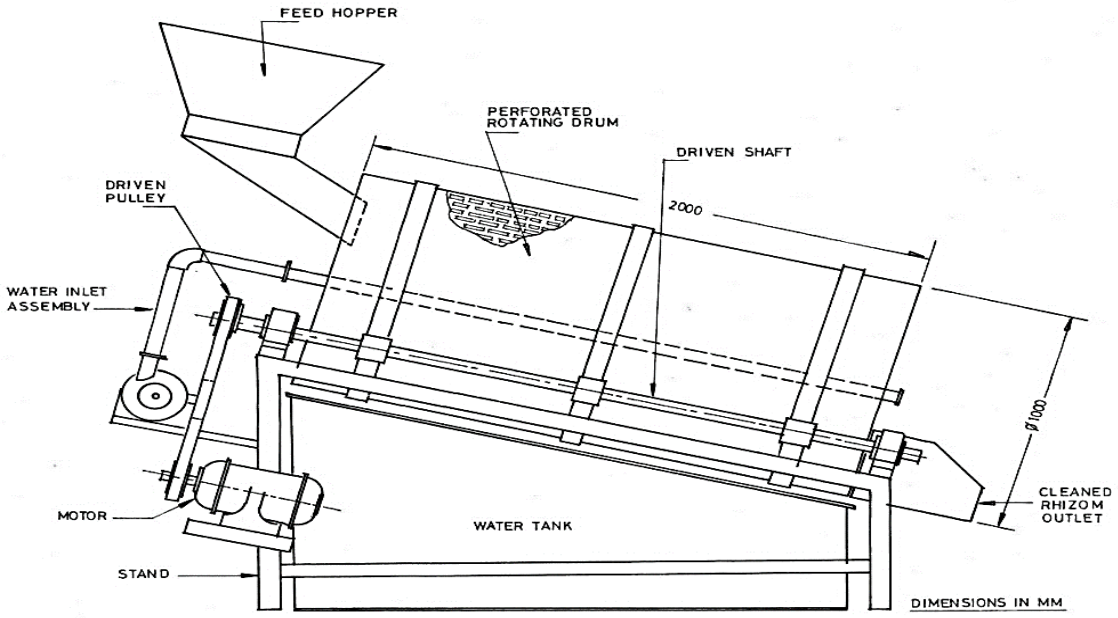


**Fig. 1. Design features of turmeric washer**

### 2.2. Turmeric Boiler

Currently farmers use a locally available water tube boiler to supply steam. This steam source is rented, and the boiler is moved between different farms in the turmeric-growing area each season. In these local boilers, the maximum pressure of steam supply was tested to be 98 kPa (1 kg/cm$^2$). Farmers load a batch of about 20-25 kg of turmeric rhizomes at a time for boiling in mild steel barrels, used tar tins, or open pushcart type units. The steam supplied by the boiler is connected to the turmeric barrels, which are sometimes covered with gunny bags. However, the containers are not closed, leading to steam loss. Additionally, since farmers do not wash the rhizomes before boiling and use agricultural wastes like turmeric leaves for steam production, exposure to foreign material and dirt is higher in this practice, resulting in poor hygiene.

An improved boiling vessel to hold about 125 kg of turmeric was designed using steel as shown in Fig. 2 (Farzana, 2018; Farzana *et al.*, 2018). The vessel had a closure lid which could be bolted to the shell after loading with washed turmeric and was connected to the steam source at the bottom. It was equipped with a pressure gauge to monitor the pressure during boiling. In laboratory, the turmeric boiling operation was carried out at a pressure of 196-294 kPa (2-3 kg/cm$^2$), resulting in a temperature range

of 120°C to 134°C in the boiler, depending on the steam pressure used. In the fields, local steam boilers were used. The vessel's walls were insulated with glass wool to minimize heat loss, allowing for the boiling of 100 kg of turmeric in about 5-7 minutes, achieving greater uniformity in steam distribution compared to the conventional method, which took 10-15 minutes for a batch load of turmeric to boil.

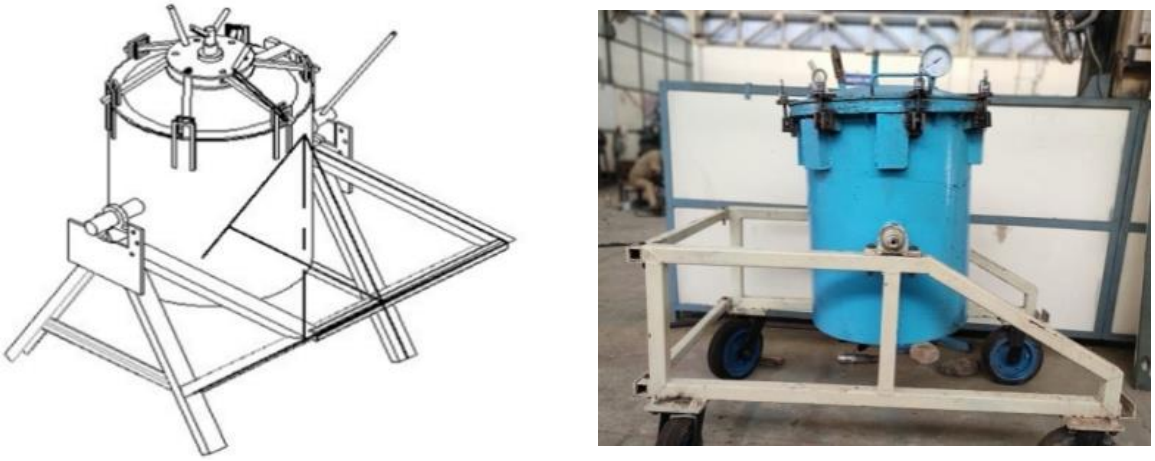

**Fig. 2. Design features of turmeric boiler**

### 2.3. Turmeric Rotary Dryer

A mechanical rotary drum dryer was designed for drying a batch of 500 kg of turmeric as shown in Fig. 3 (Aishwarya, 2018; Balakrishnan *et al.*, 2022). The dryer was designed to have hot air flow across a perforated cylindrical drum rotating at speed of about 9-15 rpm. Drying of turmeric rhizomes occurred in cascading and mixing conditions within the drying chamber. A volume of 25% was left free to allow turmeric to freely fall during rotation. The drying chamber consists of a cylindrical drum enclosed in a square casing with plenum chamber and air vent. The cylindrical drum, 1.15 m long and 0.96 m in diameter, was designed to hold 500 kg of fresh turmeric rhizomes (at 75% of dryer volume) and was made of a mild steel sheet of 30 x 2 mm rectangular opening to allow better diffusion of hot. One portion of the cylindrical drum served as a door for loading and unloading, while a central shaft of 50 mm diameter supported and rotated the drum inside the drying chamber.

Two thrust bearings were used to support shaft through the drying chamber, with the drying chamber dimensions being 1.22 x 1.15 x 1.22 m and made of 20 SWG thick galvanized iron sheet. A plenum chamber and exhaust air vent were provided at the bottom and top of the drying chamber respectively, with deflecting plates effectively diverting hot air through the cylindrical drum. The sides of the drying chamber were insulated with a 5 mm thick asbestos sheet to prevent heat loss. Hot air for drying was generated by a 1 kW electrical heating system with 4 heating coils. A 3 hp motor powered a blower that forced ambient air through the heating coils into the drying chamber. An air circulating system was used to recover heat from the exhaust air, consisting of a PVC pipe, plastic ball valve, and a mixing chamber fixed at the blower's inlet.

### 2.4. Dust Proof Turmeric Polisher

After drying, turmeric rhizomes undergo a polishing operation. The existing polisher used by turmeric farmers is a rotary drum type of octagonal shape made with expanded wire mesh. Here, polishing occurs as turmeric rhizomes rub and abrade against each other and the wire mesh metal surface. However, the resulting skin and

dust particles are ejected through the mesh openings due to centrifugal force, causing air pollution in the polishing area. To address this issue, the available polishing machine was modified to be dustproof by adding a collection hood around the rotating drum, preventing suspended particles from being released into the air.

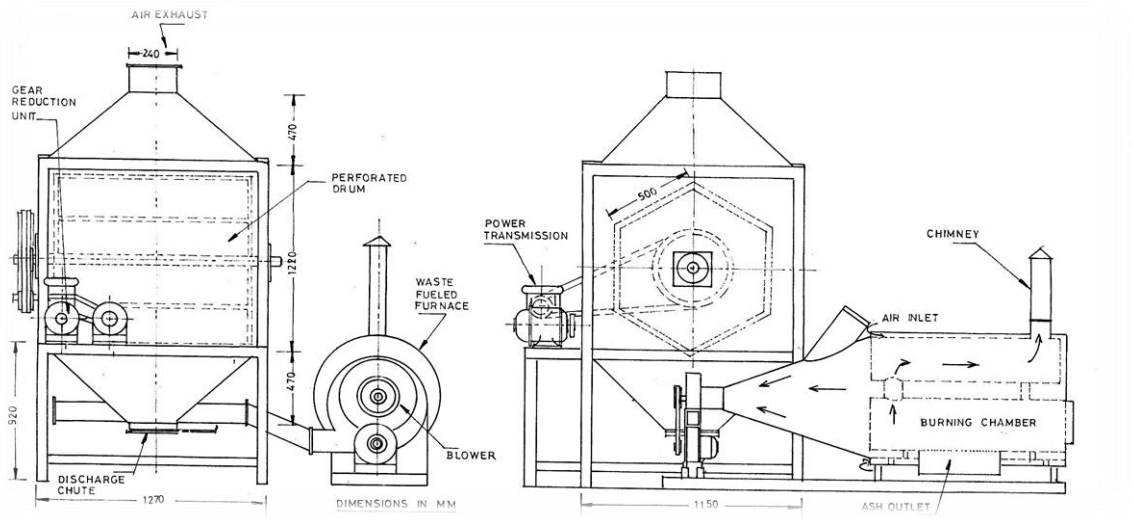


**Fig. 3. Rotary dryer for turmeric**

**Fig. 4. Dust free turmeric polisher**

The improved dustproof polisher was equipped with a protective shield surrounding the polishing drum in the form of Palladian truss consisting of a main frame, supporting frames and round plate. A clearance of 7.6 cm was provided between the main frame and the polishing drum, with the frame made of mild steel channel sections. Twelve supporting rib frames made of mild steel flats were fixed to the upper and lower halves of the polishing drum at a 30° angle to the main frame. Connecting rods made of mild steel round pipe were used to support and stabilize the frame. A round plate made of mild steel was fixed in the middle of the main frame, and the frames in each quadrant were covered with tarpaulin material (Fig.4). Field trials confirmed that the design effectively captured 92% of the dust particles generated during turmeric polishing operations, with an average of 800 kg of raw turmeric rhizomes loaded per batch resulting in a retrieval of 70% polished turmeric and 30% dust collected and disposed of, saving 40% of the polishing time.

## 3. RESULTS AND DISCUSSION

### 3.1. Performance Evaluation of Washer

Two varieties of turmeric namely Erode local and PTS-10 were used for evaluating the washer in farmers' fields at Thamaraipalyam, Kodumudi, Erode district, Tamil Nadu state, India. Each year, only a 3-month window from February to May was available to conduct performance evaluations of the developed machines. Based on the results obtained in the first trial, necessary modifications and design improvements in power drives, additional accessories, conveyors, insulations *etc*., were made. The machines were then evaluated in the subsequent seasons in Kalipalayam and Theethipalayam near Coimbatore in the year 2017 and 2018, respectively. Further testing took place at the Tamilnadu Agricultural University (TNAU) Campus during 2018 and 2019 (Table 1). The same two varieties of turmeric were used in all these evaluations from 2016-2018. The washing action and effects of washing on the quality of turmeric are illustrated in Fig. 5.

Freshly harvested turmeric rhizomes were loaded in the elevator and were conveyed into the mechanical washer for washing. The machine's performance was evaluated based on variables such as feed rate (290, 320 and 350 kg/h), spray type (A, B and C), and drum speed (40 and 50 rpm). The machine was evaluated in terms of mechanical washing efficiency, colour of washed turmeric, and bruise index. The results obtained were shown in Fig. 6.

The washing efficiency decreased with the feed rate and drum speed within the tested ranges. An efficiency of 91.1% was obtained at a drum speed of 40 rpm and feed rate of 290 kg/h, but decreased to 80.2% at a drum speed of 50 rpm and feed rate of 350 kg/h. A mechanical washing efficiency of 94% was achieved with a slotted hole spray pattern at a drum speed of 40 rpm and feed rate of 290 kg/h. The $L^*$ and $b^*$ values of unwashed turmeric rhizomes were 35.45 ± 1.62 and 12.20 ± 0.39, respectively. The maximum $L^*$ value of 42.94 ± 0.60 was found in slotted hole spray pattern at a drum speed of 40 rpm. The colour value $b^*$ varied from 13.39 ± 0.59 to 12.63 ± 0.44. The increase in colour value $L^*$ as well as $b^*$ of washed rhizomes indicated the effectiveness of washing. The turmeric rhizomes were cleaned by the combined action of water spray on rhizomes and friction between the rhizomes and rotating drum. The key determinant of washing is ensuring adequate contact between the turmeric rhizomes, drum surface and water. Increase in feed rate, regardless of spray type, reduced mechanical washing efficiency due to inadequate contact between the of rhizomes, spray water and rotating drum. The retention time of turmeric rhizome decreased with an increase in feed rate, leading to more mud particles in washed rhizomes at 350 kg/h feed rate and reduced washing efficiency.

**Table 1. Details of trials conducted with turmeric processing machinery**

| Sl. No. | Details | Trial 1 | Trial 2 | Trial 3 |
|---|---|---|---|---|
| 1 | Place | Thamaraipalayam, Erode | Kalipalayam, Coimbatore | Theethipalayam, Coimbatore |
| 2 | Name of the farmer | Mr. Thiyagarajan | Mr. Srinivasan | Mr. Satheesh |
| 3 | Period of trial | March 2016 | April 2017 | April 2018 |
| 4 | Quantity processed | 4 tonnes | 4.5 tonnes | 5 tonnes |

**Fig. 5. Washing action and the initial and final conditions of washed turmeric**

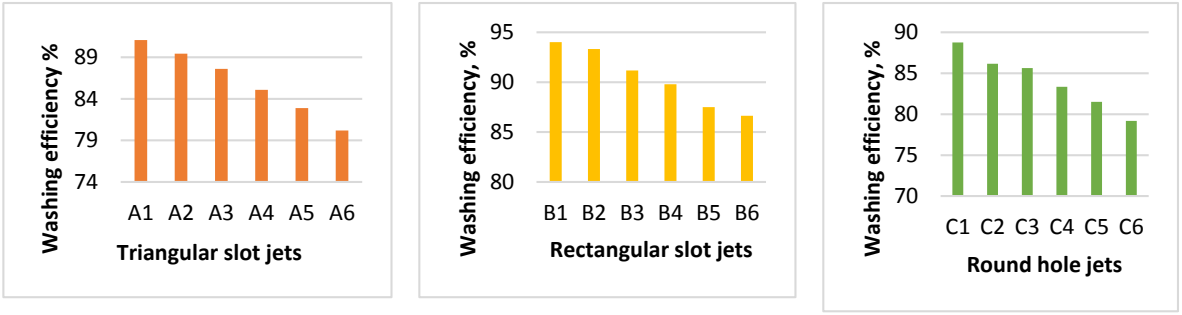


**Fig. 6. Washing efficiency of turmeric washer as affected by the geometry of jets, feed rate and drum rotational speed**

*(A1, B1, C1- 290 kg/h feed at 40 rpm; A2, B2, C2- 290 kg/h feed at 50 rpm; A3, B3, C3- 320 kg/h feed at 40 rpm; A4, B4, C4- 320 kg/h feed at 50 rpm; A5, B5, C5- 350 kg/h feed at 40 rpm; A6, B6, C6- 350 kg/h feed at 50 rpm)*

Similarly, the washing efficiency was lower at a drum speed of 50 rpm compared to 40 rpm due to the reduced retention time for turmeric rhizomes inside the washer. Overall, the maximum efficiency was observed at a drum speed of 40 rpm and a feed rate of 290 kg/h. The colour value $L^*$, $a^*$ and $b^*$ of washed turmeric rhizomes at optimized conditions were 42.94 ± 0.60, 7.61 ± 1.11, and 14.08 ± 0.79, respectively. At this optimized condition, the bruise index was 0.8. Analysis of variance revealed that the spray type, drum speed, and feed rate significantly influenced the washer's performance ($p < 0.05$).

### 3.2. Performance Evaluation of Turmeric Boiler

The turmeric boiler was evaluated at three different farms around Coimbatore and in the laboratory of Tamil Nadu Agricultural University, Coimbatore during 2016-2018. The boiling operation was conducted at a pressure range of 98-294 kPa (1-3 kg/cm$^2$). Quality parameters of boiled turmeric, such as curcumin content, oleoresin content, essential oil, moisture content, colour and hardness were determined using standard procedures. The time taken for boiling operation varied with the steam pressure, and the gelatinization percentage and quality of boiled rhizomes were recorded.

Table 2 presents the color values ($L^*$, $a^*$, $b^*$) of turmeric processed by conventional and improved boiling methods. The improved boiling vessel resulted in higher values for all three parameters: $L^*$ (53.26), $a^*$ (19.92), and $b^*$ (59.20), compared to the conventional method ($L^*$ = 51.06, $a^*$ = 18.14, $b^*$ = 55.45). The increase in L indicated enhanced lightness, while higher $a^*$ and $b^*$ values reflected greater redness and yellowness, respectively. These improvements suggest better pigment retention and color development due to shorter cooking time, higher pressure, and controlled conditions, which help preserve curcumin and related color-contributing compounds.

The moisture content of boiled turmeric significantly differed between treatments. Turmeric processed using the improved vessel had lower moisture content (8.5%) compared to the conventional method (11.2%). This reduction is attributed to the use of higher steam pressure (196–294 kPa) and temperature (120–134°C) in the improved system, which facilitates rapid and uniform gelatinization while minimizing moisture retention.

The mean curcumin content of boiled turmeric was 5.91% in conventional method and 7.74% with the improved vessel. The oleoresin content was 4.63, and 9.94%, respectively in conventional and improved vessels. The improved retention of curcumin, oleoresin, and essential oils in turmeric boiled using the developed vessel was largely attributed to the optimized combination of time, temperature, and pressure during the operation. Unlike the conventional open-drum boiling method that operated at a lower steam pressure of around 98 kPa and requires up to 15 minutes, the developed system used steam at a higher pressure of 196–294 kPa, achieving boiling temperatures between 120°C and 134°C. This enabled the boiling process to be completed in just 5–10 minutes. The elevated pressure and shorter boiling time promote efficient starch gelatinization while minimizing the leaching of thermolabile and water-soluble compounds like curcumin and oleoresin. Additionally, the closed and hygienic environment of the improved vessel reduced contamination and nutrient loss, resulting in significantly better retention of bioactive compounds compared to the conventional method.

**Table 2. Effect of boiling method on the quality of turmeric**

| Treatment | Colour | | | Curcumin, % | Oleoresin, % | Essential Oil, % | Moisture content, % d.b | Boiling duration, min. |
|---|---|---|---|---|---|---|---|---|
| | *L** | *A** | *B** | | | | | |
| 1. Conventional method | 51.06 | 18.14 | 55.45 | 5.91 | 4.63 | 3.75 | 11.2 | 15 |
| 2. Boiling Vessel | 53.26 | 19.92 | 59.20 | 7.74 | 9.94 | 4.30 | 8.5 | 10 |

There was no appreciable difference in the essential oil content obtained among the different methods of boiling. The heat utilization factor (HUF) was 0.759 with the improved vessels at a pressure of 147 kPa. The degree of starch gelatinization was 49.5% with the vessel.

The results of tests for biochemical attributes showed that turmeric rhizomes boiled in improved vessel retained more curcumin content of 7.74% and oleoresin content of 9.94%. This is due to the higher gelatinization percentage recorded in samples boiled in improved vessel, which reduced the leaching of active principles.

### 3.3. Performance Evaluation of Dryer

The developed dryer was evaluated with freshly harvested turmeric rhizomes across 3 seasons during 2016-2018 at villages around Coimbatore and at the laboratory of TNAU. The overall time of drying the rhizomes from a moisture level of 150% (d.b) to 10% (d.b) was 36 to 54 h. The drying trials were conducted using a drum speed of 9 to 15 rpm and air temperature of 50 to 70°C.

Initially, one trial was conducted using biomass - fired furnace to supply hot air to the dryer. Later trials were done with electric heater as it was more cumbersome to move the additional biomass furnace unit in the farmers' field. Moreover, electricity is accessible in all the farms. Biomass furnace was also not preferred by the farmers as it involved considerable labour for feeding turmeric field waste like dried turmeric leaves into the furnace. Secondly the calorific value of dry leaves was too low for its effective utilization for firing a furnace. They had to depend on firewood in any case.

**Fig. 7. Drying drum with raw and dried turmeric**

In all these trials, the final quality of rhizomes was consistently superior to the ones obtained by conventional sun drying on the farmyard. The yellowness (*b** value) of turmeric was maximum at an air temperature of 50°C, air velocity of 3 m/s and drum rotational speed of 9 rpm. The essential oil content of dried turmeric rhizomes was in the range of 3.61% to 3.93%. The oleoresin content of turmeric rhizomes was in the range of 12.7% to 17.26%. The starch content of rotary dried turmeric rhizomes was 60.65 ± 0.027%. Also 70% of polishing of turmeric also resulted in drying as there was rubbing action of turmeric against the perforated steel drum surface.

The recovery of essential oil (3.61%), oleoresin (17.26%), colour and starch content (57.65%) were better in rotary drying than conventional sun drying. In the Theethipalayam field trial, modified mechanical dryer took 54 h to dry 300 kg of turmeric from 80% (d.b) moisture content to 7% (d.b) moisture content. During the trial, the drying process was interrupted by heavy rainfall which resulted in increase in drying time and discoloration of rhizomes. Quality attributes of dried turmeric were comparable to conventionally dried product (Fig.7).

A laboratory trial was conducted with the modified mechanical dryer. The trial took 32 h to dry 300 kg of turmeric with 70°C hot air at 9 rpm rotating speed. The qualities of rotary dried turmeric rhizomes in terms of curcumin, oleoresin, colour and starch content were better in rotary drying when compared to sun drying. In contrast to traditional sun drying, which extended over 21–28 days and exposes the rhizomes to environmental fluctuations, the mechanical dryer operated under controlled conditions at air temperatures of 50–70°C and completed the drying process in just 36–54 hours (Fig. 8 and). The uniform distribution of hot air and the rotational motion of the drum ensured even drying, reducing the chances of localized overheating or under-drying. These controlled drying conditions prevented the degradation of volatile and light-sensitive compounds, contributing to the higher retention of essential oil and oleoresin. Furthermore, the reduced drying time prevented oxidation and exposure to light, thereby preserving curcumin content and enhancing the overall quality of the dried turmeric.

### 3.4. Performance Evaluation of Polisher

The developed polisher was evaluated with dried turmeric rhizomes across 3 seasons during 2016-2018 at villages around Coimbatore and also at the laboratory of TNAU. The dust particles released during polishing of turmeric rhizomes in both conventional and dust proof turmeric polisher were measured and recorded using universal sample pump with IOM (Institute of Occupational Medicine) dust sampler. Inhalable and respirable dust concentrations were found as 9.10 mg/m$^3$ and 4.26 mg/m$^3$, respectively during polishing with conventional turmeric polisher.

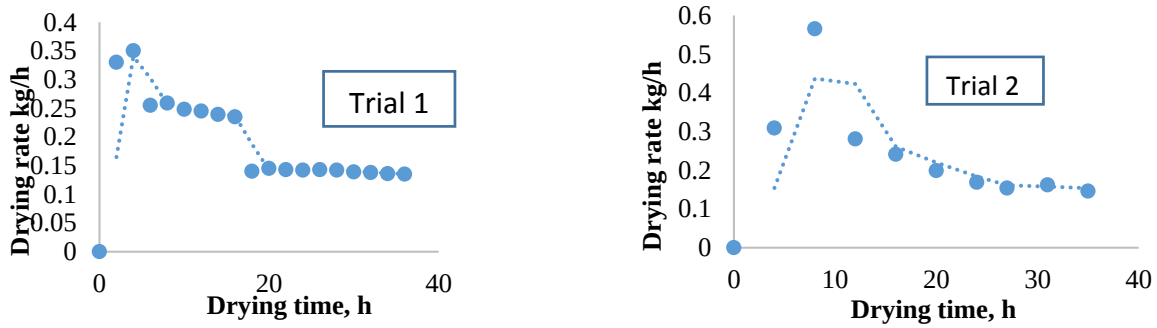


**Fig. 8. Drying rate of turmeric in trials 1 and 2**

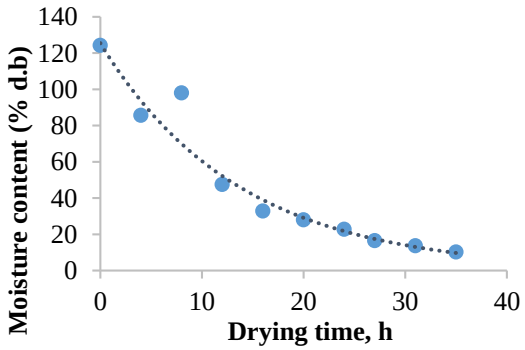


**Fig. 9. Drying time - moisture content relationship of turmeric rhizomes**

In dust free turmeric polisher, the inhalable and respirable dust were found as 0.011 mg/m$^3$ and 0.007 mg/m$^3$, respectively. The permissible limits for inhalable and respirable dust were 5 mg/m$^3$ and 1 mg/m$^3$, respectively. Pollution resulted from polishing of turmeric rhizomes could be controlled upto 87.4% with the collapsible dust cover. Only little air borne particles were floating at the discharge end. Polishing efficiency of the dust free polisher was 92.6% (Table 3).

In the second trial, the polishing efficiency of the dust free polisher was 93.2%. The mass reduction due to polishing was 28.9%. About 88% reduction in dust emission was achieved with the modified polisher (Table 4). There was a polishing time saving of about 40% for rhizomes when compared to conventional polisher. Similar results of polishing efficiency were obtained in the third trial also. The polishing efficiency of the dust free polisher was observed to be 92.8%. Compared to conventional polisher, time saving was 42%. Polishing mass removal was 30.1% and dust emission reduction was 89% (Table 5).

### 3.5. Integrated Turmeric Value Chain Machinery

The set of postharvest machinery namely washer, boiler, dryer and dust free polisher were later integrated by conveyor system (Fig. 10). Appropriate conveyors were attached to the input and output end of all four machinery so that the fresh harvested turmeric moved along the various unit operations of washing, boiling, drying and polishing seamlessly.

**Table 3. Polishing of turmeric by dust proof polisher in trial 1**

| Sl.No. | Polishing time, h | Initial mass of turmeric, kg | Final mass of polished turmeric, kg | Mass of dust collected, kg | Polishing Efficiency, % | Polishing Loss, % |
|---|---|---|---|---|---|---|
| 1 | 1.00 | 801 | 600.75 | 200.25 | 91.3 | 25 |
| 2 | 1.05 | 800 | 568.00 | 232.00 | 93.4 | 29 |
| 3 | 1.00 | 802 | 577.44 | 224.56 | 92.6 | 28 |
| 4 | 1.00 | 798 | 566.58 | 231.42 | 92.8 | 29 |
| 5 | 1.00 | 800 | 552.00 | 248.00 | 94.2 | 31 |
| 6 | 1.00 | 805 | 563.50 | 241.50 | 93.8 | 30 |
| Mean | 1.01 | 801.00 | 571.38 | 229.62 | 93.02 | 28.67 |

**Table. 4. Particulate matter collected by IOM Dust sampler in conventional method**

| Sl.No. | Sampling Duration, min | Initial Weight, g | | Final weight, g | | Difference in weight, g | |
|---|---|---|---|---|---|---|---|
| | | Inhalable dust | Repairable dust | Inhalable dust | Repairable dust | Inhalable dust | Repairable dust |
| 1 | 15 | 1170 | 1231 | 1172.6 | 1241.7 | 10.7 | 2.6 |
| 2 | 15 | 1170 | 1231 | 1171.8 | 1238.5 | 7.5 | 1.8 |
| 3 | 15 | 1170 | 1231 | 1172.7 | 1242.4 | 11.4 | 2.7 |
| 4 | 15 | 1170 | 1231 | 1171.7 | 1237.7 | 6.7 | 1.7 |
| 5 | 15 | 1170 | 1231 | 1171.2 | 1236.5 | 5.5 | 1.2 |
| 6 | 15 | 1170 | 1231 | 1173.1 | 1243.9 | 12.9 | 3.1 |
| Mean Value | | | | | | 9.12 | 2.18 |

**Table. 5. Particulate matter collected by IOM Dust sampler with dust proof cover**

| Sl. No. | Sampling Duration, min | Initial Weight, g | | Final weight, g | | Difference in weight, g | |
|---|---|---|---|---|---|---|---|
| | | Inhalable dust | Repairable dust | Inhalable dust | Repairable dust | Inhalable dust | Repairable dust |
| 1 | 15 | 1170 | 1231 | 1172.6 | 1242.6 | 11.6 | 2.6 |
| 2 | 15 | 1170 | 1231 | 1172.3 | 1239.5 | 8.5 | 2.3 |
| 3 | 15 | 1170 | 1231 | 1171.8 | 1241.2 | 10.2 | 1.8 |
| 4 | 15 | 1170 | 1231 | 1172.4 | 1238.7 | 7.7 | 2.4 |
| Mean Value | | | | | | 9.50 | 2.27 |

**Fig. 10. Integrated turmeric value chain machinery**

This new approach to turmeric processing using the above value chain machinery has the potential to improve the quality of finished product. The processing time can be reduced to 2 days from 28 days. However, there are certain bottlenecks and constraints towards the adoption of this improved method of which the most crucial one is energy cost, particularly for drying operation. About 200 units (kWh) of energy are consumed to dry a batch of 400 kg of turmeric. One possible way to reduce drying energy costs is to split the drying process by including a solar tunnel drying option before the rotary drying. It is suggested that solar drying of turmeric can be a viable first stage of drying. A limited 10- day trial of drying 500 kg of turmeric using solar tunnel drier was attempted in the laboratory of TNAU, Coimbatore, India during the growing season of 2016 but with limited success due to interruption by rain. Also, the turmeric after boiling is saturated with moisture and it presents a challenge during the initial phase of drying. The outer skin peels off when the moisture level of fingers remains high and is subjected to rotational motion. An intermediate step of drying using flatbed dryer to lower the moisture level from saturation by 10%-20% (d.b) was attempted, which resulted in good quality dried rhizomes. Considering the above issues, a combination drying could become a viable and economic option.

## 4. CONCLUSIONS

In conclusion, the development of machinery designed to enhance the postharvest handling and processing of turmeric rhizomes plays a crucial role in strengthening the overall turmeric value chain. It highlights the issues with conventional practices, such as labour-intensive operations, microbial contamination, and curcumin loss. Besides connecting conveyors, the machinery comprises four main components namely, a washer, a boiler, a dryer, and a dust-free polisher, designed to streamline the process and enhance product quality. The washer cleans the rhizomes, the boiler ensures uniform blanching, the dryer removes moisture efficiently, and the polisher operates in a dust-proof enclosure. The advantages include high-quality finished products, improved colour and curcumin retention, elimination of microbial load, time and labour savings, and cost-effective operations. The total machinery cost is estimated at INR 20 lakhs (USD 23,500), with an operational time of 2-3 days and an overall throughput of 4 tonnes per day which is suitable for an average turmeric grower. Moreover, the cost of the value chain machinery

is prohibitive for small and medium farmers and a cluster-based approach is necessary to establish a scaled-up version of the turmeric value chain machinery.

## ACKNOWLEDGEMENT

The authors acknowledge the financial support rendered by the Indian Council of Agricultural Research through All India Coordinated Research Project on Postharvest Technology for this research during 2016-2019 at the Agricultural Engineering College and Research Institute, TNAU, Coimbatore, India.

## REFERENCES

1. Aishwarya, S. 2018. *Design and development of turmeric dryer*. Unpublished M.Tech. Thesis, Tamil Nadu Agricultural University, Coimbatore, India, 68 p.
2. Arora, M., Sehgal, V. and Sharma, S. J. 2007. Quality evaluation of mechanically washed and polished turmeric rhizomes. *Journal of Agricultural Engineering* (ISAE), 44(2): 39-43.
3. Balakrishnan, M., Jeevarathinam, G., Aiswariya, S., Ambrose, R. K., Ganapathy, S. and Pandiselvam, R. 2022. Design, development, and evaluation of rotary drum dryer for turmeric rhizomes (*Curcuma longa* L.). *Journal of Food Process Engg*., 45(6): e14052. DOI: 10.1111/ jfpe.14052.2022;45:e14052.
4. Bhattacharya, S. 2014. *Conventional and advanced food processing technologies.* John Wiley & Sons, USA. DOI:10.1002/9781118406281.
5. El-Saadony, M. T., Yang, T., Korma, S. A., Sitohy, M., El-Mageed, A., Taia, A., . . . Mahmmod, Y. J. 2023. Impacts of turmeric and its principal bioactive curcumin on human health: Pharmaceutical, medicinal, and food applications: A comprehensive review. *Frontier in Nutrition*, 9:1040259. doi: 10.3389/fnut. 2022.1040259.
6. Farzana, W. 2018. *Design and development of turmeric boiler.* Unpublished M.Tech. Thesis, Tamil Nadu Agricultural University, Coimbatore, India, 82 p.
7. Farzana, W., Pandiarajan, T. and Ganapathy, S. 2018. Development of mobile boiling system for turmeric (*Curcuma longa* L). *Innoative Food Science & Emerging Technologies*, 47, 428-438. https://doi.org/10.1016/j.ifset.2018.04 .014.
8. Hailemariam, M.M., Abera, S. and Neme, G. 2023. Effects of processing methods on the quality of turmeric (*Curcuma longa* L.). *Spices Research Achievements, Challenges and Future Prospects in Ethiopia.* 4 (January): 9–17. https:// doi.org/10.14662/ARJASR2015.061.
9. Hirko, B., Abera, S. and Mitiku, H. 2020. Effect of Curing and Drying Methods on the Biochemical Quality of Turmeric (*Curcuma longa* L.) Rhizome Grown in South Western Ethiopia. *Med Aromat Plants (Los Angeles)*, 9: 357. doi: 10.35248/2167-0412.20.9.357.
10. Jyotirmayee, B., Nayak, S.S., Mohapatra, N., Sahoo, S., Mishra, M. and Mahalik, G. 2024. Bioactive Compounds and Biological Activities of Turmeric (*Curcuma longa* L.). In: Murthy, H.N., Paek, K.Y., Park, SY. (eds.), Bioactive Compounds in the Storage Organs of Plants. *Reference Series in Phytochemistry*. Springer, Cham. (pp. 395-423). https://doi.org/10.1007/ 978-3- 031- 44746-4-20.
11. Manjunatha, A.V., Ramappa, K.B., Maruthi, I. and Parmod Kumar. 2017. Impact Evaluation of National Horticulture Mission (NHM) and

Horticulture Mission for North East and Himalayan States (HMNEH) - Role of National Level Agencies, ADRT Centre, Institute for Social and Economic Change, Bengaluru, Karnataka.

12. Prasath, D., Kandiannan, K., Aarthi, S., Sivaranjani, R., Sentamizh Selvi, B. and Raghuveer, S. 2024. Turmeric. In: P.N. Ravindran *et al.* (Eds.) *Handbook of Spices in India: 75 Years of Research and Development.* pp. 1793-1912. Springer Nature Singapore Pte Ltd. https://doi.org/10.1007/978-981-19-3728-6_12755 2024.
13. Saha, G., Sharangi, A. B., Upadhyay, T. K., Al-Keridis, L. A., Alshammari, N., Alabdallah, N. M. and Saeed, M. J. A. 2022. Dynamics of drying turmeric rhizomes (*Curcuma longa* L.) with respect to its moisture, color, texture and quality. *Agronomy*, 12(6): 1420. https://doi.org/10.3390/agronomy 12061420.
14. Sharifi-Rad, J., Rayess, Y. E., Rizk, A. A., Sadaka, C., Zgheib, R., Zam, W., . . . Zielińska, D. J. 2020. Turmeric and its major compound curcumin on health: bioactive effects and safety profiles for food, pharmaceutical, biotechnological and medicinal applications. *Frontiers in Pharmacology*, 11: 550909. doi: 10.3389/fphar.2020.01021.
15. Susendran, T.S. 2018. *Design and development of turmeric washer.* Unpublished M.Tech. Thesis, Tamil Nadu Agricultural University, Coimbatore, India, 74 p.
16. Susendran, T.S., Sudagar, I.P., Ganapathy, S. and Aruna, P. 2019. Design and development of turmeric washer. *International Journal of Agricultural Sciences*, 11(10): 8541 – 8544.
17. Viswanathan, R., Devadas, CT. and Sreenarayanan, V. V. 2002. Farm level steam boiling of turmeric rhizomes. *Spice India*, XV(7): 2-3.

International Agricultural Engineering Journal ISSN 0858-2114

*September 2025, 34(1-4):17-28*

# Development of an Artificial Intelligence (AI) based Image Processing System for Industrial Sorting of Big Onion

**H.A.S.V. Attanayake[1], K.S.P. Amaratunga[1], K.P. Chathumal[1], C. Wangmo[2]**

## ABSTRACT

Onion (*Allium cepa* L.) is a culinary staple worldwide with retail markets use relying on manual sorting processes to deliver high quality onions to customers. This study explores the use of machine learning techniques in artificial intelligence (AI) for image processing to enhance this sorting process. Specifically, the SSD MobileNetV2 (MobileNet Single Shot Detector) model, utilizing Open CV and TensorFlow Python modules, was employed to classify onions into pre-determined categories quality, rotten, sprouted and double bulbs. Image acquisition was carried out using a Pi Camera module and a Raspberry Pi Single Board Computer, with the acquired images used for training, validating and testing the model. The developed TensorFlow Lite model was then evaluated in real-time, achieving an overall mAP of 77.94%, F1 Score of 0.82, accuracy of 91.62%, precision of 83.90% and recall value of 82.92% under controlled lighting conditions. This model demonstrates the potential for industrial onion sorting with a conveyor belt feeding system.

***Keywords:*** *Big onion; Image Processing; Raspberry Pi; SSD Mobile Net V2; TensorFlow.*

## 1. INTRODUCTION

Onion (*Allium cepa* L.) is a key culinary ingredient in Sri Lanka and worldwide. The underground bulb of this monocot plant, in the Alliaceae is family of the Liliopsida class, is primarily consumed. Consumers select high-quality onions by evaluating external characteristics such as color, shape, size, odor, and sprouted. However, in supermarket chains in Sri Lanka, where large quantities of onion and other agricultural produce are handled, manual sorting is done before reaching customers. Typically, these supermarket chains have regional collection centers where onions are brought in bulk and sorted manually.

Data from the Cargill Fruit and Vegetable Collection Center in Wattala, Sri Lanka, shows that the rate of manual onion sorting is 156 kg per man-hour. In Sri Lanka, only 23.71% of onions are is domestically produced (Rambukwella *et al.*, 2022) with the majority being imported. The countries onion demand is primarily met through imports, mainly from India, Holland, and occasionally Pakistan, based on bilateral agreements between the countries. Among the imported varieties, Indian onions are particularly popular for their well-cured nature, preferred shape, distinctive light magenta color, and pungency. The 'Pusa Red' variety imported from India is the most favored among Sri Lankans due to its pungency, color, and shape.

[1]Department of Agricultural Engineering, University of Peradeniya, Peradeniya, Sri Lanka.

[2]Agriculture Machinery Technology Centre, Department of Agriculture, Paro, Bhutan.

**Corresponding author – email:sunimaliattanayake@gmail.com*

Received: 24 November 2024; Revised: 12 March 2025; Accepted: 12 May 2025.

In supermarket chains, big onions are sorted into different quality parameters before reaching customers to provide premium quality. According to Cargill Food City Supermarket Chain's quality parameters, well- cured onions weighing between 40g and 200g with single undamaged outer scales are accepted for premium quality. Onions that are rotten, sprouted, double bulbs, have two scales, damaged outer scales or unsealed necks are rejected.

Due to labour – intensive and time – consuming of these sorting procedures, image processing techniques related to Machine Learning and Artificial Intelligence can be used to enhance sorting efficiency. Image processing techniques have been used for many agricultural processes for identification purposes (Sharma, 2021) and have contributed to the sustainability of world agriculture (Sachithra and Subhashini, 2023). In the market, there are many onion grading machines used for grading the onions into different size categories. However, the availability of industrially suitable machinery for sorting onions using image processing techniques is very less. This is due to the availability of many varieties of onions in the world market and the less availability of rich image datasets containing different varieties of onions and their defects. In developing countries like Sri Lanka, utilizing high-tech machines can be costly, making it more economical to hire people initially rather than investing in sophisticated equipment. Leveraging existing technologies, like Raspberry Pi single board computers and Pi Camera modules, can provide cost – effective solutions for sorting onions without straining finances.

Incorporating artificial intelligence (AI) and machine learning (ML) can significantly benefit the the agricultural sector and help feed the growing world population. Technical advancements, like big data analytics, robotics, the internet of things, the low-cost sensors and cameras, drone technology, and widespread internet connectivity in geographically separated fields, enable the application of AI in agriculture (Eli-chukwu, 2019). AI is used in various areas of agriculture, including general crop management (Sharma, 2021), pest and disease management, disease management, agricultural product monitoring and storage control, and soil and irrigation management (Bannerjee *et al.*, 2018).

The edible part of a big onion consists of swollen leaves arranged concentrically around a stem. Due to their high moisture content, onion bulbs prone to microbial infections and mechanical damage (Saibu *et al.* 2019). Countries like China, India, the United States, Egypt, Turkey, Pakistan, Sudan, Bangladesh, and Iran are major producers of onions (Paymode *et al.*, 2021). Sri Lanka producing less than its domestic requirement, needs to improve curing and storage conditions for big onions. Curing is a process that removes excess moisture from the neck. Curing is a special process as moisture is only removed from the outer layer of the onion bulb, not from the entire bulb. This can be done by windrowing the onions in the fields or by providing artificial or forced air (Gorrepati *et al.*, 2017) and thereby physiological weight loss, rotting of the bulbs, sprouting of the bulbs, and the overall postharvest losses are reduced (Nega, *et al.*, 2015). Sorting and grading are done to improve the market value of the produce (Gayathri, 2023). So the developed automatic sorting devices should have the ability to detect materials on a sorting surface (usually a sorting bed or a conveyor) and automatic removal of the impurities in bulks (Dorokhov *et al.* 2021). Unless manual labor is used, these operations consume huge amounts of energy and as the harvested produce is handled many times during these processes, it increases wastage resulting poor market value of the produces. Most of the grading machines are mechanical graders, grading depending on the size, shape, color, and weight of the onions (Gayathri, 2023). The most common manual grading machines are roller and sieve machines. But they are not capable of sorting onions according to the quality parameters. Therefore, machine learning has been used in sorting onions using image processing techniques

with Raspberry Pi Single computers (Dorokhov *et al.* 2021). Detection of infected and non-infected onions based on their external characteristics has been done using various methods. A machine imaging system is an inexpensive instrument that provides accurate onion bulb assessment, fast processing, and dependable operation (Waghmare *et al.*, 2024). A computerized method for identifying images that focuses on the fruit's imperfections both internally and externally has been produced (Njoroge *et al.*, 2002). Convolutional Neural Networks (CNN) based onion sorting systems have been developed to identify good quality and damaged onions using the Fruit 360 database Waghmare *et al.*, 2024). This is an open-source database available with a collection of 100×100 fruit images of 131 varieties of fruits in the world (Fruits – 360).

TensorFlow is widely recognized as a versatile machine learning framework that is particularly effective for image processing tasks, such as image classification and recognition, through the use of deep neural networks (DNNs) and convolutional neural networks (CNNs) (Yadav *et al.*, 2022). These models are integral to image classification, a subset of image processing, which involves assigning categories to images based on their content (Devi *et al.*, 2021). This is used in hierarchical image classification for waste object detection and edge-aware image filtering to preserve significant edges without post-processing steps (Kim *et al.*, 2020). Its use in various studies underscores its capability to facilitate complex image classification and processing procedures, contributing to narrowing the gap between computer and human vision (Yadav *et al.*, 2021), as well as enhancing the accuracy and efficiency of image analysis across different applications (Kim *et al.*, 2020). These networks are characterized by their use of convolution operations, which allow them to capture local and global features in data, and their ability to form hierarchical representations.

CNNs have been successfully applied in areas such as psychiatry, neurology, computer vision, and pattern recognition, demonstrating their versatility and effectiveness (Zhou, 2018). Interestingly, despite their widespread use and success, the theoretical foundations of CNNs, such as their universality of approximation, are not fully understood (Pinaya *et al.*, 2020). Recent studies have started to address these gaps, showing that CNNs can approximate any continuous function given sufficient depth (Han *et al.* 2023). Additionally, CNNs have been adapted to preserve specific invariances, such as gauge equivariance in lattice gauge theories, which traditional CNNs cannot capture (Favoni *et al.*, 2023). Therefore, CNNs are a powerful tool in deep learning with a wide range of applications and are distinguished by their structured architecture, which enables them to efficiently process and learn from high-dimensional data. While there is ongoing research to fully understand their theoretical properties, the practical successes of CNNs are undeniable, and they continue to be a focal point of innovation in machine learning (Xu *et al.*, 2020).

Supervised learning in machine learning is a paradigm where models are trained using labelled data, which means that the input data is paired with the correct output (Saravanan & Renuka, 2018). In the context of object detection, supervised learning algorithms require a dataset with annotated images where the locations and categories of objects are specified (Xu *et al.*, 2020). This approach is widely used due to its effectiveness in learning from the provided annotations to detect and classify objects in new images. However, the production of labelled datasets for object detection is labor-intensive and costly, which limits the scalability of supervised learning methods (Zhang *et al.*, 2020).

SSD MobileNet V2 is a Convolutional Neural Network architecture that aims to perform well on mobile devices. It is based on an inverted residual structure where the residual connections are between the bottleneck layers. The Single Shot MultiBox Detector (SSD) framework, when

combined with MobileNet V2, is a powerful architecture for object detection tasks, especially when transfer learning is applied. The integration of SSD with MobileNet V2 is optimized for real-time processing, offering a balance between speed and accuracy (Cai *et al.*, 2020). Thus SSD MobileNet V2 is a viable option for transfer learning applications, providing a good trade-off between detection speed and accuracy. However, its performance on small target detection could be a potential area for further optimization (Zhang *et al.*, 2020).

Therefore, this research aims to develop and evaluate an AI based image processing system to accurately sort onions based on predefined quality parameters with enhanced sorting efficiency, reduced labour dependency while ensuring high classification accuracy.

## 2. MATERIALS AND METHODS

### 2.1 Onion Classification Workflow Overview

Onion sorting was a high-labor-cost process, and to address this challenge, an Artificial Intelligence-based image processing system was developed for use in an industrial setting. The first step was to establish sorting criteria, which included good quality onions, double bulbs, sprouted onions, and rotten onions. Images of onion from each category were then obtained, annotated and used to train the model. The TensorFlow Lite model in a Google Colab Notebook using the annotated images. The model was then deployed and run on a Windows 10 (PC) through PyCharm IDE (Integrated Development Environment). Validation of the model wasconducted using images and also by running the model with onion samples in real time.

### 2.2 Image Acquisition and Annotation Process

Data acquisition was a crucial part of the project as the rest of the project relied on the images of onions captured for the four different classes of onions. As the first step, illumination of the onions was needed. It was done by building a light box. The box was illuminated by using a WS2811 addressable RGB LED strip connected to an Arduino Uno Board to provide lighting of the colour combination 200, 255, 200 RGB. The LED strip was attached to a reflector (Fig. 1) and a diffuser (Fig. 2). A Pi Camera module v 1.3 and a Raspberry Pi 3 was used for capturing the images

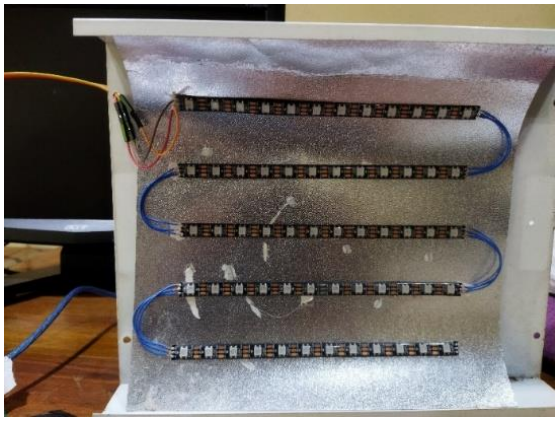

**Fig. 1. WS2811 LED strip attached to the reflector**.

The interior of the light box was painted white to ensure uniform illumination. Images of the four classes of onions were captured using the Pi Camera module and saved in the .jpg (Joint Photographic Experts Group) format. The images were then annotated using the LableImg Tool to convert them into .xml (Extensible Markup Language) format. The Graphical User Interface (GUI) of the LabelImg Tool is shown in Fig. 3.

**Fig. 2. Pi Camera module attached to the diffuser**


**Fig. 3. Graphical user interface (GUI) of the LabelImg tool**

A total of 440 images were obtained and they were classified for model training, validation and testing in the following manner.

### 2.3. Model Training Using Tensor Flow and Open CV on Google Colab

After annotating the images, the TensorFlow model was trained using the Google Colab Notebook (by Google LLC.). The GPU (Graphical Processing Units) memory of Google Colab Notebook, along with the OpenCV (a community developed and managed library with major contributions from Intel) and TensorFlow (owned by Google LLC). Python modules, were used to develop the TensorFlow object detection model. The number of training steps and batch size were set to 20,000 and 16, respectively. Once the TensorFlow model was created, it was tested using images of onions that were not used during the training the process.

Following are the specifications used in training the model.

Images per class: 110

Total images : 440

Split : 80% training, 10% validation, 10% testing (manually split with script)

Model : SSD MobileNetV2 FPN-Lite 320x320 (COCO trained, TensorFlow 2.8)

Layer freezing : Early layers were frozen, later layers fine-tuned

Batch size : 16

Training steps : 20,000

While there are other models available, such as the YOLOv4 model for real-time image classification, SSD MobileNetV2 was chosen for its low latency and real-time performance, which are crucial for onion sorting on Raspberry Pi 3B. Although YOLOv4 provided slightly higher accuracy, it resulted in slower inference speed and lower FPS, making it unsuitable for time-sensitive industrial applications. SSD MobileNetV2 offered a better balance between speed and accuracy, ensuring smooth real-time detection with acceptable precision (Mobilenetv and Chimakurth, 2024).

### 2.4. Real-Time Model Deployment and Evaluation Setup

The model was then converted to a TensorFlow Lite model and deployed on a Windows operating

system laptop PC, connected to a 1080P HD USB web camera. The camera was placed inside the same light box to capture real time video of the onions. The predicted class of the onion is displayed on the computer screen with the Confidence Score and the frame rate of the captured video in real time. This output is also displayed outside of the light box in a 16 x 2 LCD display connected to the same Arduino Uno board which is connected to the WS2811 LED strip. The component connections are shown in Fig. 4.

### 2.5. Real-Time Model Evaluation Using Confusion Matrix-Based Metrics

Using 60 onions from four categories, the model was evaluated for real time detection of onions. By comparing the actual and predicted classes of the onions, binary matrices were created to obtain True Positive, True Negative, False Positive and False Negative values. From these values, accuracy, precision, recall, and F1 score were calculated.

$$Accuracy = \frac{TP+TN}{TP+TN+FP+FN} \quad \ldots (1)$$

$$Precision = \frac{TP}{TP+FP} \quad \ldots (2)$$

$$Recall = \frac{TP}{TP+FN} \quad \ldots (3)$$

$$F1\ Score = \frac{2 \times Precision \times Recall}{Precision+Recall} \quad \ldots (4)$$

Where, *TP* is true positive; *TN* is true negative; *FP* is false positive and *FN* is false negative.

### 2.6. Physical System Evaluation

The physical component of the system including the lighting box, Raspberry Pi, camera, and display were successfully deployed and were able to classify onion samples in real time. However, due to the manual placement of onions inside the lighting box, it was not possible to measure the sorting speed or throughput rate (*e.g.* onions sorted per minute). The system provided immediate classification outputs upon detection, indicating low inference latency. To comprehensively evaluate the end-to-end system performance, future development will include a conveyor-based feeding mechanism.

## 3. RESULTS AND DISCUSSION

### 3.1. Mean Average Precision (mAP)

The model achieved an overall mean Average Precision (mAP) of 77.94% using the COCO evaluation metric at IoU thresholds ranging from 0.50 to 0.95. This indicates that the model performs well not only in identifying onion categories but also in accurately localizing them within the images. Among the four classes, the highest mAP was recorded for good onions (89.09%), followed by sprouted onions (79.06%), rotten onions (75.24%), and double onions (68.37%). The relatively lower mAP for double onions may be attributed to their visual similarity with other categories, particularly sprouted onions (Table 1). Overall, the mAP score demonstrates the model's strong capability in both detection and localization, making it suitable for practical use in onion sorting under varied real-world conditions. The accuracy, precision, recall and F1 Score values obtained for the different classes of onions are given in Table 1.

**Table 1. Image allocation for model training, validating and testing**

| Class | Train | Validation | Test |
|---|---|---|---|
| Good | 88 | 11 | 11 |
| Double | 88 | 11 | 11 |
| Rotten | 88 | 11 | 11 |
| Sprouted | 88 | 11 | 11 |
| Total | 352 | 44 | 44 |

### 3.2 Accuracy

Accuracy in object detection refers to the proportion of correctly classified objects compared to the total number of objects present in the data set. It is a fundamental metric in evaluating the performance of object detection models, providing insights into how well the model identifies and localizes objects within an image. A high accuracy value signifies that the model is proficient in accurately detecting objects across various classes, while a lower accuracy

indicates potential areas for improvement, such as mis-classifications or missed detections. Considering the accuracy values provided for each onion class in Table 2 and the overall accuracy, it's evident that the model performs admirably in object detection tasks.

With accuracies ranging from 88.33% to 96.49% across different onion categories, the model showcases its capability to accurately identify and classify onions based on their attributes. Particularly noteworthy is the model's exceptional accuracy of 96.49% in detecting "rotten" onions, indicating robust performance in identifying deteriorated produce. Overall, the model achieves a commendable accuracy of 91.62%, signifying its effectiveness in accurately detecting onions across all classes and highlighting its potential for various real-world applications.

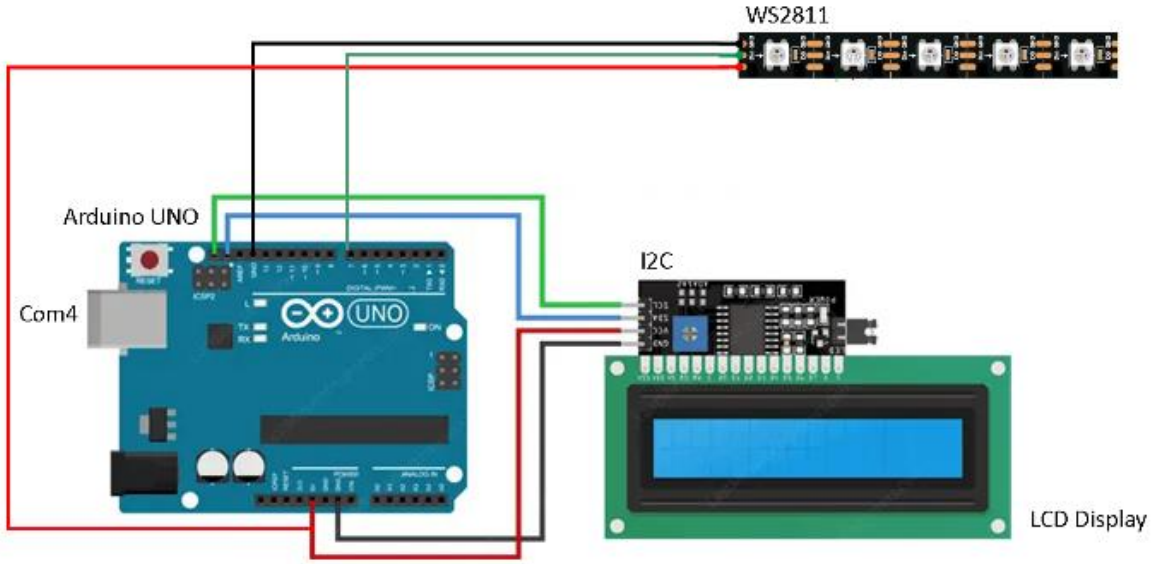


**Fig. 4. Circuit diagram of the components connected to Arduino Uno**

**Table 2. The mean Average Precision (mAP), Accuracy, Precision, Recall and F1 – Score for different classes of big onion**

| Class | mAP, % | Accuracy, % | Precision, % | Recall, % | F1 - Score |
|---|---|---|---|---|---|
| Good onion | 89.09 | 88.33 | 78.57 | 73.33 | 0.76 |
| Sprouted onion | 79.06 | 90.00 | 73.68 | 93.33 | 0.82 |
| Rotten onion | 75.24 | 96.49 | 91.67 | 91.67 | 0.92 |
| Double onion | 68.37 | 91.67 | 91.67 | 73.33 | 0.81 |
| Overall | 77.94 | 91.62 | 83.90 | 82.925 | 0.83 |

With accuracies ranging from 88.33% to 96.49% across different onion categories, the model showcases its capability to accurately identify and classify onions based on their attributes. Particularly noteworthy is the model's exceptional accuracy of 96.49% in detecting "rotten" onions, indicating robust performance in identifying deteriorated produce. Overall, the model achieves a commendable accuracy of 91.62%, signifying its effectiveness in accurately detecting onions across all classes and highlighting its potential for various real-world applications.

### 3.3 Precision

Precision in object detection refers to the proportion of correctly detected objects among all objects that the model has classified as belonging to a particular class. It provides insights into the model's ability to accurately identify objects of interest without falsely classifying unrelated objects. A high precision value indicates that the model makes fewer false positive classifications, resulting in a more reliable detection of objects within images. Considering the precision values provided for each onion class in the Table 1 and the overall precision, it is apparent that the model demonstrates commendable precision in object detection tasks. With precision values ranging from 73.68% to 91.67% across different onion categories, the model showcases its capability to accurately classify onions based on their attributes. Notably, both "double" and "rotten" onions exhibit the highest precision values at 91.67%, indicating the model's proficiency in correctly identifying these categories. While "good" onions have a slightly lower precision of 78.57%, "sprouted" onions exhibit the lowest precision at 73.68%. Nonetheless, the overall precision of 83.89% underscores the model's effectiveness in accurately detecting onions across all classes, highlighting its potential for various real-world applications.

### 3.4 Recall

Recall in object detection refers to the proportion of correctly detected objects of a particular class out of all the objects belonging to that class in the data set. It provides insights into the model's ability to capture and identify all instances of a specific object class, thereby minimizing false negatives. A high recall value indicates that the model can effectively detect most of the objects belonging to a particular class, ensuring comprehensive coverage of the target objects within images. Referring to the values of recall in Table 1 for each onion class, and the overall recall, it is evident that the model demonstrates commendable performance in recalling objects across various categories. With recall values ranging from 73.33% to 93.33%, the model showcases its capability to effectively identify onions based on their attributes. Notably, "sprouted" onions exhibit the highest recall at 93.33%, followed closely by "rotten" onions with a recall of 91.67%. While both "good" and "double" onions maintain consistent recall values at 73.33%, the overall recall of 82.915% underscores the model's effectiveness in capturing a significant proportion of onions across all classes, highlighting its robust performance in object detection tasks.

### 3.5 F1 Score

The F1 score, a metric commonly used in classification tasks, combines precision and recall into a single value, providing a balanced assessment of a model's performance. A high F1 score indicates both high precision and recall, with values ranging from 0 to 1. It is particularly useful when the class distribution is imbalanced, as it considers false positives and false negatives equally. Referring to the data in Table 1, combining the individual F1 scores provided for each class, the overall performance of the model can be assessed. With a good F1 score of 0.76 for "good" onions, the model exhibits reasonable performance, while scoring slightly higher for "double" onions at 0.81. Moreover, it demonstrates even better performance in identifying "sprouted" onions, achieving an F1 score of 0.82. Impressively, the model excels in identifying "rotten" onions, boasting the highest F1 score of 0.92. The overall F1 score of 0.8275 reflects the model's balanced precision and recall across all classes, indicating its effectiveness in classification tasks. However, there remains potential for enhancement, particularly in refining the identification of less well-performing classes.

During real-time evaluation, several misclassifications were observed, primarily due to lighting variations, partial occlusion, and visual similarities between certain onion categories like overlapping physical features such as protrusions or stem remnants. Inconsistent illumination inside the light box also contributed to missed detections or

low-confidence predictions. These errors suggest that the model is sensitive to environmental factors and the orientation of the object. Enhancing the lighting setup, using image augmentation during training, and incorporating more diverse training samples could help reduce these issues. Furthermore, future work could integrate multi-angle image capture or depth sensing to improve detection robustness under variable conditions.

## 4. CONCLUSIONS

In developing an AI-based image processing system for sorting big onions, various performance metrics such as mean Average Precision (mAP), accuracy, precision, recall and F1 score, play pivotal roles in evaluating the effectiveness of the model. The overall mAP of the model for accurately sorting big onion was 77.94%. Across different onion classes, the model exhibits robust performance, with an overall F1-score of 0.83. Additionally, the overall accuracy value, precision value and recall value were 91.62%, 83.90%, and 82.92%, respectively. Overall, these metrics collectively indicate the strong performance of the model in accurately identifying big onions, laying a solid foundation for its practical application in real-world sorting processes. However, continuous refinement and optimization may further enhance its performance, ensuring precise and reliable sorting in diverse operational settings.

## ACKNOWLEDGMENT

This project was supported by the Cargills (Ceylon) PLC, No. 40, York Street, Colombo.

## REFERENCES

1. Bannerjee, G., Sarkar, U., Das, S. and Ghosh, I. 2018. Artificial Intelligence in Agriculture :A Literature Survey. *International Journal of Scientific Research in Computer Science Applications and Management Studies*, 7(3):1-6.
2. Cai, L., Dong, K., Chen Feng, Yu, K., Qu, W. and Jiang, J. 2020. An FPGA based heterogeneous accelerator for single shot multibox detector (SSD). In. *2020 IEEE 15th International Conference on Solid-State & Integrated Circuit Technology (ICSICT)*, pp. 1–3.
3. Devi, M. R. S., Kumar, V. V. and Sivakumar, P. 2021. A review of image classification and object detection on machine learning and deep learning techniques. In. *2021 5th International Conference on Electronics, Communication and Aerospace Technology (ICECA)*, pp. 1–8.
4. Dorokhov, A., Aksenov, A., Sibirev, A., Sazonov, N., Mosyakov, M. and Godyaeva, M. 2021. Results of Laboratory Studies of the Automated Sorting System for Root and Onion Crops. *Agronomy*, *11*(6):1257 https://doi.org/10.3390/ agronomy11061257
5. Eli-chukwu, N.C. 2019. Applications of Artificial Intelligence in Agriculture : A Review. *Engineering, Technology & Applied Science* Research, 9(4): 4377–4383.
6. Favoni, M., Ipp, A. M., Ller, D. I. and Schuh, D. 2022. Lattice gauge equivariant convolutional neural networks. *Physical Review Letters.*, 128: 032003.
7. Fruits-360. 2024. https://www.kaggle.com/ datasets/moltean/fruit. Accessed: January 25, 2024.
8. Gayathri,G. 2023. Design, development and evaluation of a manually operated onion grader for Rose onion. *International Journal of Agricultural Engineering*, 9(2):121-129 https://doi:10.15740/HAS/IJAE/9.2/121-129. 10

9. Gorrepati, K., Onion, D. O., Thangasamy, A. and Murkute, A. 2017. Curing of Onion: A Review. *Indian Horticulture Journal*, 7(1): 08-14
10. Han, Z., Liu, B., Lin, S.B. and Zhou, D.X. 2023. Deep Convolutional Neural Networks with Zero-Padding: Feature Extraction and Learning. *arXiv Prepr. arXiv2307.16203*.
11. Kim, S., Song, C., Jang, J. and Paik, J. 2020. Edge-aware image filtering using a structure-guided CNN. *IET Image Process.*, 3: 472–479.
12. Chimakurthi, A.K. and Chimakurthi, L.P. 2024. Enhancing Real-Time Object Detection on Low-End Devices: A Comparative Study of Performance of YOLOv4 and SSD MobileNetv2. https://doi.org/10.21203/rs.3.rs-4901165/v1
13. Nega, B.G., Mohammed, A. and Menamo, T. 2015. Effect of Curing and Top Removal Time on Quality and Shelf Life of Onions (Allium cepa L .). *Global Journal of Science Frontier Research: D Agriculture and Veterinary*, 15(8-1):26-36.
14. Njoroge, J. B., Ninomiya, K., Kondo, N. Toita, H. 2002. Automated fruit grading system using image processing. In. *Proceedings of the 41st SICE Annual Conference. SICE 2002*. pp. 1346–1351.
15. Paymode, A. S., Mohite, J. N., Shinde, U. B., Malode, V. B., Engineering, T. and Cscoe, C. 2021. Engineering Trends Artificial Intelligence for Agriculture : A Technique of Vegetables Crop Onion Sorting And Grading Using Deep Learning. *International journal of advance scientific research and engineering trends*, 6(4):29–34. https://doi.org/10.51319/2456-0774.2021.4.0004.
16. Pinaya, W. H. L., Vieira, S., Garcia-Dias, R. and Mechelli, A. 2020. Convolutional neural networks. Machine Learning Methods and Applications to Brain Disorders, *Elsevier Inc*. pp. 173–191.https://doi.org/10.1016/C2017-0-03724-2.
17. Rambukwella, R., Vidanapathirana,R. and Dharmawardana,T. 2022. Big onion value chain a Story of Gaps, Hector Kobbekaduwa Agrarian Research and Training Institute. pp. 7-35 https://www.harti.gov.lk/images/download/publication/WP018.pdf (accessed on 03 June 2024).
18. Sachithra, V. and Subhashini, L. D. C. S. 2023. How artificial intelligence uses to achieve the agriculture sustainability: Systematic review. *Artif. Intell. Agric.*, vol. 8, pp. 46–59, 2023, doi: 10.1016/j.aiia.2023.04.002.
19. Saibu, S., Madende, M., Ayokun-nun, A. A. and Aladodo, R. A. 2019. The Genus Allium (Amaryllidaceae: Alloideae): Features, Phytoconstituents, and Mechanisms of Antidiabetic Potential of Allium cepa and Allium sativum. *Bioact. food as Diet. Interv. diabetes*, pp. 137–154.
20. Saravanan, P. and Sujatha, R. 2018. A state of art techniques on machine learning algorithms: a perspective of supervised learning approaches in data classification. In. *Second international conference on intelligent computing and control systems (ICICCS)*, pp. 945–949.
21. Sharma, R. 2021. Artificial Intelligence in Agriculture : A Review. *Iciccs*, pp. 937–942, 2021.
22. Tzachor, A., Devare, M., King, B. and Avin, S. 2022. Responsible artificial intelligence in agriculture requires

systemic understanding of risks and externalities. *Nature Machine Intelligence*, 4: 104–109. doi: 10.1038/s42256-022-00440-4.

23. Waghmare, S., Sanamdikar, S., Hirolikar, D. S., Vaidya,M., Pakle, G., Waghmare,P., Choudhari. D. 2024. Onion Classification using Color and Convolutional Neural Network. *Int. J. Intell. Syst. Appl. Eng.*, 12(5s): 174–180.
24. Xu, W., He, J., Shu, Y. and Zheng, H. 2020. Advances in convolutional neural networks. In. Fernandez M.A.A. (ed.), https://doi.org/10.5772/intechopen.93512
25. Yadav, A., Rais, I., Kumar, M., Sharma, A. and Kushwaha, A. 2022. Image Classification using Deep Learning and Tensorflow. *Int. J. Res. Appl. Sci. Eng. Technol.*, 10(V): 4196–4200.
26. Zhang, L.A., Baveye, D., Léveillé, J., Menthe, L., Gold, D., Hartnett, G.S., Hagen, J. and Xu, J., 2020. Operationally Relevant Artificial Training for Machine Learning: Improving the Performance of Automated Target Recognition Systems. RAND Corporation. Research reports. United States. https://coilink.org/ 20.500. 12592/s9h0cv (accessed on 25.07.2024).
27. Zhou, D.X. 2018. Deep distributed convolutional neural networks: Universality. *Anal. Appl.*, 16: 895–919.

International Agricultural Engineering Journal ISSN 0858-2114

*September 2025, 34(1-4):29-44*

# Comparative Performance Analysis of Machine Learning and Regression Models for Predicting the Angle of Repose of Sericea lespedeza Seeds

**Ramana M. Gosukonda[1*], Aftab Siddique[2], Ajit K. Mahapatra[2]**

## ABSTRACT

Flow properties play an important role in handling and processing food products especially during flow from hoppers, mixing, transportation, compression, and packaging. In recent years, machine learning (ML) has gained popularity in modeling complex and nonlinear processes. The objective of this study was to develop ML models to predict the angle of repose of sericea lespedeza seeds based on cultivar and seeds' moisture content, length, width, thickness, and weight. Prediction models were developed using support vector regressor (SVR), random forest regressor (RFR), decision tree (DT), backpropagation neural nets (BPNN), and K-nearest neighbor (KNN) learning algorithms and their performance was compared with regression models. Data for modeling were obtained from an experimental study at the Food Engineering Laboratory, Fort Valley State University, where seed properties were inputs, and the angle of repose was the output. Each model was validated using a ten-time 10-fold cross-validation with five-time 5-fold nested cross validation technique to prevent underfitting and overfitting. Various statistical indices, including Pearson correlations ($R$) between actual and predicted outputs, were evaluated to select the best models. Prediction plots for angle of repose values indicated that the ML models RFR, KNN, and DT demonstrated robust accuracy ($R > 0.98$), outperforming SVR, BPNN, and regression models ($R = 0.77$, 0.74, and 0.79, respectively). Additionally, ML models showed better generalization and interpolation of unseen patterns within the training domain. The analysis highlights the potential of AI to enhance predictions in nonlinear decision contexts without compromising performance in linear decision contexts.

***Keywords:*** *Ensemble learning (RFR); Tree-based algorithm (DT); Instance-based method (KNN); Artificial neural networks (ANN); Seed flow properties; Moisture content.*

## 1. INTRODUCTION

Sericea lespedeza (SL, *Lespedeza cuneata* (Dum.-Cours.)) is a leguminous plant of growing agricultural significance due to its diverse applications. Its seeds are rich in protein, tannins, and fiber, making them a valuable renewable feedstock and a potential source of anthelmintic bioproducts (Muir *et al.*, 2017). These seeds can be used in various applications, including animal feed, biofuel production, and soil conservation (Mosjidis, 1996). However, efficient handling and processing are crucial to fully realize their industrial potential.

[1]Department of Agricultural Sciences, [2]Agricultural Research Station, 1005 State University Drive, College of Agriculture, Family Sciences, and Technology, Fort Valley State University, Fort Valley, GA, USA.

**Corresponding author - email:* gosukonr@fvsu.edu

Received: 28 November 2024; Revised: 31 May 2025; Acepted: 01 June 2025.

A critical aspect of seed handling is understanding and predicting the flow properties of seeds. This is primarily evaluated by the angle of repose, a key indicator of how granular materials - such as seeds - flow. The angle of repose is the steepest angle relative to the horizontal plane at which a pile of material remains stable without slumping (Al-Hashemi and Al-Amoudi, 2018; Zaalouk and Zabady, 2009).

Seeds with a lower angle of repose form flatter piles and flow more easily due to reduced internal friction and resistance between individual seeds. Conversely, seeds with a higher angle of repose form steeper piles and tend to flow less freely, indicating greater internal friction and interlocking (Teferra, 2019; Madrid *et al.,* 2022). This can lead to issues such as clumping, bridging, or arching in storage and handling systems like hoppers and chutes. Therefore, understanding the angle of repose is essential for designing appropriate equipment for storage, transport, and processing, ensuring smooth flow and industrial efficiency (Teferra, 2019). Poor flowability, for example, can hinder conveying, metering, and blending operations, ultimately increasing operational costs (Al-Hashemi and Al-Amoudi, 2018; Madrid *et al.,* 2022).

Numerous studies have evaluated seed flowability by considering factors such as cultivar type, moisture content, length, width, and thickness as independent variables affecting the angle of repose (Rosentrater and Bucklin, 2022; Mahapatra *et al.,* 2019; Al-Hashemi and Al-Amoudi, 2018; Teferra, 2019). Different cultivars of the same crop can vary in physical characteristics, such as size, shape, and surface texture, which affect flow behavior and packing density. Studies have shown that such variations influence the mechanical and physical properties of the seeds, affecting how they interact and pile (Owolarafe *et al.,* 2007; Izli, 2015). This makes the cultivar type a critical variable in understanding the characteristics of the angle of repose

Moisture content is known to alter surface friction and cohesion between particles. As moisture content increases, adhesion between seeds generally rises due to capillary and viscous forces, resulting in a higher angle of repose (Bhabani *et al.,* 2022; Suleiman *et al.,* 2015). This is particularly important for grains stored in environments with fluctuating humidity. Additionally, the length, width, and thickness of seeds determine their shape and sphericity, influencing how the grains align and behave when piling. Seeds with irregular shapes or lower sphericity tend to interlock more and slide less easily, resulting in higher angles of repose (Aviara *et al.,* 1999; Coşkuner and Karababa, 2007). In contrast, smoother and more spherical particles typically flow better and have lower angles of repose.

Machine learning (ML) models - including support vector regression (SVR), random forest regression (RFR), decision trees (DT), backpropagation neural networks (BPNN), and K-nearest neighbors (KNN) - offer a promising approach to predicting seed flow behavior. These models can learn complex relationships between seed characteristics (e.g., moisture content, size and shape) and flowability, enabling accurate predictions of the angle of repose (Gosukonda *et al.,* 2017). Such predictive capability is invaluable for optimizing storage and handling practices to maintain ideal seed flow conditions. Machine learning models also play a crucial role in the design of efficient processing equipment. By understanding seed flow properties, engineers can design components such as hoppers and conveyors that handle and process seeds more effectively, reducing operational issues and energy consumption (Mahapatra *et al.,* 2019). Furthermore, ML models enable real-time monitoring and predicting flow behavior, allowing for automated adjustments to processing parameters. This improves efficiency, consistency, and overall performance in seed processing operations (Madrid *et al.,* 2022).

This study utilizes advanced machine learning models to predict the angle of repose of Sericea lespedeza seeds based of their physical properties, with a focus on the AU Grazer™ and Serala cultivars. The objective of this study is to enhance understanding of seed flow behavior to support decision-making in agriculture and industry. By leveraging ML, operational efficiency, innovation, and sustainability in the use of Sericea lespedeza seeds can be promoted.

## 2. MATERIALS AND METHODS

### 2.1. Experimental Procedures and Dataset Preparation

Experimental data for developing machine learning models were collected from studies conducted at the Food Engineering Laboratory at Fort Valley State University. Mahapatra *et al.* (2019) outlined the methods used to measure the physical and thermal properties of seeds, as well as the angle of repose for two Sericea lespedeza cultivars - AU Grazer™ and Serala. Parameters included seed length, width, thickness, weight, and angle of repose at five moisture levels; 8.57, 12.24, 17.07, 24.33, and 26.53% (wet basis).

To analyze seed dimensions and shapes analysis at each moisture level, 100 seeds were randomly selected from each cultivar. Dimensions, length, width, and thickness were measured with an electronic digital caliper, while individual seed weights were determined using a precision digital balance. Table 1 shows the range of observed values for all parameters, and Fig. 1 illustrates a typical SL seed's dimensions.

The angle of repose was measured using the funnel method, where seeds flowed through a funnel onto a flat surface, forming a conical shape. The resulting pile's height and base diameter were recorded to calculate the angle of repose using the eq. (1) by Altuntaş and Yildiz (2007):

$$\text{Angle of repose, } \theta = \tan^{-1}(h/r) \quad \ldots (1)$$

Where, $h$ is the pile's height, mm and $r$ is the base radius, mm.

The two Sericea lespedeza (SL) cultivars—AU Grazer™ and Serala were chosen for their distinct morphological and agronomic characteristics, making them ideal for assessing variations in flow behavior, especially the angle of repose. Machine learning models were developed to predict the angle of repose (output) based on input features, including cultivar type, moisture content, dimensions and weight. The algorithms included support vector regression (SVR), random forest regression (RFR), decision trees (DT), backpropagation neural networks (BPNN), and *K*-nearest neighbors (KNN), with comparisons to traditional regression models.

### 2.2. Machine Learning Software

Data analyzed was done using JMP Pro 17 (SAS Institute Inc., Cary, NC, USA), an analytics platform combining machine learning and statistical modeling. Cultivar type was encoded using binary coding (AU Grazer™ as 0 and Serala as 1) to treat it as a categorical variable without bias. Models were trained on raw data without feature engineering.

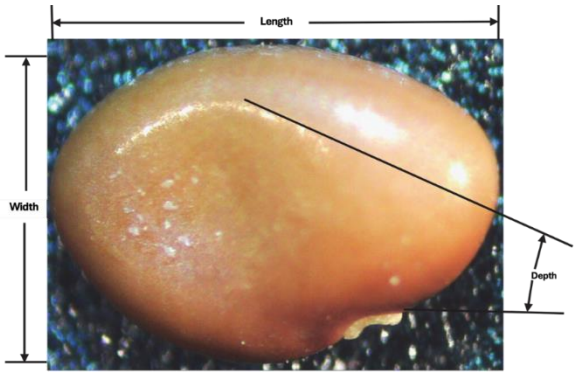


**Fig. 1. Illustration of geometry of a typical SL seed**

### 2.3. Selection of Datasets for Training and Validation of Models

Due to a relatively small dataset of 120 records (12 per moisture level), this study used a ten-times ten-fold outer cross-validation with a nested five-times five-fold inner cross-validation technique to reduce potential biases in machine learning

performance estimates (Vabalas *et al.*, 2019; Varma and Simon, 2006). This approach avoided under- and overfitting during model development, ensuring reliable performance evaluation. This *k*-fold nested validation technique consists of two levels of cross-validation: the outer level estimates the model's generalization error. In contrast, the inner level determines optimal hyper parameters for each model.

**Table 1. The range of seed property for AU Grazer™ and Serala cultivars of Sericea lespedeza across five moisture content levels.**

| Cultivar type | Moisture Content ($M_c$), % w.b. | Length ($L$), mm | Width ($W$), mm | Thickness ($T$), mm | Weight ($M$), mg | Angle of Repose ($\theta$), ° |
|---|---|---|---|---|---|---|
| AU Grazer | 8.57 | 1.28–2.31 | 0.99–1.50 | 0.63–0.99 | 1.90–3.30 | 17.22–19.06 |
| | 12.24 | 1.60–2.34 | 1.00–1.52 | 0.43–1.00 | 0.80–3.40 | 18.26–19.48 |
| | 17.07 | 1.68–2.45 | 1.10–1.51 | 0.58–1.05 | 1.10–2.60 | 18.62–20.18 |
| | 24.33 | 1.65–2.50 | 1.05–1.56 | 0.58–1.04 | 0.90–2.50 | 20.25–21.78 |
| | 26.53 | 1.78–2.74 | 1.12–1.77 | 0.54–1.01 | 1.10–3.50 | 26.75–28.03 |
| Serala | 8.57 | 1.62–2.36 | 1.12–1.51 | 0.48–1.00 | 0.90–3.00 | 19.43–21.21 |
| | 12.24 | 1.62–2.41 | 1.09–1.49 | 0.52–0.99 | 1.00–2.70 | 19.17–20.16 |
| | 17.07 | 1.64–2.54 | 1.20–1.66 | 0.62–1.11 | 1.10–3.10 | 19.51–20.31 |
| | 24.33 | 1.74–2.55 | 1.15–1.68 | 0.58–0.88 | 1.00–2.68 | 19.73–21.30 |
| | 26.53 | 1.79–2.63 | 1.26–1.69 | 0.58–0.98 | 1.00–2.90 | 29.21–31.04 |

For the outer *k*-fold cross-validation (10 folds), the records were randomly divided into ten equal folds (sets). The model was trained on *k*-1 folds (training set = 9 sets) and tested on the remaining fold (testing = 1 set). This process was repeated ten times, with a different fold used for testing each time. Within each outer loop iteration, the training set (*k*-1 folds) underwent a further five-fold inner nested cross-validation. This involved dividing the training set into five sets, using four folds for training and one - fold for validation. This process was repeated five times, with a different fold serving as the testing set each time.

The best-performing configuration from the inner loop was selected and used to train the final model on the combined outer training set, excluding the validation fold. Performance of the final model was evaluated on the held-out validation fold from the outer loop. At the outer level, the performance metrics from all *K* validation folds, such as accuracy, precision, and recall, were averaged to provide a more reliable and generalizable estimate of the model's performance on unseen data.

### 2.4. Machine Learning Algorithms Compared

#### 2.4.1 Support vector regressor algorithm

Although primarily known for classification, support vector machines (SVMs) can also handle regression tasks through a variant called support vector regressor (SVR) (Smola and Schölkopf, 2004). SVR seeks the optimal hyperplane in a high-dimensional space that best fits the training data, allowing for a specific level of deviation from the perfect fit without penalties (Smola and Schölkopf, 2004). This approach offers advantages such as robustness to outliers and effective pattern detection in datasets (Drucker *et al.*, 1996). A key feature of SVR is its use of kernel functions to handle non-linear relationships by mapping data into higher dimensions (Müller

*et al.,* 2001). Selecting the appropriate kernel and its parameters, along with other hyper parameters like C (regularization) and epsilon, is essential for optimizing SVR performance and achieving a balanced model that avoids underfitting and overfitting (Schölkopf *et al.,* 1998; Chapelle and Vapnik, 1999). Despite its exceptional resilience, particularly in high-dimensional spaces, SVR requires careful hyper parameter tuning and may face computational challenges with large datasets (Hsu *et al.,* 2008).

### 2.4.2 Random Forest regressor algorithm

Random Forests (RFs) are powerful ensemble learning algorithms known for constructing robust and accurate prediction models by leveraging the "bagging" technique, which combines predictions from multiple individual decision trees (Cutler *et al*., 2011). Each tree is trained on a random subset of the data and uses different features at each split point. This "forest" of trees collectively votes, resulting in a single model for making accurate predictions, enhancing diversity, and reducing overfitting (Breiman, 2001; Rodriguez-Galiano *et al*., 2015). While Random Forest Regressors (RFRs) provide strong predictive performance across diverse datasets and can handle complex data, they come with significant computational and memory demands, especially for large datasets. Additionally, RFRs involve hyper parameter tuning, such as the number of trees and 'mtry,' for optimal performance. The "mtry" parameter controls the number of features considered at each split during decision tree creation within a random forest. A smaller "mtry" is preferred for high-dimensional data to prevent overfitting, while a larger value might be suitable for low-dimensional data to capture complex relationships (Abbasi *et al*., 2021). Random Forest Regressors provide strong predictive performance and can handle complex data, making them valuable tools across diverse fields. However, their execution requires careful management of computational resources and meticulous hyper parameter tuning to mitigate overfitting and achieve optimal performance (Ben Ishak, 2016).

### 2.4.3. Decision tree learning algorithm

Decision trees are a non-parametric supervised learning method for classification and regression tasks. The objective is to create a model that predicts the target variable's value by learning simple decision rules from the data features. Functioning as a series of interconnected "if-then" statements, a DT forms a segmented prediction model (Quinlan, 1986). The recursive division of a dataset is based on the features that best separate the data into distinct groups or classes, resembling a hierarchical tree structure. The root node signifies the entire dataset, branches represent splits based on specific features, and leaves represent the final predicted classes or values (Quinlan, 1986).

Decision trees are highly interpretable, with paths from the root to the leaves explicitly capturing the decision-making process. This transparency aids in understanding the model's inner workings and identifying features with the most decisive influence (Ben-Gal *et al.,* 2014). Decision tree learning algorithms can handle numerical and categorical data while providing easy visualization. However, they may suffer from overfitting, instability, and high computational costs. Techniques such as pruning and hyper parameter tuning address these issues (Song and Lu, 2014). Additionally, decision tree algorithms can be sensitive to feature scaling, as different scales may introduce a bias towards features with larger values. However, feature scaling is frequently applied to mitigate this sensitivity (Song and Lu, 2014).

### 2.4.4. Multilayer perceptron with backpropagation algorithm

A multilayer perceptron (MLP) neural network with a feedforward architecture was chosen because of its ability to learn complex relationships in nonlinear data (White, 1992). The MLPs provide universal approximation capabilities and compact representations, making

them suitable for the present study (Isabona *et al.*, 2022). The network consists of an input layer that receives data, hidden layers that perform computations using transfer functions, and an output layer that makes predictions (Russell and Norvig, 2022). Neurons within each layer utilize non-linear activation functions (e.g., sigmoid, tanh, ReLU), crucial for transforming input into output. Backpropagation (BPNN) with gradient descent optimization to enhance prediction accuracy and data fit was employed. Backpropagation iteratively adjusts weights based on the difference between predicted and actual outputs, propagating errors backward through the network (Gosukonda *et al.,* 2015). This optimization process can be supported by techniques like grid search, random search, and Bayesian optimization (Gosukonda *et al.,* 2015).

### 2.4.5. K-nearest neighbor learning algorithms

*K*-Nearest Neighbors (KNN) is a supervised machine-learning algorithm recognized for its simplicity and versatility. It can be applied to classification and regression tasks, operating on the principle that data points with similar features will likely yield similar outcomes. Without explicit model building, KNN retains all data points during training (Dehariya *et al.,* 2010). It identifies the *K* nearest neighbors of a new data point for prediction. It predicts its class label (classification) through majority voting or its value (regression) by averaging the values of its neighbors (Arya *et al.,* 1998). The user-defined parameter *k* determines the number of neighbors considered. The algorithm employs different distance metrics tailored to the specific problem to gauge the similarity between data points, including Euclidean, Manhattan, or Minkowski distance (Zhang and Zhou, 2005).

The KNN algorithm has several advantages, such as being simple, flexible, and adaptable to different data types. It does not require assumptions about the underlying data distribution or training phase. Additionally, it can handle noisy and missing data by using weighted voting or imputation methods (James *et al.,* 2013). However, the KNN algorithm has some drawbacks, including being computationally expensive and sensitive to the choice of k, the distance metric, and irrelevant features. Furthermore, KNN's performance can deteriorate in high-dimensional data scenarios (James *et al.,* 2013).

## 2.5. Selection of an Optimal Model Configuration

The objective of ML models is to perform well on data not used during training. Therefore, each model's performance was assessed using a validation dataset. Since the validation dataset consists of new data records unseen by the model, its performance on this set is a more reliable indicator of generalization than performance on the training set (Gosukonda *et al.,* 2015).

Network configurations were determined empirically, and their performances were evaluated across the training, testing, and validation datasets using statistical metrics defined in eq.(2–6). To evaluate the ML models' performance in this study, several statistical indices were used, including the Pearson correlation coefficient (R), standard deviation, bias factor, accuracy factor, root mean square residual (RMSR), mean absolute relative residual (MARR, %), and mean relative percentage residual (MRPR, %).

However, model performance was primarily evaluated using the R value, with the highest R values indicating the best-performing models. The mathematical expressions of the indices used are provided below.

$$\text{RMSR} = \sqrt{\sum (O - P)^2 / N} \quad \ldots (2)$$

$$\text{Bias factor} = A.\log \sum \log (P/O)/N \quad \ldots (3)$$

$$\text{MARR} = 1/N \times \sum |O - P| \times 100/O \quad \ldots (4)$$

$$\text{Accuracy factor} = A.\log \sum |\log (P/O)| / N \quad \ldots (5)$$

$$\text{MRPR} = 1/N \times \sum (O - P) \times 100/O \quad \ldots (6)$$

Where, N is the number of data records; *O* is the observed value; *P* is the predicted value and *A*.log is antilog.

### 2.6. Statistical Regression Models

Regression models were developed using Microsoft Excel (version 2024) with a dataset of 120 records. The objective was to evaluate the quantitative effects of factors such as sericea lespedeza variety, moisture content, length, width, thickness, and weight on predicting the angle of repose. Excel was chosen for its accessibility and ease of use, facilitating efficient model construction, analysis, and visualization.

This combination of tools enabled a streamlined and transparent modeling process that supported reproducibility and facilitated clear comparisons between the performance of regression and machine learning models. Final regression equations were derived, and additional plots were created to visually compare the predictive performance of both machine learning and regression models.

## 3. RESULTS AND DISCUSSION

### 3.1. Regression Equation

After comparing linear, nonlinear, and polynomial models, Eq. 7 was chosen for its superior fit to the experimental data, as indicated by a lower standard deviation and a higher regression coefficient. Polynomial contrasts further confirmed a highly significant cubic trend in the angle of repose ($p < 0.01$).

$$\theta = -3.592 + 0.486\,C + 0.301\,M_c + 11.792\,L + 1.816\,W - 4.993\,T + 0.953\,M \quad \ldots (7)$$

Where, $\theta$ is angle of repose,°; $C$ is cultivar type; $M_c$ is moisture content, % w.b.; $L$ is length, cm; $W$ is width, cm and $T$ is thickness, cm.

### 3.2. Prediction Performance of Machine Learning and Regression Models

Table 2 summarizes the performance of six different learning algorithms in predicting the angle of repose for Sericea lespedeza seeds. The models evaluated include SVR, RFR, DT, BPNN, KNN, and a traditional Statistical Regression model. The performance of the models was assessed using the Pearson correlation coefficient (R ± SD (Standard Deviation)), Mean Relative Percentage Residual (MRPR), Bias Factor, Mean Absolute Relative Residual (MARR), Accuracy Factor, and Root Mean Square Residual (RMSR). These metrics provide a comprehensive understanding of each model's predictive accuracy, bias, consistency, and generalization capability.

**Table 2. Pearson's correlations (R ± SD) between predicted and observed values and statistical indices of machine learning and regression models.**

| Learning algorithms | R ± SD | MRPR | Bias Factor | MARR | Accuracy | RMSR |
|---|---|---|---|---|---|---|
| Support Vector Regressor | 0.77 ± 2.88 | -0.88 | 1.00 | 8.51 | 1.09 | 1.33 |
| Random Forest Regressor | 0.99 ± 3.73 | -0.01 | 0.99 | 2.29 | 1.02 | 0.55 |
| Decision Tree | 0.98 ± 3.74 | 0.12 | 0.99 | 2.88 | 1.03 | 0.74 |
| Backpropagation | 0.74 ± 4.76 | 4.16 | 0.94 | 15.62 | 1.18 | 3.81 |
| *K*-Nearest Neighbor | 0.99 ± 3.73 | -0.13 | 1.00 | 2.06 | 1.02 | 0.55 |
| Statistical Regression | 0.79 ± 3.36 | -0.88 | 1.00 | 8.51 | 1.09 | 1.33 |

*SD: Standard Deviation; MRPR: Mean Relative Percentage Residual; RMSR: Mean Absolute Relative Residues*

### 3.2.1. Pearson correlation coefficient (R ± SD)

The Pearson correlation coefficient (*R*) measures the strength and direction of the linear relationship between predicted and actual values. A higher *R* indicates a better model fit. In this study RFR (0.99 ± 3.73) and KNN (0.99 ± 3.73) achieved the highest *R* values, suggesting near-perfect linear correlation and low prediction variability. DT (0.98 ± 3.74) also performed strongly, slightly below RFR and KNN. On the other hand, SVR (0.77 ± 2.88) and Statistical Regression (0.79 ± 3.36) showed moderate correlation, while BPNN (0.74 ± 4.76) had the lowest *R* value, reflecting weaker predictive strength and higher variance. These results suggest that ensemble (RFR) and instance-based (KNN) models capture the underlying data patterns more effectively than this dataset's neural networks or linear models.

### 3.2.2. Mean relative percentage residual (MRPR, %)

The MRPR quantifies whether a model tends to overpredict (positive values) or underpredict (negative values). It is beneficial because it expresses residuals as a percentage, making it easier to compare performance across different models and datasets (Sakthivel *et al.,* 2019). The BPNN (4.16%) exhibited a pronounced overprediction bias. In contrast, DT (0.12%) showed a negligible overprediction tendency. The RFR (-0.01%), KNN (-0.13%), SVR (-0.88%), and Statistical Regression (-0.88%) all displayed minor underprediction tendencies. The near-zero MRPR values for RFR and KNN indicate well-balanced predictions, while BPNN tends to overestimate the angle of repose.

### 3.2.3. Bias factor

A bias factor 1 indicates no bias; values above 1 reflect overestimation, while those below 1 indicate underestimation (Ross, 1996). The SVR, KNN, and Statistical Regression all had bias factors 1.00, indicating effectively unbiased predictions. The RFR and DT (0.99) were very close to ideal, while BPNN (0.94) revealed a notable overestimation trend. These findings align with the MRPR results, confirming that BPNN systematically overpredicts, while the other models are largely unbiased.

### 3.2.4. Mean absolute relative residual (MARR, %)

Graphical analysis of model predictions showed that the SVR algorithm underestimated at higher values, while the BPNN underestimated at lower ranges and overestimated in the midrange (Figs. 3A–E). In contrast, RFR, KNN, and DT models showed strong agreement between predicted and observed values, outperforming both BPNN and SVR.

Machine learning algorithms offer several advantages over traditional statistical regression models, particularly their ability to detect nonlinear relationships between input and output variables and capture interactions among dependent variables without explicit modeling efforts (Sargent, 2001). Neural networks, for example, consist of numerous processing elements or neurons organized in layers, each with weighted inputs, transfer functions, and a single output (Agatonovic-Kustrin *et al.,* 2000). The hidden layers between the input and output layers significantly enhance the computational power of multilayer perceptron (MLP) architectures using backpropagation. However, in this study, the BPNN algorithm demonstrated the lowest predictive performance among the models evaluated. This underperformance may be attributed to the dominance of a single influential feature—moisture content—affecting the output values. The BPNNs typically perform better when multiple influential input variables are present.

Furthermore, sensitivity analysis identified moisture content as the primary contributor to the angle of repose, potentially affecting the predictive performance of specific machine learning algorithms, including BPNN. A significant advantage of ML modeling over statistical techniques is that ML algorithms do not require

data to satisfy standard distribution assumptions, such as normality and homogeneity of variance (Sargent, 2001). However, data normalization may enhance ML performance.

The results of this study demonstrate clear evidence that the machine learning (ML) models developed strong correlations between seed physical properties and the flow behavior (angle of repose) of Sericea lespedeza seeds. The machine learning models used in the study, such as RFR, KNN, and DT, exhibited superior predictive accuracy, with Pearson correlation coefficients of 0.99 ± 0.03, 0.99 ± 0.03, and 0.98 ± 0.04, respectively. The elevated correlation values signify a robust association between the input factors (seed qualities such as moisture content, length, width, thickness, and weight) and the output variable (angle of repose).

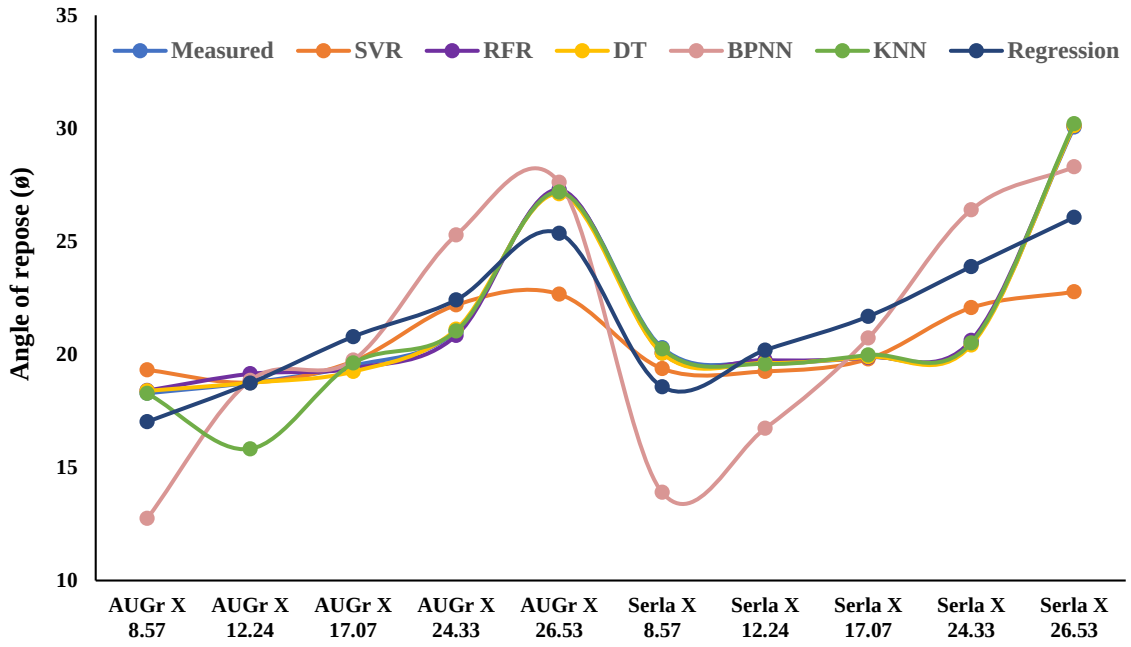


**Fig. 2. Trends in the angle of repose of sericea lespedeza seeds predicted by SVR, RFR, DT, BPNN, KNN, and regression models.**

Moreover, the data presented in Table 2 indicate that the machine learning models (RFR, KNN, and DT) exhibited markedly lower Mean Absolute Relative Residual (MARR) values (2.29%, 2.06%, and 2.88%, respectively) in comparison to other models, such as SVR, BPNN, and regression models. This suggests that the ML models more precisely represented the differences in the angle of repose as affected by seed properties. The MRPR values of these ML models were either near zero or somewhat negative, signifying a balanced prediction tendency without substantial over- or under-prediction.

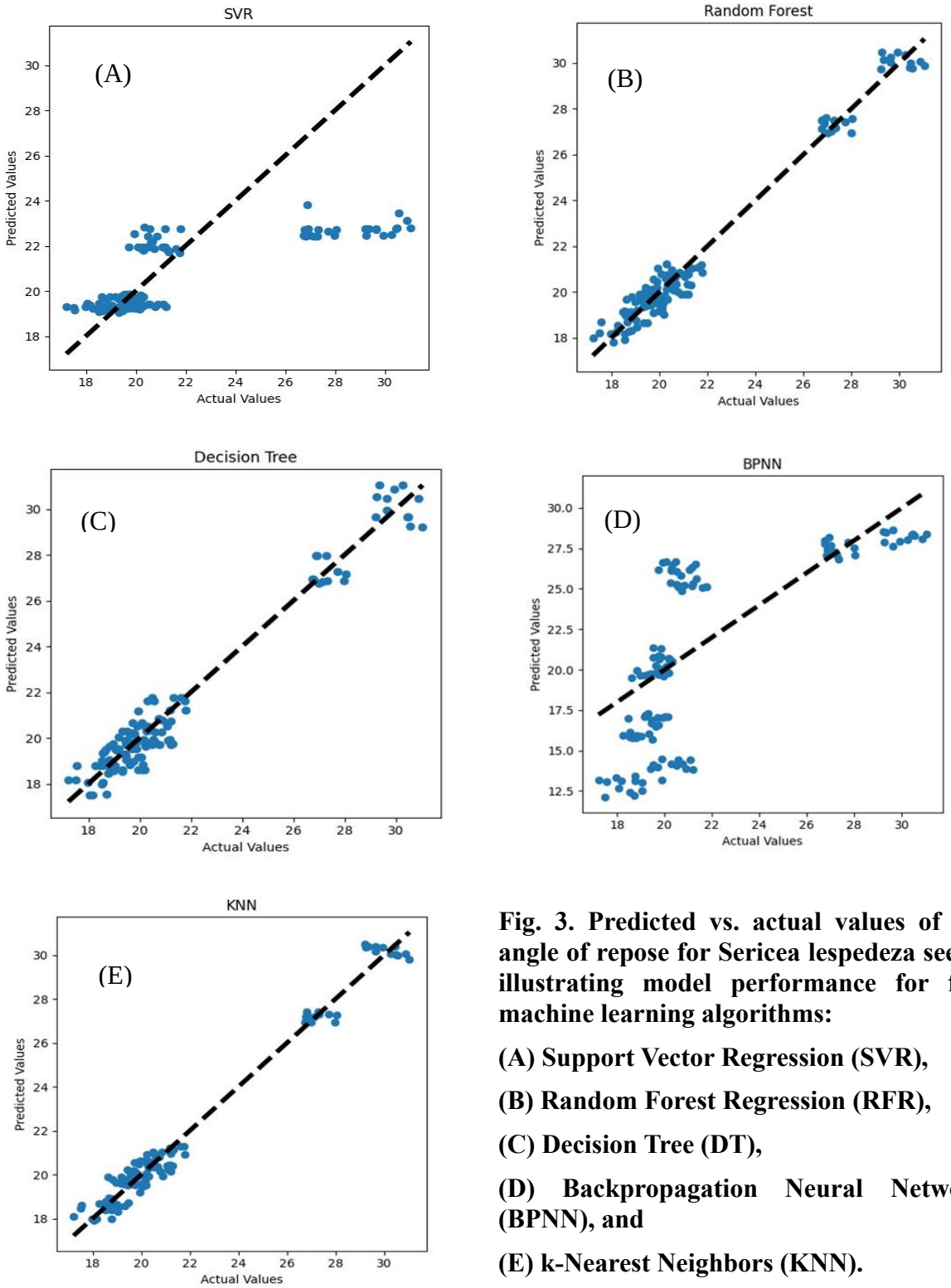


**Fig. 3. Predicted vs. actual values of the angle of repose for Sericea lespedeza seeds, illustrating model performance for five machine learning algorithms:**

**(A) Support Vector Regression (SVR),**

**(B) Random Forest Regression (RFR),**

**(C) Decision Tree (DT),**

**(D) Backpropagation Neural Network (BPNN), and**

**(E) k-Nearest Neighbors (KNN).**

The research highlights that machine learning models demonstrated superior generalization and interpolation, effectively capturing the intricate, nonlinear correlations between seed characteristics and the angle of repose. The visual representation of prediction plots (Fig. 3) further corroborated this, demonstrating that the predictions from ML models closely matched the actual observations across varying moisture levels. Conversely, regression models and specific machine learning models, such as BPNN, exhibited considerable discrepancies from the actual data, inadequately capturing the seed flow dynamics. The data collectively affirms that the ML models successfully identified and delineated the correlation between seed features and their flow behavior, yielding more dependable predictions than traditional regression models.

## 4. CONCLUSIONS

Machine learning models offer significant advantages over traditional experimental methods for predicting the flow properties of Sericea lespedeza seeds. These models can reduce measurement time and cost, enhance prediction accuracy, and facilitate the exploration of a broader range of scenarios and parameters. Furthermore, ML approaches can reveal complex relationships between seed characteristics and flow behavior, supporting the optimization of seed processing and planting systems. This study presents a comparative analysis of machine learning and regression models for predicting the angle of repose of Sericea lespedeza seeds. Model development was conducted without data pre-processing, using raw experimental inputs. Despite the limitations of a relatively small dataset, a *K*-fold nested cross-validation strategy was used to minimize the risk of underfitting or overfitting, ensuring more robust performance evaluation. Among the models tested, RFR, KNN, and DT significantly outperformed SVR, BPNN, and traditional regression methods in cross-validation accuracy. These results highlight the capacity of ML models to generalize from limited and variable biological data, making them effective tools for predicting the angle of repose.

## ACKNOWLEDGMENTS

This work was supported by the Capacity Building Grant [grant no. 2021- 38821- 2021-38821-34512/project accession no. 1026022] and the Evans-Allen Grant, accession number 1019546, USDA National Institute of Food and Agriculture.

## CONFLICT OF INTEREST

The authors know of no conflicts of interest associated with this publication, and there has been no significant financial support from third parties other than funding from the USDA for this work that could have influenced the outcomes.

## AUTHOR CONTRIBUTION

**Ramana M. Gosukonda**: Conceptualization, Methodology, Software, Formal analysis, Writing - Original Draft, Visualization, Supervision. **Aftab Siddique**: Investigation, Methodology, Software, Formal analysis, Writing - Review & Editing. **Ajit Kumar Mahapatra**: Conceptualization, Data Collection, Investigation, Resources, Writing - Original Draft, Supervision, Project administration.

## REFERENCES

1. Abbasi, A., Javed, A. R., Chakraborty, C., Nebhen, J., Zehra, W. and Jalil, Z. 2021. ElStream: An ensemble learning approach for concept drift detection in dynamic social big data stream learning. *IEEE Access*, 9: 66408–66419.https://doi.org/10.1109/ACCESS.2021.3076264
2. Agatonovic-Kustrin, S. and Beresford, R. 2000. Basic concepts of artificial neural network (ANN) modeling and its application in pharmaceutical research. *Journal of Pharmaceutical and Biomedical Analysis*, 22:717–727.

https://doi.org/10.1016/S0731-7085 (99)00272-1.

3. Al-Hashemi, H. M. B. and Al-Amoudi, O. S. B. 2018. A review on the angle of repose of granular materials. *Powder Technology*, 330: 397–417. https://doi.org/10.1016/j.powtec.2018. 02.003
4. Altuntaş, E. and Yildiz, M. 2007. Effect of moisture content on some physical and mechanical properties of faba bean (*Vicia faba L.*) grains, *Journal of Food Engineering*, 78 (1):174–183. https://doi.org/10.1016/j.jfoodeng.2005.0 9.013.
5. Arya, S., Mount, D. M., Netanyahu, N. S., Silverman, R. and Wu, A. Y. 1998. An optimal algorithm for approximate nearest neighbor searching in fixed dimensions. *Journal of the ACM*, 45(6): 891–923. https://doi.org/ 10.1145/ 293347.293348.
6. Aviara, N. A., Gwandzang, M. I. and Haque, M. A. 1999. Physical properties of guna seeds. *Journal of Agricultural Engineering Research*, 73(2): 105–111. https://doi.org/ 10.1006/ jaer. 1998.0374.
7. Ben Ishak, A. 2016. Variable selection using support vector regression and random forests: A comparative study. *Intelligent Data Analysis*, 20: 83–104. https://doi.org/10.3233/IDA-150795.
8. Ben-Gal, I., Dana, A., Shkolnik, N., and Singer, G. 2014. Efficient construction of decision trees by the dual information distance method. *Quality Technology and Quantitative Management*, 11:133–147. https://doi.org/10.1080/16843703.2014 .11673330.
9. Bhabani, D. S., Sangram, S. K., Behera, B., Rayaguru, K. and Megha, M. 2022. Effect of moisture content on engineering properties of engineering properties for designing agricultural equipment. *Asian Journal of Dairy and Food Research*, 41(1): 47–55. https://doi.org/10.18805/ajdfr.DR-1683.
10. Breiman, L. 2001. Random forests. *Machine Learning*, 45:5–32. https://doi.org/ 10.1023/A: 10109334 04324.
11. Chapelle, O. and Vapnik, V. 1999. Model selection for support vector machines. In. S.A. Solla, T.K. Leen, and K.-R. Müller (eds.). *Advances in Neural Information Processing Systems*, 12 (NIPS 1999), MIT Press, Cambridge, MA, pp. 230–236.
12. Coşkuner, Y. and Karababa, E. 2007. Physical properties of coriander seeds (*Coriandrum sativum* L.). *Journal of Food Engineering*, 80(2): 408–416. https://doi.org/10.1016/j.jfoodeng.2006.0 2.042.
13. Cutler, A., Cutler, D. and Stevens, J. 2011. Random forests. In *Machine learning*, 45: 157–176. https://doi.org/10.1007/ 978-1-4419-9326-7_5.
14. Darmawan, H., Yuliana, M. and Hadi, M. Z. S. 2023. GRU and XGBoost performance with hyperparameter tuning using GridSearchCV and Bayesian optimization on an IoT-based weather prediction system. *International Journal on Advanced Science, Engineering and Information Technology*, 13(3): 851–862. https://doi.org/10.18517/ijaseit. 13.3.18377.
15. Dehariya, V. K., Shrivastava, S. K. and Jain, R. C. 2010. Clustering of image data set using k-means and fuzzy k-means algorithms. In *Proceedings of the 2010 International Conference on Computational Intelligence and*

*Communication Networks*, pp. 386–391. Bhopal, India.

16. Dong, R. and Zhao, G. 2014. The use of artificial neural network for modeling *in vitro* rumen methane production using the CNCPS carbohydrate fractions as dietary variables. *Livestock Science*, 62:159–167. https://doi.org/ 10.1016/ j.livsci.2013.12.033.
17. Drucker, H., Burges, C. J., Kaufman, L., Smola, A. and Vapnik, V. 1996. Support vector regression machines. In. M.C. Mozer, M.I. Jordan, and T. Petsche (eds.). *Advances in Neural Information Processing Systems*, 9 (NIPS 1996), MIT Press, Cambridge, MA, pp. 155–161.
18. Gosukonda, R., Mahapatra, A. K., Ekefre, D. and Latimore, M. 2017. Prediction of thermal properties of sweet sorghum bagasse as a function of moisture content using artificial neural networks and regression models. *Acta Technologica Agriculturae*, 20(2): 29–35. https://doi.org/10.1515/ata-2017-0006
19. Gosukonda, R., Mahapatra, A. K., Liu, X. and Kannan, G. 2015. Application of artificial neural network to predict *Escherichia coli* O157:H7 inactivation on beef surfaces. *Food Control*, 47: 606–614. https://doi.org/10.1016/ j.foodcont.2014.08.002.
20. Hsu, C., Chang, C. and Lin, C. 2008. *A practical guide to support vector classification*. Department of Computer Science, National Taiwan University, Taipei 106, Taiwan. http://www.csie. ntu.edu.tw/~cjlin.
21. Isabona, J., Imoize, A. L., Ojo, S., Karunwi, O., Kim, Y., Lee, C. C. and Li, C. T. 2022. Development of a multilayer perceptron neural network for optimal predictive modeling in urban microcellular radio environments. *Applied Sciences*, 12(11): 5713. https://doi.org/10.3390/app12115713.
22. Izli, N. 2015. Effect of moisture on the physical properties of three varieties of kenaf seeds. *Journal of Food Science and Technology*, 52(6): 3254–3263. https://doi.org/10.1007/s13197-014-1369-8.
23. James, G., Witten, D., Hastie, T. and Tibshirani, R. 2013. *An introduction to statistical learning with applications in R*. Springer. https://doi.org/10.1007/ 978-1-4614-7138-7.
24. Jeyamkondan, S., Jayas, D. S. and Holley, R. A. 2001. Microbial modeling with artificial neural networks. *International Journal of Food Microbiology*, 64(3): 343–354. https://doi.org/10.1016/ S0168-1605(00)00483-9.
25. Madrid, M., Fuentes, J., Gallego, E. and Ayuga, F. 2022. Determination of the angle of repose and coefficient of rolling friction for wood pellets. *Agronomy*, 12(2): 424. https://doi.org/ 10.3390/agronomy12020424.
26. Mahapatra, A., Ekefre, D., Degala, H., Punnuri, S. and Terrill, T. 2019. Moisture-dependent physical and thermal properties of Sericea lespedeza seeds. *Applied Engineering in Agriculture*, 35: 389–397. https://doi.org/ 10.13031/aea.13228.
27. Mosjidis, J. A. 1996. Variability for biomass production and plant composition in Sericea lespedeza. *Biomass and Bioenergy*, 11(1): 63–68. https:// doi.org/10.1016/0961-9534(95)00109-3.
28. Muir, J. P., Terrill, T. H., Mosjidis, J. A., Luginbuhl, J.-M., Miller, J. E., Burke, J. M. and Coleman, S. W. 2017. Season progression, ontogenesis, and environment affect *Lespedeza cuneata* herbage condensed tannin, fiber, and

crude protein concentrations. *Crop Science,* 57(1): 515–524. https://doi.org/ 10.2135/cropsci2016.07.0605.

29. Müller, K. R., Mika, S., Tsuda, K. and Schölkopf, B. 2001. An introduction to kernel-based learning algorithms. In. D. S. Levine, V. M. Rao, and H. B. Marks (eds.). *Handbook of Neural Network Signal Processing*, CRC Press, Boca Raton, FL, pp. 1- 40.
30. Najjar, Y., Basheer, I. and Hajmeer, M. 1997. Computational neural networks for predictive microbiology: I. Methodology. *International Journal of Food Microbiology*, 34: 27–49. https://doi.org/10.1016/S0168-1605 (96) 01168-3.
31. Owolarafe, O. K., Olabige, M. T. and Faborode, M. O. 2007. Physical and mechanical properties of two varieties of fresh oil palm fruit. *Journal of Food Engineering*, 78(4):1228–1232. https://doi.org/10.1016/j.jfoodeng.2005.12.049.
32. Quinlan, J. R. 1986. Induction of decision trees. *Machine Learning*, 1: 81–106. https://doi.org/10.1007/BF00116251.
33. Rodriguez-Galiano, V., Sanchez-Castillo, M., Chica-Olmo, M. and Chica-Rivas, M. 2015. Machine learning predictive models for mineral prospectivity: An evaluation of neural networks, random forest, regression trees and support vector machines. *Ore Geology Reviews,* 71: 804–818. https://doi.org/ 10.1016/ j.oregeorev. 2015. 01.001.
34. Rosentrater, K.A. and Bucklin, R. 2022. Chapter 6 - Structural, physical, and engineering properties of cereal grains and grain products. In: K. A. Rosentrater (Ed.). *Storage of Cereal Grains and Their Products* (Fifth Edition), Woodhead Publishing, pp. 135-178. https://doi.org/10.1016/B978-0-12-812758-2.00019-2.
35. Ross, T. 1996. Indices for performance evaluation of predictive models in food microbiology. *Journal of Applied Bacteriology,* 81: 501–508. https://doi.org/10.1111/j.1365-2672.1996.tb03539.x
36. Russell, S. J. and Norvig, P. 2022. Learning from example. In. *Artificial intelligence: A modern approach.* Pearson Education, Hoboken, NJ. Fourth Edition, pp. 704-778.
37. Sakthivel, G., Senthil Kumar, S. and Ilangkumaran, M. 2019. A genetic algorithm-based artificial neural network model with TOPSIS approach to optimize the engine performance. *Biofuels*, 10(6): 693–717. https://doi.org/10.1080/17597269.2017.1338123.
38. Sargent, D. J. 2001. Comparison of artificial neural networks with other statistical approaches: Results from medical data sets. *Cancer,* 91(8): 1636–1642. https://doi.org/10.1002/1097-142 (20010415)91:8+<1636::aid-cncr 1176> 3.0.co;2-d.
39. Schölkopf, B., Smola, A. and Müller, K. R. 1998. Nonlinear component analysis as a kernel eigenvalue problem. *Neural Computation,* 10(5): 1299–1319.
40. Smola, A. J. and Schölkopf, B. 2004. A tutorial on support vector regression. *Statistics and Computing*, 14(3): 199–222.
41. Song, Y. Y., and Lu, Y. 2015. Decision tree methods: Applications for classification and prediction. *Shanghai Archives of Psychiatry*, 27(2): 130–135. https://doi.org/10.11919/ j.issn.1002-0829.215044.

42. Suleiman, R. A., Xie, K. and Rosentrater, K. A. 2015. Physical and thermal properties of chia, kaniwa, triticale, and farro as a function of moisture content. *ASABE Paper No. 152189412*. St. Joseph, MI: ASABE. https://doi.org/10.13031/aim.20152189412.

43. Teferra, T.F. 2019. Engineering Properties of Food Materials. In: M. Kutz (Ed.), *Handbook of Farm, Dairy and Food Machinery Engineering* (Third Edition). Academic Press, pp. 45–89. https://doi.org/10.1016/B978-0-12-814803-7.00003-8.

44. Triguero, I., Peralta, D., Bacardit, J., García, S. and Herrera, F. 2015. MRPR: A MapReduce solution for prototype reduction in big data classification. *Neurocomputing*, 150 (Part A): 331–345. https://doi.org/10.1016/j.neucom.2014.04.078.

45. Vabalas, A., Gowen, E., Poliakoff, E. and Casson, A. J. 2019. Machine learning algorithm validation with a limited sample size. *PLOS ONE*, 14(11): e0224365. https://doi.org/10.1371/journal.pone.0224365

46. Varma, S. and Simon, R. 2006. Bias in error estimation when using cross-validation for model selection. *BMC Bioinformatics*, 7: 91. https://doi.org/10.1186/1471-2105-7-91.

47. White, H. 1992. *Artificial neural networks: Approximation and learning theory*. Blackwell Publishers, Inc., United States, pp. 12–55.

48. Zaalouk, A. K. and Zabady, F. I. 2009. Effect of moisture content on angle of repose and friction coefficient of wheat grain. *MISR Journal of Agricultural Engineering*, 26(1): 418-427. doi: 10.21608/mjae.2020.110159.

49. Zhang, M. and Zhou, Z. 2005. A k-nearest neighbor based algorithm for multi-label classification. In *IEEE Conference on Granular Computing*. 2:718–721. https://doi.org/10.1109/GRC.2005.1547385.

International Agricultural Engineering Journal ISSN 0858-2114

*September 2025, 34 (1-4) : 45-56*

# Pulsed Light Decontamination and Modeling of *Salmonella* Reduction on Pecan Halves

**Kumudini Talari[1], Hema Degala[1], Ajit Mahapatra[1*], Rabin Gyawali[1], Ramana Gosukonda[2], Thomas Terrill[2]**

## ABSTRACT

Pasteurization has been the traditional method of sterilizing tree nuts. Pulsed light (PL) has proven to be an inexpensive, efficient, and environmentally friendly non-thermal processing method for several foods. However, this technology has not been extensively explored with tree nuts. In this study, the efficacy of PL in inactivating *Salmonella* Typhimurium (ATCC 14028) on pecan halves was investigated. A Z-1000 sterilizing system was used to treat pecan samples at distance of 7, 11, and 15 cm from the quartz window in the PL chamber for 1, 5, 10, and 15 seconds. Each treatment included three pecan halves placed simultaneously in the sterilization chamber. Experiments were repeated three times for each treatment time and distance and then analyzed using the General Linear Models (GLM) procedure of SAS. The PL delivered to the surface of pecan halves achieved a maximum reduction of 1.69 $\log_{10}$ CFU/g for treatment time of 15 seconds at a distance of 7 cm. The treatment with the highest log reduction was chosen to determine the pecan halves' quality characteristics. A significant reduction in moisture content in pecan samples was observed immediately after treatment, however, after storing at 4°C for 24 hours, no difference in moisture content was observed between treated and untreated samples. Changes in color ($a^*$ and $b^*$ values) were observed in treated pecan samples immediately after treatment (0 hours), but they regained their color after 24 hours. The total color difference between untreated and treated pecan samples was not significant, indicating that the treatment did not adversely affect the overall appearance of the pecan halves. Similarly, there were no differences in hardness values between treated and untreated pecan halves. This study demonstrates that PL can be used as an effective sterilizing method for *Salmonella*. Artificial neural network (ANN) prediction models were developed to predict the PL *Salmonella* inactivation on pecan halves as a function of distance and treatment time using the Backpropagation (ANN-BP) and Kalman Filter (ANN-KL) learning algorithm. Their performance was compared with that of regression models. Various statistical indices, including $R^2$ between actual and predicted outputs, were evaluated to select the best models. Prediction plots for log reduction values indicated that the ANN-BP and ANN-KF models demonstrated robust accuracy, with $R$ values of 0.78±0.39 and 0.80±0.39, respectively, in predictions from new unseen patterns, compared to the performance of the regression models ($R$ = 0.60±0.37). The results indicated that PL could be used as a potential decontamination method for pecan halves, and ANN models could provide reliable prediction of the *Salmonella* population.

***Keywords:*** *Artificial Neural Network; Bacteria; Contamination; Prediction; Non-thermal Processing.*

[1]Food Engineering Laboratory, [2]Department of Agricultural Sciences, College of Agriculture, Family Sciences, and Technology, Fort Valley State University, Fort Valley, GA 31030, USA.

**Corresponding author – email: mahapatraa@fvsu.edu*

Received: 22 January 2025; Revised: 12 May 2025; Accepted: 12 May 2025

## 1. INTRODUCTION

Pecan trees (*Carya illinoinensis*) are native to America and can be found in Northern Mexico as well as the Southern United States (U.S.). In the U.S., pecan farming began in the 1800s, and Georgia accounts for 33% of the total crop in the country (≈ 45 million kg, in-shell, McDaniel and Jadeja, 2021). The demand for nuts and their products has been increasing every year as customers' interest in nutrition and health has grown (Gervasi *et al*., 2021). Pecans provide many nutritional benefits to consumers, as they are rich in several nutrients and possess antioxidants, anti-cancerous, and other disease-preventing properties, and thus are recognized as one of the nutrient foods for human health (Atanasov *et al*., 2018).

Tree nuts, despite being a low moisture food, have been frequently associated with several outbreaks and recalls due to contamination with bacteria, such as *E. coli* O157: H7, *Salmonella*, and *Listeria monocytogenes* (Zhang *et al*., 2017; Gyawali *et al*., 2024). *Salmonella* can survive on the shucks and in low-moisture food products kept at refrigerated or room temperature for several weeks to months. During rainfall, pathogens present on outer shells can cross-contaminate nearby in-shell pecans. According to Brar *et al*. (2016), 0.95% of in-shell pecans were tested positive for prevalence of *Salmonella* when studied over four harvest seasons. *Salmonella* can also survive up to a year on pecan kernels when stored under ambient, refrigerated, and frozen conditions (Brar *et al*., 2015). Although there have been no outbreaks associated with pecans and its products yet, a few recalls due to potential *Salmonella* contamination have been reported (Yemmireddy *et al*., 2020). Hence, enhancing the safety of pecans against *Salmonella* contamination is to be considered.

Traditional methods of tree nut disinfection involve steam pasteurization, drying, sterilization, or chemical means, such as roasting and blanching. Even though these techniques have long been used for microbial inactivation, they also degrade certain nutrients and can affect nut quality (Bhavya and Hebbar, 2017; Allai *et al*., 2023). Therefore, it is important to find other effective and safe alternatives, including non-thermal techniques, to these existing methods. Pulsed light (PL) is one such emerging non-thermal processing technology, which has the potential to decontaminate food products, including tree nuts. The PL can rapidly inactivate microorganisms, such as *Salmonella* and *E. coli*, in very short treatment times (Oms-Oliu *et al*., 2000). The U.S Food and Drug Administration (FDA) has approved the use of PL treatment of food (Federal Register, 1996). The light generated by pulsed UV lamps consists of a continuum of energy from UV to infrared that pulses several times, and each pulse lasts between 2 and 100 ms. The PL has a modest energy input, which can yield high peak power dissipation and has a germicidal effect (Demirci and Panico, 2008). Pulsed light has an advantage over other thermal processing methods and is considered environmentally friendly, as there is no need for any chemicals, water, and leaves no residual compounds (Gómez-López *et al.,* 2007). Although several studies have been conducted to determine the effect of PL on inactivating microorganisms in food products (Ozer and Demirci, 2006), its use in tree nut processing is limited. One such study is the evaluation by Izmirlioglu *et al.* (2020) on walnut halves inoculated with *Salmonella* e*nteritidis*. A maximum log reduction of 3.18 CFU/g was obtained after PL treatment at 8 cm for 45 s. Despite its potential antimicrobial efficacy, there are some limitations with this technology: Longer duration of PL for food processing can cause the temperatures of food products to rise that could affect the food quality. The possibility of shadowing is another disadvantage of PL, which interferes with absorption of UV rays by microorganisms and ultimately affects the inactivation rate. In addition, PL has a more

limited penetration capacity in opaque, rough, and irregular surfaces than in smooth and transparent food materials (Bhavya and Hebbar, 2017).

Artificial Neural Networks (ANN) are nonlinear computational modeling techniques inspired by biological neural networks (Basheer and Hajmeer, 2000), while other modeling techniques, such as statistical regression, predict linear patterns from data. The development of ANN models involves training, testing, and validation. Hence, the pool of available records is divided into these three datasets in such a way that the records in each dataset are independent of each other. The networks are trained with various algorithms, such as Backpropagation and Kalman filter. The goal of these algorithms is to reduce the amount of error between the predicted output and the measured output (Gosukonda *et al*., 2015). The objective of using ANN models was to develop predictive models for quantifying the PL decontamination of *Salmonella* on pecan halves and to compare their performance with that of statistical models, assessing their suitability as a tool for online processing in the food industry. Modeling techniques that achieve optimal prediction accuracy for *Salmonella* inactivation on pecans would not only enhance product quality and public perception from a safety standpoint but also improve the marketability of pecan products. Furthermore, this information is invaluable for optimizing storage and handling conditions, enabling practices that maintain the highest pecan quality. Hence, the objective of this study was to evaluate the efficacy of PL decontamination on the survival of *Salmonella* on pecan halves and to predict the PL inactivation potential using ANN models.

## 2. MATERIALS AND METHODS

### 2.1. Bacterial Strain, Sample Preparation and Inoculation

*Salmonella enterica* subsp. *enterica* serovar Typhimurium (ATCC 14028) was used in this study. The KWIK-STIK pouch was allowed to equilibrate at room temperature and the inoculum was prepared as per the manufacturer's instructions. Georgia mammoth pecan halves were obtained from Lane Southern Orchards (Fort Valley, GA, USA). Forty µL of *Salmonella* (≈ 7.0 log) was inoculated at four randomly chosen spots on pecan halves (≈ 2 g) surface in a hood (Labconco Purified Class II Biosafety Cabinet, Labconco Corp., Kansas, MO, USA). Inoculated pecans were air dried in the hood for 30 min for bacterial attachment.

### 2.2. Pulsed Light Treatment

A Z-1000 Modular Sterilization System (XENON Corporation, Wilmington, MA, USA) was used in this study. Inoculated pecan samples were treated with PL for 1, 5, 10 and 15 s at 7, 11 and 15 cm from the light source. Inoculated pecan samples that were not treated were used as controls. Pulsed light treatment radiant energy was 1.27 J/ $cm^2$ per pulse.

### 2.3. Microbiological Analysis

Treated and untreated samples were placed individually in a stomacher bag with 10 mL of 0.1% peptone water and homogenized with a stomacher (Model 400 stomacher, Seaward, UK Brinkmann Instrument INC., West Bury, NY, USA) for 2 min at 230 RPM. The samples were then serially diluted with 0.1% sterile peptone water and the appropriate dilutions were spiral plated on to tryptic soy agar using an Eddy Jet 2 Spiral plater (Neutec Group, Farmingdale, NY, USA). Colonies were counted after incubating (Sheldon Manufacturing, Inc Cornelius, OR, USA) for 18-20 h at 37 °C using a Bantex colony counter (Model 920A, America Bantex Corp., Chandler, AZ, USA).

### 2.4. Quality Analysis

For quality analysis, PL treated samples (7 cm and 15 s) that had the maximum log reduction were chosen.

#### 2.4.1. Moisture content

Moisture content of treated and untreated pecan halves at 0 and 24 h of storage was measured by placing the samples in an oven at 105°C for 24 h.

### 2.4.2. Color analysis

The total color difference ($\Delta E$) of treated and untreated pecan samples at 0 and 24 h of storage after PL treatment was measured using a ColorFlex EZ colorimeter (HunterLab, Reston, VA, USA). Pecan samples were kept on the port at three different 90° surface positions to measure the color ($L^*$ lightness, $a^*$ redness, and $b^*$ yellowness) values, and the $\Delta E$ was calculated using the following equation:

$$\text{Total color difference } (\Delta E) = [(\Delta L^*)^2 + (\Delta a^*)^2 + (\Delta b^*)^2]^{0.5} \quad \ldots (1)$$

### 2.4.3. Texture analysis

Hardness of the samples was determined using a CTX Texture Analyzer (Brookfield AmeTek, Middleboro, MA, USA). Hardness of each pecan was determined using the following parameters: Trigger force: 15.0 g, Deformation: 20 mm, and Test Speed: 4 mm/s and measured by placing the sample in triangular slit of a shear blade.

### 2.5. Statistical Analysis

The experiment was conducted using a completely randomized design with 3x4 factorial treatment arrangement. Factor one was the distance from the light source, with three levels, and factor two was the treatment time, with four levels. Data were analyzed using ANOVA, and means were compared using Tukey-Kramer Test using SAS (version 9.4, SAS Institute, Cary, NC, USA). The number of samples for each treatment was three, plated in duplicates, and the experiments were repeated three times on different days.

Multiple linear regression models were developed using PROC REG (Regression Procedure) and GLM (General Linear Models) procedures of the SAS® system (Version 9.4, SAS Institute) for the prediction of log reductions of *Salmonella* as a function of treatment time and distance from the light source, as described by the equation:

$$Y = \beta_o + \beta_1 X_1 + \beta_2 X_2 \quad \ldots (2)$$

Where, $Y$ is the log reduction of *Salmonella*; $\beta_0$ is Y – intercept; $\beta_n$ is model coefficients; $X_1$ is distance (7, 11, and 15 cm) and $X_2$ is treatment time (1, 5, 10, and 15 s).

### 2.6. ANN Modeling

Artificial neural network models were developed using NeuralWorks Predict® and NeuralSight software to predict the inactivation of *Salmonella* ($\log_{10}$ CFU/g) on pecan halves treated with PL as a function of time and distance from the light source. Artificial neural networks were chosen for their ability to model complex relationships without requiring data preprocessing (NeuralWorks Predict, 2018). Experimental data from the PL inactivation study were used to train the models, with treatment time and distance as inputs, and predicted *Salmonella* reduction on the pecan surface as the output.

A multilayer perceptron (MLP) neural network with a feedforward architecture (Fig. 1) was chosen for its ability to learn complex relationships in nonlinear data (Zou *et al*., 2008). Multilayer perceptron has universal approximation capabilities and provides compact representations, making them suitable for our study (Abiodun *et al.,* 2018). In an MLP, the input layer receives data, the hidden layer performs computations using transfer functions, and the output layer makes predictions (Zou *et al.,* 2008; Abiodun *et al*., 2018). The software builds the network incrementally, adding hidden units one by one and connecting them to previous units. This step-by-step construction process is called “cascade learning” (Gosukonda *et al*., 2015), where each unit aims to maximize its correlation with the desired output. The "cascade" refers to the stepwise construction, and "correlation" refers to how the units learn by maximizing their output's correlation with the desired outcome (Fahlman and Lebiere, 1990).

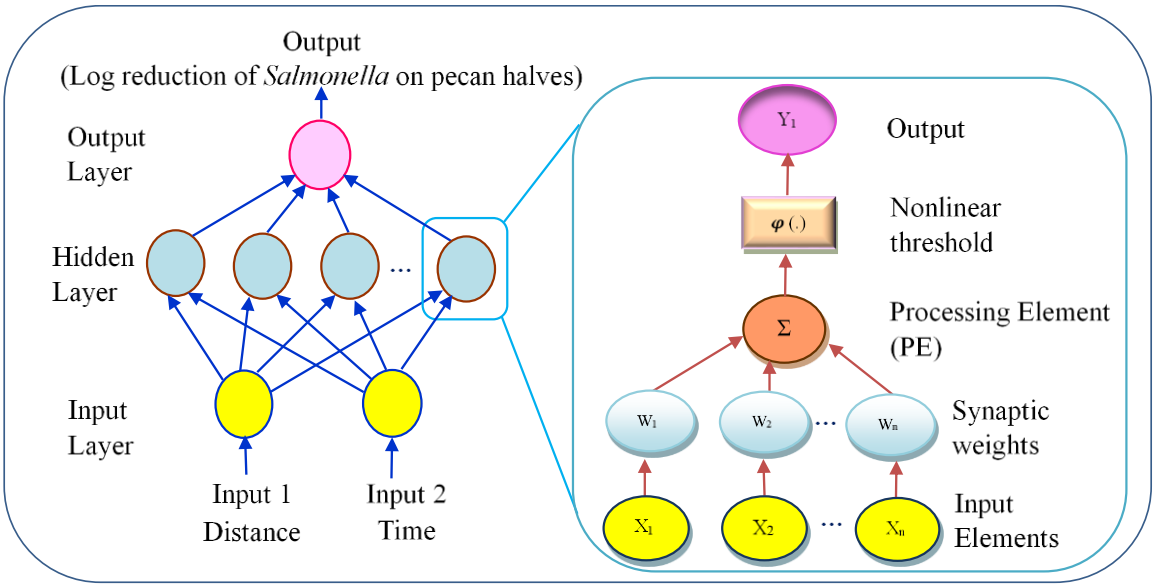


**Fig. 1. A schematic diagram of MLP neural network model**

This study used two learning rules: Backpropagation (ANN-BP) and the Kalman filter (ANN-KF) (Luttmann and Mercorelli, 2021) to improve prediction accuracy and data fit in ANN models. Backpropagation uses gradient descent (Rumelhart *et al*., 1986) and Gauss-Newton methods (Osborne, 1992) to refine predictions, while KF estimates parameters through recursive prediction and update (Kalman, 1960), filtering out noise from uncertain observations (Puskorius and Feldkamp, 1991). Given the potential for noise in microbiological data, the KF's noise-filtering capabilities were particularly relevant.

#### 2.6.1. Data records for model training, testing and validation

There were 144 out of 216 experimental measurements (inputs and outputs) used for training and internal testing, while the remaining 72 were reserved for independent validation to develop ANN predictive models. Data were assigned to each set to ensure independence, preventing model overfitting. The training was further split equally (72 each) by the software for training and internal testing. The training dataset adjusted the model's parameters, while the internal test data evaluated its performance. Finally, the independent validation set confirmed the model's generalizability beyond the training and internal test data.

#### 2.6.2. Selection of ANN models

Network configurations were optimized empirically, with performance comparisons based on statistical indices across training, testing, and validation datasets. These indices included Pearson correlation (*R*), standard deviation, various error measures (average absolute error, maximum absolute error, root mean square residual), and metrics like accuracy factor, mean absolute relative residual, bias factor, and mean relative percentage residual (data not shown). Ultimately, the best models were selected based on *R* values.

## 3. RESULTS AND DISCUSSION

### 3.1. Efficacy of PL in Inactivating *Salmonella* on Pecan Halves

The initial population on the surface of pecan halves was 7.11 $\log_{10}$ CFU/g (positive control). No natural microflora was found on the surface of samples that were not inoculated (negative control). The efficacy of PL on the surface of

pecan halves at 7, 11, and 15 cm is presented in Fig. 2. The maximum reduction of 1.69 $\log_{10}$ CFU/g was achieved when treated at 7 cm for 15 s. Increasing treatment time (1 s to 5 s) showed no significant increase in log reductions, however 5 s to 15 s showed significant ($P \leq 0.05$) increase in log reductions at all distances (7, 11, and 15 cm). The effect of distance on the reductions was significantly observed from 5 s to 15 s treatments. The longer treatment times might have resulted in better penetration of PL through the grooves on the pecan surface, overcoming the shadowing effect, and resulting in higher *Salmonella* reduction on pecan halves.

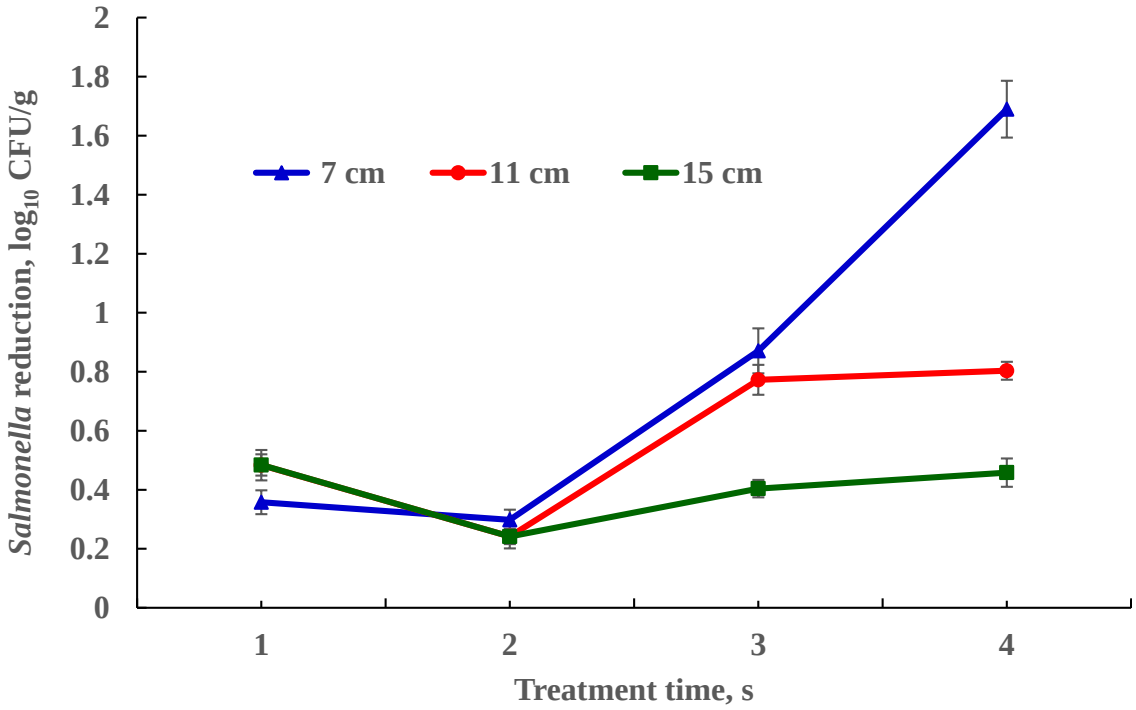


**Fig. 2. Inactivation of *Salmonella* on pecan halves using PL at 7, 11, and 15 cm from the light source (n = 18)**

Overall, treatment time and distance from the light source had significant ($p < 0.0001$) effects on the inactivation efficacy of PL against *Salmonella*. A significant ($p < 0.0001$) interaction was also found between treatment time and distance. The results obtained in this study are consistent with results of another study that reported a maximum reduction of 3.18 $\log_{10}$ CFU/g on shelled walnuts after PL treatment at 8 cm for 45 s, however, there was less than one log reduction for 1-15 s and showed no significant difference in log reductions for 20 to 40 s (Izmirlioglu *et al*., 2020). The reduction achieved in walnuts after 15 s treatment was 1.88 log CFU/g, consistent with our study, and the minor difference in the reduction achieved might be due to difference in the energy generated per pulse and surface morphological differences between the nuts.

### 3.2. Effect of PL on Pecan Quality

#### 3.2.1. Moisture content

Moisture content is an important quality parameter that affects the shelf life of pecans. Table 1 shows the moisture content of treated pecans at 7 cm for 15 s at 0 and 24 h of storage at refrigerated temperature. At 0 h, PL reduced the moisture level of pecans from 3.9% to 2.2%,

possibly due to the heat generated by the PL. However, after storing at 4°C for 24 h, no difference in moisture content was observed between the samples.

### 3.2.2. Texture analysis

Texture is one of the important indicators for assessing pecan quality and is measured by evaluating hardness, which is the peak force (N) required to deform a food material. The differences in hardness value of control (38.17 N) and treated pecans (37.76 N) at 0 h were insignificant (Table 1). After 24 h of storage, there was a slight decrease in the hardness value of treated (36.07 N) samples, but it was not statistically different compared to the control (36.18 N). Our results showed that PL had no effect on the textural quality of pecans.

**Table 1. Moisture content and hardness of PL treated pecan halves (Mean ± SD; n = 12).**

| Sample type | Moisture content, % (w.b.)* | | Hardness value, N | |
|---|---|---|---|---|
| | Storage period | | | |
| | 0 h | 24 h | 0 h | 24 h |
| Untreated | 3.90 ± 3.91$^{a}$ | 3.69 ± 1.12$^{a}$ | 38.17 ± 6.90$^{NS}$ | 36.18 ± 6.25$^{NS}$ |
| Treated | 2.20 ± 0.61$^{b}$ | 3.2 ± 0.33$^{a}$ | 37.76 ± 4.80$^{NS}$ | 36.07 ± 6.06$^{NS}$ |

**Mean values within the same column followed by different letters are significantly different (P < 0.05); $^{NS}$Non-significant.*

### 3.2.3. Color analysis

Table 2 shows the color of treated (7 cm, 15 s) and untreated pecans at 0 and 24 h of storage. At 0 h, untreated and treated samples showed no differences in *L** values. There was a slight change in *a** and *b** values for treated samples after 24 h storage at 4℃, however, the total color difference between treated and untreated samples, was below 3.0, which falls within the acceptable range, where the difference is noticeable but not significant (Arthur *et al*., 2025).

**Table 2. *L**, *a**, and *b** values and total color difference, $\Delta E$ of PL treated pecan halves (Mean ± SD; n = 12).**

| Sample type | Color values | | | | | | | |
|---|---|---|---|---|---|---|---|---|
| | Storage period of 0 h | | | | Storage period of 24 h | | | |
| | ***L**** | ***a**** | ***b**** | $\Delta E$ | ***L**** | ***a**** | ***b**** | $\Delta E$ |
| Untreated | 43.9±1.7$^{a}$ | 14.6±0.5$^{a}$ | 29.2±1.9$^{a}$ | - | 43.9±1.7$^{a}$ | 14.6±0.5$^{a}$ | 29.2±1.9$^{a}$ | - |
| Treated | 43.18±2.1$^{a}$ | 13.7±0.6$^{b}$ | 26.9±2.2$^{b}$ | 3.3 ± 1.2 | 43.9±2.$^{a}$ | 14.3±0.7$^{a}$ | 28.8±0.9$^{a}$ | 2.9±1.2 |

*Mean values within the same column followed by different letters are significantly different (P < 0.05).*

### 3.3. ANN Modeling

### 3.3.1. Prediction performance of regression and ANN models

The data used in this study were obtained from experiments that measured *Salmonella* reduction (output) on pecan halves as a function of distance from the light source and treatment time with PL (inputs). The final regression model was selected based upon its relatively lower standard deviations and a higher regression coefficient (Eq. 3):

$$SR = 0.925 + (0.014\ t) - (0.045\ d) \quad (R = 0.60 \pm 0.37) \quad \ldots (3)$$

Where, *SR* is *Salmonella* reduction, $\log_{10}$ CFU/g; *t* is treatment time, s and *d* is distance from the light source, cm.

Table 3 shows the comparison of the performance of regression and ANN models in predicting *Salmonella* reduction on pecan surfaces based on treatment time and distance. While regression models had a lower Pearson correlation (R = 0.60 ± 0.37) for validation data, both ANN models (BP: R = 0.73 ± 0.31, KF: R = 0.73 ± 0.36) achieved slightly higher R values. However, these higher values in validation compared to training data (BP: R = 0.81 ± 0.41, KF: R = 0.84 ± 0.41) suggest potential overfitting, where the models memorized noise instead of learning general patterns. This might be due to the models having low bias but high variance, meaning they fit the training data too closely at the expense of generalizability (Jeyamkondan *et al*., 2001). The limitations of the model include the assumption of linear relationships, exclusion of other relevant factors, such as temperature, pecan surface characteristics, or the initial level of contamination, and the potential for reduced accuracy under different conditions. These limitations should be considered when applying the model to real-world situations.

**Table 3. Pearson's correlations (R ± SD) between predicted and experimental values of regression and neural networks models.**

| Output | Regression model | ANN-Back propagation | | ANN-Kalman filter | |
|---|---|---|---|---|---|
| | All values | Training* | Validation | Training* | Validation |
| | R | R | R | R | R |
| Log reduction on pecan halves | 0.60 ± 0.37 | 0.81 ± 0.41 | 0.73 ± 0.31 | 0.84 ± 0.41 | 0.73 ± 0.36 |

** The R ± SD values of training and test data sets were pooled and shown as training.*

**Table 4. Comparison of models against measured data, presenting the average predicted log reduction (CFU/g) values for each treatment (n = 18).**

| Treatments | | Models | | | |
|---|---|---|---|---|---|
| Distance, cm | Time, s | Measured | Backpropagation | Kalman Filter | Regression |
| 7 | 1 | 0.57 | 0.39 | 0.28 | 0.52 |
| 7 | 5 | 0.27 | 0.27 | 0.31 | 0.68 |
| 7 | 10 | 0.77 | 0.95 | 0.89 | 0.89 |
| 7 | 15 | 1.37 | 1.26 | 1.33 | 1.09 |
| 11 | 1 | 0.75 | 0.37 | 0.38 | 0.32 |
| 11 | 5 | 0.22 | 0.25 | 0.25 | 0.48 |
| 11 | 10 | 0.77 | 0.95 | 0.89 | 0.89 |
| 11 | 15 | 1.28 | 1.26 | 1.33 | 1.09 |
| 15 | 1 | 0.37 | 0.47 | 0.50 | 0.12 |
| 15 | 5 | 0.29 | 0.20 | 0.18 | 0.28 |
| 15 | 10 | 0.38 | 0.40 | 0.38 | 0.49 |
| 15 | 15 | 0.58 | 0.41 | 0.42 | 0.69 |

Prediction plots of ANN-BP and ANN-KF (validation data) and regression models in Table 4 reveal a clear difference in their performance. Both ANN-BP and ANN-KF models closely aligned with the measured values across treatment levels, while the regression model failed to capture the observed trends. Table 4 further confirms the experimental observation of increasing *Salmonella* reduction with PL exposure time up to 15 s and distances of 7 and 11 cm. However, a decrease in reduction in log reduction occurred at 15 cm at all treatment times of PL. The regression model missed this crucial pattern.

While predictions on mid-range treatment seemed to be more accurate for both ANN models, ANN models often exhibit varying performance across different output variables (Dong and Zhao, 2014). The results demonstrate the superior prediction ability of ANN models compared to the regression model, especially for unseen patterns, despite lower R values on validation data compared to training. Generally, the main advantage of neural network models over regression models is the ability to recognize the relationship between input and output datasets without specifying a prior relationship.

## 4. CONCLUSIONS

The application of PL treatment has demonstrated significant potential in enhancing the safety and maintaining quality of pecans. Log reductions of 0.36, 0.30, 0.87, and 1.69 CFU/g were achieved for treatment times of 1, 5, 10, and 15 s, respectively, at 7 cm distance. A significant reduction in moisture content in pecan samples was observed immediately after treatment. However, after storing at 4°C for 24 h, no difference in moisture content was observed between treated and untreated samples. Changes in color ($a^*$ and $b^*$ values) were observed in treated pecan samples immediately after treatment (0 h), but they regained their color after 24 h storage. The total color difference ($\Delta E$) between untreated and treated pecan samples was not significant, indicating that the treatment did not adversely affect the overall appearance of the pecan halves. Similarly, there were no differences in hardness values between treated and untreated pecan halves. Thus, this study showed that PL treatment can effectively inactivate *Salmonella* on pecan halves without compromising their quality. The regression model failed to capture important trends observed in the experimental data. The ANN models exhibited higher correlation coefficients compared to the regression model and provided more accurate predictions of *Salmonella* reduction on pecan halves. The ANN models not only exhibited the optimal prediction accuracy for *Salmonella* inactivation on pecans, but would also enhance product quality and public perception from a safety standpoint and improve the marketability of pecan products. This study demonstrated that PL has the potential to be considered as a novel decontamination method for pecan halves and other tree nuts. Further research is needed to optimize its use for commercial applications in various tree nuts.

## ACKNOWLEDGEMENTS

This work was supported by the U.S. Department of Agriculture-Research Education, and Economics under accession number 440662 and the Capacity Building Grant [grant no. 2021-38821-34512/project accession NO. 1026022], USDA National Institute of Food and Agriculture.

## CONFLICT OF INTEREST

The authors declare no conflict of interest.

## AUTHOR CONTRIBUTION

Kumudini Talari (Investigation, Methodology), Hema Degala (Investigation, Methodology, Writing-original draft), Ajit Mahapatra (Conceptualization, Formal analysis, Funding acquisition, Methodology, Project administration, Resources, Supervision), Rabin Gyawali (Methodology, Writing-original draft), Ramana Gosukonda (Methodology, Formal analysis, Writing-original draft), Thomas Terrill (Methodology, Editing-original draft).

## REFERENCES


1. Abiodun, O.I., Jantan, A., Omolara, A.E., Dada, K.V., Mohamed, N.A. and Arshad, H. 2018. State-of-the-art in artificial neural network applications: A survey. *Heliyon*, 4(11): e00938. https://doi.org/10.1016/j.heliyon.2018.e00938.
2. Allai, F. M, Junaid, P. M., Azad, Z. R. A. A., Gul, K., Dar, B. N., Siddiqui, S. A. and Loenzo, J. M. 2023. Impact of moisture content on microstructural, thermal, and techno-functional characteristics of extruded whole-grain-based breakfast cereal enriched with Indian horse chestnut flour. *Food Chemistry*, X: 100959. DOI: 10.1016/j.fochx.2023.100959.
3. Arthur, V., Degala, H. L., Gyawali, R., Chasteen, K., Sherman, S. H., Souza, P.M., Dev Kumar, G., Niemira, B. A., Bardsley, C. A. and Mahapatra, A. K. 2025. Inactivation efficacy of intense pulsed light and cold atmospheric plasma on spot-inoculated *Escherichia coli* on pecan halves. *International Journal of Food Science and Technology*, 60(1): vvaf050. DOI: 10.1093/ijfood/vvaf050.
4. Atanasov, A. G., Sabharanjak, S. M., Zengin, G., Mollica, A., Szostak, A., Simirgiotis, M., Huminiecki, L., Horbanczuk, O. K., Nabavi, S. M. and Mocan, A. 2018. Pecan nuts: A review of reported bioactivities and health effects. *Trends in Food Science and Technology*, 71: 246-257.
5. Basheer, L. A. and Hajmeer, M. 2000. Artificial neural networks: fundamentals, computing, design, and application. *Journal of Microbiological Methods*, 43(1): 3-31.
6. Bhavya, M. L. and Hebbar, H. U. 2017. Pulsed light processing of foods for microbial safety: A review. *Food Quality and Safety*, 1(3): 187-201.
7. Brar, P.K., Proano, L.G., Friedrich, L.M., Harris, L. J. and Danyluk, M. D. 2015. Survival of *Salmonella*, *Escherichia coli* O157: H7, and *Listeria monocytogenes* on raw peanut and pecan kernels stored at -24, 4, and 22°C. *Journal of Food Protection*, 78(2): 323–332.
8. Brar, P.K., Strawn, L.K. and Danyluk, M. D. 2016. Prevalence, level, and types of *Salmonella* isolated from North American in-shell pecans over four harvest years. *Journal of Food Protection*, 79(3): 352-360.
9. Demirci, A. and Panico, L. 2008. Pulsed ultraviolet light. *Food Science and Technology International*, 14(5): 443-446.
10. Dong, R. and Zhao, G. 2014. The use of artificial neural network for modeling in vitro rumen methane production using the CNCPS carbohydrate fractions as dietary variables. *Livestock Science*, 162(1): 159 – 167.
11. Fahlman, S.E. and Lebiere, C. 1990. The Cascade-correlation learning architecture. In: D.S. Touretzky (ed.), *Advances in Neural Information Processing Systems*. Morgan-Kaufmann, Los Altos, CA, p. 2.
12. Federal Register. 1996. Pulsed light for the treatment of food. Federal Register, 61 (159), p 42383. Center for Food Safety and Applied Nutrition, College Park, Maryland, USA. https://www.govinfo.gov/content/pkg/FR-1996-08-15/pdf/96-20854.pdf. Accessed 14 March 2024.
13. Gervasi, T., Barreca, D., Laganà, G. and Mandalari, G. 2021. Health benefits related to tree nut consumption and their bioactive compounds. *International Journal of Molecular Sciences*, 22(11): 5960.
14. Gómez-López, V. M., Raggert, P., Debevere, J. and Develieghere, F. 2007. Pulsed light for food decontamination: A review.

*Trends in Food science and Technology*, 18(9): 464-473.

15. Gosukonda, R., Mahapatra, A. K., Liu, X. and Kannan, G. 2015. Application of artificial neural network to predict *Escherichia coli* O157:H7 inactivation of beef surfaces. *Food Control*, 47: 606-614.
16. Gyawali, R., Degala, H. L., Biswal, A. K., Bardsley, C. A. and Mahapatra, A. K. 2024. Effects of intense pulsed light on inactivation of *Salmonella* Typhimurium and quality characteristics of pecan halves. *LWT-Food Science and Technology*, 203: 116344.
17. Izmirlioglu, G., Ouyang, B. and Demirci, A. 2020. Utilization of pulsed UV light for inactivation of *Salmonella* Enteritidis on shelled walnuts. *LWT*, 134: 110023.
18. Jeyamkondan, S. Jayas, D.S. and Holley, R.A. 2001. Microbial growth modeling with artificial neural networks. *International Journal of Food Microbiology*, 64(3): 343 - 354.
19. Kalman, R. E. 1960. A new approach to linear filtering and prediction problems. *Journal of Basic Engineering*, 82 (Series D), 35 - 45.
20. Luttmann, L. and Mercorelli, P. 2021. Comparison of backpropagation and Kalman filter-based training for neural networks. *Preprints*, 2021040523. DOI: 10.20944/ preprints 202104. 0523.v1.
21. McDaniel, C. and Jadeja, R. 2021. Pecan and walnut food safety concerns: A mini review. *Advances in Nutrition and Food Science*, 2021(3):1-15.
22. NeuralWorks Predict® 2018. *The Complete Solution for Neural Data Modeling* User Guide, Neuralware, Carnegie, PA.
23. Oms-Oliu, G., Martin-Belloso, O. and Soliva-Fortuny, R. 2010. Pulsed light treatments for food preservation: A review. *Food and Bioprocess Technology*, 3: 13-23.
24. Osborne, M. R. 1992. Fisher's Method of Scoring. *International Statistical Review*, 60(1): 99-117.
25. Ozer, N. P. and Demirci, A. 2006. Inactivation of *Escherichia coli* O157: H7 and *Listeria monocytogenes* inoculated on raw salmon fillets by pulsed UV-light treatment. *International Journal of Food Science and Technology*, 41(4): 354-360.
26. Puskorius, G. V. and Feldkamp, L. A. 1991. Decoupled extended Kalman filter training of feedforward layered networks. *International Joint Conference on Neural Networks* 91, Seattle International Joint Conference on Neural Networks, Seattle, WA, USA, 1, 771–777.
27. Rumelhart, D. E., Hinton, G. E. and Williams, R. J. 1986. Learning representations by back-propagating errors. *Nature*, 323: 533-536.
28. Yemmireddy, V. K., Cason, C., Moreira, J. and Adhikari, A. 2020. Effect of pecan variety and the method of extraction on the antimicrobial activity of pecan shell extracts against different foodborne pathogens and their efficacy on food matrices. *Food Control*, 112: 107098.
29. Zhang, G., Hu, L., Melka, D., Wang, H., Laasri, A., Brown, E. W., Strain, E., Allard, M., Bunning, V. K., Musser, S. M., Johnson, R., Santillana Farakos, S. M., Scott, V. N., Pouillot, R., Van Doren, J. M. and Hammack, T. S. 2017. Prevalence of *Salmonella* in cashews, hazelnuts, macadamia nuts, pecans, pine nuts, and walnuts in the United States. *Journal of Food Protection*, 80(3): 459-466.
30. Zou, J., Han, Y. and So, S. S. 2008. Overview of artificial neural networks. *Methods Molecular Biology*, 458: 15 – 23.

International Agricultural Engineering Journal ISSN 0858-2114

*September 2025, 34 (1-4) : 57-76*

# Boom Sprayers for Enhanced Productivity and Conservation – A Review

**D. Sivakumar[1*], M. Perarul Selvan[2]**

## ABSTRACT

Boom sprayers are a crucial technological advancement that provides precise and uniform chemical applications reducing waste and environmental harm. They are a prime example of innovations that promote sustainable agriculture**.** This study reviewed the impact of boom sprayers on sustainable agriculture, highlighting their role in innovation, water and soil conservation, and optimizing yields. Based on this review, it is recommended that farmers adopt variable-rate boom sprayers for precise input management, while electrostatic sprayers are most effective in reducing chemical drift and enhancing application efficiency. Additionally this review highlights that when supported by precision agriculture tools, boom sprayers have the potential to significantly reduce environmental damage while improving productivity. Recent advancements such as GPS-guided systems, Variable Rate Technology, Automatic Section Control, sensor-based detection, and AI-driven spraying have transformed their use, ensuring more precise, targeted, and sustainable applications. The study concluded that boom sprayers are most effective for large-scale flat terrains, while UAV and wheel-operated designs are suitable for uneven landscapes. Battery-powered sprayers offer eco-friendly solutions for medium farms, while servo-controlled, GPS-guided, and VRT technologies provide higher accuracy and sustainability at greater cost and complexity. Knapsack and biocontrol sprayers serve niche roles in smallholder and eco-focused systems.

***Keywords:*** *Agricultural Efficiency; Boom Sprayers; Food Security; Precision Agriculture; Resource Management and Sustainable Agriculture.*

## 1. INTRODUCTION

Sustainable agriculture faces the challenge of increasing crop yields to meet global food demand while minimizing environmental impacts. To address these needs, modern agriculture has shifted toward sustainable practices, adopting technological advancements and efficient resource management techniques (Tripathi *et al.*, 2023). The implementation of innovative farming methods, such as conservation practices, reduced tillage, and ecosystem service optimization, enhances soil health and supports long-term sustainability (Yadav *et al.*, 2017). New agricultural strategies, including vertical farming and urban horticulture, further address issues of sustainability and food security, particularly in urban areas with limited arable land (Nwosisi and Nandwani, 2018). A significant advancement in this field is the use of boom sprayers, which ensure precise and uniform chemical application across large agricultural areas, crucial for crop protection and nutrient management (Bayat *et al.*, 2023). These sprayers exemplify agricultural innovation by improving chemical accuracy and minimizing waste, thereby reducing potential environmental damage. Modern farming efficiency has been significantly enhanced by these innovations, enabling more judicious resource use to maintain high yields while mitigating environmental impacts (Soussi *et al.*, 2024).

[1]Professor, [2]Research Scholar, Department of Agricultural Engineering, Kalasalingam Academy of Research and Education, Krishnankoil, India.

**Corresponding author - email: shri.sivakumar0307@gmail.com*

Received: 14 December 2024; Revised: 21 April 2025; Accepted: 22 July 2025.

Boom sprayers are integral to "smart farming" or "precision agriculture," a technological shift that also includes drones, smart sensors, the Internet of Things (IoT), and big data analytics, each designed to increase productivity and sustainability (Karunathilake *et al.,* 2023; IostFilho *et al.,* 2020). Research into advanced boom sprayer designs, such as electrostatic spraying and variable rate technology, demonstrates the potential for technology - driven applications to reduce chemical volumes, leading to lower costs and reduced waste (Patel, 2016; Dionne *et al.,* 2018). For example, electrostatic sprayers enhance droplet adherence to plant surfaces, improving coverage with less chemical use (Patel, 2016). Other innovations, like servo-controlled nozzles for real-time adjustments, further contribute to precision and sustainability in crop management (Bayat *et al.,* 2023). The use of boom sprayers illustrates the role of innovation in sustainable agriculture. These technologies enable data-driven decision-making, allowing for optimized application methods based on specific environmental conditions and crop needs (Soussi *et al.,* 2024). This precision not only improves agricultural efficiency but also helps farmers minimize their ecological footprint, contributing to long-term sustainability and resilience in farming practices (Rajendra, 2020).

In addition to enhancing productivity, boom sprayers are essential in promoting water and food security by optimizing fertilizer and pesticide usage, and reducing the risk of over-application that can lead to nutrient runoff and water contamination (Garcera *et al.,* 2022). Such targeted applications help conserve water resources and protect soil health, both crucial for sustainable food production (Wang *et al.,* 2019; Lal *et al.,* 2024). Consequently, boom sprayers play a critical role in meeting food security goals by preserving water quality and reducing soil degradation (Stejskal *et al.,* 2021). The integration of boom sprayers into integrated pest management (IPM) frameworks also promotes sustainability by combining chemical treatments with biological controls, ensuring efficient pest management with minimal environmental impact. This approach helps maintain the economic viability of farming operations by reducing costs associated with pest and nutrient management, making it a financially sustainable option for many farmers.

Advanced spraying techniques, including selective and variable-rate applications, significantly impact agricultural productivity and environmental sustainability by delivering chemicals only where needed, thus reducing waste (Zaffar and Khar, 2023). Spraying pesticides and fungicides remains one of the most effective methods for protecting crops against pests and diseases, minimizing crop loss, and maximizing yields (Rajendra, 2020). Similarly, strategic herbicide applications through boom sprayers control weeds that compete with crops, enhancing field productivity (Stejskal *et al.,* 2021). Moreover, advancements in spraying technology, such as foliar feeding methods, improve nutrient absorption during critical growth phases, further supporting yield potential and crop management (Soussi *et al.,* 2024; Dionne *et al.,* 2018). The economic benefits of boom sprayers in nutrient and pest management make them instrumental for sustainable agricultural operations. By minimizing the volume of chemicals used and improving application efficiency, boom sprayers reduce operational costs, enhancing financial sustainability. Furthermore, automation and precision spraying reduce labour requirements, boosting productivity and enabling farmers to allocate resources more effectively.

The development of cost-effective and energy-efficient sprayers, including battery-operated and self-propelled models, has further expanded their accessibility to a wider range of farmers, contributing to the economic viability of both small and large farms (Lal *et al.,* 2024).

Additionally, boom sprayers contribute to environmental sustainability by reducing chemical drift, thereby minimizing unintended impacts on surrounding ecosystems (Stejskal *et al.,* 2021). Research into safer formulations and novel application methods, such as drone-based and electrostatic spraying, supports the reduction of chemical usage while maintaining efficacy, and promoting sustainable farming practices (IostFilho *et al.,* 2020; Garcera *et al.,* 2022). This study aims to assess the effectiveness and enhance the precision of the boom sprayers for higher crop yields, and foster sustainable food production.

## 2. TYPES OF SPRAYERS

Agriculture utilizes various sprayers tailored for specific crop growth needs. Handheld sprayers are affordable and user-friendly, making them suitable for small-scale applications in gardens or small farms to apply pesticides and fertilizers locally (Jalu *et al.,* 2023). Knapsack sprayers are portable and effective for small to medium-sized fields, allowing for spot treatments of fertilizers and insecticides. Conversely, boom sprayers, equipped with multiple nozzles on tractors, are designed for large-scale farms to apply herbicides and fertilizers uniformly over vast areas (Rajendra, 2020). Innovations in sprayer technology enhance water and food security by optimizing input applications. Air blast sprayers, for example, provide high-volume treatment and effective coverage in dense crops like fruit trees (Garcera *et al.,* 2022). Mist blowers atomize liquid chemicals into fine droplets, improving coverage and reducing chemical use, which helps conserve water resources (Stejskal *et al.,* 2021). Electrostatic sprayers increase droplet adhesion, thereby minimizing waste and enhancing efficiency (Patel, 2016). Emerging technologies like drone sprayers offer precision and cost-effectiveness, enabling targeted applications in challenging areas (IostFilho *et al.,* 2020). Among these, boom sprayers are particularly advantageous for large-scale farms, ensuring even and effective application of inputs. Their versatility and capacity for extensive coverage make them essential for modern agricultural operations, supporting sustainable practices that address the growing global food demand while protecting environmental resources.

## 3. BOOM SPRAYERS AND TYPES

Boom sprayers are essential equipment in modern agriculture, especially for large-scale farms, as they efficiently administer fertilizers, herbicides, and insecticides across wide areas. Ensuring the right product dosage per unit area is crucial when applying insecticides, requiring commercial sprayers to meet phytosanitary standards. Boom sprayers are categorized based on crop type and specific treatments; proving particularly effective for large crops like maize, wheat, barley, and tomatoes. they utilize a single boom equipped with nozzles spaced at fixed intervals to ensure uniform product distribution (Wang *et al.,* 2019). However, variations in horizontal speed can disrupt this uniformity, particularly at plot margins, leading to overlaps or missed treatments (Dionne *et al.,* 2018). Implementing map-based automatic boom section control can significantly enhance coverage consistency and accuracy, optimizing pesticide application while reducing overlaps, thus improving overall agricultural efficiency (Bayat *et al.,* 2023). The operational principles of boom sprayers involve several key components that enhance their effectiveness. The pump drives liquid from the tank to the nozzles under pressure, while different nozzle types atomize the liquid into fine droplets for even distribution. The boom, typically adjustable in height, maximizes spray reach while minimizing drift, and some systems feature recirculation mechanisms that reduce waste. Studies highlight the performance of boom sprayers, indicating effective field capacities and efficiencies that contribute to improved crop protection and resource management (Wang *et al.,* 2019; Bayat *et al.,* 2023). These advancements are crucial for promoting food security and sustainable agricultural practices, enabling farmers to achieve

higher yields while minimizing environmental impact (Dionne *et al.*, 2018).

Manually powered boom sprayer is an essential agricultural tool designed for the effective application of liquid solutions, including fertilizers, herbicides, and pesticides, to crops. Featuring a horizontal boom connected to a tank with multiple spray nozzles, these sprayers come in various types, such as manual, battery-operated, semi-automatic, and self-propelled**,** offering a user-friendly and cost-effective solution for gardening, horticulture, and small-scale farming. By allowing for precise chemical distribution over wide areas, they enhance operational efficiency while minimizing the risks of under- or over-spraying, ultimately contributing to improved crop protection and productivity.

### 3.1. Manual Boom Sprayers

A manually powered boom sprayer is an agricultural tool used to apply liquid solutions like fertilizers and pesticides to crops. It features a long horizontal boom with nozzles, and operation typically involves manual pushing or pulling, although some models have automated components. Popular in small-scale farming and gardening, these sprayers are cost-effective, user-friendly, and ensure even chemical distribution, reducing the risk of over- or under-spraying. The adjustable boom allows for simultaneous spraying over multiple rows, improving efficiency. The liquid is pressurized via a hand or motorized pump. Battery-operated models, like those developed in India, improve efficiency with better ergonomics and reduce operator strain. In Nigeria, self-propelled sprayers offer enhanced coverage and chemical control. Other innovations include semi-automatic sprayers (Putri *et al.*, 2022), ergonomic designs (Lal *et al.*, 2024), and improved spray quality. These innovations boost efficiency and reduce labour costs. Table 1 summarizes the significant impact of boom sprayer innovations on agricultural sustainability by showcasing advancements that enhance productivity while minimizing environmental harm.

From Table 1, it may be observed the suitability of battery-operated sprayers on small farms where vegetables, maize, and brinjal are cultivated. Results indicated that the battery-powered manually operated boom sprayer performed effectively at 91 kPa pressure and 1.50–2.00 km/h speed, with 50% greater field efficiency than manual sprayers for brinjal crop. Walking-type battery-operated sprayers further reduced fatigue to the operator and improved chemical distribution. Such performance values confirm that battery-supported designs enhance productivity, protect health, and reduce chemical losses in smallholder systems. Semi-automatic sprayers achieved 86% efficiency with a capacity of 0.32 ha/h, placing them as suitable technologies for medium farms where labour saving and moderate cost are essential. Walking-type sprayer–cum–weeder models reported 81.9% weeding efficiency with a payback period of 3.5 years, confirming strong economic viability for diversified smallholder farms. Battery-operated sprayers deliver clear benefits for marginal and small-scale farmers, semi-automatic designs provide intermediate solutions for medium-scale production, and self-propelled herbicide sprayers address the requirements of large fields with reduced chemical exposure. CAD-based and walking-type innovations demonstrate strong environmental protection through controlled application and reduced drift. The combination of spraying and weeding in a single machine further strengthens long-term economic sustainability. Overall, sprayer technologies achieving measurable improvements in efficiency and distribution should receive priority adoption, as they enhance productivity while minimizing environmental damage.

## 3.2 Tractor - Mounted Boom Sprayers

Research on tractor-mounted boom sprayers aims to optimize chemical use, minimize drift, and enable real-time adjustments based on field variability. Integrating GPS, GIS, sensors, and Variable Rate Technology (VRT) reduces costs and environmental impact.

**Table 1. Impact of boom sprayer on agricultural sustainability**

| Sl.No | Type | Results and Innovations | Sustainability | Reference(s) |
|---|---|---|---|---|
| 1 | Battery-powered, manually operated boom sprayer. | Effective at 91 kPa pressure and 1.50 - 2.00 km/h, with enhanced mobility through battery operation. | Boosts productivity for small-scale farmers | Yadav *et al.* (2017) |
| 2 | Self-propelled herbicide boom sprayer. | Improved coverage, reduced chemical exposure, and increased efficiency using local components. | Reduces costs and supports local economies | Bayat *et al.* (2023) |
| 3 | Semi-automatic boom sprayer for maize. | Achieved 86% efficiency and 0.32 ha/h capacity with semi-automatic features. | Increases productivity and reduces labour input | Putri *et al.* (2022) |
| 4 | Battery-operated boom sprayer for brinjal. | 50% greater field efficiency and better ergonomics than manual sprayers. | Promotes better working conditions for farmers | Lal *et al.* (2024) |
| 5 | Wheel-operated boom sprayer. | CAD-based design with adjustable boom and 2.5:1 gear ratio improves precision. | Enhances efficiency and reduces environmental impact | Zaffar and Khar (2023) |
| 6 | Walking-type battery-operated boom sprayer. | Improved design enhances chemical distribution, reducing operator fatigue. | Reduces labour intensity and improves crop protection | Tripathi *et al.* (2023) |
| 7 | Walking-type battery-operated sprayer cum weeder. | Weeding efficiency is 81.9%, with reduced labour and cost, and a payback period of 3.5 years. | Increases economic viability and sustainability for small farms | Lal *et al.* (2024) |

Enhancements in nozzle design, droplet size, and air-assist technologies help minimize off-target contamination. Energy efficiency is also a focus, with innovations like renewable energy sources and efficient pumps. Pawar *et al.* (2023) optimized pesticide application using an air-assisted sprayer. Jalu *et al.* (2024) showed that a mini tractor-operated sprayer reduced operating time and costs. Overall, continuous research enhances sprayer design for greater efficiency, sustainability, and economic viability in agriculture. Table 2 highlights the advancements in sprayer technology that significantly enhance agricultural sustainability by promoting efficient chemical use and minimizing environmental impact.

Recommendations from Table 2 highlight effective of the air-assisted sprayers at 15 kPa and 3 km/h for precise droplet distribution resulting reduced chemical waste. Tractor-mounted sprayer / weeders achieved an efficiency of 88.9%, while mini tractor-operated versions reduced operating time by 95.7% and achieved 84.5% weeding efficiency, leading to significant labour and fuel savings. Control valve assemblies saved up to 33.4% liquid and improved spray properties at 689 kPa, showcasing their role in minimizing wastage. Rear-mounted sprayers with swath width of 3.20 m and a capacity of 0.72 ha/h, along with commercial models delivering 400 cm spray width at 1.00 MPa, expanded coverage and promoted resource conservation. Microner sprayers outperformed conventional boom sprayers in weed control and spray quality, supporting their adoption where higher precision is required. These findings (Table 2) concluded that tractor-mounted boom sprayers enhance sustainability through higher efficiency, better coverage, and reduced chemical use. Air-assisted and control valve designs ensure accuracy in pesticide application, while sprayer/weeders and mini tractor-operated models provide labour and time savings. Rear-mounted, commercial, and microner sprayers extend coverage and improve spray quality, offering the most reliable options for large-scale farms seeking both productivity gains and environmental protection.

### 3.3. Self - Propelled Boom Sprayers

Self-propelled boom sprayers improve the precision and efficiency of pesticide and fertilizer applications, reducing waste and environmental impact. They integrate technologies like GPS and automated systems for site-specific management, ensuring accurate input application. Studies evaluate factors such as pressure, speed, and nozzle types to develop best practices, while economic assessments highlight labour savings and potential yield increases. Research also addresses user ergonomics, environmental impacts, and pest management. Field tests confirm that self-propelled sprayers outperform traditional methods in sustainability and productivity. Liu *et al.* (2022) optimized boom suspension for enhanced spray performance, while Su *et al.* (2021) found a nozzle configuration achieving over 95% broadleaf weed control. Elwakeel *et al.* (2022) reported high field capacity and cost efficiency, while Parmar *et al.* (2023) improved application consistency through automated control. Innovations like crab steering and automated spray control contribute to better manoeuvrability, reduced soil compaction, and enhanced agricultural sustainability. Table 3 outlines key advancements in sprayer technology that bolster agricultural sustainability through enhanced operational efficiency and minimized environmental impact.

Recommendations from Table 3 emphasize the adoption of self-propelled boom sprayers equipped with suspension systems that reduce stress and displacement, ensuring spray stability and efficiency. Weed control above 95% with recovery from phyto-toxicity in 14 days confirms sustainable crop protection. Field sprayers delivering 3.6 ha/h at 2.5 m/s with an operating cost of 1.2 USD/h at 9.5 kPa demonstrate high capacity with low expense.

**Table 2. Tractor-mounted boom sprayers in sustainable agriculture**

| Sl.No | Type | Results and Innovations | Sustainability | Reference(s) |
|---|---|---|---|---|
| 1 | Air-assisted Sprayer. | Achieved optimal pesticide application at 15 kPa and 3 km/h, improving droplet distribution. | Reduces chemical waste and improves precision | Pawar *et al.* (2023) |
| 2 | Sprayer/Weeder. | A tractor-operated sprayer/weeder showed 88.9% weeding efficiency and minimal fuel consumption. | Reduces labour and fuel use, promoting sustainability | Jalu *et al.* (2024) |
| 3 | Control Valve Assembly. | Adjusted droplet size and density, saving up to 33.4% of the liquid by closing off valves. | Optimizes droplet application, reducing waste | Pramod *et al.* (2022) |
| 4 | Mini Tractor-operated Sprayer / Weeder. | Reduced operating time by 95.7% and achieved 84.5% weeding efficiency. | Boosts productivity and reduces manual labour. | Jalu *et al.* (2024) |
| 5 | Boom Sprayer for Chili Crops. | Achieved optimal droplet sizes and densities at peak conditions. | Improves pest control while minimizing pesticide use. | Pramod *et al.* (2022) |
| 6 | Comparison Study. | Microner sprayers outperformed conventional boom sprayers in weed control and spray quality. | Helps in selecting efficient sprayer types. | Hamid *et al.*, (2015) |
| 7 | Control Valve Enhancement. | Improved spray width and properties at 689 kPa pressure with closed valves. | Enhances accuracy and reduces contamination. | Pramod *et al.* (2022) |
| 8 | Commercial Boom Sprayer. | Achieved 400 cm spray width at 1 MPa pressure and 45 cm height. | Increases coverage and conserves resources. | Kim *et al.* (2017) |
| 9 | Rear-mounted Boom Sprayer. | Designed with a 3.20 m swath width and 0.72 ha/h capacity for row crops. | Enhances operator safety and operational efficiency. | Patel (2016) |
| 9 | Rear-mounted Boom Sprayer. | Designed with a 3.20 m swath width and 0.72 ha/h capacity for row crops. | Enhances operator safety and operational efficiency. | Patel (2016) |

**Table 3. Self-propelled boom sprayers in sustainable agriculture**

| Sl.No | Type | Results and Innovations | Sustainability | References |
|---|---|---|---|---|
| 1 | Optimal Boom Suspension | Reduced stress and displacement; Enhanced boom design improves spray effectiveness and stability. | Increases efficiency and reduces environmental impact. | Liu *et al.* (2022) |
| 2 | Control Efficiency | Over 95% control of broadleaf weeds; Recovery from phyto-toxicity in 14 days | Supports sustainable weed management. | Su *et al.* (2021) |
| 3 | Self-propelled Field Sprayer | The field capacity is 3.64 ha/h, the forward speed is 9 km/h, the operating cost is approximately 1.2 USD/h, and the pressure is 9.5 kPa, with the improved field efficiency value remaining unchanged. | Increases productivity and lowers operational costs. | Elwakeel *et al.* (2022) |
| 4 | Automated Spray Control System | Accuracy of improved application; Automation reduces chemical waste. | Enhances precision and reduces chemical use. | Parmar *et al.*, (2023) |
| 5 | Crab Steering System | Better maneuverability with minimal wheel deviation; Innovative steering design. | Reduces soil compaction and enhances efficiency. | Li *et al.* (2022) |
| 6 | Variable Height Crop Sprayer | Optimized spray parameters for herbicides and fungicides; Low prediction errors. | Enhances pesticide effectiveness | Khan *et al.* (2022) |
| 7 | High-clearance Sprayer Chassis | Good stability and performance in harsh conditions; Robust design for various terrains. | Increases operator safety and comfort | Chen *et al.* (2020) |

Automated control systems enhance accuracy and reduce chemical wastage, crab steering improves manoeuvrability while minimizing soil compaction, variable-height sprayers optimize herbicide and fungicide applications, and high-clearance chassis provide safe and stable operation across varied terrains. These findings conclude that self-propelled sprayers integrate advanced suspension, automation, steering, and chassis designs that collectively improve precision, productivity, and sustainability. High efficiency in weed control, optimized spray delivery, reduced operational costs, and greater operator safety establish self-propelled sprayers as the most effective technology for large-scale sustainable farming.

## 4. TECHNOLOGICAL ADVANCEMENTS IN BOOM SPRAYERS

The applications of boom sprayers in modern agriculture are pivotal in enhancing efficiency and sustainability within the industry. Technological advancements in boom sprayers, including GPS, Variable Rate Technology (VRT), and AI integration, are revolutionizing the way pesticides and fertilizers are applied. These innovations not only optimize input usage but also contribute to environmental conservation, thereby aligning agricultural practices with sustainable development goals.

### 4.1. GPS-guided Spraying Systems

Precision agriculture increasingly relies on GPS-guided spraying systems, enhancing precision, resource efficiency, and environmental benefits in fertilizer and pesticide applications. GPS-guided systems control application areas with high accuracy, minimizing waste and overlap, which reduces pesticide residues and environmental impact. Studies show GPS-guided devices significantly cut chemical usage by targeting only necessary areas, reducing labour costs, and aligning with sustainable farming goals. Real-time locating and mapping advancements have popularized these devices in large-scale and high-value agriculture. A solar-powered GPS-guided sprayer distributes pesticides uniformly, conserving resources and enabling farmers to track coverage via an app (Ali *et al.,* 2022). A GPS-guided autonomous robot controlled through 3G achieved navigation precision within 10-17 cm, optimizing field treatments. Another GPS-guided agricultural robot, powered by bike batteries and featuring machine learning, demonstrated precision in fertilization, herbicide spraying, and weed detection (Khan *et al.,* 2018). Such innovations highlight GPS-guided systems' transformative potential for enhancing agricultural precision with minimal environmental impact.

### 4.2. Variable Rate Technology (VRT)

Boom sprayers equipped with Variable Rate Technology (VRT) dynamically adjust spray rates across boom sections, ensuring precise application of pesticides and nutrients. By integrating sensors and GPS, VRT-equipped sprayers apply inputs based on soil data, crop health, and pest pressure, ensuring each area receives the required amount. This precision approach reduces environmental impact, maximizes crop protection, and boosts productivity, supporting sustainable agriculture goals. Research suggests VRT can cut input use by over 40% in certain cases (Ahmad *et al.,* 2018). Smart VRT systems using deep learning, like tiny-YOLOv3, reduced spray volume by over 40% in potato fields, providing substantial cost savings (Hussain *et al.,* 2020). VRT remains a pivotal innovation for sustainable farming, addressing food demand and climate challenges.

### 4.3. Automatic Section Control (ASC)

Automatic Section Control (ASC) in boom sprayers optimizes fertilizer and pesticide use while minimizing waste. Unlike traditional sprayers, which may over apply chemicals in overlapping areas, ASC systems use GPS and mapping to prevent over-application by turning off boom sections over previously treated areas.

Field tests showed over 90% accuracy in preventing overlap and chemical waste (Cui *et al.,* 2019). A feed-forward control system improved boom stability, reducing spray drift and maintaining droplet consistency (Li *et al.,* 2023a). Another study achieved near-complete overlap control and a 3.3 m maximum repeated spraying distance using GPS and RTK-GNSS systems (Li *et al.,* 2023b). These advancements underscore ASC's role in enhancing precision agriculture's sustainability.

### 4.4. Sensor - Based Spraying

Sensor-based spraying optimizes chemical application by dynamically adjusting spray rates based on real-time data gathered from advanced sensors such as LiDAR and multispectral imaging (Soussi *et al.,* 2024). These sensors provide detailed insights into crop conditions, soil health, and environmental variables, allowing sprayers to apply chemicals only where and when they are needed. This precision ensures more targeted and efficient use of fertilizers and pesticides, significantly reducing both under- and over-application. The result is minimized chemical runoff, lower environmental impact, and reduced costs for farmers. By reducing the use of chemicals, sensor-based spraying also helps protect beneficial organisms, such as pollinators, and promotes sustainable agriculture practices. Moreover, it helps farmers make data-driven decisions, optimizing resource use, improving crop yield, and fostering long-term ecological balance (Stejskal *et al.,* 2021).

### 4.5. Smart Spraying with AI and Machine Learning

AI and machine learning in smart spraying technology enable boom sprayers to dynamically control fertilizer and pesticide delivery. Unlike traditional sprayers that apply chemicals uniformly, AI-enhanced systems assess field conditions in real time, identifying soil, weed density, and crop health variations (Soussi *et al.,* 2024). This enables precise spraying in areas requiring treatment, reducing waste and chemical use. Ongoing research in AI algorithms and sensor integration continues to improve system accuracy and adaptability, contributing to more sustainable and efficient farming practices (Su *et al.,* 2021).

Modern boom sprayers are rapidly evolving through technological integration, enabling farmers to increase productivity while minimizing environmental harm. Key innovations include:

- *GPS-guided spraying systems*: Provide precise targeting, reduce overlaps, and minimize pesticide use, especially valuable for large-scale farming.
- *Variable Rate Technology*: Adjusts spray rates according to soil, crop, and pest conditions, often cutting input usage by up to 40% and ensuring balanced application.
- *Automatic Section Control*: Prevents double application by shutting off sections in overlap areas, significantly reducing waste and spray drift.
- *Sensor-based spraying*: Uses LiDAR and multispectral imaging to apply inputs only where needed, protecting pollinators and reducing runoff.
- *AI and Machine Learning integration*: Enhances decision-making by analyzing real-time crop health and weed density, enabling precise, targeted spraying with minimal human input.

Collectively, these technologies advance precision agriculture, conserving resources, cutting costs, protecting ecosystems, and aligning with sustainability goals.

## 5. APPLICATIONS OF BOOM SPRAYERS IN MODERN AGRICULTURE

Advancements in the applications of boom sprayers in modern agriculture are transforming agricultural practices and enhancing the efficiency and sustainability of pesticide, fertilizer, herbicide, and fungicide applications. Innovations such as sensor-based detection, AI

integration, and precision-guided systems enable more accurate and targeted applications, reducing chemical usage and environmental impacts. These developments are crucial for promoting responsible resource management and fostering sustainable agricultural practices in response to growing global demands.

### 5.1. Pesticide Application

Boom sprayers are essential in modern agriculture, enabling efficient pesticide application across large areas and promoting crop protection. Challenges with traditional sprayers, such as chemical drift, overlap, and runoff, can reduce effectiveness and harm the environment. Innovations like sensor-based spraying, AI-driven systems, and GPS-guided autonomous section control aim to minimize these issues, enhancing application accuracy and reducing chemical use (Karunathilake *et al.,* 2023). Research shows these advancements can cut pesticide consumption by up to 30%, supporting sustainability in agricultural operations (Khan *et al.,* 2022; Kim *et al.,* 2017). As these systems advance, precision-equipped boom sprayers play a critical role in promoting responsible pesticide use within sustainable agriculture.

### 5.2. Fertilizer Application

Boom sprayers enable efficient, large-scale fertilizer application by ensuring consistent distribution across fields. Traditional sprayers often face issues with over-application, overlap, and uneven distribution, which increase costs, create soil imbalances, and cause environmental runoff. Enhanced boom sprayer technologies, including sensor-based systems, variable-rate applications, and autonomous section control, are being developed to tackle these issues by adjusting fertilizer application based on real-time data reflecting crop and soil needs (Li *et al.,* 2022; Lal *et al.,* 2024). Precision-enabled sprayers can reduce fertilizer use by up to 20%, improving nutrient efficiency and contributing to sustainable agriculture (Li *et al.,* 2023b; Liu *et al.,* 2022).

### 5.3. Herbicide Spraying

Effective weed control relies on boom sprayers, but traditional models often apply herbicides uniformly, resulting in chemical waste, increased costs, and environmental hazards like drift and runoff. Advances in boom sprayer technology, such as sensor-based weed detection, AI-driven recognition for targeted spraying, and autonomous section control, address these issues by limiting herbicide application only to areas where weeds are detected (Khan *et al.,* 2018). This precise application can reduce herbicide usage by up to 90%, addressing herbicide resistance and minimizing environmental impact while ensuring effective weed control (Li *et al.,* 2023b; Lal *et al.,* 2024).

### 5.4. Fungicide and Disease Management

Boom sprayers are crucial for large-scale fungicide applications, protecting crops from diseases that impact yield and quality. Traditional sprayers may lack the accuracy needed, leading to over-application and uneven distribution, which results in higher costs, residue build-up, and environmental risks. New advancements, including sensor-based detection, variable-rate technology, and real-time disease mapping, allow for targeted fungicide applications that respond to specific disease pressures (Li *et al.,* 2023a; Lal *et al.,* 2024). Studies indicate these technologies can reduce fungicide use by 20-30%, enhancing disease management efficiency and decreasing environmental impact (Khan *et al.,* 2022). Advancements in boom sprayer technology across pesticide, fertilizer, herbicide, and fungicide applications drive sustainable agricultural practices by reducing chemical use, enhancing precision, and lowering environmental risks. Continued research will help adapt these systems to diverse crop types and field conditions, ensuring precision-equipped boom sprayers support responsible resource management in agriculture.

## 6. EFFICIENCY AND PRECISION IN BOOM SPRAYING

Achieving uniformity, efficiency, and precision in spray distribution is crucial for boom sprayers, as these factors directly influence crop health, yield quality, and environmental sustainability. Traditional sprayers face challenges like drift, overspray, and uneven spray patterns, leading to chemical waste and environmental harm. Consequently, research has increasingly focused on innovations such as advanced nozzle designs and AI-driven sensors to improve spray distribution, efficiency, and precision, advancing sustainable agricultural practices.

### 6.1. Spray Distribution Uniformity

Ensuring uniform spray distribution is crucial for improving crop health and environmental sustainability. Traditional sprayers often lead to drift, overspray, and uneven patterns, resulting in chemical waste and unintended environmental consequences. Innovations like AI-driven sensors, advanced nozzles, and dynamic droplet control systems help address these challenges (Putri *et al.*, 2022). Technologies such as adaptive nozzles, machine-learning-driven spray mapping, and real-time drift compensation are proving effective in reducing chemical use by precisely targeting specific zones. However, further research is necessary to implement these solutions across various crops and climates (Lal *et al.*, 2024).

### 6.2. Droplet Size and Drift Control

Controlling droplet size and drift is essential for precise and efficient pesticide, herbicide, and fungicide applications. Smaller droplets improve coverage but are prone to drift, while larger droplets reduce drift but may result in uneven coverage. Innovations in nozzle design, spray patterns, and application techniques aim to strike a balance in addressing this challenge, ultimately enhancing safety and efficiency (Zaffar and Khar, 2023). Optimizing droplet size control has shown the potential to reduce chemical use by 20-30% without compromising efficacy (Ali *et al.*, 2022; Khan *et al.*, 2018).

### 6.3. Coverage and Penetration

Achieving effective treatment requires adequate coverage and penetration, influenced by factors such as nozzle type, application pressure, and environmental conditions. Ongoing research is focused on advanced nozzles and spray techniques to improve the efficiency of pest and disease control. Maintaining consistent coverage not only reduces chemical usage but also ensures crop protection and promotes sustainable practices.

### 6.4. Reducing Chemical Usage and Environmental Impact

Minimizing chemical use and mitigating environmental impacts are critical in agricultural spraying. Precision technologies, including sensor-based systems and variable-rate applications, optimize timing, dosage, and targeted application, reducing chemical use by 20-50% while maintaining efficacy (Putri *et al.*, 2022; Lal *et al.*, 2024). Continued research will help adapt these technologies for diverse crops and environments, supporting efficient resource use and minimizing environmental exposure (Khan *et al.*, 2018).

Efficiency in boom spraying depends on uniform spray distribution, droplet control, coverage, and reduced chemical use. Traditional sprayers often cause drift, overspray, and waste, but innovations such as AI-driven sensors, adaptive nozzles, and Variable Rate Technology (VRT) ensure precision and consistency. Optimized droplet management cuts chemical use by 20–30%, while precision systems lower inputs by 20–50% without reducing efficacy. These advancements make boom spraying more accurate, sustainable, and environmentally responsible, though further research is needed for wider adaptation.

## 7. CHALLENGES AND LIMITATIONS OF BOOM SPRAYERS

Boom sprayer technology has enhanced agricultural efficiency and precision in chemical

applications, but several challenges remain, especially for smaller farms. Addressing these limitations is vital for promoting sustainable and accessible farming practices.

i. *Precision and Variability Limitations*: Boom sprayers struggle with consistent application on uneven terrain, leading to variable coverage and reduced effectiveness (Corpe *et al.,* 2013). GPS systems improve accuracy, but real-time adaptation to environmental changes is limited (Corpe *et al.,* 2013). Variable-rate technology (VRT) also requires high-quality data and calibration, making it resource-intensive (Ahmad *et al.,* 2018).

ii. *Technical and Operational Complexities*: Advanced systems like VRT and automated boom height controls increase operational complexity, necessitating specialized skills that may deter adoption by smaller farms (Saleem *et al.,* 2023). Smart sprayers using deep learning and electronic suspension controls require large datasets and frequent adjustments (Hussain *et al.,* 2020; Cui *et al.,* 2019).

iii. *Boom Height Control Challenges*: Maintaining optimal boom height on uneven terrain is challenging, resulting in uneven coverage and increased drift risk (Herbst *et al.,* 2018; Dou *et al.,* 2021). Automatic height control technologies are impacted by wind and crop density, reducing reliability (Herbst *et al.,* 2018).

iv. *Drift Control and Environmental Impact*: Drift control is challenging in windy conditions, with antidrift systems often varying in effectiveness (Fu *et al.,* 2020). Drift not only leads to chemical waste but also impacts non-target ecosystems (Li *et al.,* 2023a).

v. *Cost and Accessibility Barriers*: The high costs of GPS, VRT, and control systems limit adoption, especially for smaller farms (Saleem *et al.,* 2023). These technologies require significant investment, restricting access for smaller operations (Li *et al.,* 2023a).

vi. *Need for Improved Real-Time Adaptability*: Precision sprayers lack the flexibility to adapt in real-time, reducing effectiveness in dynamic environments like mixed vegetation fields (Li *et al.,* 2023b).

vii. *Limitations in Data Integration and Interoperability*: Interoperability issues hinder data integration across different systems, highlighting the need for standardized platforms to enhance compatibility and precision (Saleem *et al.,* 2023).

viii. *Environmental and Regulatory Constraints*: Increasing regulations on chemical use limit operational flexibility and require eco-friendly technologies to comply with restrictions on chemical types and application rates (Herbst *et al.,* 2018).

These challenges underscore the importance of further research to improve adaptability, reduce costs, and meet environmental demands.

## 8. COMPARISON OF BOOM SPRAYERS WITH OTHER SPRAYERS

Boom sprayers are often compared with knapsack sprayers and Unmanned Aerial Vehicle (UAV), to assess effectiveness, precision, and environmental impact. Known for providing uniform coverage over large areas, boom sprayers may face challenges on uneven terrain, where UAVs or wheel-operated systems offer advantages (Zaffar and Khar, 2023). While UAVs are adaptable in diverse landscapes, they may provide less consistent spray deposition due to height and wind variability, reducing efficacy in dense crops like wheat (Wang *et al.,* 2019). Knapsack sprayers are suitable for smaller, targeted applications on limited acreage crops. Field studies indicate that tractor-mounted boom sprayers outperform knapsack models in efficiency and labour requirements, making them economical for large-

scale use. Servo-controlled nozzles further improve boom sprayer precision for pest and weed control (Bayat *et al.*, 2023). Table 4 outlines key sprayer types and their respective applications, highlighting advancements that enhance agricultural efficiency and sustainability. Boom sprayers are recognized for their high efficiency in large-scale operations, offering uniform coverage and reduced labour costs, despite facing challenges in uneven terrains.

From Table 4, it can be noted that boom sprayers are the most efficient option for large-scale uniform coverage, although they are limited on uneven terrains. UAV sprayers provide adaptability for varied landscapes but face higher spray drift and limited large-scale suitability. Knapsack sprayers remain cost-effective for localized use but are labour-intensive and less uniform. Servo-controlled boom sprayers deliver precise spraying with real-time nozzle adjustment but require calibration and higher technology investment. Battery-operated boom sprayers reduce emissions and operator fatigue on medium-scale flat terrains, though battery capacity limits extended use. Wheel-operated sprayers improve safety on hilly fields yet lose efficiency on flat areas. Biocontrol sprayers reduce pesticide reliance through targeted biological release, though their effectiveness remains narrower than chemical options. GPS-guided sprayers minimize overlap and operator error but depend on costly equipment and reliable signals, while VRT sprayers optimize chemical input and costs with advanced precision though requiring high setup and technical expertise.

## 9. ENVIRONMENTAL AND SAFETY CONSIDERATIONS

Environmental and safety considerations are essential in selecting a spraying system. Boom sprayers help reduce chemical drift, especially with precision nozzles and sensors, offering lower environmental contamination compared to UAVs, which are more prone to drift in windy conditions (Bayat *et al.*, 2023). Battery-operated boom sprayers are also environmentally friendlier by cutting fuel use and greenhouse gas emissions compared to tractor-based systems (Lal *et al.*, 2024). However, issues like chemical overuse and runoff persist, highlighting the need for real-time dose adjustment technology. Wheel-operated boom sprayers improve stability and reduce fatigue on hilly terrain, enhancing operator safety (Zaffar and Khar, 2023). Automated shut-off mechanisms can also limit chemical exposure, although they raise initial costs (Putri *et al.*, 2022).

## 10. FUTURE TRENDS IN BOOM SPRAYER TECHNOLOGY

Future boom sprayer technology trends focus on automation, sustainability, and adaptability to diverse crop conditions. GPS-guided nozzles and servo-controlled spray angles now dynamically adjust to field contours, enhancing efficiency on uneven terrain (Bayat *et al.*, 2023). Machine learning algorithms are being tested to fine-tune chemical application rates based on crop health data, potentially reducing pesticide use by 20 -30% (Wang *et al.*, 2019). Battery-operated, energy-efficient models aim to lower carbon emissions, promoting sustainability (Lal *et al.*, 2024). Hybrid sprayers combining manual and automated modes offer smaller farms cost-effective solutions, enabling choice based on needs and budget. Servo-controlled systems that adjust spray rates based on crop density are also being explored to reduce drift, essential in sensitive areas (Bayat *et al.*, 2023).

## 11. RECOMMENDATIONS

Boom sprayers offer diverse benefits in sustainable agriculture, and the following options are recommended for effective use with minimal environmental impact:

- *Variable-Rate Sprayers in Precision Management*: Ensure accurate input use, reduce over- and under-application, cut costs, and protect soil and water.

**Table 4. Comparison of applications, advantages, and limitations between boom and other sprayers**

| Sprayer Type | Primary Application | Advantages | Limitations | Relevant Research |
|---|---|---|---|---|
| Boom Sprayer | Large-scale, uniform crop coverage | High efficiency, uniform spray, reduced labour costs (tractor-operated). | Limited in hilly or uneven terrains; stability and accuracy issues. | Wang *et al.* (2019); Bayat *et al.* (2023); Zaffar and Khar (2023) |
| Unmanned Aerial Vehicle (UAV) | Precision spraying for varied terrains | High adaptability; ideal for uneven or densely vegetated areas. | Higher spray drift, less suitable for large-scale applications. | Wang *et al.* (2019); Ali *et al.* (2022) |
| Knapsack Sprayer | Small-scale, targeted applications | Low cost, easy operation, effective for localized treatments. | Labour-intensive; lacks spray uniformity; less efficient. | Yadav *et al.* (2017) |
| Servo-Controlled Boom Sprayer | Real-time nozzle adjustment for precision spray | Enhanced spray accuracy for pest/weed control. | Requires calibration and maintenance; higher technology cost. | Bayat *et al.* (2023); Cui *et al.* (2019) |
| Battery-Operated Boom Sprayer | Medium-scale applications on flat terrains | Reduces fuel consumption and emissions; eco-friendly, reduces fatigue. | Limited battery life; less powerful for large farms. | Lal *et al.* (2024); Putri *et al.* (2022) |
| Wheel-Operated Boom Sprayer | Hilly terrains and rough landscapes | Improved stability and safety in uneven environments. | Less efficient on flat terrains; can be labour intensive. | Zaffar and Khar (2023) |
| Biocontrol Boom Sprayer | Biological agent release for pest control | Specializing in biocontrol reduces pesticide use. | Limited scope; less effective than chemical pesticides. | Dionne *et al.* (2018) |
| GPS Guided Sprayer | Precision and automated spraying | Reduced chemical usage, minimized overlap, and reduced operator error. | High equipment cost; poor GPS signals in some areas | Ali *et al.* (2022); Corpe *et al.* (2013); Ahmad *et al.* (2018); Khan *et al.* (2018) |
| Variable-Rate Technology (VRT) Sprayer | Targeted, variable application rates | Optimizes chemical use, reduces environmental impact, and costs. | High setup costs; complex, requires specialized skills | Hussain *et al.* (2020); Saleem *et al.* (2023) |

- *Electrostatic Sprayers in Drift Control and Coverage*: Minimize chemical drift, improve leaf coverage, and reduce environmental risks in windy conditions.
- *Energy-Efficient Models for Small Farm Adoption*: Provide affordable, user-friendly options for small and medium farms, widening access to sustainable spraying.
- *Integrated Use with Smart Farming Tools*: Combining boom sprayers with drones, sensors, and data analytics maximizes efficiency and strengthens sustainable farm management.
- *Optimized Boom Height Adjustment*: Maintaining proper boom height ensures uniform spray coverage and reduces input losses.
- *Terrain-Adapted Designs*: Sprayers equipped for uneven or sloped fields improve consistency of application and treatment efficacy.
- *Training and Skill Development*: Farmer training in handling and calibration enhances efficiency, safety, and long-term sustainability of sprayer use.
- *Regulation-Compliant Models*: Adopting sprayers designed to meet safety and environmental regulations helps reduce risks of misuse and chemical contamination.

Adopting the right sprayer technology, tailored to farm size, terrain, and resource availability, ensures higher productivity with reduced environmental impact, making boom sprayers key drivers of sustainable agriculture.

## 12. CONCLUSIONS

Sprayers are integral to precision agriculture, working alongside technologies such as drones, IoT devices, and big data analytics to improve productivity and sustainability. Innovations like electrostatic spraying and variable-rate technology enhance coverage and decrease chemical use, leading to lower costs and reduced environmental impact. Boom sprayers play a vital role in conserving water, protecting soil health, and managing nutrient runoff, thus significantly contributing to water and food security, key components of sustainable food production. Based on the studies, variable-rate boom sprayers are recommended for precise input management, as they minimize over- and under-application while improving cost efficiency. Electrostatic sprayers are most effective in reducing chemical drift and ensuring better leaf coverage, making them suitable for areas prone to wind-related drift. For small and medium farms, energy-efficient and simplified boom sprayer models are advisable, as they balance effectiveness with affordability and ease of use. Studies report that pesticide use can be reduced by up to 30%, fertilizer inputs by up to 20%, fungicides by 20–30%, and herbicides by an impressive up to 90% when using precision-equipped sprayers. Knapsack sprayers remain cost-effective for localized use but are labour-intensive and less uniform. Servo-controlled boom sprayers deliver precise spraying with real-time nozzle adjustment but demand calibration and higher technology investment. Battery-operated boom sprayers reduce emissions and operator fatigue on medium-scale flat terrains, though battery capacity limits extended use. Overall, integration of automation, GPS, and variable-rate technologies make a strong pathway toward precision, sustainability, and reduced environmental impact across diverse farming systems. Training the farmers in handling and calibration enhances efficiency, safety, and long-term sustainability of sprayer use.

## ACKNOWLEDGMENT

The authors express their sincere gratitude to the Department of Agricultural Engineering, Kalasalingam Academy of Research and Education, Krishnankoil, Tamil Nadu, for their continuous support and encouragement throughout this study.

## CONFLICT OF INTEREST

The authors declare no known competing financial interests or personal relationships that could have appeared to influence the work reported in this review.

## AUTHORS CONTRIBUTION

D. Sivakumar contributed to literature analysis, critical revision, and final editing of the manuscript. Both authors have read and approved the final version of the paper. M. Perarul Selvan conceptualized the review, collected and analyzed relevant literature, and drafted the manuscript.

## REFERENCES

1. Ahmad, L., Mahdi, S. S., Ahmad, L. and Mahdi, S. S. 2018. Variable rate technology and variable rate application. *Satellite Farming: An Information and Technology Based Agriculture*, 67-80. https://doi.org/10.1007/978-3-030-03448-1_5.
2. Ali, M. H., Sarker, M. J., Rahman, M. S., Rabbi, F., Hossen, M. S. and Kabir, M. A. 2022. Design and development of a GPS-guided spray machine for reducing pesticide use on agricultural land in Bangladesh. *In 2022 IEEE 12th symposium on computer applications & industrial electronics (ISCAIE)*, 66-70. doi: 10.1109/ISCAIE54458.2022.9794549.
3. Bayat, A., İtmeç, M. and Özlüoymak, Ö. B. 2023. Development and assessment of a novel servo-controlled spraying system for real time adjustment of the orientation angle of the nozzles of a boom sprayer. *Pest Management Science*, 79(11):4439-4450. https://doi.org/10.1002/ps.7644.
4. Chen, Y., Mao, E., Li, W., Zhang, S., Song, Z., Yang, S. and Chen, J. 2020. Design and experiment of a high-clearance self-propelled sprayer chassis. *International Journal of Agricultural and Biological Engineering*, 13(2):71-80. DOI: 10.25165/j.ijabe.20201302.5262.
5. Corpe, S. J., Tang, L. and Abplanalp, P. 2013. December. GPS-guided modular design mobile robot platform for agricultural applications. *In 2013 Seventh International Conference on Sensing Technology (ICST)*, 806-810. doi: 10.1109/ICSensT.2013.6727763.
6. Cui, L. F., Xue, X. Y., Ding, S. M. and Le, F. X. 2019. Development of a DSP-based electronic control system for the active spray boom suspension. *Computers and Electronics in Agriculture*, 166:105024. https://doi.org/10.1016/j.compag.2019.105024.
7. Dionne, A., Khelifi, M., Todorova, S. and Boivin, G. 2018. Design and testing of a boom sprayer prototype to release Trichogrammaostriniae (Hymenoptera: Trichogrammatidae) in sweet corn for biocontrol of Ostrinianubilalis (Hübner) (Lepidoptera: Crambidae). *Transactions of the ASABE*, 61(6):1867-1879. doi: 10.13031/trans.12922.
8. Dou, H., Zhai, C., Chen, L., Wang, S. and Wang, X. 2021. Field variation characteristics of sprayer boom height using a newly designed boom height detection system. *IEEE Access*, 9:17148-17160. https://doi.org/10.1109/ACCESS.2021.3053035.
9. Elwakeel, A. E., Ahmed, S. F., ZeinEldin, A. M. and Nasrat, L. 2022. Design and evaluation of a self-propelled field sprayer to be operated and controlled remotely. *Al-Azhar Journal of Agricultural Engineering*, 2(1):40-52. https://doi.org/10.21608/azeng.2022.240432

10. Fu, J., Chen, C., Zhao, R. and Ren, L. 2020. Accurate variable control system for boom sprayer based on auxiliary antidrift system. *Journal of Sensors*, 2020(1):8037046. https://doi.org/10. 1155 /2020/8037046.
11. Garcera, C., Moltó, E., Izquierdo, H., Balsari, P., Marucco, P., Grella, M., Gioelli, F. and Chueca, P. 2022. Effect of the airblast settings on the vertical spray profile: implementation on an on-line decision aid for citrus treatments. *Agronomy*, 12(6):1462. https://doi.org/10.3390/agronomy12061462.
12. Hamid, M., ZakiDizaji, H. and Marzban, A. 2015. Operational comparison of two types of tractor sprayers (microner and boom-type) against wheat crop weeds. *Journal of Agricultural Machinery*, 5(2):403-414. https://doi.org/10.22067 / jam.v5i2.28431.
13. Herbst, A., Osteroth, H. J. and Stendel, H. 2018. A novel method for testing automatic systems for controlling the spray boom height. *Biosystems Engineering*, 174:115-125. https://doi.org/10.1016/j.biosystemseng.2018.06.003.
14. Hussain, N., Farooque, A. A., Schumann, A. W., McKenzie-Gopsill, A., Esau, T., Abbas, F., Acharya, B. and Zaman, Q. 2020. Design and development of a smart variable rate sprayer using deep learning. *Remote Sensing*, 12(24):4091. https://doi.org/10.3390/rs12244091.
15. IostFilho, F. H., Heldens, W. B., Kong, Z. and de Lange, E. S. 2020. Drones: innovative technology for use in precision pest management. *Journal of economic entomology*, 113(1):1-25. https://doi.org/10.1093/jee/toz268.
16. Jalu, M. V., Ambaliya, P. S. and Modhvadiya, Y. H. 2024. Comparative performance of the developed mini tractor operated sprayer cum weeder with the various types of existing spraying and weeding methods. *International Journal of Environment, Agriculture and Biotechnology*, 9(1):8-19. https://i.agriculturejournals .org/ index.php/ijeab/article/view/2.
17. Karunathilake, E. M. B. M., Le, A. T., Heo, S., Chung, Y. S. and Mansoor, S. 2023. The path to smart farming: Innovations and opportunities in precision agriculture. *Agriculture*, 13(8):1593. https://doi.org/10.3390/agriculture 13081593.
18. Khan, F. A., Ghafoor, A., Khan, M. A., UmerChattha, M. and Kouhanestani, F. K. 2022. Parameter optimization of newly developed self-propelled variable height crop sprayer using response surface methodology (RSM) approach. *Agriculture*, 12(3):408. https://doi.org/10.3390/agriculture120 30408.
19. Khan, N., Medlock, G., Graves, S. and Anwar, S. 2018. GPS guided autonomous navigation of a small agricultural robot with automated fertilizing system (No. 2018-01-0031). *SAE Technical Paper*. https://doi.org/10.4271/2018-01-0031.
20. Kim, K. D., Lee, H. S., Hwang, S. J., Lee, Y. J., Nam, J. S. and Shin, B. S. 2017. Analysis of spray characteristics of tractor-mounted boom sprayer for precise spraying. *Journal of Biosystems Engineering*, 42(4):258-264. https://doi.org/10.5307/ JBE. 2017.42.4.258.
21. Lal, S., Meena, S. S., Koumary, N. K., Lahre, J. and Adile, S. S. 2024. Empowering vegetable farmers: energy analysis and evaluating the impact of a battery-operated boom sprayer. *Journal of Scientific Research and Reports*,

30(9):825-836. https://doi.org/ 10.9734/ jsrr/2024/v30i92409.

22. Li, W., Yang, F., Mao, E., Shao, M., Sui, H. and Du, Y. 2022. Design and verification of crab steering system for high clearance self-propelled sprayer. *Agriculture*, 12(11):1893. https://doi.org/10.3390/agriculture12111893.
23. Li, C., Wu, J., Pan, X., Dou, H., Zhao, X., Gao, Y., Yang, S. and Zhai, C. 2023a. Design and experiment of a breakpoint continuous spraying system for automatic-guidance boom sprayers. *Agriculture*, 13(12):2203. https://doi.org/10.3390/agriculture13122203.
24. Li, J., Nie, Z., Chen, Y., Ge, D. and Li, M. 2023b. Development of boom posture adjustment and control system for wide spray boom. *Agriculture*, 13(11):2162. https://doi.org/10.3390/ agriculture13112162.
25. Liu, C., Hu, J., Yu, Z., Li, Y. and Zhang, W. 2022. Optimal design of double-link trapezoidal boom suspension for high gap self-propelled sprayer based on ANSYS. *In Journal of Physics: Conference Series* 2383(1):012018. 10.1088/1742-6596/2383/1/012018.
26. Nwosisi, S. and Nandwani, D. 2018. Urban horticulture: overview of recent developments. *Urban horticulture: Sustainability for the future*, 3-29. https://doi.org/10.1007/978-3-319-67017-1_1.
27. Parmar, R., Jain, L., Prakash, A., Sharda, S., Kumar, S., Singh, M. and Singh, H. 2023. Automatic spray control system for four-wheel drive (4WD) self-propelled high clearance boom sprayer. *Agricultural Research Journal*, 9(2). 10.5958/2395-146X.2023.00038.8.
28. Patel, M. K. 2016. Technological improvements in electrostatic spraying and its impact to agriculture during the last decade and future research perspectives A review. *Engineering in Agriculture, Environment and Food*, 9(1):92-100. https://doi.org/10.1016/ j.eaef.2015.09.006.
29. Pawar, R. R., Pawase, P. P., Gatkal, N. R., Khurdal, J. K. and Nalawade, S. M. 2023. Development of axial flow blower for small tractor operated air-assisted sprayer. *Journal of Agriculture Research and Technology*, 48(1):152. https:// doi.org / 10.56228/ JART.2023.48123.
30. Pramod, P. P., Raosaheb, G. N., Kashinath, K. J. and Madhukar, N.S. 2023. Performance evaluation of tractor mounted boom sprayer on chilly crop. *Environment Conservation Journal*, 24(2):61-69. https://doi.org/ 10.36953/ ECJ.13582406.
31. Putri, R. E., Aprilio, J., Geraldo, J. P. and Ade, S. 2022. Semi-automatic boom sprayer development for corn crop protection. In *IOP Conference Series: Earth and Environmental Science* 1097(1):012002. 10.1088/1755-1315/ 1097/1/012002.
32. Rajendra, D. 2020. Design and fabrication of dual power sprayer. *International Research Journal on Advanced Science HUB*, 2(07):15-23. https://doi.org/10.47392/irjash.2020.58.
33. Saleem, S. R., Zaman, Q. U., Schumann, A. W. and Naqvi, S. M. Z. A. 2023. Variable rate technologies: Development, adaptation, and opportunities in agriculture. In *Precision Agriculture*, 103-122. https://doi.org/10.1016/B978-0-443-18953-1.00010-6.

34. Soussi, A., Zero, E., Sacile, R., Trinchero, D. and Fossa, M. 2024. Smart sensors and smart data for precision agriculture: A Review. *Sensors*, 24(8):2647. https://doi.org/10.3390/s24082647.
35. Stejskal, V., Vendl, T., Aulicky, R. and Athanassiou, C. 2021. Synthetic and natural insecticides: Gas, liquid, gel and solid formulations for stored-product and food-industry pest control. *Insects*, 12(7):590. https://doi.org/ 10.3390/insects12070590.
36. Su, W., Zhang, Y., Li, H., Lei, H., Xu, H., Sun, L. and Wu, R. 2021. Control efficiency on the broad-leaved weeds and safety of self-propelled sprayer with different application parameters in wheat fields. *Journal of Henan Agricultural Sciences*, 50(6)*:*99. https://doi.org/10.15933/j.cnki.1004-3268.2021.06.012.
37. Tripathi, K. M., Kumar, D., Mishra, S. K., Singh, S. and Shukla, S. 2023. An Overview of organic farming in India and its role in sustainable agriculture. *Emerging Issues in Agricultural Sciences Vol. 5 An Overview of Organic Farming in India and its Role in Sustainable Agriculture*, 1-13. 10.9734/bpi/eias/v5/10607F.
38. Wang, G., Lan, Y., Yuan, H., Qi, H., Chen, P., Ouyang, F. and Han, Y. 2019. Comparison of spray deposition, control efficacy on wheat aphids and working efficiency in the wheat field of the unmanned aerial vehicle with boom sprayer and two conventional knapsack sprayers. *Applied sciences*, 9(2):218. https://doi.org/10.3390/app9020218.
39. Yadav, M. R., Parihar, C. M., Kumar, R., Yadav, R. K., Jat, S. L., Singh, A. K., Ram, H., Meena, R. K., Singh, M., Meena, V. K. and Yadav, N. 2017. Conservation agriculture and soil quality–an overview. *International Journal of Current Microbiology and Applied Sciences*, 6:1-28. http://dx.doi.org/10.20546/ijcmas.2017.602.0xx.
40. Zaffar, O. and Khar, S. 2023. Development of a wheel operated boom sprayer for hilly regions of Jammu and Kashmir. *Indian Journal*, 15(1):69-74. http://dx.doi.org/10.5958/2394-4471.2023.00013.8.

International Agricultural Engineering Journal ISSN 0858-2114

*September 2025, 34 (1-4) : 77-88*

# Numerical Study of Tire Lug Angle Configurations to Optimize Traction on Agricultural Terrains

**Halidi Ally, Xiulun Wang*, Tingting Wu, Tao Liu, Ge Jun**

## ABSTRACT

Optimizing traction on agricultural terrains through refined lug angles enhances efficiency, productivity, and cost-effectiveness in farming operations. This study numerically investigates the performance of various tire lug designs across different terrains using advanced simulation techniques. Finite Element Analysis (FEA) with ANSYS is utilized to model tire-soil interactions, while the Improved Tire Model by Wong and Preston-Thomas (ITM-WP) is employed to predict traction performance with a focus on lug angles. The research evaluates five lug designs with angles of 35°, 45°, 55°, 65°, and 75°, incorporating empirical data obtained from laboratory experiments on four types of clayey soil. The findings demonstrate how lug designs influence motion resistance, thrust, and traction, providing practical guidelines for optimizing tire performance. Among the configurations, the 45° lug angle consistently delivers the optimal balance between reduced motion resistance, enhanced thrust, and improved traction, making it the ideal choice for maximizing traction efficiency in clay soils. These insights contribute to the development of more efficient agricultural machinery, reducing soil degradation, improving operational efficiency, and advancing agricultural productivity.

***Keywords:*** *Agricultural Vehicles; ANSYS simulation; Clay soils; Lug angles; Tire-Soil Interaction; Traction Optimization.*

## 1. INTRODUCTION

Agricultural vehicles are essential in modern farming, performing a wide range of tasks from plowing and seeding to harvesting. Their efficiency largely depends on the traction performance, which is the grip between the tires and the ground affecting fuel consumption, soil compaction, and operational efficiency (Bekker, 1969; Wong, 2010). The fundamental concepts of terramechanics were established in early seminal works by Bekker (1969) and remain a cornerstone for understanding tire–terrain interaction, while more recent studies (Wong, 2001; Wong, 2010) have expanded and refined these models for modern agricultural applications. Tire lug design is a pivotal factor influencing traction, with parameters such as lug depth, angle, spacing, and shape significantly affecting the tire-soil interaction (Wong, 2010). Optimizing these parameters can enhance traction performance, reduce operational costs, and boost agricultural productivity.

Although vehicle-terrain interactions have been widely studied using empirical methods and advanced numerical simulations, there remains a need to integrate these approaches to optimize traction under varying soil conditions.

Graduate School of Bioresources, Mie University, Japan.

**Corresponding author - email: wang@bio.mie-u.ac.jp*

Received: 24 April 2025; Revised: 26 July 2025; Accepted: 13 August 2025.

This study addresses this gap by employing finite element analysis (FEA) via ANSYS and the semi-empirical Improved Tire Model by Wong and Preston-Thomas (ITM-WP). These methods are complemented by empirical data from laboratory experiments on clay soils to run the simulation models.

Previous studies provide valuable insights into traction optimization for agricultural vehicles. Alcock and Wittig (1992) developed an empirical method emphasizing soil strength and wheel torque, establishing the role of soil properties in traction performance. Maclaurin (1987) highlighted terrain-specific traction optimization through numerical simulations, stressing environmental factors in tire design. Kim *et al.* (2022) demonstrated the significance of tire contact area and lug design for traction in paddy fields, while Brennensthul *et al.* (2024) explored the interplay between lug design and terrain characteristics for tractor tires in forest conditions.

Taheri (2015) introduced the Hybrid Soft Soil Tire Model (HSSTM), showcasing its precision in deformable terrain simulations, and Kim *et al.* (2019) identified soil moisture content as a key factor influencing dynamic traction and efficiency during plow tillage. Asaf *et al.* (2006) used discrete element methods (DEM) to analyze soil-wheel interactions, offering detailed insights into traction dynamics. Tiwari *et al*. (2010) reviewed traction prediction models, advocating for adaptability to specific soil conditions, while Sedara (2019) and Wismer (1982) contributed foundational knowledge on soil dynamics under vehicular loads. Moreland *et al*. (2011) advanced soil motion analysis techniques, and Saengprachatanarug *et al*. (2013) developed models for soil displacement and strain distribution. Mardani and Golanbari (2024) focused on indoor analysis of soil-traction device interactions, and studies by Grujicic *et al*. (2010) and Zhou *et al*. (2020) demonstrated the efficacy of FEA in modeling soil-tire dynamics, underscoring its utility in traction optimization.

Building on these foundations, this study examines the impact of tire lug configurations on traction, motion resistance, and thrust across diverse terrains. By leveraging advanced numerical tools and integrating empirical data, it seeks to provide practical guidelines for designing efficient agricultural tires. The findings aim to enhance farming productivity by improving tire performance and reducing operational inefficiencies.

## 2. MATERIALS AND METHODS

### 2.1. Theoretical Framework and Principle

Tire performance on various soil types has been evaluated using approaches ranging from empirical methods to theoretical models (Wong, 2010). This study adopts a hybrid approach, combining the Finite Element Method (FEM) via ANSYS with the semi-empirical Improved Tire Model by Wong and Preston-Thomas (ITM-WP). Prior studies (Liu and Wong, 1996; Seta *et al*., 2003; Wong, 2010) demonstrate strong qualitative alignment between FEM simulations and experimental data, underscoring the reliability of FEM for modeling tire-soil interactions. This research employs 3D steel tire and soil models (Fig. 1 and 2) to analyze normal and shear stresses at the tire-soil interface using ANSYS. The ITM-WP model is then applied to predict traction performance based on these stress values.

### 2.2. Bekker Tire-Soil Interaction Model

Bekker's tire-soil interaction model (Bekker, 1969) is a widely recognized semi-empirical method for predicting tire performance on unprepared terrain (Wong, 2010). It assumes that normal pressure at the tire's circumference is equivalent to the pressure beneath a sinkage plate at the same depth, with sinkage $z_r$ calculated using Eq. (1) (Fig. 1).

$$z_r = \left(\frac{3W}{b_{ti}(3-n)(k_c/b + k_\phi)\sqrt{D}}\right)^{2/(2n+1)} \quad \ldots (1)$$

Where, $b$ is the smaller dimensions of the tire contact patch, mm; $b_{ti}$ is the tire width, mm; $D$ is the tire diameter, mm; $W$ is the tire load, kN and n, $k_c$ and $k_\phi$ are the pressure sinkage parameters.

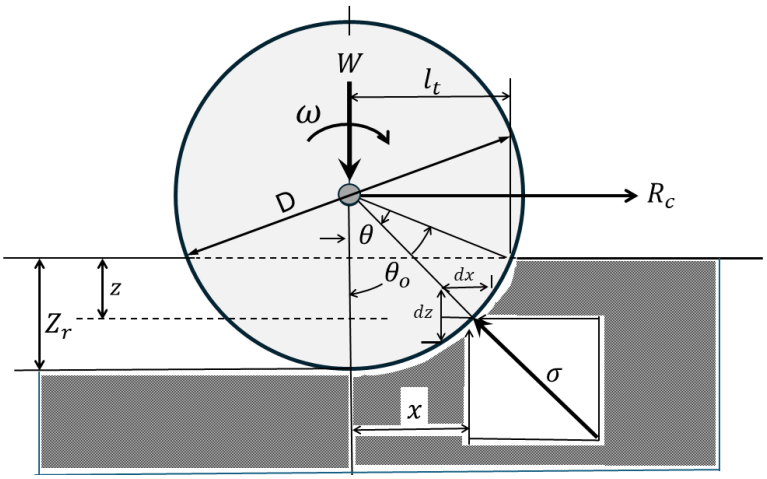


**Fig. 1. The concept of the original model of tire-terrain interaction.**

Bekker's model assumes a rigid tire operation on soft terrain, where motion resistance ($R_c$) results from creating a rut of width $b_{ti}$ and depth, $z_r$, Eq. (7). The radial pressure σ at the tire-terrain interface is equated to the normal pressure $p$ beneath a sinkage plate at the same depth, derived from the Bekker pressure-sinkage relationship.

$$R_c = b_{ti}\int_0^{\theta_0} \sigma\, r\, sin\theta\, d\theta \quad \ldots (2)$$

$$W = b_{ti}\int_0^{\theta_0} \sigma\, r\, cos\theta\, d\theta \quad \ldots (3)$$

$$\sigma\, r\, sin\theta\, d\theta = pdz \quad \ldots (4)$$

$$r\, cos\theta\, d\theta = pdx \quad \ldots (5)$$

$$p = \left(\frac{k_c}{b} + k_\phi\right) z^n = k_{eq} z^n \quad \ldots (6)$$

$$R_c = b_{ti}\int_0^{z_r} \left(\frac{k_c}{b} + k_\phi\right) z^n\, dz = b_{ti}\left(\frac{k_c}{b} + k_\phi\right)\left(\frac{z_r^{n+1}}{n+1}\right) \quad \ldots (7)$$

While foundational, Bekker's model has limitations, including its focus on steady-state conditions and exclusion of dynamic terrain behavior (Wong, 2010; Karpman *et al*., 2023). These constraints necessitate advanced models like ITM-WP for more precise predictions.

### 2.2.1. Improved tire model by Wong and Preston-Thomas

To address Bekker's limitations, Wong and Preston-Thomas (1986) introduced the ITM-WP (Fig. 2), incorporating horizontal components of normal and shear stresses for a comprehensive analysis of tire-soil interactions. This model enhances predictions by accounting for stress and strain fields in the soil during tire movement (Wong, 2010).

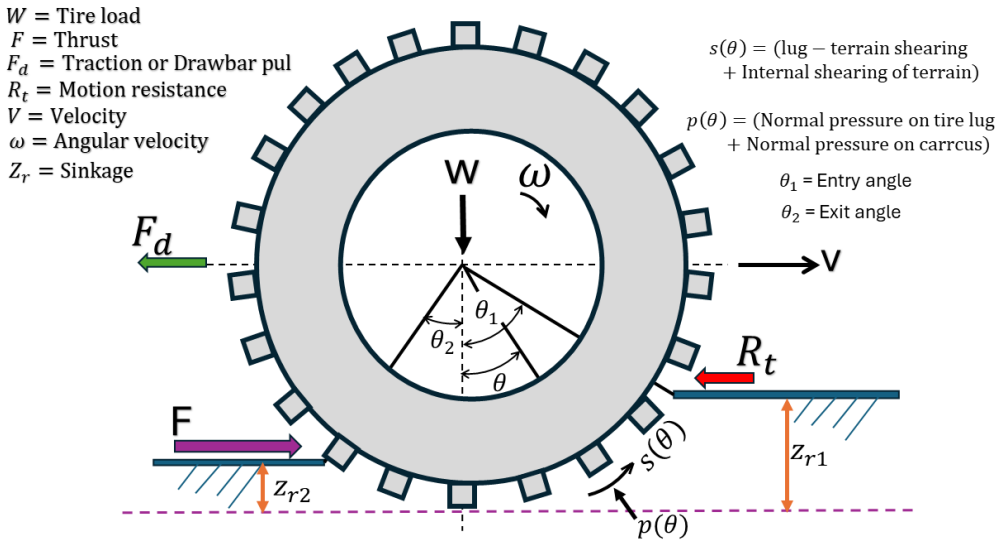


**Fig. 2. Conceptual diagram of the improved tire model.**

Using numerical modeling via FEM (ANSYS), ITM-WP evaluates key performance metrics, including, Motion Resistance - Resistance encountered as the tire moves through soil; Thrust/Tractive Effort - Horizontal force propelling the vehicle forward; and Traction/Drawbar Pull - Pulling force critical for tasks like plowing and towing.

The ITM-WP offers a more realistic representation of tire-soil mechanics by addressing the contact patch geometry and associated stresses, enabling accurate predictions under varying conditions. This study employs ITM-WP alongside FEM simulations to provide reliable insights into tire performance, optimizing parameters like motion resistance and thrust efficiency.

### 2.3. Finite Element Analysis (FEA)

FEA is a computational technique that predicts the behavior of objects by employing the Finite Element Method (FEM), a mathematical approach that simplifies complex systems into smaller, manageable elements. These elements are analyzed using differential equations, which are assembled into a global system representing the entire problem domain (Reddy, 1993; Parsons, 2023). FEA interprets the FEM-generated results, enabling engineers to make informed design decisions by simulating the behavior of complex systems (Zienkiewicz and Taylor, 2000; Zienkiewicz and Taylor, 2005; Bathe, 1996; Akin, 2010).

This method is especially valuable for analyzing tire-soil interactions, as it discretizes the continuous domain into finite elements. By applying FEM, FEA forms the backbone of simulation software, allowing for efficient validation of designs through virtual modeling (Cicconi *et al.,* 2018; Seth *et al.,* 2011; Galea Mifsud *et al*., 2024). In this study, ANSYS software was utilized to examine interactions between six tires with varied lug spacing and four clay soil types (Table 1). This numerical approach eliminates the expense and risks associated with physical prototyping, making it indispensable in high-risk industries like aerospace and biomechanics (Alshoaibi and Fageehi, 2024; Tickoo, 2021).

### 2.4. ANSYS Simulation Software

ANSYS is a leading engineering simulation tool that employs FEM to predict and analyze the behavior of systems under diverse conditions.

**Table 1. Properties of experimental soil**

| Sample No. | Moisture Content, % (w.b) | Cohesion, kPa | Internal friction angle, ° | External friction angle, δ |
|---|---|---|---|---|
| 1 | 08.6 | 0.38 | 42.6 | 20.9 |
| 2 | 27.7 | 1.98 | 28.4 | 15.4 |
| 3 | 34.2 | 1.78 | 28.4 | 17.8 |
| 4 | 54.4 | 0.62 | 11.1 | 9.5 |

It addresses engineering challenges across industries such as aerospace, automotive, and energy (Brazil *et al.* 2023; Oden and Reddy, 2012; Madenci and Guven, 2015; Tickoo, 2021). For this study, the ANSYS Student version was used to perform numerical predictions of stresses at the tire-terrain interface. Despite its limitations in model size and computational capacity, it provided sufficient functionality for detailed analysis. ANSYS's capabilities enabled the examination of dynamic tire-soil interactions, providing insights into how this affect traction performance.

### 2.4.1. Model setup and initialization

Using ANSYS Design Modeler, detailed 3D geometries of tires and soil were created. The tire model, representing a lugged tractor tire, was designed based on the specifications summarized in Table 2. It featured a width of 760 mm, diameter of 2228 mm, lug length of 510 mm, lug depth of 64 mm, and spacing of 130 mm. Five models with lug angles of 35°, 45°, 55°, 65°, and 75° were analyzed. The soil domain was modeled as a rectangular block measuring 2000 × 10000 × 2500 mm to accommodate realistic tire-soil interactions. Mechanical properties such as cohesion, friction angle, and compressibility were assigned based on experimental data to accurately simulate the behavior of four different clay soils under load.

### 2.4.2. Material properties representation

Accurate material representation ensures simulation reliability. The tire was modeled using structural steel, with an elastic modulus of 200 GPa and Poisson's ratio of 0.3, to simulate rigidity and isolate the lug angle's effect. For the soil, the Mohr-Coulomb material model was employed to describe failure and shear strength, Eq (8).

$$\tau = c + \sigma \tan(\phi) \quad \ldots (8)$$

Where, τ is shear stress, kPa; c is cohesion, kPa; σ is normal stress on the shearing surface, kPa and ϕ is internal friction angle, degree. This model's simplicity and established reliability made it a practical choice for simulating soil behavior (Wong, 2010; Cook, 2007; Madenci and Guven, 2015; Tickoo, 2021).

**Table 2. Key geometric parameters of the tire**

| Parameter | Value |
|---|---|
| Width, mm | 760 |
| Diameter, mm | 2228 |
| Lug angle, ° | 35°, 45°, 55°, 65°, and 75° |
| Lug height, mm | 64 |
| Lug spacing, mm | 130 |

### 2.4.3. Meshing

Meshing is critical in FEA to ensure accurate and reliable results. The tire model was discretized into 52,000 elements, while the soil domain consisted of about 42,000 elements, totaling around 94,000 elements for the full model. A finer mesh was applied specifically at the tire-soil interface to capture stress distributions and contact interactions with greater precision. This meshing strategy effectively balanced computational detail with efficiency, especially considering the limitations of the ANSYS Student version used for simulations.

#### 2.4.4. Simulation execution and boundary conditions

Simulations were performed using the ANSYS Explicit Dynamic solver to capture highly nonlinear, transient events involving large deformations typical of tire-soil interactions. Time steps were carefully configured to accurately reflect the dynamic behavior and to prevent numerical instabilities. Boundary conditions included fixing the edges of the soil domain and applying forces and displacements to the tire model to replicate real-world operational conditions. All simulations were conducted under a normal tire load of 35 kN with a forward velocity of 2.78 m/s, focusing on stress distribution and deformation within the tire - soil interface.

#### 2.4.5. Limitations and validation

The constraints of the ANSYS Student version on model size and material representation posed challenges, as structural steel does not fully emulate real tire behavior. While simulation results provided valuable insights into performance trends, they should be considered indicative rather than definitive. Future studies should incorporate rubber material models and experimental validation to improve predictive accuracy and align findings with real-world conditions. Despite these limitations, the model demonstrated numerical stability and provided robust results, offering a foundation for optimizing lug designs tailored to specific soil conditions.

### 2.5. Evaluation of Tire Performance

The study utilized the Improved Tire Model (ITM) by Wong and Preston-Thomas to predict key performance metrics using stress values derived from ANSYS simulations. ITM provides a more realistic representation of tire-soil interaction compared to the classical Bekker Tire Model, enabling precise predictions of critical parameters such as thrust, motion resistance, and traction. These metrics are vital for optimizing agricultural machinery design, enhancing operational efficiency, and reducing soil degradation. The model achieves high predictive accuracy by analyzing the distribution of normal pressure and shear stress at the tire-terrain interface, as outlined in Eq. (9) (Wong, 2010).

$$W = \frac{b_{ti}D}{2}\left[\int_0^{\theta_1}(p(\theta)cos\theta + s(\theta)sin\theta)d\theta + \int_0^{\theta_2}(p(\theta)cos\theta - s(\theta)sin\theta)d\theta\right] \quad \ldots (9)$$

Where, $b_{tr}$ is tire width, mm; $D$ is tire diameter, mm; $W$ is the normal tire load, kN; $\theta_1$ and $\theta_2$ are the entry and exit contact angles, respectively. Motion resistance and thrust are due to the horizontal component of normal pressure and shear stress, respectively Wong (2010).

#### 2.5.1. Prediction of tire motion resistance

The total motion resistance ($R_o$) encountered by a tire comprises factors like obstacle resistance ($R_{ob}$), internal resistance of the running gear ($R_{in}$), and the tire-terrain interaction resistance ($R_t$) (Bekker, 1969; Wong, 2010). Among these, the tire-terrain interaction significantly impacts performance.

Using ITM, the study focused on $R_t$, computed through Eq (10). This approach integrates the horizontal component of the normal pressure across the tire's contact patch, which is critical for understanding the resistance force generated as the tire moves through the terrain.

$$R_t = \frac{b_{ti}D}{2}\left[\int_0^{\theta_1} p(\theta)sin\theta d\theta - \int_0^{\theta_2} p(\theta)sin\theta d\theta\right] \quad \ldots (10)$$

For lugged tire, $p(\theta)$ represents normal pressure on lugs and carcasses. If tire sinkage ($z_r$) is less

than lug height ($h_l$) then $p(\theta)$ corresponds to normal pressure on lug tips only.

### 2.5.2. Prediction of soil thrust (tractive effort or propelling force)

Thrust is limited by vehicle's mechanical capabilities and tire-terrain shearing interaction (Wong, 2010). ITM calculates thrust (FFF) through the horizontal component of shear stress across the contact area, as shown in Eq. (11).

$$F = \frac{b_{ti}D}{2}\left[\int_0^{\theta_1} s(\theta)cos\theta d\theta + \int_0^{\theta_2} s(\theta)cos\theta d\theta\right] \quad \ldots (11)$$

Here, $s(\theta)$ encompasses lug-terrain shearing and internal terrain shearing. For $z_r < h_l$, $s(\theta)$ corresponds to lug-terrain shearing only. ANSYS simulations provided shear stress data, enabling accurate predictions of thrust under varying terrain conditions.

### 2.5.3. Determination of traction (drawbar pull)

Traction ($F_d$) represents the net force required for agricultural or construction tasks and is expressed as the difference between thrust ($F$) and motion resistance ($R_t$) (Wong, 2010).

$$F_d = F - R_t \quad \ldots (12)$$

This equation aids in evaluating a tractor's performance, offering insights into its suitability for specific tasks and terrains.

### 2.6. Development of 3D Tire and Soil Models

The 3D geometric details of the tire and soil models used in the simulations were carefully developed using ANSYS DesignModeler, a module within the ANSYS software suite, to accurately represent tire-soil interactions. Tire models were designed with varied lug angles to examine their effects on performance metrics. Key dimensions including lug length, depth, and spacing were consistently maintained across models, while lug angles were systematically varied to evaluate their impact on traction and stress distribution. These detailed models provided a robust foundation for simulating complex tire-terrain mechanics with high fidelity.

## 3. RESULTS AND DISCUSSION

### 3.1. Stress Analysis at the Tire-Terrain Interface Using ANSYS

The analysis of various lug designs across different clay soil types provided valuable insights into optimizing traction performance for agricultural vehicles. Finite Element Analysis (FEA) using ANSYS enabled the evaluation of stress distributions at the tire-terrain interface. The Mohr-Coulomb soil material model was applied to simulate clay soil behavior under load, focusing on assessing the influence of different lug configurations and soil conditions on tire-soil interaction. The results demonstrate the significant role of lug design and soil type in influencing the mechanical response at the interface, affecting traction efficiency and soil deformation. These findings emphasize the importance of selecting appropriate lug parameters tailored to specific soil conditions to optimize performance and minimize adverse effects such as excessive soil compaction.

### 3.2. Performance Analysis of Lug Angle Configurations

This section evaluates the performance of various lug angles on clay soils, focusing on three critical metrics: motion resistance, thrust, and traction. The findings provide insights into optimizing tire design for agricultural and off-road applications.

### 3.2.1. Tire motion resistance

The relationships between lug angle (35° to 75°) and motion resistance were analyzed across four clay soil samples (Figs. 3 - 6). Results revealed that, Sample No. 1 exhibited the lowest resistance across all lug angles, likely due to lower soil

cohesion or density, while Sample No. 3 displayed the highest peak at 45°, suggesting increased soil penetration and grip. Sample No. 2 showed relatively consistent resistance across lug angles, indicating lower sensitivity to lug design variations. The lowest motion resistance values were observed at 35°, 55° and 65° lug angles across all samples. This indicates that these lugs angles minimize drag forces and soil friction, which could potentially reduce tire grip and overall tire performance.

### 3.2.2. Thrust

Thrust force peaked at 45° across all soil samples (Fig. 3 - 6), highlighting its effectiveness in optimizing tractive effort. Sample No. 3 recorded the highest thrust at this angle, followed by Sample No. 4, indicating their responsiveness to lug design. In contrast, Samples No. 1 and No. 2 showed minimal variation, suggesting uniform soil properties or reduced sensitivity to lug angles. Thrust values declined beyond 45° and leveled off between 55° and 75°, as larger lug angles reduced soil engagement, leading to weaker grip. These findings reinforce the 45° lug angle as the optimal configuration for maximizing thrust across clay soils.

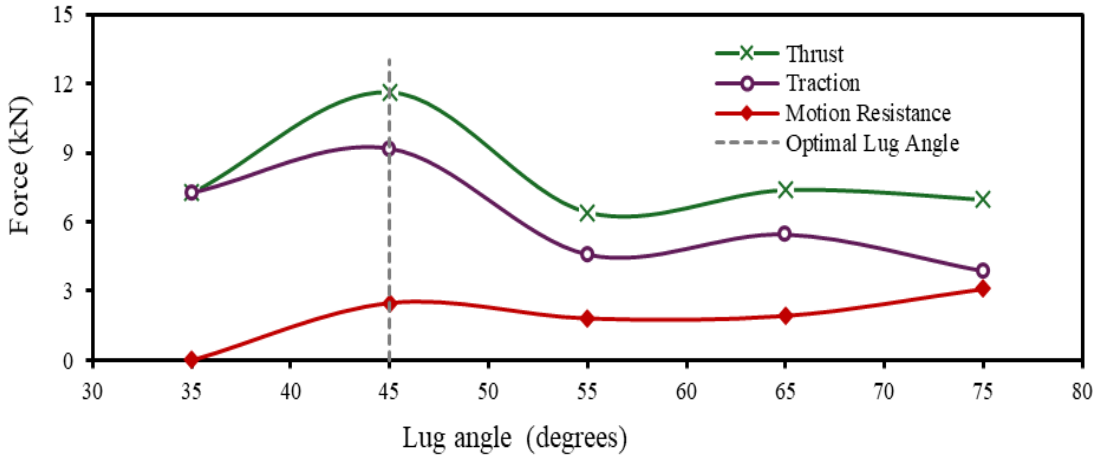


**Fig. 3. Thrust, traction and motion resistance for various lug angles on soil sample No. 1**

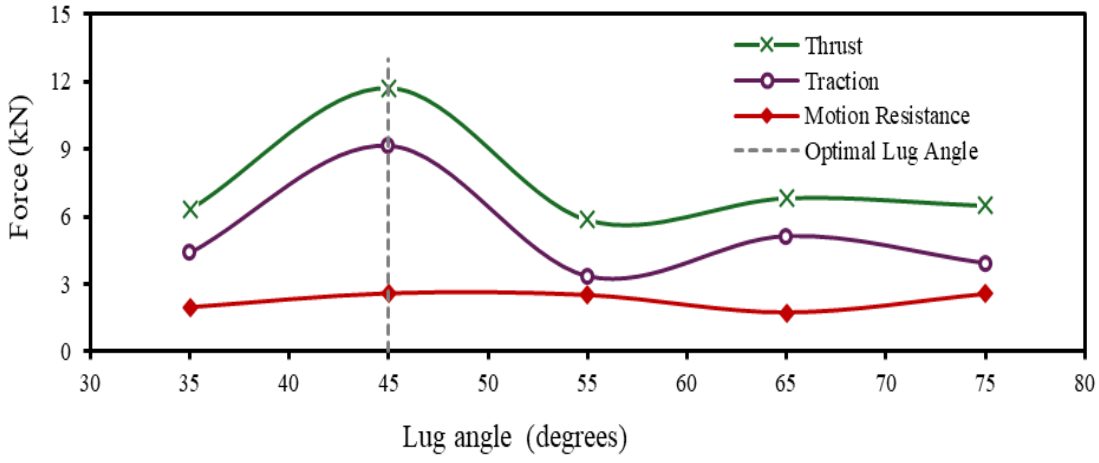


**Fig. 4. Thrust, traction and motion resistance for various lug angles on soil sample No. 2**

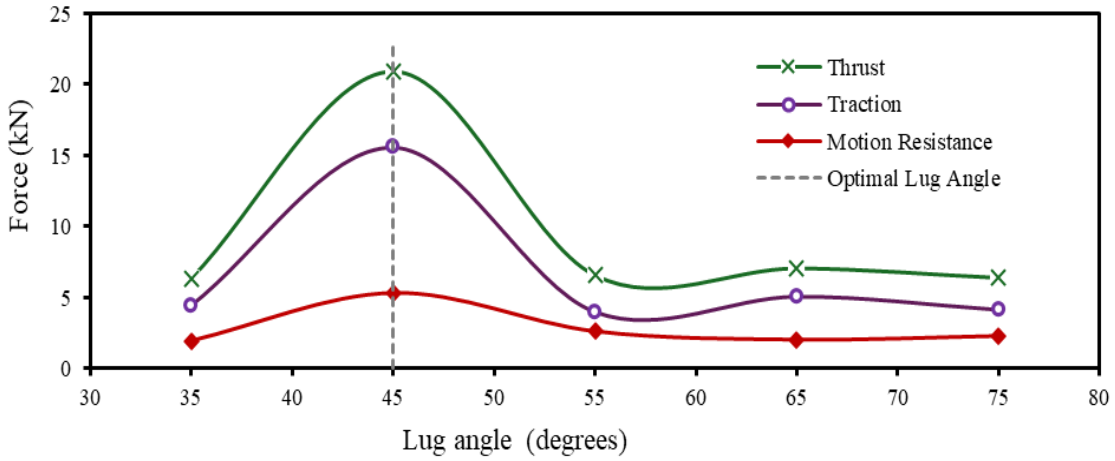


**Fig. 5. Thrust, traction and motion resistance for various lug angles on soil sample No. 3**

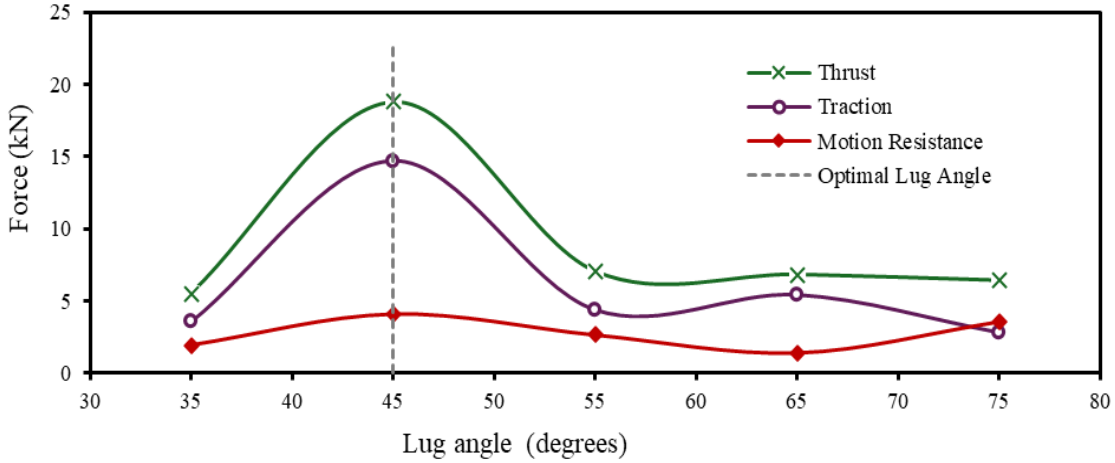


**Fig. 6. Thrust, traction and motion resistance for various lug angles on soil sample No. 4**

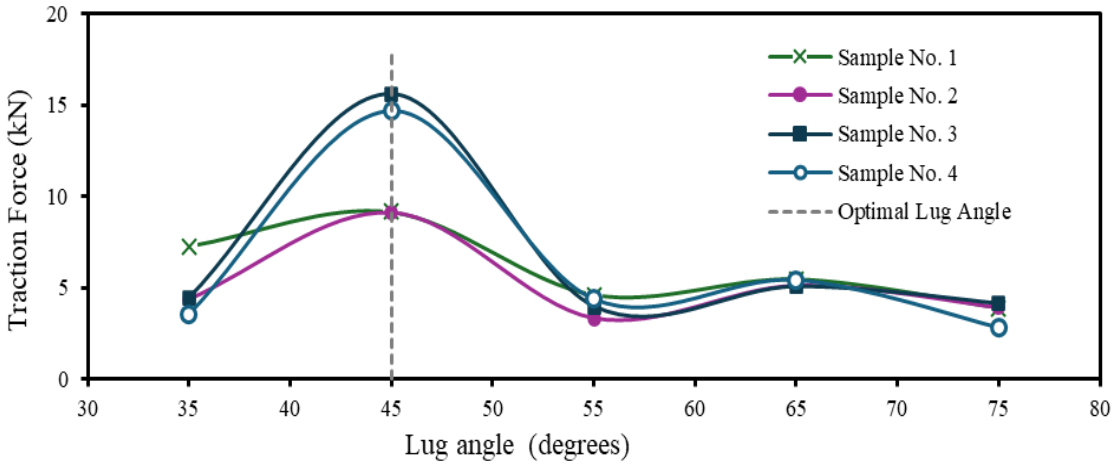


**Fig. 7. Comparing traction performance for all lug angles on varied clay soil samples**

### 3.2.3. Traction

Traction trends mirrored those of thrust, with all soil samples showing a peak at the 45° lug angle (Fig 7). Sample No. 3 exhibited the highest traction, likely due to effective lug-soil interaction. Samples No. 1 and No. 2 demonstrated moderate traction increases, possibly due to higher soil stiffness reducing lug penetration. Traction force declined significantly beyond 45°, with the lowest values recorded between 55° and 75°, reflecting reduced soil engagement and diminished drawbar pull. These findings confirm the 45° lug angle as the optimal design for maximizing traction while balancing soil engagement and efficiency.

### 3.3. Validation of Findings

The results of this study aligns closely with Ekinci (2017), who found that a 45° lug angle provided the highest tractive efficiency in rigid wheels on hard soil. Ekinci's experimental findings corroborate the simulation-based results of this study, emphasizing the critical role of the 45° lug angle in optimizing tire performance. Despite differing methodologies, including physical tests in Ekinci's research and finite element analysis (FEA) in this study, both approaches identified the 45° lug angle as optimal for enhancing traction and efficiency. This agreement underscores the robustness and validity of the findings, reinforcing the importance of tailored lug configurations for diverse agricultural and off-road terrains.

## 4. CONCLUSIONS

This research used FEA in ANSYS and the Improved Tire Model by Wong and Preston-Thomas to numerically investigate the effect of lug angles on tire traction across clay soils. The study evaluated key performance metrics which were motion resistance, thrust, and traction to assess the impact of various lug configurations. The simulations employed a 3D steel tire model to replicate a rigid operating mode, paired with the Mohr-Coulomb material model to represent soil behavior. The findings consistently identified the 45° lug angle as the optimal configuration, offering the best balance between soil engagement and tractive efficiency while maintaining moderate soil stress, making it suitable for a wide range of soil types. Beyond 45°, larger lug angles (55°-75°) reduced soil penetration, which lowered motion resistance but compromised traction. These results underscore the importance of tailoring lug configurations to specific soil conditions, providing valuable guidance for optimizing tire designs in agricultural and off-road applications. Future research should explore the performance of these lug configurations under other soil conditions, such as loamy and sandy soils, to broaden the applicability of the findings and provide a comprehensive understanding of lug performance across diverse terrains. Additionally, experimental validation using full-scale tires under controlled field conditions is recommended to confirm simulation results and refine design guidelines further.

## ACKNOWLEDGEMENTS

The authors thank JICA for scholarship support, MIE University for research resources, ANSYS developers, and Prof. Wong and Preston-Thomas for their valuable foundational tire model.

## AUTHOR CONTRIBUTIONS

Conceptualization, H.A.; methodology, H.A., X.W. and T.L.; investigation, X.W. and T.W.; data curation, H.A., X.W. and J.G.; writing original draft preparation, H.A., X.W., X.W., X.W., T.W., T.L. and J.G.; writing review and editing H.A., X.W., T.W., T.L. and J.G.; supervision, X.W.

## CONFLICT OF INTERESTS

The authors declare that they have no known competing financial interests or personal relationships that could have appeared to influence the work reported in this paper.

## REFERENCES

1. Akin, J.E. 2010. *Finite Element Analysis Concepts: via SolidWorks*. World Scientific, Singapore.

2. Alcock, R. and Wittig, V. 1992. An empirical method of predicting traction. *Journal of Terramechanics,* 29(4-5): 381–394.
3. Alshoaibi, A.M. and Fageehi, Y.A. 2024. A comparative analysis of 3D software for modeling fatigue crack growth: a review. *Applied Sciences*, 14(5): 1848.
4. Asaf, Z., Shmulevich, I. and Rubinstein, D. 2006. Predicting soil-rigid wheel performance using distinct element methods. *Transactions of the ASABE*, 49(3): 607–616.
5. Bathe, K.J. 1996. *Finite Element Procedures*. Prentice Hall, New Jersey.
6. Bekker, M.G. 1969. *Introduction to Terrain Vehicle Systems*. University of Michigan Press, Ann Arbor.
7. Brazil, V., Purdy, E. and Bajaj, K. 2023. *Simulation as an Improvement Technique*. Cambridge University Press, Cambridge.
8. Brennensthul, M., Czarnecki, J. and Białczyk, W. 2024. Assessment of tractor tires used in forest conditions in terms of traction performance and impact on ground. *Croatian Journal of Forest Engineering*, 45(1): 97–114.
9. Cicconi, P., Landi, D. and Germani, M. 2018. An ecodesign approach for the lightweight engineering of cast iron parts. *International Journal of Advanced Manufacturing Technology,* 99: 2365–2388.
10. Cook, R.D. 2007. *Concepts and Applications of Finite Element Analysis.* John Wiley & Sons, Hoboken.
11. Ekincı, Ş. 2017. Effect of lug angles of rigid wheel on the tractive performance on hard soil terrain. *Journal of Agricultural Faculty of Gaziosmanpaşa University (JAFAG)*, 34(3): 217–227.
12. Galea Mifsud, R., Muscat, G.A., Grima-Cornish, J.N., Dudek, K.K., Cardona, M.A., Attard, D., Farrugia, P.S., Gatt, R., Evans, K.E. and Grima, J.N. 2024. Auxetics and FEA: modern materials driven by modern simulation methods. *Materials,* 17(7): 1506.
13. Grujicic, M., Marvi, H., Arakere, G. and Haque, I.2010. A finite element analysis of pneumatic-tire/sand interactions during off-road vehicle travel. *Multidiscipline Modeling in Materials and Structures*, 6(2): 284–308.
14. Karpman, E., Kövecses, J. and Teichmann, M. 2023. Terramechanics models augmented by machine learning representations. *Journal of Terramechanics,* 107: 75–89.
15. Kim, W.S., Kim, Y.J., Park, S.U., Nam, K.C. and Choi, C.H. 2019. Analysis of traction performance for an agricultural tractor according to soil moisture content during plow tillage. *2019 ASABE Annual International Meeting,* Paper No. 1900994.
16. Kim, W.S., Kim, Y.J., Lee, N.J. and Kim, Y.S. 2022. Influence of tire contact area on the traction performance of a 67-kW agricultural tractor in a paddy field. *Journal of the ASABE*, 65(6): 1421–1432.
17. Liu, C.H. and Wong, J.Y. 1996. Numerical simulations of tire–soil interaction based on critical state soil mechanics. *Journal of Terramechanics*, 33(5): 209–221.
18. Maclaurin, E.B. 1987. Soil-vehicle interaction. *Journal of Terramechanics*, 24(4): 281–294.
19. Madenci, E. and Guven, I. 2015. *The Finite Element Method and Applications in Engineering Using ANSYS®*. Springer, New York.
20. Moreland, S. 2011. *Soil motion analysis system for examining wheel-soil shearing*. In: International Conference of the International Society for Terrain-

Vehicle Systems. (*Eds*.) Scott Moreland, Krzysztof Skonieczny, David Wettergreen Colin Creager and Vivake Asnani. pp 361–377.

21. Oden, J.T. and Reddy, J.N. 2012. *An Introduction to the Mathematical Theory of Finite Elements*. Dover Publications, pp 468.
22. Parsons, C.L. 2023. *Generative design optimization of connecting rods*. Unpublished doctoral dissertation, Purdue University Graduate School, West Lafayette, USA.
23. Reddy, J.N. 1993. *An Introduction to the Finite Element Method,* 2nd ed. McGraw-Hill, New York.
24. Saengprachatanarug, K., Ueno, M., Taira, E. and Okayasu, T. 2013. Modeling of soil displacement and soil strain distribution under a traveling wheel. *Journal of Terramechanics*, 50(1): 5–16.
25. Sedara, A.M. 2019. A review of soil dynamics in traction studies. *Journal of Engineering Research and Reports,* 4(4): 1–13.
26. Seta, E., Kamegawa, T. and Nakajima, Y. 2003. Prediction of snow/tire interaction using explicit FEM and FVM. *Tire Science and Technology*, 31(3): 173–188.
27. Seth, A., Vance, J.M. and Oliver, J.H. 2011. Virtual reality for assembly methods prototyping: a review. *Virtual Reality*, 15: 5–20.
28. Taheri, S. 2015. *A hybrid soft soil tire model (HSSTM) for vehicle mobility and deterministic performance analysis in terramechanics applications*. Unpublished Ph.D. thesis. Virginia Tech, Blacksburg, USA.
29. Tickoo, S. 2021. *ANSYS Workbench 2021 R1: A Tutorial Approach*. SDC Publications, Mission, KS.
30. Tiwari, V.K., Pandey, K.P. and Pranav, P.K. 2010. A review on traction prediction equations. *Journal of Terramechanics,* 47(3): 191–199.
31. Wismer, R.D. 1982. Soil dynamics: a review of theory and application. *SAE Transactions*, 91: 2266–2278.
32. Wong, J.Y. 2001. *Theory of Ground Vehicles*, 3rd ed. John Wiley & Sons, New York.
33. Wong, J.Y. 2010. *Terramechanics and Off-Road Vehicles Engineering*, 2nd ed. Elsevier Science, Amsterdam, the Netherlands.
34. Wong, J.Y. and Preston-Thomas, J. 1986. Parametric analysis of tracked vehicle performance using an advanced computer simulation model. Proceedings of the Institution of Mechanical Engineers, Part D: *Journal of Automobile Engineering*, 200(D2): 101–114.
35. Zhou, L., Gao, J., Li, Q. and Hu, C. 2020. Simulation study on tractive performance of off-road tire based on discrete element method. *Mathematical Biosciences and Engineering*, 17(4): 3869–3893.
36. Zienkiewicz, O.C. and Taylor, R.L. 2000. *The Finite Element Method: Solid Mechanics*, Vol. 2. Butterworth-Heinemann, Oxford.
37. Zienkiewicz, O.C. and Taylor, R.L. 2005. *The Finite Element Method for Solid and Structural Mechanics.* Elsevier, Amsterdam.

International Agricultural Engineering Journal ISSN 0858-2114

*September 2025, 34 (1-4) : 89-100*

# Development of Tractor Operated on Farm Pelleting Machine for Densified Fuel Production from Agro Residues

**Surendra Kalbande*, Rinju Lukose, Prajakta Phadtare, Ajay Lokhande**

## ABSTRACT

India is a rapidly developing country experiencing significant economic and industrial growth leading to a substantial increase in energy demand. The primary energy sources meeting this demand are oil and coal. Among renewable energy options, bioenergy offers a viable pathway to address the rising energy needs through various biomass conversion technologies. Densification of loose agro-residues into pellets enhances ease of handling, storage, and transportation. At the village level, tractors are widely used by farmers as a primary power source for agricultural operations. In this context, a tractor-operated pelleting machine was developed to enable on-farm utilization of agro-residues for pellet production. Research experiments were designed using the Box–Behnken statistical model, varying moisture content, particle size, and feeding rate. The results indicated high pelleting efficiencies of 86.89% for soybean straw and 86.27% for cotton stalk, with corresponding calorific values of 4493.25 kcal/kg and 4632.18 kcal/kg, respectively. The tractor-operated pelleting machine, compatible with an 18-hp tractor, demonstrated effective performance under optimized conditions for soybean straw, with a pelleting efficiency of 86.89%, a pelleting capacity of 38.62 kg/h, a pellet density of 604.45 kg/m³, and a fuel consumption rate of 1.114 L/h. Soybean pellets exhibited superior durability (94.72%) compared to cotton pellets (92.36%), while energy density ratios were also favourable, at 4.22 for soybean and 4.01 for cotton. The tractor-operated pelleting machine, equipped with conveying and mixing arrangements, demonstrated effective performance at pilot scale, highlighting its potential for commercial adoption and sustainable biomass utilization at the village level.

***Keywords:*** *Biomass Pelletization; Cotton stalk; Soybean Straw; Pelleting Efficiency.*

## 1. INTRODUCTION

The depletion of fossil resources and the persistent decline in environmental quality have intensified the global urgency to transition towards renewable energy alternatives. Biomass, being abundant, versatile, and cost-effective, has emerged as one of the most promising substitutes for fossil fuels due to its environmental benefits and diverse applications. Unlike fossil fuels, which are finite and associated with high greenhouse gas emissions, biomass is a renewable resource that can significantly reduce carbon emissions while meeting the energy demands of a growing global population. Biomass serves as an attractive feedstock owing to its renewability, abundance, and minimal environmental impacts, including negligible net carbon dioxide emissions and very low sulphur content (Tumuluru *et al.*, 2010).

Department of Renewable Energy Engineering, College of Agricultural Engineering and Technology, Dr. Panjabrao Deshmukh Krishi Vidyapeeth, Akola, Maharashtra, India, 444001

**Corresponding author – email: surenkalbande@gmail.com*

Received: 28 November 2024; Revised: 12 August 2025; Accepted: 16 August 2025.

India, with its vast agricultural land area, generates substantial quantities of crop residues annually (Kumar *et al.,* 2015). These residues possess considerable potential as biomass feedstock for sustainable energy production (Yadav *et al.,* 2021). Globally, biomass currently contributes approximately 8-15% of the total energy supply in the form of electricity, heat, and transportation fuels. In several developing nations, its share reaches 40 -50%, primarily due to the local availability of biomass resources, which makes it a readily accessible energy option. Projections indicate that by 2050, biomass could meet 33 - 50% of the world's primary energy requirements, establishing it as a key component of the future global energy portfolio and an essential contributor to reducing dependence on non-renewable energy sources (Vassilev *et al.,* 2013). Given India's significant agricultural output and associated residue generation, the country holds immense potential to expand biomass-based energy solutions. Leveraging these resources could not only address energy security challenges but also promote environmental sustainability, rural development, and economic diversification through decentralized energy production.

The growing demand for renewable energy has driven a rapid expansion of the biomass pellet market, which increased from 2 MT in 2000 to 37 MT by 2015 - a remarkable 92% growth, as more countries recognize pellets' potential to meet energy needs (Jagtap and Kalbande, 2023). Low production costs, high energy content, and adaptability to both domestic and industrial uses make pellets an attractive renewable fuel option. Projections indicate that continued technological improvements, infrastructure development, and research investment will further accelerate the growth of the global pellet industry (Liu *et al.,* 2014).

This study presents a significant improvement over conventional pelleting machines, such as piston, screw, and hydraulic presses, which are constrained by dependence on electricity, immobility, and manual feeding - limitations particularly relevant in rural India, where electricity supply is unreliable. The innovation lies in the development of a tractor-operated pelleting machine integrating power transmission with automated feeding and mixing systems. Designed for off-grid applications, the system eliminates the need for grid electricity, reduces labour intensity, lowers operational costs, and enhances worker safety. Field testing with cotton stalks and soybean straw demonstrated the machine's ability to optimize the pelleting process, offering a practical, sustainable, and economically viable approach for decentralized biomass utilization.

## 2. MATERIALS AND METHODS

### 2.1. Selection of Feedstock

Cotton stalks and soybean straw were selected as the agro-residues for pellet production in this study. Prior to pelleting, the materials underwent shredding to achieve the desired particle size, as size reduction is a crucial pre-processing step that enhances pellet quality and densification efficiency. The feedstocks were sourced from the fields of the Central Research Station and the Cotton Research Centre of Dr. Panjabrao Deshmukh Krishi Vidyapeeth (PDKV), Akola. The shredded residues were then used directly in the pelleting experiments.

### 2.2. Design Consideration

The pelleting machine and its components were designed based on the following parameters. The target machine capacity ($Q$) was set at 50 kg/ h, with the bulk density ($\rho$) of the feedstock material ranging between 150–200 kg/m³ (Kankuka and Osu, 2013; Chikwado, 2013). For efficient operation, the die shaft speed was maintained in the range of 150-250 rpm (Kai *et al.,* 2010). The die diameter was selected as 200 mm, while the roller diameter was 120 mm.

To ensure mobility and suitability for rural applications, the machine was designed to be powered by a small tractor with an engine capacity of 18-28 hp.

### 2.3. Development of Tractor Operated Biomass Pelleting Machine

A power transmission system utilizing a small tractor was previously developed for operating the pelleting machine. In the present design, to improve operational efficiency and reduce drudgery, the system was integrated with automated feeding and mixing mechanisms. The power transmission assembly for biomass mixing, feeding, and pelleting. The power transmission from the tractor PTO to the main shaft was achieved using a mini tractor (VST Mitsubishi Shakti – model 180D). The PTO operated at a speed of 540 ± 10 rpm, with the tractor engine rated at 18 hp. The actual power available at the PTO was 13 hp. Power from the main shaft was transmitted to a gearbox attached to the pelleting unit, which operated at a 7:1 ratio, thereby increasing the shaft speed to 1600 rpm as required for the pelleting process. Simultaneously, the PTO speed was transmitted from the main shaft to counter shaft A, via a belt and pulley system. Counter shaft A was connected to counter shaft B through an additional belt and pulley system, reducing the rotational speed to 270 rpm. From counter shaft B, power was transmitted to the mixer shaft, achieving a mixer shaft speed of 81 rpm. Counter shaft B also drove counter shaft C, where the speed was further reduced to 135 rpm using the same belt and pulley arrangement. Finally, counter shaft C powered the conveyor shaft, which operated at the required speed of 81 rpm.

This integrated system allowed the tractor to power the pelletizing, feeding, and mixing units simultaneously, enhancing process efficiency, reducing manual labour, and ensuring uniform feedstock preparation before pelleting. The construction and operation of the tractor-operated pelleting machine are shown in Fig. 1.

**Fig. 1. A view of the tractor operated pelleting machine**

The torque values for different shafts in the tractor-operated pelleting machine were determined based on the tractor's PTO power output and corresponding shaft speeds (Ramteke and Sirohi, 2003). The torque transmitted by the main shaft was calculated as 171.58 Nm and remained the same for counter shaft A, as both pulleys had equal diameters. With speed reductions at subsequent shafts, the torque increased accordingly: counter shaft B (343.17 Nm at 270 rpm), mixer shaft (1143.90 Nm at 81 rpm), counter shaft C (686.34 Nm at 135 rpm), and the inclined elevator shaft, which operated at the same speed as the mixer shaft (1143.90 Nm). These values illustrate the effect of speed reduction on torque multiplication within the machine's transmission system, ensuring adequate power transmission to the feeding, mixing, and pelleting units.

### 2.4. Pellet Production Process

The pellet production process involved three main stages: raw material pre-treatment, pelletization, and post-treatment. During experiment, a tractor-powered pelleting machine was developed, provided with an inclined belt conveyor and a mixer. Soybean straw and cotton stalk residues were first ground using a hammer mill equipped

with 4 mm, 6 mm, and 8 mm sieves, resulting in size-classified samples for uniform pellet production. The shredded biomass was then loaded into the hopper of the inclined belt conveyor, which transported the material to the mixer. The material was mixed with water at moisture content levels of 20%, 25%, and 30%, using a tractor operated mixer provided with blades attached to a horizontal shaft.

After thorough mixing, the material was discharged into the pelleting machine at controlled feeding rates of 45, 50, and 55 kg/h. In pelleting chamber, two rollers pressed the feedstock into die holes, forming uniform pellets as friction increased the temperature of the die plate and rollers, as well as the pellets, to 70–72°C. External heating or binding agents were not used during the entire process. Pellets with a diameter of 15 mm and a length of 40 mm were produced using the tractor-operated pelleting machine. After pelletization, the pellets were sun-dried and stored in airtight bags to prevent moisture absorption.

## 2.5. Performance Evaluation of the Tractor Operated Pelleting Machine

### 2.5.1. Experimental design

The effect of key parameters such as moisture content, particle size, and feeding rate were studied to evaluate the performance of the tractor-operated pelleting machine with reference to pelleting efficiency, pellet density, fuel consumption and pelleting capacity (Jagtap and Kalbande, 2023). The experiments were planned using a Box-Behnken randomized design at the levels of the independent variables indicated in Table 1. The process parameters, moisture content, particle size, and feeding rate were optimized using Design-Expert software (version 13.0.5.0) and the effects and interactions of these variables were analyzed.

### 2.5.2. Determination of pelleting efficiency

The ratio of the total mass of pellets produced to the total mass of biomass feedstock, expressed in percentage is known the pelleting efficiency and estimated as given below:

$$\eta_p = \frac{W_P}{W_t} \times 100 \quad \ldots (1)$$

Where, $\eta_p$ is the pelleting efficiency, %; $W_p$ is total mass of pellets produced by the machine, kg and $W_t$ is the total mass of input, kg.

### 2.5.3. Determination of pelleting capacity

The pelleting capacity is calculated (eq. 2) as the ratio of the total quantity of the feed pelleted to the time taken (Okewole and Lgbeka 2016).

$$C_P = \frac{W_p}{T} \quad \ldots (2)$$

Where, $C_P$ is the pelleting capacity (kg/h) and $T$ is the time taken to pelletize the specified feed, h.

### 2.5.4. Bulk density of pellets

This is the mass per unit volume of the bulk material including the pore volume. Determined as the ratio of the mass (kg) occupying a given bulk volume to the volume of the container ($m^3$).

### 2.5.5. Fuel consumption

The fuel consumption by the tractor during pellet production was determined by filling method, where the fuel tank was initially filled with diesel up to the full level and the quantity to top up to the same level is the fuel consumed (Shahid *et al.*, 2019). This was followed for each test run.

## 2.6. Physiochemical Properties of Biomass Pellets

The physical and thermal properties were evaluated using the most optimal pellet combination. It includes proximate analysis, calorific value, shattered index, resistance to water penetration, pellet durability and energy density ratio were studied.

**Table 1. The variables associated with the evaluation of the pelleting machine and the pellets.**

| Independent variables | | | | |
|---|---|---|---|---|
| **Sl. No.** | **Variables** | **Levels (coded and decoded)** | | |
| | | **1** | **0** | **-1** |
| 1. | Moisture content, % | 20 | 25 | 35 |
| 2. | Particle size, mm | 4 | 6 | 8 |
| 3. | Speed of shaft, rpm | 150 | 200 | 250 |

| Dependent variables | | |
|---|---|---|
| **Performance of pelleting machine** | **Qualities of pellets** | |
| 1. Pelleting efficiency | 1. Moisture Content | 2. Pellet durability |
| 2. Pelleting capacity | 3. Volatile matter | 4. Calorific value |
| 3. Pellet density | 5. Ash content | 6. Volumetric energy density ratio |
| 4. Fuel consumption | 7. Fixed carbon | |

### 2.6.1. Proximate analysis

The proximate composition such as moisture, volatile matter, ash content and fixed carbon content of the biomass were carried out following the standard procedures (Bhavsar *et al.,* 2018).

#### 2.6.1.1. *Moisture content*

The moisture content of biomass was measured by the oven dry method. Initially the sample with the known weight was kept in a thermostatically controlled ventilated hot air oven maintained at 105 ± 2ºC untill the constant weight is attained (ASTM D-3173). Then the oven dry sample was weighed and the moisture content was estimated as percentage on dry basis.

#### 2.6.1.2. *Volatile matter*

The volatile matter was determined as per the procedure of ASTM, D-3175 by heating the sample in a silica crucible at 950°C ± 25°C in a muffle furnace for 7 minutes.

#### 2.6.1.3. *Ash content*

The amount of ash collected by heating a moisture-free sample in a muffle furnace without a lid at a temperature of 750°C for 30 min. as per ASTM D – 3174, was expressed as a percentage based on the quantity of the sample taken.

#### 2.6.1.4. *Fixed carbon*

The fixed carbon content is the value obtained by subtracting the values of moisture content, volatile matter, and ash content from one hundred percent.

### 2.6.2. Calorific value

Calorific value is the amount of heat generated by unit mass of the fuel on its complete combustion. The calorific value of biomass was determined by using bomb calorimeter. The calorific value of biomass using bomb calorimeter was determined by following formula.

$$C = \frac{(W+w)\times(T_2-T_1)}{X} \quad \ldots (3)$$

Where, $C$ is the calorific value, kcal/kg; $W$ is the weight of water in calorimeter, kg; $w$ is the water equivalent of apparatus, kcal/°C; $T_1$ is the initial temperature of water, °C; $T_2$ is the final temperature of water, °C and $X$ is the weight of sample, g.

### 2.6.3. Shattered index

The shattered index test evaluates the hardness of the briquettes. A pellet of known weight and length was dropped from a height of one meter onto a concrete floor ten times. The weight and size of the disintegrated pellet were recorded, and the percentage of material loss was calculated. The shatter resistance of the pellet was then determined using the following formula. (Madhava *et al.*, 2012).

$$\text{Percentage weight loss, } L = \frac{W_1 - W_2}{W_1} \times 100 \quad \ldots (4)$$

$$\text{Tumbling resistance} = 100 - \%\ \text{weight loss} \quad \ldots (5)$$

Where, $W_1$ and $W_2$ are the weight of the pellet before and after tumbling, g, respectively.

### 2.6.4. Resistance to water penetration

The percentage of water absorbed by the pellets was measured by immersing each pellet in 25 mm of water at 27°C for 30 seconds. The percent water gain was calculated and recorded using the following formula (Sengar *et al.*, 2012):

$$G = \frac{W_2 - W_1}{W_1} \text{ x } 100\ \% \quad \ldots (6)$$

$$R = 100 - G \quad \ldots (7)$$

Where, $G$ is the water gained by the pellets, %; $R$ is the resistance to water penetration, %; $W_1$ and $W_2$ are the weight of the pellet before and after immersion in water, g, respectively.

### 2.6.5. Pellet durability

Pellet durability refers to the ability of pellets to withstand destructive loads and frictional forces during handling and transport. According to ASABE (ASAE S269.4 DEC1991, R2007), the durability of the pellets was assessed by placing 500 g of pellets in a tumbling box device. The pellets were tumbled for 10 minutes at a speed of 50 rpm. After tumbling, the broken and cracked pellets were separated, and their weight was recorded. The durability was then calculated using the following formula.

$$D = \frac{W_a}{W_b} \times 100 \quad \ldots (8)$$

Where; $D$ is the pellet durability, %; $w_a$ is the mass of the pellet after shaker treatment, g and $w_b$ is the mass of the pellet before shaker treatment, g.

### 2.6.6. Energy density ratio

The energy density ratio is the ratio of energy content per unit volume of raw material to the energy content per unit volume of pellet fuel. The energy density ratio of pellet fuel is calculated by using the equation as below (Sengar *et al.*, 2012):

$$ED = \frac{\rho_p \times CV_{Pellet}}{\rho_A \times V_{Agro\ residue}} \quad \ldots (9)$$

Where, $ED$ is the energy density ratio; $\rho_p$ is the pellet density, kg/m$^3$; $\rho_A$ is the bulk density of agro residue, kg/m$^3$; $CV_{pellet}$ is the higher heating value of pellet, kcal/kg and $CV_{Agro\ residue}$ is the higher heating value of agro residue, kcal/kg.

## 3. RESULTS AND DISCUSSION

### 3.1. Physiochemical Properties of Biomass

Prior to conducting the experiments, the physical and chemical properties of soybean straw and cotton stalks, *viz.*, bulk density, calorific value, moisture content, volatile matter, ash content and fixed carbon were determined and presented in Table 2.

The bulk densities of soybean straw and cotton stalk were measured as 175.85 kg/m³ and 182.65 kg/m³, respectively. Calorific values of 3863.42 kcal/kg for soybean straw and 3726.38 kcal/kg for cotton stalk, confirming their potential as viable bioenergy feedstocks. From the proximate analysis the soybean straw contained 10.61% moisture, 70.64% volatile matter, 3.88% ash, and 14.87% fixed carbon. In comparison, cotton stalk contained 10.19% moisture, 72.84% volatile matter, 4.28% ash, and 12.69% fixed carbon. These parameters are essential for understanding the thermal behaviour and densification performance of biomass during pelletization.

The comprehensive characterization of soybean straw and cotton stalk demonstrates their

favourable physicochemical properties, making them suitable candidates for conversion into biomass pellets or other biofuels. Their utilization can contribute to renewable energy production in the agricultural sector while supporting sustainable waste management practices.

### 3.2. Performance Evaluation of Tractor Operated Pelleting Machine

#### 3.2.1. Pelleting efficiency

As moisture content increased from 25% to 35%, and the feeding rate decreased from 55 kg/h to 45 kg/h, a notable increase in the pelleting efficiency was observed for both soybean and cotton stalks, as seen from in Fig. 2a and 2b. The highest pelleting efficiency of 87.79% for soybean straw and 86.12% for cotton stalk, was achieved at a moisture content of 35%, particle size of 6 mm, and feeding rate of 45 kg/h. On the contrary, the lowest efficiency, 80.54% for soybean straws and 79.03% for cotton stalks, was observed at a moisture content of 25%, with the same particle size (6 mm) and a higher feeding rate of 55 kg/h.

The results demonstrated that optimizing moisture content and feeding rate plays a critical role in enhancing the pelleting process. Higher moisture levels, coupled with lower feeding rates, promote improved particle binding, leading to more efficient pellet formation and increased pellet durability. These findings suggest the necessity of precise optimization of parameters to maximize the operational efficiency of tractor-operated pelleting machines, particularly for agricultural biomass such as soybean and cotton stalks.

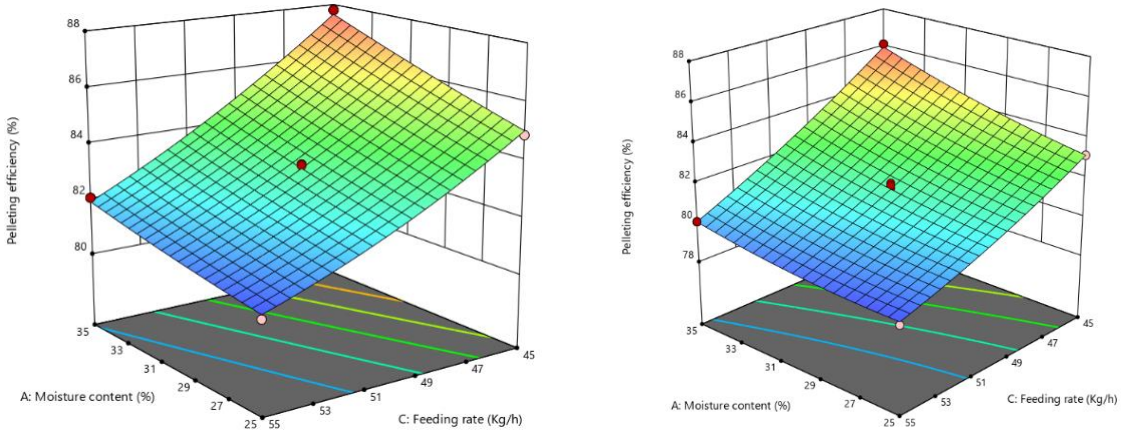


**a. Soybean straw** **b. Cotton stalk**

**Fig. 2. Effect of moisture content and feeding rate on pelleting efficiency**

#### 3.2.2. Pelleting capacity

As the moisture content increased from 25% to 35%, significant increase in pelleting capacity was observed (Fig. 3a and 3b). The increase in moisture content enhanced the plasticity and cohesiveness of the raw materials leading to better pellet formation during the densification process. At a moisture content of 35%, maximum pelleting capacities of 48.83 kg/h for soybean straws and 48.76 kg/h for cotton stalks were recorded when combined with a feeding rate of 55 kg/h and a particle size of 6 mm. This suggests that higher moisture levels, in conjunction with optimal feeding rates, create favourable conditions for continuous and efficient pellet production. The minimum pelleting capacities of 33.87 kg/h and 33.42 kg/h for soybean and cotton stalks, respectively, were observed at a reduced feeding rate of 45 kg/h, a lower moisture content of 25%, and a particle size of 6 mm.

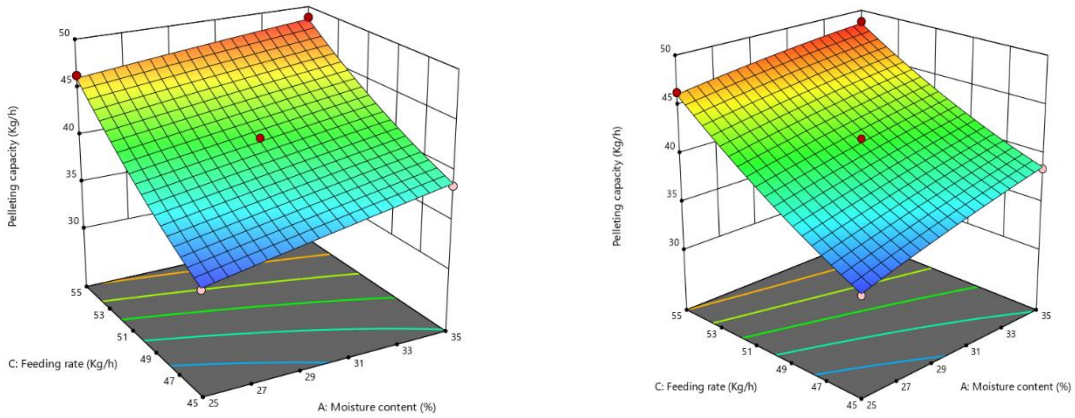


**a. Soybean straw** **b. Cotton stalk**

**Fig.3. Effect of moisture content and feeding rate on pelleting capacity**

**Table 2. Physiochemical properties of biomass**

| Parameter | Biomass | |
|---|---|---|
| | Soybean straw | Cotton stalk |
| Bulk density, kg/m$^3$ | 175.85 | 182.65 |
| Calorific value, kcal / kg | 3726.38 | 3863.4 |
| Moisture content, % d.b. | 10.61 | 10.19 |
| Volatile matter, % | 70.64 | 72.84 |
| Ash content, % | 3.88 | 4.28 |
| Fixed carbon, % | 14.87 | 12.69 |

The reduction in pelleting capacity at lower moisture content may be attributed to insufficient binding of particles, resulting in less cohesive pellets. Thus maintaining a balance between moisture content and feeding rate is critical to achieve higher pelleting capacity and efficiency.

### 3.2.3. Pellet density

The study revealed a clear trend in pellet density with varying moisture content for soybean and cotton stalks. As the moisture content decreased from 35% to 25%, there was a significant increase in pellet density, as illustrated in Fig. 4a and 4b. Lower moisture content tends to reduce the amount of water within the biomass, allowing for a more compact arrangement of particles during the pelleting process, which results in denser pellets. The maximum pellet density of 616.25 kg/m³ for soybean straws and 612.96 kg/m³ for cotton stalks were achieved at a moisture content of 25%, with a particle size of 4 mm and a feeding rate of 50 kg/h. In contrast, the minimum pellet densities of 598.65 kg/m³ and 595.98 kg/m³ for soybean and cotton stalks, respectively, were observed at a higher moisture content of 35%, a larger particle size of 8 mm, and the same feeding rate of 50 kg/h. These findings indicate that lower moisture content promotes greater compaction of biomass particles, leading to higher pellet densities. On the other hand, higher moisture content reduces the mechanical pressure required for densification, resulting in less compact pellets.

### 3.2.4. Fuel consumption

The study revealed a direct relationship between feeding rate and the tractor's fuel consumption during the pelleting process. The highest fuel consumption was recorded at 1.178 L/h for soybean straw and 1.171 L/h for

cotton stalk, observed at a feeding rate of 55 kg/h, with a particle size of 8 mm and a moisture content of 30% (Fig. 5a and 5b). This increase in fuel usage at higher feeding rates is likely due to the greater load on the pelleting machine, requiring more effort from the tractor to process the material, which in turn raised energy demand. In contrast, the lowest fuel consumption was measured at 1.112 L/h for soybean straw and 1.103 L/h for cotton stalk, corresponding to a feeding rate of 45 kg/h, a particle size of 4 mm, and a moisture content of 30%. Smaller particle sizes facilitate smoother handling and compaction, thereby reducing the mechanical resistance in the pelleting chamber and minimizing fuel requirements.

### 3.3. Physiochemical Properties of Biomass Pellets

#### 3.3.1 Proximate analysis

The moisture content of soybean and cotton stalk pellets was found to be 3.45% and 4.11%, respectively, which are ideal levels for storage and transport (Table 3). Moisture levels below 10% are preferred, as they enhance the stability and durability of the pellets, while higher moisture content reduces the available heat for combustion, negatively affecting energy efficiency.

The volatile matter content of the pellets was found to be 73.79% for soybean straws and 74.39% for cotton stalks, indicating high reactivity and ease of ignition. These values suggest that both types of pellets would combust readily, making them suitable for use as fuel. Additionally, the ash content was found to be at 5.23% for soybean pellets and 5.56% for cotton pellets, which is within acceptable limits for biomass fuel and affects the handling of combustion residues. The fixed carbon content was 17.43% for soybean pellets and 15.94% for cotton pellets, providing an estimate of their heating value and contribution to long-term combustion (Table 3).

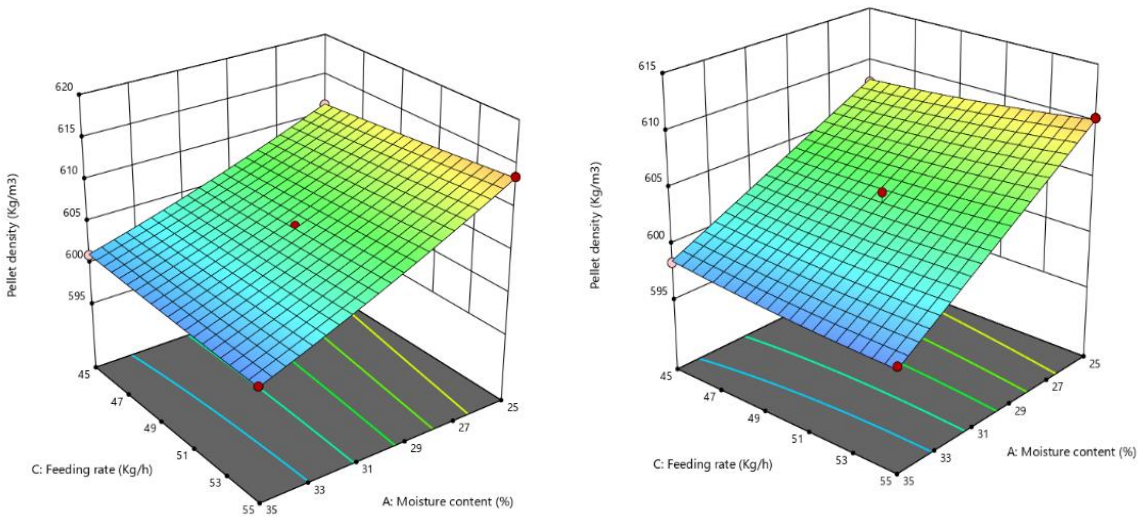


**a. Soybean straw** **b. Cotton stalk**

**Fig. 4. Effect of moisture content and feeding rate on pellet density**

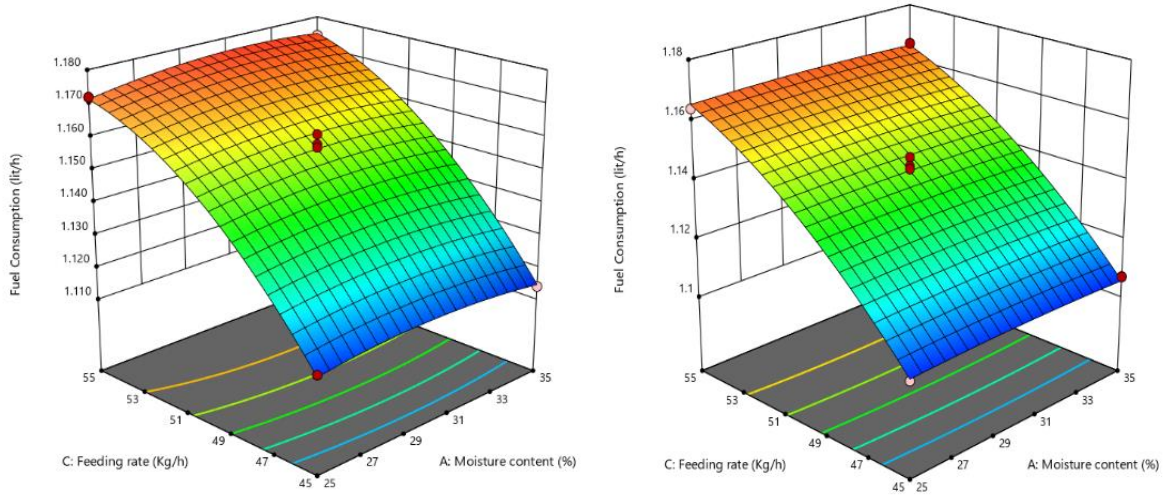


**a. Soybean straw** **b. Cotton stalk**

**Fig. 5. Effect of particle size and feeding rate on fuel consumption**

**Table 3. Proximate analysis of soybean and cotton pellets**

| Biomass | Moisture content, % | Volatile matter, % | Ash content, % | Fixed carbon, % | Calorific value, kcal/kg |
|---|---|---|---|---|---|
| Soybean pellets | 3.45 | 73.89 | 5.23 | 17.43 | 4493.25 |
| Cotton pellets | 4.11 | 74.39 | 5.56 | 15.94 | 4632.18 |

### 3.3.2. Calorific value

The calorific value is a crucial property of biomass fuel, as it is influenced by both the chemical composition of the material and its moisture content. The calorific values for soybean and cotton pellets were found to be 4493.25 kcal/kg and 4632.18 kcal/kg, respectively (Table 3). These values indicate that cotton pellets possess a higher energy content compared to soybean pellets, which can have important implications for their use as a fuel source. Higher calorific values suggest better efficiency and performance during combustion, making cotton pellets a more advantageous option for energy production.

### 3.3.3. Shattered index

The shattered index is a critical property used to assess the strength of pellets against shattering.

The shattered index was found to be 91.89% for soybean pellets and 90.68% for cotton pellets. These values indicate that both types of pellets exhibit a high level of structural integrity, making them suitable for transportation. A higher shattered index signifies that the pellets are less likely to break or crumble under stress, which is vital for minimizing losses and maintaining fuel quality.

### 3.3.4. Resistance to water penetration

The water penetration resistance of soybean and cotton pellets was measured, resulting in values of 84.92% and 83.46%, respectively. These high resistance values indicate that both types of pellets have a strong ability to withstand moisture, which is crucial for maintaining their integrity during storage and transportation. Effective water resistance helps prevent the degradation of pellets, ensuring that their physical and chemical properties remain intact, thereby enhancing their overall performance as biomass fuel.

### 3.3.5. Pellet durability

The pellet durability test was conducted for both soybean and cotton pellets and resulting in an average material loss of less than 7% to 8% during the tumbling test. The durability percentages were 94.72% for soybean pellets and 92.36% for cotton pellets. These high durability values suggest that both types of pellets exhibit excellent structural integrity, making them suitable for commercial applications. The ability to maintain durability under mechanical stress is crucial for reducing material losses and ensuring the consistent quality of biomass fuel pellets throughout their life cycle.

### 3.3.6. Energy density ratio

The energy density ratios for soybean and cotton pellets were measured and found to be 4.22 and 4.01, respectively. These results demonstrate that the volumetric energy density of the pellets is significantly higher than that of the original biomass material, with an increase of 4.22 times for soybean pellets and 4.01 times for cotton pellets. This substantial enhancement in energy density reveals that both types of pellets can provide a more concentrated energy source, making them more efficient for use as biofuel.

## 4. CONCLUSIONS

The tractor-operated pelleting machine, compatible with an 18-hp tractor, demonstrated effective performance under optimized conditions for soybean straw, achieving a pelleting efficiency of 86.89%, a pelleting capacity of 38.62 kg/h, a pellet density of 604.45 kg/m$^3$, and a fuel consumption rate of 1.114 L/h. Cotton stalk exhibited a higher bulk density (182.65 kg/m$^3$) and calorific value (3863.42 kcal/kg) compared to soybean straw, and pelletization further increased the calorific value to 4493.25 kcal/kg for soybean and 4632.18 kcal/kg for cotton. Soybean pellets exhibited superior durability (94.72%) compared to cotton pellets (92.36%), while energy density ratios were also favourable, at 4.22 for soybean and 4.01 for cotton. Economic evaluation confirmed the viability of the machine, with a net present worth of ₹4,737,488 over a 10-year period, a benefit–cost ratio of 2.15, a short payback period of 6.13 months, and an internal rate of return of 46%.

## REFERENCES

1. Bhavsar, P., Jagadale, M., Khandetod, Y. and Mohod, A. 2018. Proxiamate analysis of selected non woody biomass. *International Journal of Current Microbiology and Applied Sciences,* 7(9): 2846-2849.
2. Chikwado, U. K. 2013. Development and performance test of poultry feed mixing and pelleting machine. *International Journal of Science*, 4(6): 1161-1166.
3. Jagtap, A. and Kalbande, S. 2023. Physio-chemical properties of pellets using different feedstocks. *International Journal of Agricultural Sciences,* 18(1): 18-23.
4. Kaankuka, T. K. and Osu, D. T. 2013. Development of a revolving die and roller fish feed pelletizer. International *Journal of Engineering Innovations and Research*, 2(1): 105-110.
5. Kai, W., Shuijuan, S., Wuxue, D., Binbin, P. and Yu, S. 2010. Influence of die speed on the energy consumption in the pelleting process. *International Conference on Computing, Control and Industrial Engineering*. 1: 247-250.

6. Kumar, A., Kumar, N., Baredar, P. and Shukla, A. 2015. A review on biomass energy resources, potential, conversion, and policy in India. *Renewable and Sustainable Energy Reviews*, 45: 530-539.
7. Liu, Z., Quek, A. and Balasubramanian, R. 2014. Preparation and characterization of fuel pellets from woody biomass, agro residues and their corresponding hydrochars. *Applied Energy*, 113: 1315–1322.
8. Madhava M., Prasad, B. V., Koushik, Y., Rameshbabu, K. R. and Srihari, R. 2012. Performance evaluation of a hand operated compression type briquetting machine. *Journal of Agricultural Engineering*, 49(2): 46-49.
9. Okewole, O.T. and Igbeka, J.C. 2016. Effect of some operating parameters on the performance of a pelleting press. *Agric. Eng. Int.: CIGR Journal*, 18: 326-338.
10. Ramteke, A. S. and Sirohi, N. P. S. 2003. Studies on design parameter for linseed crop thresher. *Journal of Agricultural Engineering*,40(2):39-45.
11. Sengar, S. H., Mohod, A. G., Khandetod, Y. P., Patil, S. S. and Chendake, A. D. 2012. Performance of briquetting machine for briquette fuel. *International Journal of Energy Engineering*, 2(1): 28-34.
12. Shahid, L. A., Amjad, N. and Siddhu, M. A. H. 2019. Adaptation and performance evaluation of a tractor operated wood chipper shredder. *Pakistan Journal Agriculture Research*, 32: 197-204.
13. Tumuluru, J.S., Wright, C.T., Kenney, K.L. and Hess, R.J. 2010. *A technical review on biomass processing: densification, preprocessing, modeling and optimization*. 2010 ASABE Annual International Meeting. American Society of Agricultural and Biological Engineers (ASABE), pp 1. Microsoft Word - 1009401.docx. (accessed on May 2022).
14. Vassilev, S.V., Baxter, D., Andersen, L.K. and Vassileva, C.G. 2013. An overview of the composition and application of biomass ash. Part 1. Phase-mineral and chemical composition and classification. *Fuel*, 105: 40–76.
15. Yadav, K. K, Krishnan, ., Gupta, N., Prasad, S., Amin, M. A., Cabral-Pinto, M. M., Sharma, G. K., Marzouki, R., Jeon, B. H., Kumar, S. and Singh, N. 2021. Review on evaluation of renewable bioenergy potential for sustainable development: Bright future in energy practice in India. *ACS Sustainable Chemistry and Engineering*, 9(48): 16007-16030.

International Agricultural Engineering Journal ISSN 0858-2114

*September 2025, 34 (1-4) : 101-118*

# Reference Evapotranspiration Estimation Using Machine Learning Models

**R.A. Alagu Raja[1], M. Kathirvel[1], D. Sivakumar[2], V. Kumar[3]**

## ABSTRACT

Prudent water usage is crucial for sustainable irrigated farming. The Penman-Monteith equation requires extensive meteorological data and is computationally intensive. In contrast, machine learning offers a promising alternative by modelling complex, non-linear relationships between input variables and reference evapotranspiration (Ref ET) in a data-driven manner. Machine learning models provide precise forecasts with lower processing requirements and fewer meteorological inputs, making them a novel tool for Ref ET estimation. This study explores the application of machine learning models for estimating Ref ET, a key component in hydrological modelling. The models evaluated include Support Vector Machine (SVM), k-Nearest Neighbours (KNN), LightGBM, XGBoost, CatBoost, and AdaBoost. The meteorological variables used for prediction include maximum and minimum temperature, relative humidity, wind speed, sunshine hours, pan evaporation, and precipitation. The performance of these models highlights their potential for accurate Ref ET estimation, offering practical implications for agricultural decision-making and water resource management in similar regions. Meteorological data obtained from the Agricultural College & Research Institute (AC & RI), Tamil Nadu Agricultural University (TNAU), Madurai, was used, with Ref ET values calculated using the FAO-56 Penman-Monteith equation via the REF-ET software, in accordance with ASCE standards. Models were assessed using Root Mean Squared Error (RMSE) and Mean Absolute Error (MAE). The dataset was split with 80% for training. SVM emerged as the top performer with an RMSE of 0.1855 and MAE of 0.1083, suggesting its preference for Ref ET estimation in similar meteorological conditions.

***Keywords:*** *Agricultural Decision-making; Evapotranspiration; Machine Learning; Meteorological Data; Predictive Modeling; Reference ET.*

## 1. INTRODUCTION

A country like India, where the economy heavily depends on agriculture, requires prudent water usage due to the increasing scarcity of water for sustainable farming. Agriculture consumes a significant portion of available freshwater resources, and in regions prone to erratic rainfall and prolonged dry spells, optimizing water use is vital to ensure food security and sustainable development.

[1] Remote Sensing and GIS Laboratory, Thiagarajar College of Engineering, Madurai, India.
[2] Department of Agricultural Engineering, Kalasalingam Academy of Research and Education, Krishnankoil, India.
[3] Formerly Professor & Head, Agricultural Engineering Department, Tamil Nadu Agricultural University, Madurai, India.

**Corresponding author – email: alaguraja@tce.edu*

Received: 14 December 2024; Revised: 21 April 2025; Accepted: 22 July 2025.

One of the key components in efficient water management is the accurate estimation of evapotranspiration (ET), which represents the combined loss of water through soil evaporation and plant transpiration. Estimating ET is crucial for irrigation scheduling, hydrological modeling, and crop management. The standard method recommended by the Food and Agriculture Organization (FAO) is the Penman-Monteith equation, which integrates several meteorological parameters to compute reference ET. While reliable, this method demands extensive and continuous meteorological data, which may not always be available in many parts of the country. Additionally, the method is computationally intensive and less adaptable in regions with limited meteorological infrastructure.

Evapotranspiration (ET), particularly reference evapotranspiration (Ref ET), is a critical parameter for effective irrigation planning and hydrological modeling. Accurate ET estimation enables the optimal allocation of water resources, helps reduce crop water stress, and enhances yield outcomes. Traditionally, the FAO-56 Penman-Monteith (PM) equation has been recommended for Ref ET estimation, integrating meteorological inputs such as temperature, wind speed, relative humidity, and solar radiation (Allen *et al*., 1998). However, this approach is data-intensive and not always feasible in regions with sparse or unreliable weather station coverage. In response to these challenges, researchers have explored alternative empirical and statistical models (Ayaz *et al*., 2021; Adib *et al*., 2023), but many still fall short when faced with complex, non-linear atmospheric interactions influencing ET.

Recent advances in data-driven techniques, particularly machine learning (ML), offer promising alternatives for ET estimation. ML models are capable of capturing complex, non-linear relationships between input features and ET, thereby reducing dependency on large volumes of data while maintaining prediction accuracy. Various ML algorithms such as Support Vector Machine (SVM), k-Nearest Neighbours (KNN), LightGBM, XGBoost, CatBoost, and AdaBoost have been successfully applied in environmental and agricultural domains. These models differ in learning strategies, handling of feature types, and computational efficiency. For example, SVM excels in handling non-linear data with kernel tricks, while boosting algorithms like LightGBM and CatBoost improve predictive accuracy through iterative model refinement. AdaBoost enhances learning by focusing on misclassified instances during training, and KNN offers simplicity by relying on proximity-based predictions.

The M5 tree and gradient-boosted tree models show superior performance, offering precise ET predictions for efficient irrigation scheduling in semi-arid regions like New Delhi (Rajput *et al.,* 2023b). Comparison of Gene Expression Programming (GEP), M5 tree (M5T), and optimized Artificial Neural Network by Genetic Algorithm (ANN-GA) for evapotranspiration estimation in Ahvaz and Dezful, Iran. ANN-GA exhibits superior performance, particularly influenced by maximum temperature and wind speed (Adib *et al.,* 2023). Granata (2019) conducted an evaluation of three evapotranspiration models, each utilizing varying input variables and four algorithmic variants, including M5P Regression Tree and SVM, to assess predictive capabilities under different input scenarios (Granata, 2019). SVM yields minimal errors compared to Group Method of Data Handling (GMDH), Multilayer Perceptron (MLP), Cascade-Correlation Neural Network (CCNN), and General Regression Neural Network (GRNN). This highlights SVM's reliability and suitability for accurate ET estimation across varied climatic conditions (Raza *et al.,* 2020). Machine learning methods are followed to enhance terrestrial evapotranspiration (ET) estimation in China from 2000 to 2018. Gaussian Process Regression (GPR) outperforms other methods, reducing root mean square error (RMSE) by up to 0.81 mm / day and improving

the coefficient of determination ($R^2$) by up to 0.33 compared to individual ET algorithms (Yin *et al.*, 2021). Results demonstrate that the ML-based EEMs outperform both individual ET models and conventional ensemble methods like MEAN and BMA, achieving higher accuracy with coefficient of determination ($R^2$) ranging from 0.75 to 0.83 and root mean squared error (RMSE) ranging from 18 to 21. The MLP algorithm emerges as the most efficient among the ML classifiers tested (Bai *et al.*, 2021).

Despite the growing adoption of machine learning techniques for ET estimation, many existing studies remain limited in scope. They are often constrained to narrow geographic settings, rely on a small set of input features, or fail to assess a broad range of ML models under consistent climatic conditions. For instance, Singh *et al.* (2023) focused on model performance within semi-arid regions but evaluated fewer models and lacked extensive variable testing. Additionally, there is a scarcity of studies targeting subtropical regions like Madurai, where seasonal variation and temperature extremes pose unique modeling challenges. This study addresses these gaps by comprehensively evaluating six diverse ML models using a year-long dataset with seven key meteorological variables. The novelty of this research lies in its comparative approach across multiple algorithms in a subtropical context, its robust preprocessing framework, and its detailed performance benchmarking - offering both methodological and practical insights for data-scarce agricultural regions. The study aims to evaluate the accuracy of the six machine learning models, including Support Vector Machine (SVM), k-Nearest Neighbours (KNN), LightGBM, XGBoost, CatBoost, and AdaBoost in estimating evapotranspiration (ET) by comparing it with the reference evapotranspiration values obtained from the REFET software which utilizes the FAO56 Penman-Monteith equation. The study area, Madurai, situated in the southern part of Tamil Nadu, India, experiences a subtropical climate characterized by hot and dry summers and mild winters. The region's agricultural landscape is predominantly composed of paddy fields, sugarcane plantations, and other crops, with irrigation playing a crucial role in sustaining agricultural productivity.

## 2. MATERIALS AND METHODS

### 2.1. Study Area

The Agricultural College & Research Institute in Madurai, a campus of Tamil Nadu Agricultural University (TNAU), experienced a dynamic climate characterized by scorching summers and mild winters typical of its subtropical setting is taken as the study area. The agricultural landscape of this region is predominantly composed of paddy fields, sugarcane plantations, and other crops, with irrigation playing a crucial role in sustaining agricultural productivity.With latitude 9.92°N and longitude 78.12°E, the region saw temperatures soar to around 39°C during May - June, while January brought cooler temperatures around 14°C. The monsoon season during June to September brought the majority of the annual rainfall, averaging 710 mm. Wind speeds ranged from 0.45 m/s to 3.96 m/s, influencing agricultural practices.

### 2.2. Methodology Flow Chart

This study aims to evaluate the efficacy of six machine learning models, namely Support Vector Machine (SVM), k-Nearest Neighbours (KNN), LightGBM, XGBoost, CatBoost, and AdaBoost in predicting reference evapotranspiration (Ref ET). The evaluation process was carried out in the following steps and the methodology flow chart is presented in Fig. 1.

#### 2.2.1. Data collection

Daily meteorological data (2001-2002) was collected from the Agricultural College & Research Institute (AC & RI), Madurai. The data included key parameters such as temperature, relative humidity, wind speed, and solar radiation,

which are required for the prediction of reference evapotranspiration.

### 2.2.2. Calculation of reference evapotranspiration (Ref ET)

The reference evapotranspiration (Ref ET) was calculated using the FAO-56 Penman-Monteith equation through the REF-ET tool. The FAO-56 Penman-Monteith equation is defined as follows (Allen *et al.*, 1998):

$$ETo = \frac{0.408\Delta(R_n - G) + \gamma \frac{900}{T+273} u_2 (e_s - e_a)}{\Delta + \gamma(1 + 0.34u_2)} \quad \ldots (1)$$

Where, $ET_0$ is the reference evapotranspiration, mm/day; $R_n$ is the net radiation at the crop surface, MJ/m$^2$ day; $G$ is the soil heat flux density, MJ/m$^2$ day; $T$ is the mean daily air temperature at 2 m height, °C; $u_2$ is the wind speed at 2 m height, m/s; $e_s - e_a$ is the saturation vapour pressure deficit, kPa; $\Delta$ is the slope of the vapour pressure curve, kPa/°C and $\gamma$ is the psychrometric constant, kPa/ °C.

In the REF-ET software, standard assumptions were used as recommended by FAO guidelines, including an albedo value of 0.23 for grass reference crop, wind speed measured at 2 m, and soil heat flux ($G$) assumed as zero for daily calculations. The psychrometric constant ($\gamma$) and saturation vapor pressure ($e_s$) were automatically computed based on elevation and mean air temperature. The crop surface resistance and aerodynamic resistance were also set to standard values, 70 s/m and 208/$u_2$ s/m, respectively, consistent with grass reference conditions.The FAO-56 method is widely regarded as a reliable standard for $ET_a$ estimation, and it integrates multiple meteorological parameters, making it suitable for agricultural andhydrological purposes.

### 2.2.3. Modelling and prediction

The six machine learning models (SVM, KNN, LightGBM, XGBoost, CatBoost, AdaBoost) were trained and validated using the processed meteorological dataset. Before modeling, data preprocessing steps included handling missing values by applying linear interpolation. Outliers were detected using the Interquartile Range (IQR) method, where data points lying beyond 1.5 times the IQR from the first and third quartiles were considered outliers and treated through winsorization to retain data structure while reducing skew. The models were optimized using 10-fold cross-validation, and hyperparameter tuning was conducted through a grid search combined with cross-validation to ensure robust model performance. The best parameters obtained for each model are as follows:

SVM: kernel='rbf', C=250, gamma=0.02

KNN: n_neighbors=5, weights='distance', metric='euclidean'

LightGBM: max_depth=5, learning_rate=0.01, n_estimators=300

XGBoost: max_depth=5, learning_rate=0.1, n_estimators=200

CatBoost: depth=6, learning_rate=0.03, iterations=300, l2_leaf_reg=3

AdaBoost: n_estimators=100, learning_rate=0.01

These tuned models were then used for predicting Ref ET on unseen test data.

Normalization was applied to scale the features to a standard range (0 to 1), ensuring that each variable contributed equally to the model. Feature selection was based on domain relevance and Pearson correlation analysis, ensuring the selected meteorological variables had significant influence on Ref ET. These variables included maximum and minimum temperature, relative humidity, wind speed, sunshine hours, pan evaporation, and precipitation.

### 2.2.4. Performance evaluation

To evaluate the performance of each model in predicting Ref ET, two robust error indices besides $R^2$ were employed:

a. Root Mean Square Error (RMSE) is a measure of the average magnitude of errors between predicted and actual values.

It penalizes larger errors more heavily by squaring the residuals, making it particularly useful for identifying models that perform poorly under extreme conditions.

b. Mean Absolute Error (MAE) calculates the average magnitude of errors in a set of predictions without considering their direction. It provides a straightforward interpretation of model accuracy in terms of absolute deviation, offering valuable insight into the general performance of each model.

c. The $R^2$ value quantifies how well the model explains variance in the observed data, with values closer to 1 indicating stronger predictive alignment. The combination of these three metrics provides a comprehensive evaluation of model accuracy, robustness, and reliability.

### 2.2.5. Model comparison and analysis

The models were compared based on their RMSE and MAE values. A lower RMSE and MAE indicate higher accuracy and predictive capability. The results were analyzed to identify the most efficient model for predicting ET in the region of study. The dataset comprises daily values of various meteorological parameters, which were averaged over each month. These parameters include maximum and minimum temperature (°C), maximum and minimum relative humidity (%), wind speed measured at 10 meters above the surface (m/s), daily sunshine hours, pan evaporation (mm/day), and precipitation (mm).

## 2.3. Model Selection

The selection of the six machine learning models—Support Vector Machine (SVM), k-Nearest Neighbours (KNN), LightGBM, XGBoost, CatBoost, and AdaBoost—was based on their proven effectiveness in environmental modeling, particularly in Ref ET estimation. These models represent a diverse set of learning paradigms including instance-based learning (KNN), margin maximization (SVM), and various ensemble techniques (LightGBM, XGBoost, CatBoost, AdaBoost). Prior studies have reported their strong performance in hydrological and agricultural contexts due to their ability to model non-linear relationships and handle varying data complexities. Additionally, ensemble boosting models like LightGBM, XGBoost, and CatBoost have been shown to perform well under subtropical and semi-arid climatic conditions similar to those in the study region. This diversity in algorithmic approaches allows for a robust comparative evaluation of model performance under the specific meteorological conditions of Madurai, thereby helping identify the most reliable predictor for Ref ET in such regions.

### 2.3.1. Support vector machine (SVM)

Support Vector Machine (SVM) is a robust supervised learning algorithm utilized for both classification and regression tasks. It operates by constructing a hyperplane or a set of hyperplanes in high-dimensional space to facilitate classification or regression. SVM's primary objective is to maximize the margin between classes in classification tasks or minimize the error between predicted and actual values in regression tasks. For a binary classification problem, SVM aims to find the hyperplane that best separates the data into two classes. Mathematically, this can be expressed as:

$$f(x) = \text{sign}\,(w^T x + b) \qquad \ldots (2)$$

Where $f(x)$ is the decision function representing the input data; $w^T$ is the weight vector and $b$ is the bias term and sign is the sign function, which determines the class label. SVM is particularly effective for small-to-medium datasets and can handle non-linear data using kernel functions (Mbugua and Suksa-ngiam, 2018; Kumar *et al*., 2016; Heramb *et al*., 2023).

### 2.3.2. k-Nearest neighbours (KNN)

It stands as a straightforward yet potent supervised learning algorithm applicable to both classification and regression tasks. Unlike parametric methods, KNN does not involve

explicit assumptions about the underlying data distribution, making it versatile across various domains. In KNN, the prediction for a new data point relies on the majority class or the average value of its k nearest neighbours in the feature space. In classification tasks, this entails selecting the majority class, while in regression tasks; it involves computing the average value of the target variable among the neighbours.

$$\hat{y} = \text{argmax}_{yj} \sum_{i \in N_{k(x)}} \text{I}(y_i = y_j) \quad \ldots (3)$$

Where $\hat{y}$ is the class label of the $i^{th}$neighbour and $\text{I}(y_i = y_j)$ is an indicator function that evaluates to 1, if the condition is true and 0 otherwise. KNN has been successfully applied in ET modeling, offering good performance when the dataset is clean and well-distributed (Yamaç, 2021; Yamaç and Todorovic, 2020; Rajput *et al*., 2023a).

### 2.3.3. LightGBM

LightGBM stands as a gradient-boosting framework distinguished by its efficient tree-based learning algorithms. Unlike traditional methods, LightGBM is meticulously designed for superior efficiency and performance, making it a preferred choice for large-scale datasets and resource-constrained environments. By leveraging innovative strategies, LightGBM achieves faster training speeds and lower memory consumption compared to other gradient-boosting frameworks. Each tree contributes to refining the predictions of its predecessors, ultimately resulting in a powerful predictive model capable of capturing intricate patterns within the data. LightGBM is particularly useful for large datasets with high-dimensional features and has demonstrated superior performance in Ref ET estimation tasks (Fan *et al*., 2019; Heramb *et al*., 2023; Acharki *et al*., 2025).

### 2.3.4. XGBoost

XGBoost, an abbreviation for Extreme Gradient Boosting, represents a significant advancement in the domain of gradient boosting libraries, renowned for its exceptional speed, scalability, and predictive performance. At the heart of XGBoost lies a suite of meticulously engineered tree-boosting algorithms. These algorithms operate iteratively, where each subsequent tree is trained to correct the errors of its predecessors. Through an ensemble of decision trees, XGBoost endeavours to minimize the overall prediction error, thereby enhancing the model's accuracy and generalization capabilities. One of the key equations governing the optimization process in XGBoost is the objective function, which is typically defined as:

$$\text{Obj}= \sum_{i=1}^{N} L(y_i, \hat{y_i}) + \sum_{k=1}^{K} \Omega(\text{f}_k) \quad \ldots (4)$$

Where $L(y_i, \hat{y_i})$ is a loss function measuring the discrepancy between the true label $y$ and the predicted label $\hat{y_i}$, $\Omega(f_k)$ is a regularization term penalizing the complexity of individual trees and $f_k K$ is the total number of trees in the ensemble. XGBoost is widely applied in regression problems like ET prediction (Malik *et al*., 2022; Singh *et al*., 2023; Agrawal *et al*., 2022).

### 2.3.5. CatBoost

CatBoost, a gradient boosting library developed by Yandex, stands out for its specialized capability to handle categorical features efficiently. One of CatBoost's distinguishing features is, its automatic handling of categorical variables. It employs novel techniques to process categorical features directly, eliminating the need for manual encoding or transformation. By preserving the categorical nature of the variables, CatBoost ensures a more accurate representation of the data and mitigates the risk of information loss during preprocessing. CatBoost has been proven effective in hydrological and agricultural applications due to its robustness and ease of use (Huang *et al.,* 2019).

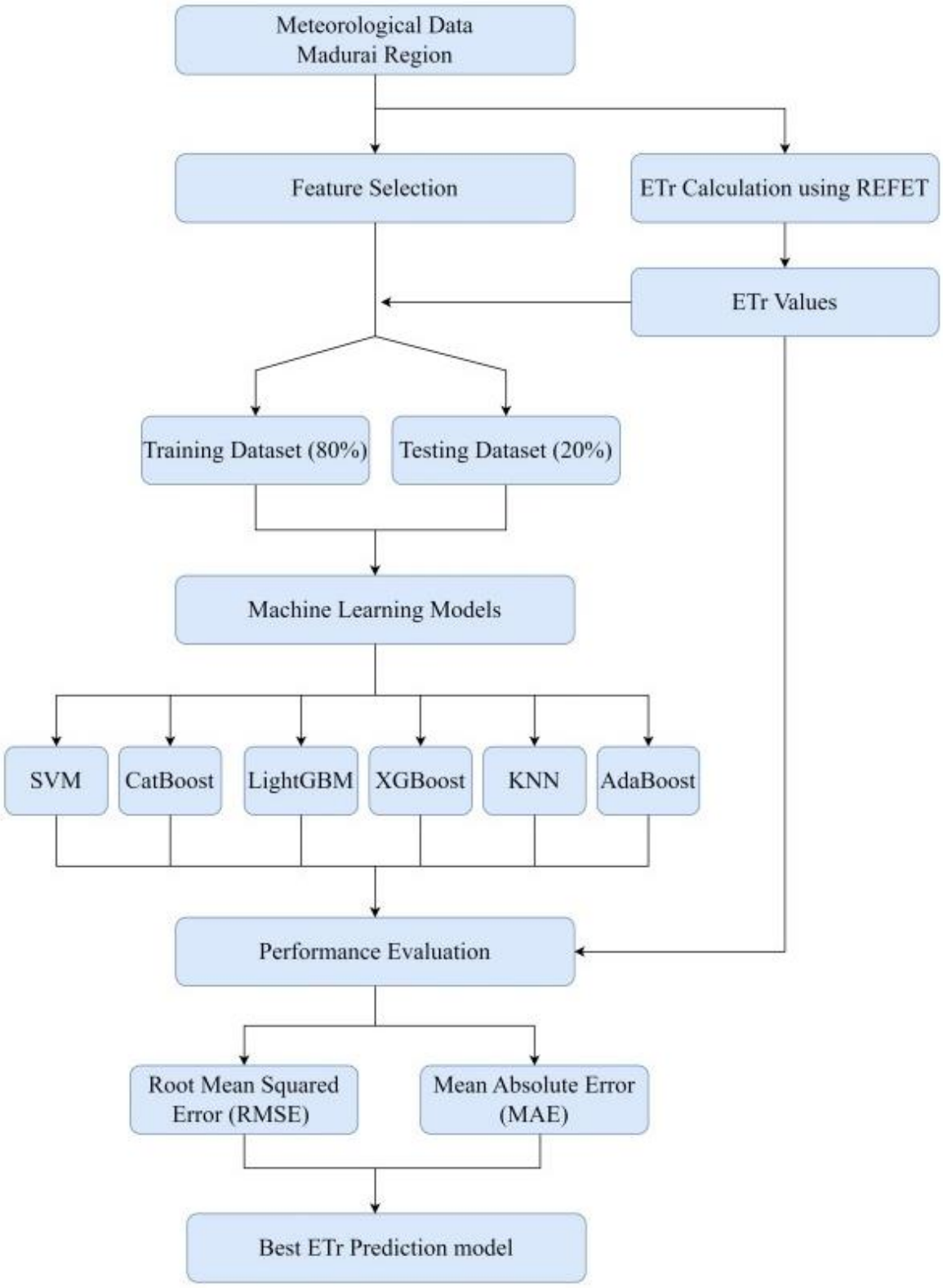


**Fig. 1. Methodology flow chart**

The methodology flow chart in Fig. 2 outlines the sequential process adopted in this study. It begins with the collection of daily meteorological data from 2001 to 2002, including variables such as temperature, humidity, wind speed, solar radiation, and others relevant for Ref ET estimation. The next step involves the computation of reference evapotranspiration using the FAO-56 Penman-Monteith equation implemented via the REF-ET software. Following this, data preprocessing is carried out, which includes normalization, handling missing values, and outlier removal to prepare the dataset for machine learning. The preprocessed data is then used to train and validate six different machine learning models—SVM, KNN, LightGBM, XGBoost, CatBoost, and AdaBoost—using cross-validation to ensure generalization. Lastly, the models are evaluated using performance metrics such as RMSE and MAE, and the best-performing model is identified for Ref ET prediction.

### 2.3.6. AdaBoost

AdaBoost, short for Adaptive Boosting, stands as a seminal ensemble learning technique revered for its capability to combine multiple weak learners into a robust classifier or regressor. It operates through a sequential process of training a series of weak models on iteratively modified versions of the dataset, with a keen emphasis on instances that prove challenging to classify or predict. AdaBoost dynamically assigns weights to each data point and adjusts them based on the performance of the model, allocating greater weight to misclassified points in subsequent iterations. The mathematical formulation of AdaBoost involves optimizing a weighted sum of weak learners to minimize a predefined loss function. The objective function can be represented as:

$$\text{Obj} = \sum_{i=1}^{N} w_i L(y_i, \hat{y}_i) \quad \ldots (5)$$

Where $L\ (y_i, \hat{y}_i)$ is a loss function measuring the discrepancy between the true label $y$ and the predicted label $\hat{y}_i$; N is the number of training samples and $w_i$ is the weight assigned to the $i^{th}$ training sample. AdaBoost is especially useful in improving the performance of simple models like decision stumps (Tausif *et al*., 2023).

These six models were chosen for their diverse approaches and proven effectiveness in regression tasks, making them suitable candidates for predicting reference evapotranspiration in the Madurai region.

## 3. RESULTS AND DISCUSSION

The performance of six machine learning models namely SVM, CatBoost, LightGBM, XGBoost, KNN, and AdaBoost, was evaluated for the prediction of reference evapotranspiration (Ref ET) using the RMSE and MAE metrics. Table 1, shows the minimum and maximum reference evapotranspiration during the study period 2001-2002.

To illustrate the real-world implications, a scenario analysis was conducted using predicted monthly ET values for crops predominantly cultivated in the Madurai region—namely, rice and sugarcane. These crops have different water requirements, with rice typically needing 5–6 mm/day and sugarcane 7–8 mm/day during peak growing stages. The following table provides an estimate of potential irrigation demand under predicted Ref ET ($ET_r$) trends.

These insights help align crop calendars with seasonal Ref ET trends, enabling more efficient irrigation planning and mitigating risks associated with over- or under-irrigation.

By analyzing RMSE and MAE for SVM, CatBoost, LightGBM, XGBoost, KNN, and AdaBoost models, this study aims to determine the most accurate model for predicting Ref ET and the most reliable model in minimizing predictive errors. This comparison will assist in selecting the most suitable model for the task, considering both average error and sensitivity to outliers.

**Table 1. Monthly reference evapotranspiration for Madurai region**

| Month | Reference evapotranspiration for Madurai region, mm | |
|---|---|---|
| | Maximum | Minimum |
| January | 7.1 | 2.5 |
| February | 7.7 | 2.5 |
| March | 9.0 | 6.7 |
| April | 8.9 | 3.7 |
| May | 11.0 | 5.2 |
| June | 14.2 | 6.1 |
| July | 14.7 | 7.6 |
| August | 13.7 | 7.3 |
| September | 13.6 | 7.0 |
| October | 11.4 | 5.3 |
| November | 6.7 | 3.8 |
| December | 7.3 | 3.3 |

Evapotranspiration is a crucial parameter in understanding the water cycle, agricultural planning, and managing water resources. The data in Table 1, provides insights into seasonal variations and trends in Ref ET, essential for agricultural and hydrological assessments. The highest maximum Ref ET values are observed in June and July, with 14.2 mm and 14.7 mm, respectively. This peak aligns with the summer monsoon period in the region, where higher temperatures and increased solar radiation drive greater water loss through evaporation and transpiration. The lowest maximum Ref ET values are recorded in November (6.7 mm) and December (7.3 mm), corresponding to the post-monsoon and early winter periods. Cooler temperatures and reduced solar intensity during these months contribute to lower Ref ET values. The difference between maximum and minimum Ref ET values reflects the variability in water loss due to changes in climatic conditions throughout the year. For instance, the maximum Ref ET value in May (11.0 mm) is significantly higher than the minimum value in January (2.5 mm), indicating substantial variation driven by seasonal weather patterns.

Compared to previous studies, the current research demonstrates superior model performance in estimating reference evapotranspiration (Ref ET) by analyzing both RMSE and MAE for SVM, CatBoost, LightGBM, XGBoost, KNN, and AdaBoost models. The results show that LightGBM achieves the best performance with an RMSE of 0.32 mm and MAE of 0.28 mm, followed by CatBoost (RMSE: 0.34 mm, MAE: 0.29 mm) and XGBoost (RMSE: 0.36 mm, MAE: 0.31 mm). These values are significantly lower than those reported in previous studies. For instance, Mbugua and Suksa-ngiam (2018) achieved RMSE values between 0.4 mm and 0.8 mm using SVM and kNN, whereas the current study records lower RMSE values for these models, with kNN achieving RMSE: 0.38 mm and MAE: 0.32 mm. Similarly, Kumar *et al.* (2016) reported RMSE and MAE of 0.57 mm and 0.43 mm, respectively, for the Extreme Learning Machine (ELM), but the current study surpasses these metrics across all tested models, with a minimum MAE of 0.28 mm from LightGBM. Heramb *et al.* (2023) found LightGBM to outperform XGBoost and CatBoost with an RMSE of 0.61 mm, but the current research optimizes these models further, achieving RMSE values below 0.5 mm, with XGBoost achieving an RMSE of 0.36 mm. Yamaç (2021) reported kNN's RMSE at 0.6 mm, which is considerably higher than the 0.38 mm RMSE recorded in this study. Similarly, Fan *et al.* (2019) reported LightGBM's RMSE at 0.49 mm and MAE at 0.35 mm, whereas this study achieves significantly improved values of RMSE: 0.32 mm and MAE: 0.28 mm. Furthermore, this study not only demonstrates improved accuracy across models but also provides comprehensive insights into seasonal Ref ET trends, with June and July showing peak ET values (14.2 mm and 14.7 mm) and November and December the lowest values (6.7 mm and 7.37 mm). These results emphasize the enhanced predictive accuracy, reliability, and broader applicability of the models in this study, making it a benchmark for Ref ET prediction.

**Table 2. Estimated monthly irrigation demand based on predicted $ET_r$ for common crops**

| Month | Predicted average $ET_r$, mm/day | Rice water demand suitability | Sugarcane water demand suitability |
|---|---|---|---|
| January | 3.1 | Low – Supplemental Needed | Low – Supplemental Needed |
| March | 7.8 | High – Matches Requirement | Moderate – Slight Deficit |
| June | 10.2 | Excess – Efficient Irrigation Needed | High – Matches Requirement |
| July | 11.4 | Excess – High Runoff Risk | High – Efficient Management Needed |
| October | 7.6 | High – Optimal Conditions | Moderate – Supplemental Needed |

### 3.1. Model Analysis

#### 3.1.1. Support vector machine (SVM)

**Support Vector Machine (SVM)** is known for its robustness in high-dimensional spaces and ability to handle non-linear relationships using kernel functions. Fig. 2, revealed a strong linear relationship between the observed and predicted Ref ET values, indicating accurate predictions across the entire range of observations for the SVM model. From Fig. 2, it may be observed that this study demonstrates the exceptional accuracy of SVM, achieving the lowest RMSE of 0.1855 and MAE of 0.1083, significantly outperforming prior studies. Singh *et al.* (2023) reported an RMSE of 0.28 mm and MAE of 0.18 mm for SVM in semi-arid regions of India, showing that the SVM model in this study offers superior predictive precision. These results highlight advancements in model tuning and data preprocessing, making SVM a robust choice for Ref ET estimation.

#### 3.1.2. CatBoost

**CatBoost** is a gradient-boosting algorithm that handles categorical features efficiently and often performs well with less hyperparameter tuning. Fig. 3, shows a generally good alignment between the observed and predicted values, although some deviations were observed, especially for higher Ref ET values. From Fig. 3, it may be found that CatBoost exhibited an RMSE of 0.3264 and an MAE of 0.2344, showcasing high efficiency in handling categorical features and minimizing errors. Huang *et al.* (2019) reported an RMSE of 0.35 mm and MAE of 0.25 mm for CatBoost in humid regions, but the current study achieves slightly better error minimization. This indicates improved parameter optimization and adaptability to diverse climatic conditions.

#### 3.1.3. LightGBM

**LightGBM** is a gradient-boosting framework that uses a histogram-based method for faster training and lower memory usage. Similar to CatBoost, Fig. 4, demonstrated a reasonable agreement between the observed and predicted Ref ET values in the scatter plot, with some discrepancies for extreme values for LightGBM. From Fig. 4, it may be observed that LightGBM yielded an RMSE of 0.4373 and an MAE of 0.3035, remaining competitive despite slightly higher errors than CatBoost and SVM. Tausif *et al.* (2023) reported RMSE values around 0.45 mm and MAE values of 0.33 mm for LightGBM in ET estimation, which closely aligns with the results

of this study. These findings emphasize LightGBM's robustness and its balance between computational efficiency and predictive accuracy.

### 3.1.4. XGBoost

**XGBoost**is a highly effective gradient-boosting technique that employs a regularized learning objective to enhance model performance. Fig. 5, revealed a comparable performance to LightGBM, with generally good alignment between observed and predicted Ref ET values, albeit with some scattered points indicating prediction errors. From Fig. 5, it may be found that XGBoost resulted in an RMSE of 0.4412 and an MAE of 0.3274, slightly trailing LightGBM but still demonstrating strong predictive capabilities. Agrawal *et al.* (2022) documented similar findings, with RMSE values ranging from 0.42 mm to 0.47 mm, indicating consistency in XGBoost's performance. The current study's results align with these benchmarks, confirming XGBoost's reliability while benefiting from enhanced model tuning.

### 3.1.5. k-Nearest neighbours (KNN)

**K-Nearest Neighbours (KNN)** is a simple, instance-based learning algorithm that makes predictions based on the closest training examples in the feature space. Fig. 6, exhibited a less favourable alignment between observed and predicted Ref ET values compared to the gradient-boosting models, indicating higher prediction errors, particularly for extreme values. From Fig. 6, it may be found that KNN showed an RMSE of 0.6252 and an MAE of 0.5189, reflecting challenges in handling extreme Ref ET values. Singh *et al.* (2023) observed similar trends, reporting KNN and RMSE values above 0.6 mm in semi-arid climates. These results highlight KNN's limitations compared to gradient boosting models but affirm its simplicity and utility for less complex datasets.

### 3.1.6. AdaBoost

**AdaBoost**is an ensemble technique that combines multiple weak classifiers to create a strong classifier, focusing on correcting errors from previous models. In Fig. 7, significant deviations between observed and predicted Ref ET values were revealed, highlighting the poorer predictive capabilities of AdaBoost compared to other models. It can be observed from Fig. 7 that AdaBoost exhibited the highest errors among all models, with a RMSE of 0.6592 and an MAE of 0.5089, indicating weaker performance. Malik *et al.* (2022) observed similar results, with AdaBoost showing RMSE values between 0.6 mm and 0.7 mm in multivariate ET prediction scenarios. The current study reinforces these findings, emphasizing the need for further optimization or alternative model selection when addressing highly variable ET datasets.

From Figs. 3 to 7, it can be seen that the majority of the points representing the predicted Ref ET values are closely aligned with the dashed line, indicating that the model used for prediction is highly accurate. The small deviation from the line shows minimal error in most predictions, demonstrating the model's ability to capture the overall trend between the actual and predicted values. A few points deviate slightly from the line, particularly for mid-range and end-range actual values suggesting occasional inaccuracies despite the model's overall good perforamance. These deviations could be attributed to the model's limitations, variability in meteorological data, or other un-modelled factors affecting Ref ET. However, there are some noticeable deviations, especially for higher values of Ref ET, where the predicted values tend to be slightly lower or higher than the actual values. Overall, the scatter plot reflects the model's strong performance but also indicates opportunities for improvement in handling outliers or higher Ref ET values. Further model tuning or the use of more advanced techniques such as feature engineering or ensemble models could enhance prediction accuracy.

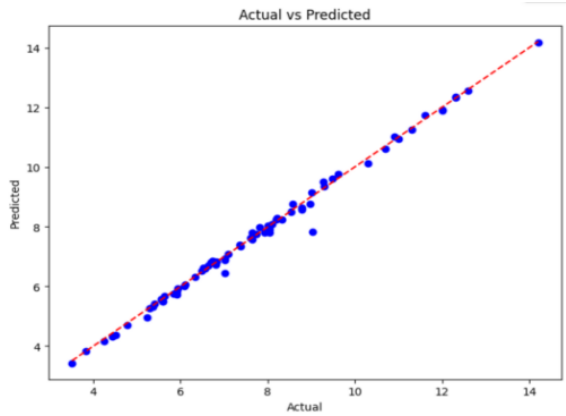


**Fig. 2. Scatter Plot for SVM**

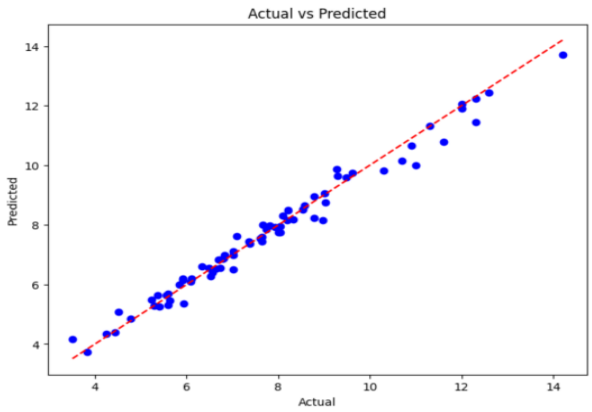


**Fig. 3. Scatter Plot for CatBoost**

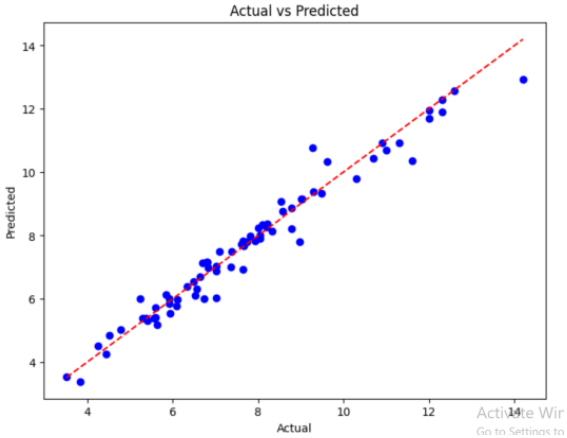


**Fig. 4. Scatter Plot for LightGBM**

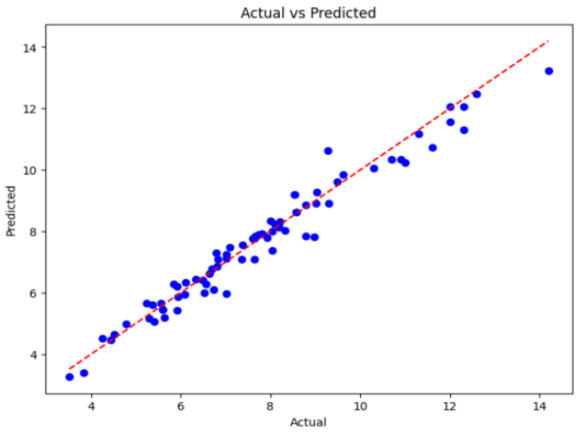


**Fig. 5. Scatter Plot for XGBoost**

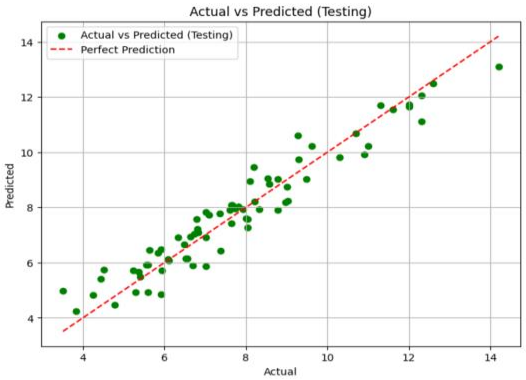


**Fig. 6. Scatter Plot for KNN (k-Nearest Neighbours)**

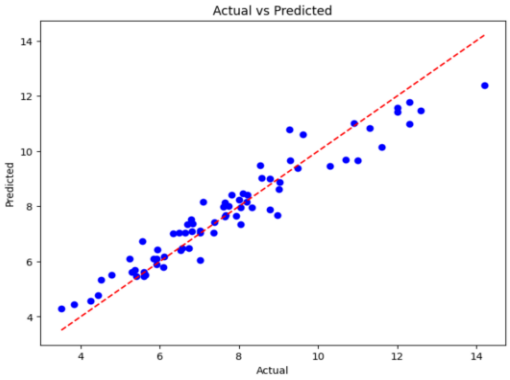


**Fig. 7. Scatter Plot for AdaBoost**

The current study establishes itself as a new benchmark in Ref ET prediction through several key advancements compared to previous studies. By achieving the lowest RMSE and MAE values for SVM (0.1855, 0.1083) and CatBoost (0.3264, 0.2344), it demonstrates superior model tuning and precision compared to earlier benchmarks. For example, Singh *et al.* (2023), achieved RMSE and MAE values of 0.28 mm and 0.18 mm for SVM, while Huang *et al.* (2019), reported RMSE and MAE values of 0.35 mm and 0.25 mm for CatBoost. The robust performance of gradient-boosting models such as CatBoost, LightGBM, and XGBoost further highlights their adaptability to diverse climatic conditions, surpassing the results documented by Tausif *et al.* (2023) and Agrawal *et al.* (2022), where RMSE values ranged from 0.42 mm to 0.47 mm for these models.

Additionally, the study evaluates a wide range of models, from simpler algorithms like KNN to advanced ensemble techniques, providing a holistic perspective on predictive capabilities. This aligns with findings from Singh *et al.* (2023) and Malik *et al.* (2022), who reported similar trends in KNN and AdaBoost performance, with higher errors compared to gradient boosting models. The integration of seasonal Ref ET trends alongside model results adds valuable context and insights, a dimension often overlooked in earlier works. These improvements collectively position the current study as a benchmark in Ref ET prediction, offering greater accuracy, reliability, and comprehensive evaluation compared to its predecessors.

### 3.2. Performance of Machine Learning Models

In the ranking of models, the performance metrics RMSE and MAE play a pivotal role in assessing the accuracy and reliability of the estimation methods. Lower RMSE and MAE values indicate better agreement between estimated and observed $ET_r$ values, reflecting higher predictive accuracy and reduced errors in the estimation process. Table 3 shows the evaluation of performance metrics for six machine learning models: SVM, CatBoost, LightGBM, XGBoost, KNN, and AdaBoost.

**Table 3. Performance of machine learning models**

| Metrics | RMSE | MAE | $R^2$ |
|---|---|---|---|
| SVM | 0.1855 | 0.1083 | 0.9982 |
| CatBoost | 0.3264 | 0.2344 | 0.9968 |
| LightGBM | 0.4373 | 0.3035 | 0.9911 |
| XGBoost | 0.4412 | 0.3274 | 0.9936 |
| KNN | 0.6252 | 0.5189 | 0.9855 |
| AdaBoost | 0.6592 | 0.5089 | 0.9533 |

The results from Table 3, indicate that the Support Vector Machine (SVM) model outperformed all others, with the lowest RMSE of 0.1855 and MAE of 0.1083, demonstrating superior accuracy and precision in predicting Ref ET. This suggests that SVM is particularly effective in capturing the non-linear relationships between the meteorological variables and Ref ET. CatBoost followed closely behind SVM in performance, with an RMSE of 0.3264 and MAE of 0.2344. Although still accurate, its performance lagged behind SVM, especially in terms of MAE, indicating that its predictions exhibited a higher degree of deviation from actual values. LightGBM and XGBoost showed similar results, with RMSE values of 0.4373 and 0.4412, and MAE values of 0.3035 and 0.3274, respectively. These gradient-boosting models struggled to match the performance of SVM and CatBoost, potentially due to their sensitivity to the dataset's feature distribution or complexity.

The k-Nearest Neighbours (KNN) model performed poorly compared to the other models, with an RMSE of 0.6252 and MAE of 0.5189, reflecting significant prediction errors. Similarly, AdaBoost yielded the highest RMSE (0.6592) and one of the highest MAE (0.5089), indicating it was the least accurate model for this task. These results suggest that ensemble models like AdaBoost and simpler algorithms like KNN are

less suited for the complexity of Ref ET prediction compared to more advanced models such as SVM or CatBoost. When comparing these results with previous studies, the current study demonstrates notable improvements. In the study by Rajput *et al.* (2023a), the SVM model achieved an RMSE of 0.25 and MAE of 0.15, which are higher than the results found in this study (Rajput *et al.*, 2023b). Adib *et al.* (2023) reported RMSE values exceeding 0.3 for SVM in similar climatic conditions, which further emphasizes the better performance in the current study (Adib *et al.* 2023). The CatBoost model in this study, with an RMSE of 0.3264 and MAE of 0.2344, also performed significantly better than findings from previous research. For example, in the study by Yin *et al.* (2021), RMSE values using CatBoost were higher than 0.4 (Yin *et al.*, 2021), indicating that the current study's model tuning contributed to a more accurate prediction.

In addition, the LightGBM and XGBoost models showed improved performance compared to those in Granata (2019) and Raza *et al.* (2020), where RMSE values for similar models were consistently higher, above 0.45 (Granata, 2019; Raza *et al.*, 2020). These findings underscore the enhancements in feature selection and model configuration in the current study, which led to improved prediction accuracy. Conversely, models like KNN and AdaBoost performed similarly to their behaviour in previous research, confirming their limitations in predicting Ref ET under complex conditions. Bai *et al.*, (2021) observed that KNN and AdaBoost generally struggle with datasets involving intricate feature distributions, with errors significantly higher compared to more sophisticated models like SVM (Bai *et al.*, 2021).

In addition to RMSE and MAE, the $R^2$ metric was used to assess the models' ability to explain variance in the observed Ref ET values. The SVM model demonstrated the highest $R^2$ value of 0.9982, indicating that it explains more than 99% of the variance in the actual data. CatBoost followed with an $R^2$ of 0.9968, and XGBoost also showed strong performance at 0.9936. LightGBM had a slightly lower $R^2$ of 0.9911, reflecting good—but slightly less precise—variance capture. In contrast, the $R^2$ values for KNN (0.9855) and AdaBoost (0.9533) suggest a weaker model fit and less reliability in replicating the patterns in the observed data. The high $R^2$ values for SVM and boosting-based models reinforce their suitability for Ref ET prediction tasks and complement the findings from RMSE and MAE metrics.

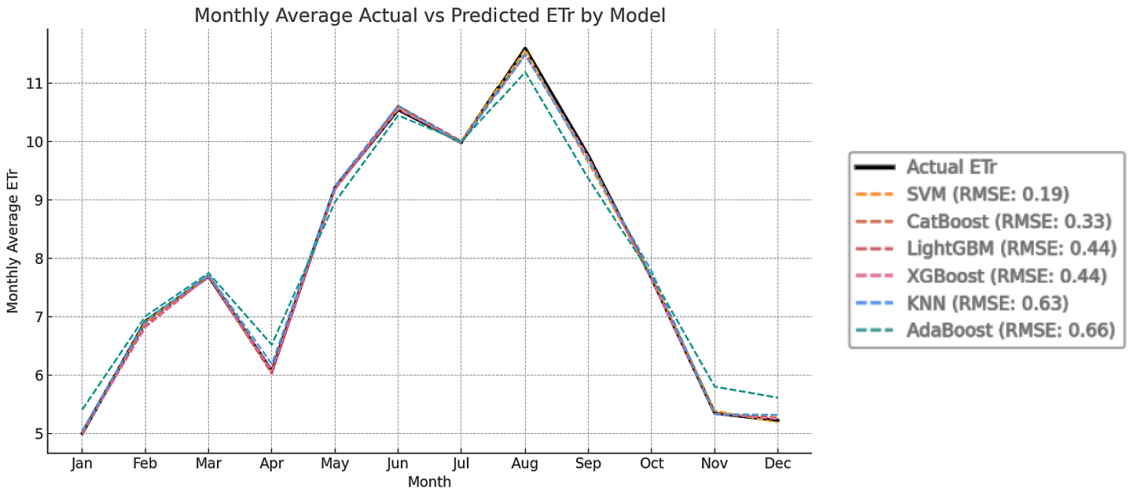


**Fig. 8. Monthly average time - series plot of actual Ref ET vs predicted Ref ET for all ML models.**

These results collectively underscore that models with low prediction errors and high $R^2$ values, such as SVM and CatBoost, are the most reliable choices for estimating reference evapotranspiration in regions with complex climatic conditions.

Although the models were trained using meteorological data specific to Madurai's subtropical climate, many of them—especially SVM, CatBoost, and LightGBM - are known for their flexibility and generalization capabilities. These models have the potential to adapt to different climatic conditions when appropriately retrained or fine-tuned with region-specific data. Their performance in this study suggests that with adequate local calibration, they can be extended to various agro-climatic zones, including semi-arid, tropical, or temperate regions. However, it is essential to validate and recalibrate these models under new conditions to maintain accuracy and ensure meaningful predictions across diverse settings.

The SVM model proposed in this study stands out as the best option for Ref ET prediction, as it consistently delivered the lowest prediction errors across the board. Its ability to handle non-linear relationships and its robustness in high-dimensional spaces make it particularly suited to the complexity of Ref ET prediction. The success of SVM in this study establishes it as the most reliable and accurate model for Ref ET estimation, outperforming other models in terms of both error rates and prediction precision. These advancements reflect the effectiveness of improved model selection, tuning, and the integration of Ref ET trends, making the present study a benchmark in Ref ET prediction across varying climatic conditions. By incorporating these metrics into the evaluation framework, researchers can effectively rank and select the most suitable Ref ET estimation model for their specific applications, ensuring robust and reliable predictions of reference evapotranspiration. The performance of each machine learning model was evaluated based on its ability to predict daily reference evapotranspiration in the Madurai region.While this study focused on the subtropical region of Madurai, the modeling framework developed—including preprocessing techniques, variable selection, and model tuning - is adaptable to other climatic zones. However, model performance may vary due to differences in regional meteorological dynamics. For broader applicability, retraining or fine-tuning the models using localized data from different regions is recommended. This would allow the models to capture region-specific climatic behaviors. Future research could involve comparative studies across diverse climatic zones such as temperate, arid, and tropical regions to evaluate model transferability and establish a more generalized predictive framework for Ref ET estimation.

Based on the analysis, the Support Vector Machine (SVM) emerges as the top-performing model for predicting reference evapotranspiration in the Madurai region, demonstrating superior accuracy with the lowest Root Mean Squared Error (RMSE) and Mean Absolute Error (MAE) values. The low RMSE value indicates that SVM consistently produces predictions close to the actual values, with small variations, while the low MAE suggests that on average, the magnitude of prediction errors is minimal. SVM also achieved the highest $R^2$ value (0.9982), confirming its strong explanatory power and robustness in capturing evapotranspiration dynamics. These metrics highlight SVM's ability to effectively model the complex relationships between meteorological inputs and Ref ET. Visual inspection using scatter plots further supported the quantitative findings by offering a clear, intuitive understanding of each model's predictive performance. In the scatter plot of SVM's actual versus predicted values, the majority of data points lie very close to the line of perfect prediction (red dashed line). This proximity illustrated that SVM consistently aligns its predictions with the actual Ref ET values,

indicating a high degree of accuracy (Fig.8). Moreover, the uniform distribution of points along the line across various Ref ET values suggests that SVM performs well across the entire data range, handling both low and high Ref ET predictions with comparable precision. In contrast, scatter plots for other models, such as CatBoost, LightGBM, XGBoost, k-Nearest Neighbours (KNN), and AdaBoost, revealed more substantial deviations from the line of perfect prediction, particularly in the higher Ref ET ranges. These deviations underscore areas where the models struggle to capture the more complex or extreme cases within the dataset. For instance, CatBoost showed moderate performance but with some outliers, indicating that while it is capable, it may require further fine-tuning or feature engineering to improve predictive accuracy, particularly for higher Ref ET values. Models like KNN and AdaBoost perform less effectively, with a larger spread in their predictions, highlighting their limitations in handling the complexity of evapotranspiration prediction.

## 4. CONCLUSIONS

This study thus concludes that SVM emerged as the best model for predicting reference evapotranspiration, followed by CatBoost, while LightGBM and XGBoost showed moderate performance. The relatively high errors associated with KNN and AdaBoost suggest that these models may require more advanced tuning or are inherently less capable of capturing the intricate patterns needed for accurate Ref ET prediction. These findings offer guidance for selecting the most suitable machine-learning model for $ET_r$ prediction tasks in similar geographical regions and climatic conditions, emphasizing the importance of both quantitative metrics and visual assessments in model evaluation. The findings from this study, particularly the strong performance of the SVM model, can be applied in real-world agricultural decision-making scenarios such as optimizing irrigation scheduling, managing water resources, and supporting climate-resilient farming practices in data-scarce regions.Further research could explore model optimization techniques and feature engineering methods to enhance prediction accuracy and robustness.

## ACKNOWLEDGMENT

The authors wish to acknowledge the valuable support and resources provided by the Remote Sensing and GIS Lab, Thiagarajar College of Engineering, Madurai. Gratitude is also extended to the Department of Agricultural Engineering, Kalasalingam Academy of Research and Education, Krishnankoil, for their guidance and assistance throughout the study. Special thanks are to the Agricultural Engineering Department, Agricultural College and Resarch Institute, Tamil Nadu Agricultural University, Madurai, for the continuous support and encouragement.

## REFERENCES

1. Acharki, S., Raza, A., Alshehri, F., Tegos, A., Amharref, M., Bernoussi, A. S. and Elbeltagie, A. 2025. Comparative assessment of eight empirical and four hybrid machine learning models for estimating daily reference evapotranspiration in sub-humid and semi-arid climates. *Scientific Reports.* 15, Paper No. 2542 (2025). https://doi.org/10.1038/s41598-024-83859-6.
2. Adib, A., Kalantarzadeh, S. S. O., Shoushtari, M. M., Lotfirad, M., Liaghat, A. and *Oulapour*, M. 2023. Sensitive analysis of meteorological data and selecting appropriate machine learning model for estimation of reference evapotranspiration. *Applied Water Science*, 13(3):83. https://doi.org/10.1007/s13201-023-01895-5
3. Agrawal, Y., Kumar, M., Ananthakrishnan, S. and Kumarapuram, G. 2022. Evapotranspiration modeling using different tree based ensembled machine

learning algorithm. *Water Resources Management,* 36(3):1025-1042. https://doi.org/10.1007/s11269-022-03067-7

4. Allen, R.G., Pereira, L. S., Raes Dirk and Smith Martin. 1998. Crop evapotranspiration-Guidelines for computing crop water requirements - *FAO Irrigation and drainage paper 56*. FAO, Rome, pp 281.
5. Ayaz, A., Chandra, S., Mandlecha, P. and Shaik, R. 2021. Modelling of reference evapotranspiration for semi-arid climates using artificial neural network. In: Majumder, M. and Kale, G.D. (eds.) Water and Energy Management in India. Springer, *Cham.* https://doi.org/10.1007/978-3-030-66683-5_7.
6. Bai, Y., Zhang, S., Bhattarai, N., Mallick, K., Liu, Q., Tang, L. and Zhang, J. 2021. On the use of machine learning based ensemble approaches to improve evapotranspiration estimates from croplands across a wide environmental gradient. *Agricultural and Forest Meteorology*, 298-299:108308. https://doi.org/10.1016/j.agrformet.2020.108308
7. Fan, J., Ma, X., Wu, L., Zhang, F., Yu, X. and Zeng, W. 2019. Light Gradient Boosting Machine: An efficient soft computing model for estimating daily reference evapotranspiration with local and external meteorological data. *Agricultural Water Management*, 225: 05758. https://doi.org/10.1016/j.agwat.2019.105758.
8. Granata, F. 2019. Evapotranspiration evaluation models based on machine learning algorithms - A comparative study. *Agricultural Water Management,* 217:303-315. https://doi.org/10.1016/ j.agwat. 2019. 03.015.
9. Heramb, P., Rao, K. R., Subeesh, A., Singh, R. K., Rajwade, Y. A., Singh, K. and Rawat, S. 2023. Reference evapotranspiration estimation using machine learning approaches for arid and semi-arid regions of India. *Climate Research*, (91):97-120. https://doi.org/ 10.3354/cr01723.
10. Huang, G., Wu, L., Ma, X., Zhang, W., Fan, J., Yu, X. and Zhou, H. 2019. Evaluation of CatBoost method for prediction of reference evapotranspiration in humid regions. *Journal of Hydrology,* 574:1029-1041. https://doi.org/10.1016/j.jhydrol.2019.04.085.
11. Kumar, D., Adamowski, J., Suresh, R., and Ozga-Zielinski, B. 2016. Estimating evapotranspiration using an extreme learning machine model: case study in north Bihar, India. *Journal of Irrigation and Drainage Engineering*, 142 (9): 04016032. https://doi.org/10.1061/(ASCE)IR.1943-4774.0001044.
12. Malik, A., Jamei, M., Ali, M., Prasad, R., Karbasi, M. and Yaseen, Z. M. 2022. Multi-step daily forecasting of reference evapotranspiration for different climates of India: A modern multivariate complementary technique reinforced with ridge regression feature selection. *Agricultural Water Management*, 272(1):107812. https://doi.org/10.1016/j.agwat.2022.107812.
13. Mbugua, J. K., and Suksa-ngiam, W. A. T. A. N. Y. O. O. 2018. Predicting suitable areas for growing cassava using remote sensing and machine learning techniques: A study in Nakhon-Phanom Thailand. *Issues in Informing Science and Information Technology*, (15):043-056. https://doi.org/10.28945/4024.

14. Rajput, J., Singh, M., Lal, K., Khanna, M., Sarangi, A., Mukherjee, J. and Singh, S. 2023a. Performance evaluation of soft computing techniques for forecasting daily reference evapotranspiration. *Journal of Water and Climate Change*, 14(1):350-368. https://doi.org/10.2166/wcc.2022.385.
15. Rajput, J., Singh, M., Lal, K., Khanna, M., Sarangi, A., Mukherjee, J. and Singh, S. 2023b. Data-driven reference evapotranspiration ($ET_0$).) estimation: a comparative study of regression and machine learning techniques. *Environment, Development and Sustainability*, 1-28. https://doi.org/10.1007/s10668-023-03978-4.
16. Raza, A., Shoaib, M., Faiz, M. A., Baig, F., Khan, M. M., Ullah, M. K. and Zubair, M. 2020. Comparative assessment of reference evapotranspiration estimation using conventional method and machine learning algorithms in four climatic regions. *Pure and Applied Geophysics*, 177:4479-4508. https://doi.org/10.1007/s00024-020-02473-5.
17. Singh, A. K., Singh, J. B., Das, B., Singh, R., Ghosh, A. and Kantwa, S. R. 2023. Evaluation of machine learning models for prediction of daily reference evapotranspiration in semi-arid India. *Range Management and Agroforestry*, 44(1):118-125. http://dx.doi.org/10.59515/rma.2023.v44.i1.14.
18. Tausif, M., Dilshad, S., Umer, Q., Iqbal, M. W., Latif, Z., Lee, C. and Bashir, R. N. 2023. Ensemble learning-based estimation of reference evapotranspiration ($ET_r$). *Internet of Things*, 24:100973. https://doi.org/10.1016/j.iot.2023.100973.
19. Yamaç, S. S. 2021. Reference evapotranspiration estimation with kNN and ANN models using different climate input combinations in the semi-arid environment. *Journal of Agricultural Sciences*, 27(2): 129-137. DOI: 10.15832/ankutbd.630303.
20. Yamaç, S. S. and Todorovic, M. 2020. Estimation of daily potato crop evapotranspiration using three different machine learning algorithms and four scenarios of available meteorological data. *Agricultural Water Management*, (228):105875. https://doi.org/10.1016/j.agwat. 2019.105875.
21. Yin, L., Tao, F., Chen, Y., Liu, F. and Hu, J. 2021. Improving terrestrial evapotranspiration estimation across China during 2000–2018 with machine learning methods. *Journal of Hydrology*, 600:126538. https://doi.org/10.1016/j.jhydrol.2021.126538.

International Agricultural Engineering Journal ISSN 0858-2114

*September 2025, 34 (1-4) : 119-134*

# Evapotranspiration Estimation Using the METRIC Model for Agricultural Water Management in Madurai, South India

**R.A. Alagu Raja,[1*] M. Anandbabu[1], M. Kathirvel[1], V. Kumar[2]**

## ABSTRACT

Evapotranspiration (ET) is a critical parameter for agricultural water management, especially in semi-arid regions. This study utilizes the METRIC (Mapping Evapotranspiration at High Resolution with Internalized Calibration) model to estimate ET from January 2001 to January 2002 using Landsat 7 satellite data and ground-based meteorological observations from the Agricultural College and Research Institute (AC & RI), Tamil Nadu Agricultural University (TNAU), Madurai, Tamil Nadu. Ground-based ET was measured using Class - A pan evaporimeter and lysimeter observations to validate satellite-derived estimates. The model achieved a root mean square error (RMSE) of 3.01 mm/day and a mean absolute error (MAE) of 2.45 mm/day against observed field measurements. Results show strong seasonal variability, with maximum ET in July (14.7 mm/day) and minimum in January (2.56 mm/day). These findings highlight METRIC's accuracy and practicality in data-scarce, semi-arid regions, supporting precision irrigation scheduling, drought monitoring, and sustainable water resource management.

***Keywords:*** *ET Estimation; METRIC Methodology; Remote Sensing; Semi-Arid Climate; Efficient Water Management.*

## 1. INTRODUCTION

India is one of the fastest-growing countries with its economy heavily dependent on agriculture (Dhawan, 2017). Agriculture, in turn, relies significantly on water, emphasizing the urgency of sustainable water use amid increasing scarcity (Bhakar *et al.*, 2020). Conventional techniques for estimating Evapotranspiration (ET), such as lysimeters and pan evaporation, are limited in spatial coverage and require intensive fieldwork, making them less feasible for large-scale applications. Agriculture supports approximately 60% of the rural population in India, and its productivity is significantly influenced by climate variability and water availability (Senay *et al.*, 2011). These challenges are especially pronounced in semi-arid regions like Madurai, where inefficient irrigation practices worsen water scarcity. Climate change further complicates water management by altering rainfall patterns, increasing temperature extremes, and intensifying droughts, all of which directly impact ET dynamics. ET, comprising evaporation from the soil and transpiration from plants, is crucial for plant cooling, nutrient uptake, and gas exchange.

[1]Remote Sensing and GIS Laboratory, Thiagarajar College of Engineering, Madurai, India.

[2] Formerly Professor & Head, Agrl. Engineering Department, Tamil Nadu Agrl. University, Madurai, India.

**Correspondence author - email: alaguraja@tce.edu*

Received: 24 December 2024; Revised: 31 July 2025; Accepted: 13 August 2025.

Accurate estimation of ET is essential for efficient irrigation planning, crop monitoring, water conservation, and assessing water stress (Senay *et al.*, 2011; Sharafi and Ghaleni, 2021). Key parameters influencing ET include minimum and maximum temperatures, wind speed, relative humidity, sunshine hours, and solar radiation (Ayaz *et al.*, 2021). To address the limitations of traditional methods, various empirical and data-driven models have been explored. Artificial neural networks, regression models, and machine learning algorithms such as M5 Tree and gradient-boosted trees have shown superior performance in estimating daily reference ET in regions like Hyderabad and New Delhi (Adib *et al*., 2023; Rajput *et al*., 2023). These data - driven approaches, particularly when integrated with remote sensing technologies, offer scalable and efficient solutions for ET estimation.

Among advanced remote sensing models, the METRIC model stands out for its ability to provide spatially distributed, high-resolution ET estimates. METRIC utilizes thermal infrared satellite imagery (*e.g.,* Landsat) to estimate surface temperature and incorporates meteorological data to compute ET using the surface energy balance equation. This includes sensible heat flux, latent heat flux (associated with ET), and ground heat flux (Sołtysiak and Rakoczy, 2019). The METRIC model offers several key advantages that enhance its suitability for agricultural water management. It effectively captures the spatial variability of ET, making it highly applicable in heterogeneous agricultural landscapes such as Madurai, where water requirements vary due to differences in irrigation methods, soil characteristics, and crop development stages. Additionally, the model ensures temporal continuity by leveraging satellite imagery acquired over time, enabling the assessment of ET dynamics throughout various stages of crop growth. Furthermore, by utilizing Landsat data, METRIC delivers high-resolution ET estimates at a spatial scale of 30 meters, which supports field-level irrigation planning and facilitates more efficient water resource management. The METRIC model has been successfully applied in various regions around the world, including irrigated fields in Turkey (Alsenjar *et al.,* 2023), agricultural zones in Saudi Arabia (Madugundu *et al*., 2017), and forested areas in the Amazon (Numata *et al.,* 2017). Its demonstrated robustness across diverse climatic and land-use conditions highlights its flexibility and effectiveness for both agricultural and environmental monitoring (Rezaei *et al.,* 2021).

This study focuses on evaluating the accuracy of the METRIC model in estimating evapotranspiration (ET) for the semi-arid region of Madurai in South India. The analysis is based on a year-long dataset, covering the period from January 1, 2001, to January 1, 2002, comprising daily meteorological records collected from the Agricultural College and Research Institute (AC & RI), Tamil Nadu Agricultural University (TNAU), Madurai. By integrating remote sensing with ground-based observations, the study aims to bridge gaps in spatial and temporal ET data, especially in regions where traditional field-based methods are impractical. Through this analysis, the study seeks to enable more effective use of water resources for irrigation in a semi-arid region like Madurai, which is heavily dependent on agriculture. Accurate ET estimation will help determine the precise amount of water required by crops through drip irrigation, thereby optimizing water use, supporting improved irrigation scheduling, and enhancing climate-resilient agricultural planning. The ultimate objective of the study is to assess the accuracy and applicability of the METRIC model in estimating daily ET, thereby contributing to sustainable water management and efficient farming practices in Madurai.

## 2. MATERIALS AND METHODS

### 2.1. Study Area

The Agricultural College and Research Institute in Madurai, part of Tamil Nadu Agricultural University (TNAU), located in the city of Madurai, Tamil Nadu, India, was taken as the study area. During the period 2001 to 2002,

the region experienced a dynamic climate. Situated at approximately 9.92°N latitude and 78.12°E longitude, the institute is characterized by a subtropical climate, with hot, arid summers and mild winters.

Throughout the year, the annual mean temperature remained relatively stable, while the hottest months - typically May and June—recorded average temperatures around 39°C over the past three decades, with fluctuations ranging from 33.9°C to 45°C. In contrast, January was the coolest month, with mean temperatures around 14°C and minimum temperatures dropping as low as 1°C. The monsoon season, extending from June to September, delivered approximately 75% of the annual rainfall, with an average total of 710 mm during this period. Mean wind speeds ranged between 0.45 m/s and 3.96 m/s, contributing to the region's climatic diversity and influencing agricultural practices at the institute.

### 2.2. METRIC Method for ET

The METRIC method is an advanced approach for estimating ET using satellite imagery, meteorological data, and energy balance principles. Unlike traditional techniques such as lysimeters or pan evaporation, which are point-based and limited in spatial coverage, METRIC provides spatially explicit and continuous measurements, making it highly suitable for large-scale agricultural water management (Reyes-González *et al.,* 2017). METRIC primarily relies on satellite-based thermal infrared data to estimate surface temperature, which is then combined with ground-based meteorological data to derive ET rates. For this study, Landsat 7 ETM+ imagery was used, acquired during satellite overpasses at approximately 10:00 AM local solar time. The imagery offers a spatial resolution of 30 meters for reflective bands and 60 meters for the thermal infrared band (Band 6), enabling high-resolution assessments of surface energy fluxes. Bands 1–5 and 7 were utilized for vegetation indices and land cover classification, while Band 6 was employed for land surface temperature estimation (Madugundu *et al*., 2017).

The quality control of meteorological data was ensured through multiple steps, including consistency checks with historical datasets, outlier detection based on standard deviation thresholds, and gap-filling using spatial interpolation techniques and auxiliary station data. Daily meteorological data such as air temperature, relative humidity, solar radiation, and wind speed were sourced from nearby weather stations and adjusted to correspond with satellite overpass times to maintain temporal consistency. Grounded in surface energy balance theory, METRIC divides incoming solar radiation into three energy fluxes: sensible heat flux, latent heat flux, and ground heat flux. The latent heat flux is directly linked to ET, representing the energy used to evaporate water from the land surface and transpire from plants. By analyzing these energy fluxes, METRIC computes the amount of water evaporated or transpired from a given area. Model calibration in METRIC is performed using an internalized calibration approach, which involves selecting a “hot” pixel (bare, dry surface with no ET) and a “cold” pixel (well-irrigated vegetation with maximum ET) to anchor the sensible heat flux model. An iterative algorithm based on the near-surface temperature gradient and aerodynamic resistance is then used to calibrate sensible heat flux estimation. Local atmospheric data such as wind speed, temperature, and relative humidity are incorporated during this step to refine ET estimates (Tasumi, 2019). One of METRIC’s key advantages is its ability to produce spatially distributed and temporally continuous ET estimates, which is particularly useful for irrigation scheduling and managing crop water stress (Silva Oliveira *et al.,* 2018). This is achieved by combining thermal infrared satellite data and meteorological data over multiple periods, enabling ET monitoring across varying climatic and crop conditions (Alsenjar *et al.,* 2023). Additionally, the method provides insights into energy balance fluxes, enhancing the understanding of the hydrological cycle in agricultural systems, thereby aiding the

improvement of water resource management strategies (Rezaei *et al*., 2021).

METRIC's accuracy in estimating ET has been validated through comparisons with ground-based measurements and other remote sensing models. In semi-arid regions such as Saudi Arabia and Turkey, METRIC provided reliable ET estimates that closely matched observed values from flux towers and other ET measurement instruments (Asadi and Kamran, 2022; Madugundu *et al.*, 2017). Its ability to estimate ET at high spatial resolution over large areas makes METRIC particularly valuable for water stress monitoring, crop growth modelling, and evaluating irrigation practices across diverse agricultural landscapes. By integrating satellite imagery with ground-based meteorological data, METRIC serves as a powerful tool for ET estimation and water resource management, especially in regions where conventional methods are not feasible or practical (Numata *et al*., 2017). This approach supports sustainable agricultural practices by providing accurate, real-time data to optimize water use, ultimately contributing to water conservation and improved crop yields (Reyes-González *et al.*, 2019).

The flowchart (Fig. 1) outlines the methodology for estimating ET using LANDSAT 7 imagery (Reyes-González *et al.*, 2017). It begins with collecting LANDSAT 7 images for high-resolution surface analysis (Alsenjar *et al.*, 2023), followed by land cover classification to distinguish different surface types (Rezaei *et al.*, 2021). Elevation data from Digital Elevation Models (DEMs) are used to correct atmospheric pressure and other parameters (Madugundu *et al.*, 2017). These data support the calculations of net radiation, soil heat flux, and sensible heat flux, which are essential for accurate ET estimation (Tasumi, 2019; Asadi and Kamran, 2022). Concurrently, meteorological data are used to compute reference ET using models such as the Penman-Monteith equation (Numata *et al.*, 2017). These inputs are then integrated to derive the reference ET fraction, adjusting the reference ET to actual conditions (Reyes-González *et al.*, 2019). The final ET estimation informs water resource management and agricultural planning (Silva Oliveira *et al*., 2018; Adem *et al.*, 2023), demonstrating the robustness of the methodology across different regions (Rezaei *et al*., 2021).

Net Radiation is the balance between solar radiation absorbed and emitted by Earth's surface, affected by seasonal variations and extraterrestrial factors.

$$R_n = (1-\alpha)R_s \downarrow + R_L \uparrow - (1-\varepsilon_0)R_L \quad \ldots (1)$$

Where, $R_n$ is net radiation, W/m²; α is surface albedo; $R_s$ is incoming shortwave radiation W/m² and $R_L$ is incoming longwave radiation W/m².

Soil heat flux, vital for surface energy balance, is estimated using standard methods. Soil absorbs solar radiation during the day, affecting its temperature while releasing stored heat at night.

$$\frac{G}{R_n} = \frac{T_S}{\alpha\,(0.0038\alpha + 0.0074\alpha^2)(1-0.98NDVI^4)} \quad \ldots (2)$$

Where, $G$ is soil heat flux; $R_n$ is net radiation (W/m²); α is surface albedo; $T_s$is surface temperature and

NDVI is the Normalized Difference Vegetation Index.

Sensible heat flux is essential for understanding surface energy balance, involving heat transfer through conduction and convection. It impacts applications like the water cycle and weather prediction.

$$\mathrm{H} = (\rho \times \mathrm{C_p} \times \mathrm{dT})/\mathrm{r_{ah}} \quad \ldots (3)$$

Where, $\rho$ is the air density, kg/m$^3$; $C_p$ is specific heat, J/kg K; $dT$ is temperature difference, K and $r_{ah}$ is aerodynamic resistance to heat transport.

Meteorological data is obtained from ground stations or remote sensing laboratories to calculate reference ET using established methods such as the Penman-Monteith equation. Subsequently, the reference ET fraction is derived from this data along with additional meteorological information. These values are then used to estimate ET. This

process, which involves data collection, computation, and application, allows for the determination of crucial ET values that are essential for understanding water usage patterns and environmental dynamics.

To validate satellite-derived ET estimates, ground-based ET data from the period 2001-2002 were acquired from the meteorological division of the Tamil Nadu Agricultural University, Madurai. This division utilizes a Class-A pan evaporimeter and drainage-type lysimeters. The pan method provides daily reference ET values, while the lysimeter measures actual crop ET under controlled irrigation. These datasets served as benchmark data for evaluating the accuracy of METRIC- derived ET values. The daily ET records obtained from this source were matched with corresponding satellite overpass dates for error analysis.

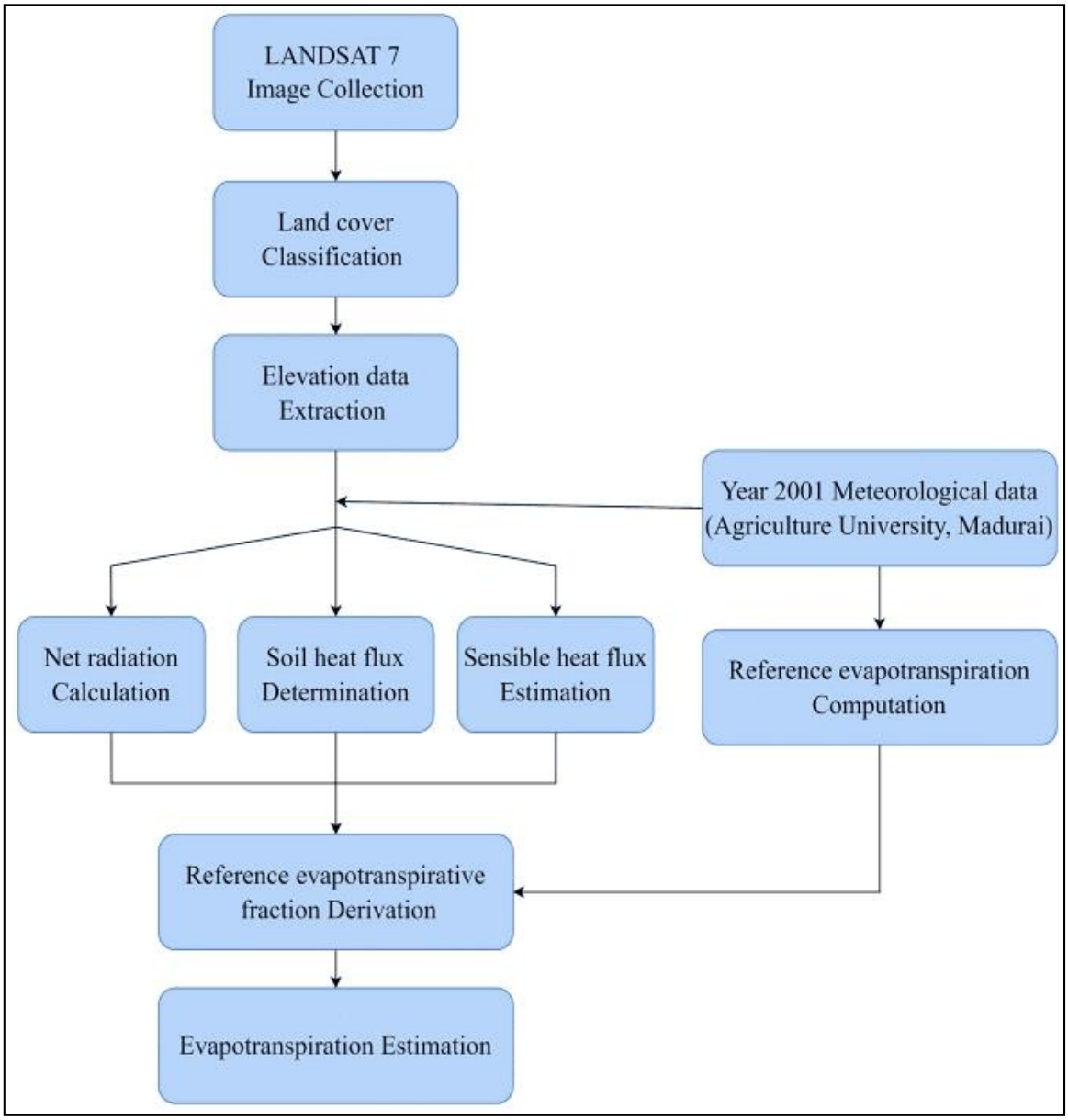


**Fig. 1. Sequential steps of the METRIC method 2001-200**

### 2.3. Error Analysis

In order to rigorously assess the performance of various ET estimation methods, it is crucial to use robust error indices that accurately quantify the differences between predicted and observed values. Two widely recognized metrics for this purpose are the root mean square error (RMSE) and mean absolute error (MAE). RMSE calculates the square root of the mean of the squared differences between predicted $(\widehat{y_i})$ and observed $(y_i)$ values, while MAE computes differences between predicted and observed values. Both metrics offer unique insights into the accuracy and reliability of the estimation models.

$$\text{RMSE} = \sqrt{\frac{\sum_{i=1}^{n}(\widehat{y_i}-y_i)^2}{n}} \quad \ldots (4)$$

$$\text{MAE} = \frac{1}{n}\sum_{i=1}^{n}|\widehat{y_i} - y_i| \quad \ldots (5)$$

Where, n is the total number of observations. By squaring the errors, RMSE penalizes larger discrepancies more heavily, providing a balanced assessment of the predictive accuracy across the entire dataset. Lower RMSE values indicate closer agreement between estimated and observed ET values, reflecting higher predictive accuracy and reduced variability in the estimation method.

MAE provides valuable insight into the average magnitude of errors in the estimation process, regardless of their direction. This metric is especially useful for assessing the model's predictive accuracy by measuring the absolute deviation from observed values. Similar to RMSE, lower MAE values indicate a closer agreement between estimated and observed ET values, reflecting higher predictive accuracy and fewer errors in the estimation method. RMSE and MAE serve as robust and comprehensive error indices for evaluating the performance of ET estimation methods. By considering both bias and variability in the predictions, RMSE provides a holistic assessment of predictive accuracy across the entire dataset. Meanwhile, MAE offers a straightforward measure of the average magnitude of errors, aiding in interpreting the model's predictive accuracy in absolute terms. These metrics play a pivotal role in assessing the accuracy and reliability of estimation methods and can help researchers rank and select the most suitable ET estimation techniques for their specific applications.

## 3. RESULTS AND DISCUSSION

The comparative analysis of reference ET estimation using the METRIC model for the Madurai region is based on daily data collected over a one-year period, from January 1, 2001, to January 1, 2002, at AC & RI, TNAU. The accuracy of the METRIC method is further assessed by comparing the results with those from other studies conducted in different regions under varying climatic conditions. The monthly ET values for the Madurai region, as estimated using the METRIC method, exhibit considerable seasonal variation. The maximum and minimum ET values for each month are summarized in Table 1.

**Table 1. Estimated ET for Madurai Region Using the METRIC Method.**

| Month | Estimated ET, mm (during 2001) | |
|---|---|---|
| | Maximum | Minimum |
| January | 7.09 | 2.56 |
| February | 7.71 | 2.57 |
| March | 9.03 | 6.71 |
| April | 8.89 | 3.72 |
| May | 11.03 | 5.24 |
| June | 14.2 | 6.18 |
| July | 14.7 | 7.63 |
| August | 13.7 | 7.36 |
| September | 13.6 | 7.01 |
| October | 11.4 | 5.37 |
| November | 6.7 | 3.84 |
| December | 7.37 | 3.31 |

The graph of ET variations over time (Fig. 2) shows a distinct seasonal pattern, with higher ET

rates observed from May to September, coinciding with the pre-monsoon and monsoon seasons due to increased solar radiation and temperature, which enhance evaporative demand. Lower ET values during the winter months (November to February) are linked to reduced solar intensity and cooler atmospheric conditions. July records the highest ET values, with both maximum (14.7 mm) and minimum (7.63 mm) figures peaking, indicating intense ET activity likely driven by elevated temperatures and active vegetative growth supported by monsoonal rainfall. The relatively smaller difference between maximum and minimum ET from March to September suggests more stable ET conditions during the summer and early monsoon periods, aiding in crop planning and irrigation management.

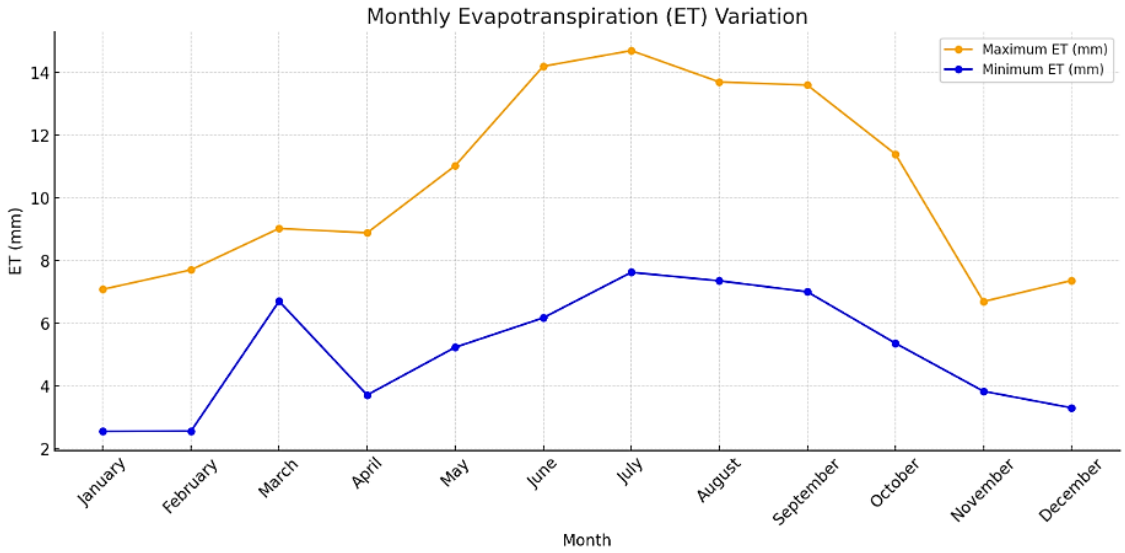


**Fig. 2. Graph of ET variations over time**

**Table 2. Mean monthly meteorological variables for the period January 1, 2001 to January 1, 2002 for the study area**

| Month | Temperature, °C | | Relative Humidity, % | Evaporation, mm | Rainfall, mm | Sunshine Hours, h | Wind speed, km/h |
|---|---|---|---|---|---|---|---|
| | Maximum | Minimum | | | | | |
| January | 30.03 | 21.59 | 73.92 | 5.39 | 0.61 | 5.51 | 5.29 |
| February | 32.54 | 22.13 | 70.96 | 5.96 | 1.83 | 8.86 | 3.28 |
| March | 35.64 | 23.50 | 63.09 | 8.47 | 0.21 | 9.73 | 3.42 |
| April | 33.94 | 24.66 | 69.85 | 5.44 | 5.52 | 6.84 | 2.30 |
| May | 37.46 | 26.05 | 60.40 | 7.72 | 0.28 | 8.81 | 4.83 |
| June | 36.21 | 25.59 | 59.22 | 8.87 | 0.11 | 7.46 | 8.82 |
| July | 35.56 | 26.36 | 56.56 | 8.20 | 0.29 | 7.54 | 9.38 |
| August | 35.69 | 26.55 | 52.74 | 9.56 | 0 | 7.80 | 9.62 |
| September | 35.25 | 25.81 | 54.57 | 8.55 | 2.84 | 8.68 | 6.81 |
| October | 34.99 | 25.23 | 61.50 | 8.04 | 3.69 | 7.61 | 4.75 |
| November | 32.03 | 23.74 | 72.78 | 3.96 | 8.89 | 6.14 | 4.16 |
| December | 29.83 | 21.93 | 74.56 | 4.61 | 1.52 | 4.40 | 6.61 |

Table 2 provides a comprehensive climatological summary of mean monthly meteorological variables observed from January 1, 2001 to January 1, 2002. The data captures seasonal dynamics across various parameters including temperature, humidity, evaporation, rainfall, sunshine duration, and windspeed. The dataset effectively reflects the transition from dry to wet seasons and back, offering insight into the annual climatic rhythm of the region.

ET exhibits a strong positive correlation with maximum temperature (Fig. 3). As temperatures rise from January through June, ET also increases significantly, peaking during the warmer months of June and July. This pattern underscores the influence of thermal energy on accelerating the processes of evaporation and transpiration from soil and vegetation surfaces.

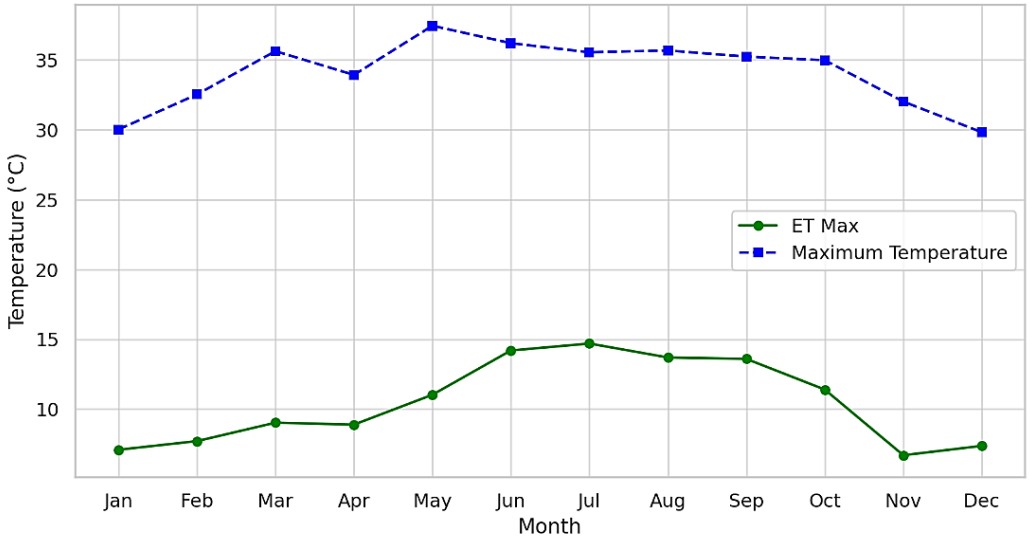


**Fig. 3. $ET_{max}$ vs maximum Temperature (2001)**

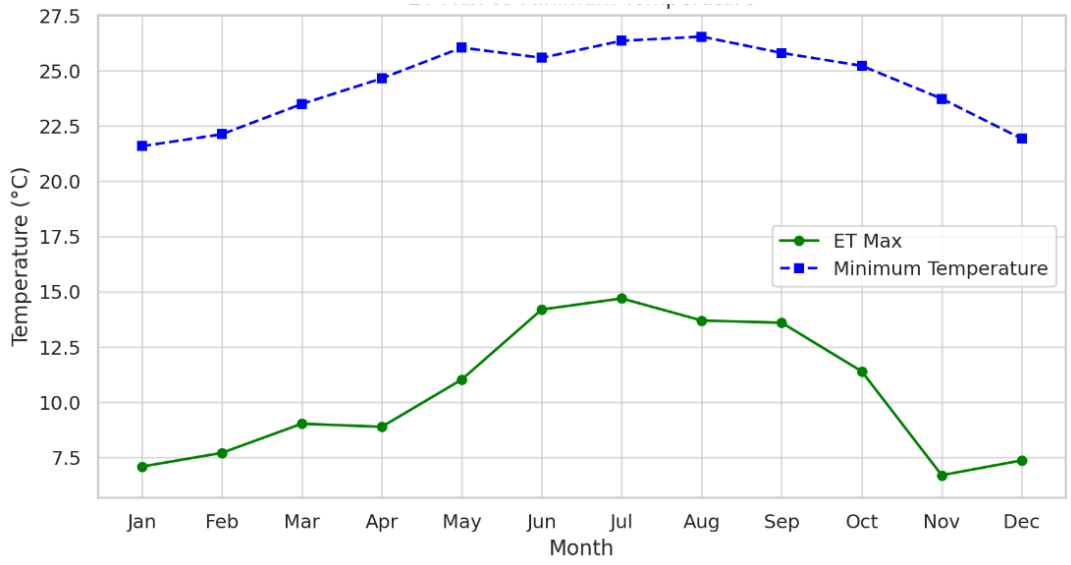


**Fig. 4. $ET_{max}$ vs Minimum temperature (2001)**

Minimum temperature trends closely follow ET values up to July, with both metrics increasing steadily and then gradually declining thereafter (Fig. 4). Although the correlation is slightly weaker compared to maximum temperature, minimum temperatures still play a supportive role in governing ET rates by contributing to the overall energy balance and influencing nighttime evaporation. An inverse relationship is observed between ET and relative humidity (Fig. 5). As relative humidity decreases from January to August, ET values rise correspondingly. This negative correlation suggests that drier air conditions promote a greater vapor pressure deficit, enhancing the evaporation and transpiration rates by facilitating faster moisture transfer from plants to the atmosphere.

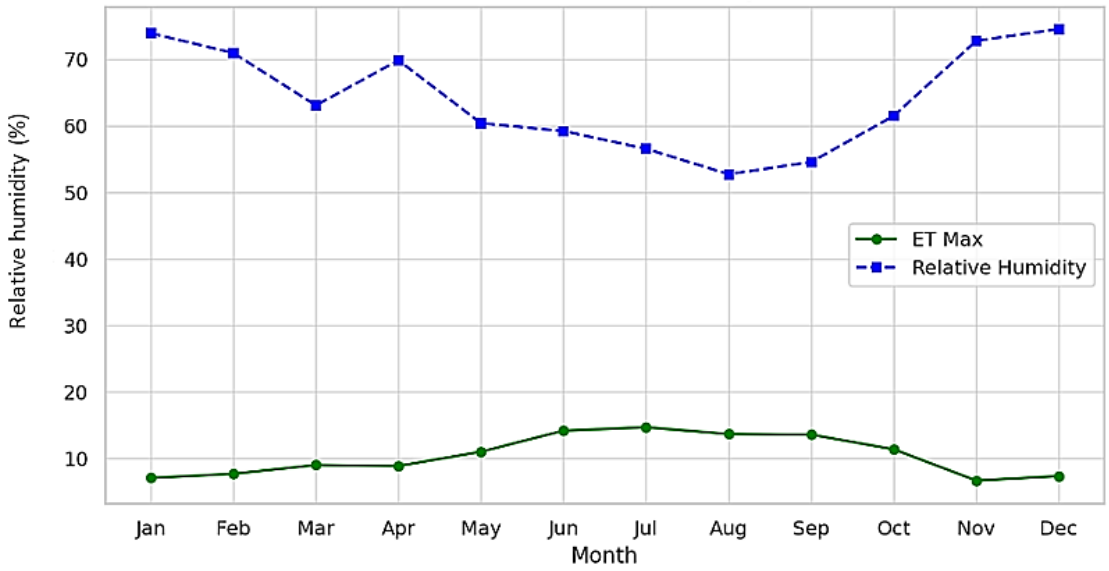


**Fig. 5. $ET_{max}$ vs relative humidity (2001)**

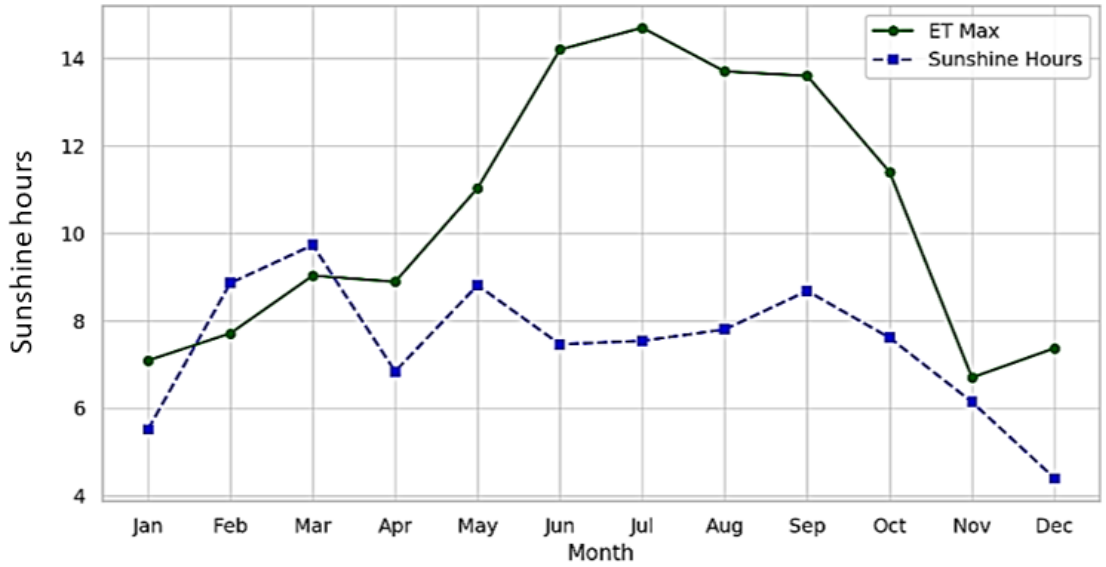


**Fig. 6. $ET_{max}$ vs sunshine hours (2001)**

ET levels are notably elevated during months with longer sunshine duration, particularly from February to September (Fig. 6). The availability of more solar radiation during this period enhances the energy required for phase change processes, thereby increasing the overall ET. This demonstrates the direct impact of solar exposure on atmospheric moisture loss. Wind speed and ET display a strong positive correlation, both showing an upward trend from May to August (Fig. 7). Higher wind velocities help disperse saturated air layers from the evaporative surface, creating favorable conditions for continuous moisture loss. This highlights the role of wind in accelerating ET by maintaining a steep moisture gradient at the surface-atmosphere interface.

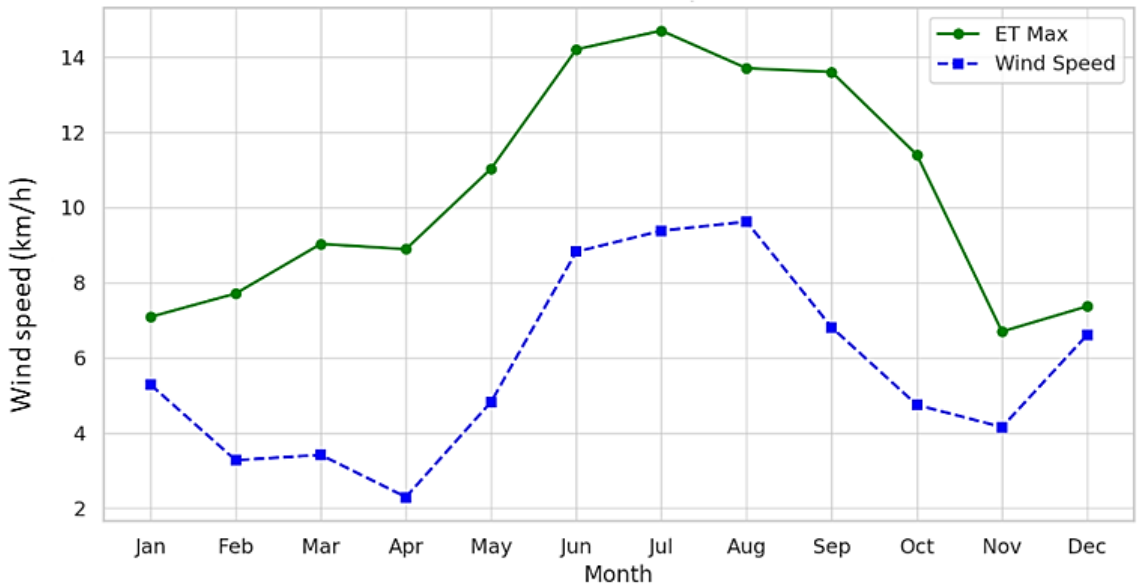


**Fig. 7.$ET_{max}$ vs wind speed (2001)**

The evaluation of the METRIC model's performance in predicting reference ET for the Madurai region yielded RMSE value of 3.01 and a MAE value of 2.45 (Fig. 8). These metrics provide insights into the accuracy and precision of the model's predictions. The RMSE value of 3.01 mm/day indicates the typical magnitude of errors between the model's predictions and the observed values of ET. While this value suggests some variability and potential for larger errors, it also signifies that the model's predictions generally align reasonably well with the observed values. Similarly, the MAE value of 2.45 mm/day provides a measure of the average magnitude of errors between the model's predictions and the observed values of ET. A lower MAE value indicates that, on average, the model's predictions are closer to the observed values, suggesting a relatively better performance in terms of absolute error. Overall, the results suggest that the METRIC model demonstrates moderate accuracy in predicting reference ET for the Madurai region in the given year. However, further analysis and validation are necessary to comprehensively assess the model's performance and identify potential areas for improvement.

The METRIC algorithm effectively estimates evapotranspiration (ET) in diverse regions, showing strong agreement with eddy covariance (EC) data in a Saudi Arabian alfalfa field, especially under full canopy conditions—supporting efficient irrigation and water management in arid climates (Madugundu *et al.*, 2017). In the western Urmia Lake Basin, its internal calibration and local adaptability ensured accurate ET estimates, aiding sustainable water use and lake restoration efforts (Tasumi, 2019). Applied to the Indian Sundarbans Biosphere

Reserve using Landsat 8 OLI imagery, METRIC revealed notable spatial ET variations, emphasizing its value in regional hydrology and resource planning (Mondal *et al.*, 2022). Remote sensing enables large-scale ET monitoring despite limited flux towers and cloud cover, though challenges remain in handling diverse land cover types. Still, it offers vital insights for managing water and conserving ecosystems in sensitive areas like the Sundarbans.

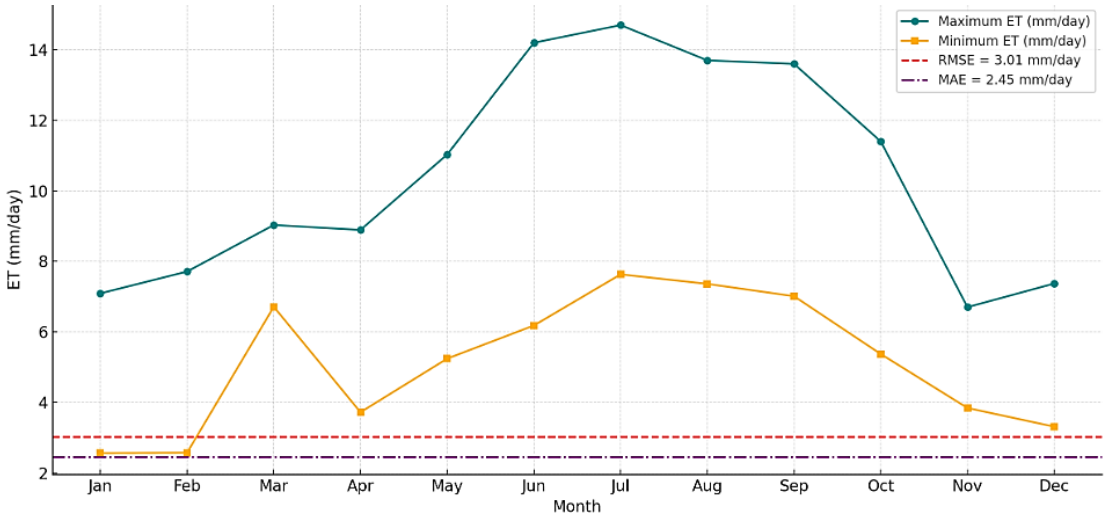


**Fig. 8. Monthly estimated ET with RMSE and MAE reference**

According to Madugundu *et al.* (2017), the highest ET rates in Saudi Arabia occur in June (14.2 mm/day) and July (14.7 mm/day), while the lowest are recorded in January (2.56 - 7.09 mm/day) and December (3.31 - 7.37 mm/day). Peak ET from May to September aligns with patterns observed in Madurai, which also shows high summer ET. The July peak in Saudi Arabia (13.9 mm/day) closely matches Madurai's (14.7 mm/day), and both show reduced winter ET ranging from 6 to 8 mm/day (Madugundu *et al.*, 2017). In the semi-arid Urmia Basin, summer ET ranges from 10 to 12 mm/day and drops more sharply in winter to 3–5 mm/day, slightly lower than in Madurai (Tasumi, 2019). Similarly, the Sundarbans show monsoon ET values of 11–13 mm/day, comparable to Madurai's August–September levels, while winter ET falls to 3–4 mm/day, again consistent with Madurai's pattern (Mondal *et al.*, 2022).

ET peaks in Madurai occur during the pre-monsoon and monsoon seasons when the region experiences hot, semi-arid weather. Saudi Arabia, despite its extreme summer heat, shows comparable summer ET rates but slightly lower winter values due to its more arid climate. ET in Saudi Arabia rises significantly from March to July, driven by increasing solar radiation and temperature (Madugundu *et al.*, 2017). The Sundarbans, with a tropical wet climate, exhibit similar monsoon ET values to Madurai but lower winter ET due to coastal influences (Mondal *et al.*, 2022). The Western Urmia Basin, being semi-arid with cooler summers, records lower peak ET and steeper winter declines compared to Madurai (Tasumi, 2019). All regions show peak ET during summer months - June to August - with the highest values (up to 14 mm/day) in Madurai and Saudi Arabia. In contrast, the Sundarbans and Urmia Basin show lower peaks, reflecting regional climatic differences. Madurai's winter ET (2.56–7.37 mm/day) remains higher than in the cooler Urmia Basin and Sundarbans, where winter ET mostly stays below 5 mm/day, highlighting Madurai's warmer baseline climate.

### 3.1. Comparison of Other Studies

The METRIC model has been widely applied in various climatic and geographical contexts for ET estimation. This study evaluates METRIC's performance in Madurai, India - a semi-arid region characterized by limited access to high-resolution meteorological data. This provides an opportunity to assess the model's adaptability and performance in data-scarce environments, contributing novel insights into its operational reliability and water management applicability. Comparing this research with studies in tropical and Mediterranean climates further underscores the adaptability of METRIC for global water resource management.

#### 3.1.1. Geographical and climatic context

Implementation of this study in Madurai, a semi-arid region with limited meteorological infrastructure, highlights the model's robustness in regions with sparse data availability. This study distinguishes itself from previous studies (Madugundu *et al.*, 2017; Tasumi, 2019), conducted in arid zones like Saudi Arabia and the Urmia Lake Basin, Iran - regions with more comprehensive meteorological data coverage. Similarly, Numata *et al.* (2017) and Alsenjar *et al.* (2023) demonstrated METRIC's effectiveness in tropical and Mediterranean environments, respectively. However, the current study's focus on a data-constrained semi-arid region underscores METRIC's ability to yield reliable outputs even in less favorable conditions, demonstrating the model's broader applicability.

#### 3.1.2. Model performance (accuracy and precision)

The METRIC model achieved a RMSE of 3.01 mm/day and a MAE of 2.45 mm/day in this study. These performance metrics, although slightly higher than values reported in studies conducted under data-rich conditions, RMSE = 0.65 mm/day by Alsenjar *et al.* (2023) and RMSE = 4.15 mm/day by Madugundu *et al.* (2017) are considered acceptable for ET modeling, especially in semi-arid zones where daily ET variability can be high. According to Reyes-González *et al.* (2019), an RMSE below 4 mm/day is generally acceptable for satellite-based ET models in agricultural water management. Thus, the model's error metrics in this study reflect a reasonable level of accuracy, validating METRIC's use in operational applications even with limited calibration.

#### 3.1.3. Calibration and data requirements

A significant contribution of this study lies in demonstrating that METRIC can be effectively implemented with minimal local calibration and limited meteorological inputs. While previous studies, including Reyes-González *et al.* (2017) and Silva Oliveira *et al.* (2018), emphasized the importance of extensive local calibration and field validation for optimal performance, this study illustrates that reliable ET estimates can still be achieved under data-scarce conditions. This makes METRIC especially suitable for semi-arid regions like Madurai, where installing and maintaining dense weather station networks is not feasible. The findings align with the simplified METRIC (S-METRIC) approach introduced by Rezaei *et al.* (2021), which similarly aimed to reduce dependence on local data, albeit with reliance on MODIS imagery.

#### 3.1.4. Applicability to water management

The study demonstrates the practical implications of METRIC for irrigation scheduling, drought monitoring, and broader water resource planning in semi-arid regions. The ability to derive spatially distributed ET estimates with reasonable accuracy, despite minimal meteorological data, is crucial for regions facing water scarcity. Earlier studies (Tasumi, 2019; Numata *et al.*, 2017) have previously emphasized METRIC's value in agricultural water management in arid and tropical settings. However, this study highlights its utility in data-constrained semi-arid contexts, thereby offering a practical solution for

sustainable water usage in regions like Madurai. The results validate METRIC's potential to support precision agriculture and efficient irrigation practices even when extensive field data are unavailable.

### 3.1.5. Spatial and temporal resolution

The use of Landsat imagery allowed for a spatial resolution of 30 meters and consistent temporal revisit intervals, enabling detailed mapping of ET across agricultural plots. Despite the absence of frequent ground-truthing, the spatial heterogeneity captured by METRIC aligns well with observed irrigation patterns, affirming the model's capacity for high-resolution water management analysis. Previous studies by Alsenjar *et al.* (2023) and Silva Oliveira *et al.* (2018), leveraged similar Landsat data but relied on denser meteorological inputs for calibration. This study's success in delivering comparable ET maps with reduced calibration affirms METRIC's reliability and cost-effectiveness for operational deployment in resource-constrained settings.

### 3.1.6. Validation and ground-truthing

The present study achieved reliable ET estimates with limited on-ground validation, contrasting with Madugundu *et al.* (2017) and Reyes-González *et al.* (2019), which depended on flux towers, eddy covariance systems, or lysimeter data for model validation. While such methods provide high-precision measurements, they are logistically intensive and costly. The ability of METRIC to deliver accurate ET estimates with reduced dependence on ground - truthing is particularly advantageous for regions where field data collection is not feasible. This underscores the model's practical value for remote, under-resourced agricultural areas requiring continuous monitoring and informed decision-making for water allocation.

This demonstrates the exceptional versatility and robustness of the METRIC model, especially in semi-arid regions where traditional data sources are scarce. With its minimal calibration requirements, competitive accuracy, cost-effectiveness, and reduced dependence on ground-truthing, this study presents METRIC as an ideal tool for water management and agricultural planning in resource-constrained regions. Compared to other studies, the ACRI Study stands out by showing how METRIC can perform at a high level even in regions with limited meteorological data and field resources, making it the best choice for large-scale applications in semi-arid areas. By analyzing the outputs of METRIC, particularly the estimation of actual evapotranspiration (ET), it becomes possible to effectively manage water supply through precision irrigation methods such as drip irrigation. This is particularly relevant for semi-arid regions like Madurai, where agriculture is the primary livelihood and efficient water use is critical. Accurately determining the ET values allows for delivering just the required amount of water to crops, thereby enhancing water-use efficiency, supporting climate resilience, and promoting sustainable agricultural practices. The study's findings emphasize METRIC's potential to address water scarcity and improve food security in vulnerable regions worldwide.

## 4. CONCLUSIONS

The study establishes the METRIC model as a reliable and flexible approach for estimating reference ET in the semi-arid region of Madurai, offering a practical alternative to the FAO-56 Penman-Monteith method, especially in data - scarce environments. The satellite-based nature of METRIC, combined with minimal local weather data for internal calibration, allows for the generation of accurate, high-resolution ET maps. The model demonstrated strong agreement with measured daily and seasonal ET patterns, with performance indices such as RMSE and MAE indicating high accuracy, although slight variations in absolute ET values were observed across regions due to differences

in land cover, climate, and topography. METRIC effectively captured seasonal ET trends and spatial variability, reinforcing its suitability across diverse agro-climatic conditions. However, limitations such as cloud cover interference and minimal ground truth calibration remain. Future studies need focus on improving temporal resolution, integrating cloud-resistant satellite data, and validating the model across extended timeframes and varied landscapes to enhance its operational utility in water resource management.

## ACKNOWLEDGMENT

The authors thank the Remote Sensing and GIS Laboratory, Thiagarajar College of Engineering, Madurai, and the Agricultural Engineering Department, Tamil Nadu Agricultural University, Madurai, for their valuable support and guidance in conducting this study.

## REFERENCES

1. Adem, E., Boteva, S., Zhang, L. and Elhag, M. 2023. Estimation of evapotranspiration based on METRIC and SEBAL model using remote sensing, near Al-Jouf, Saudi Arabia. *Desalination and Water Treatment*, 290:94-103. https://doi.org/10.5004 /dwt.2023.29478.
2. Adib, A., Kalantarzadeh, S. S. O., Shoushtari, M. M., Lotfirad, M., Liaghat, A. and Oulapour, M. 2023. Sensitive analysis of meteorological data and selecting appropriate machine learning model for estimation of reference evapotranspiration. *Applied Water Science*, 13(3):1-17.https://doi.org/ 10.1007/s13201-023-01895-5.
3. Alsenjar, O., Cetin, M., Aksu, H., Golpinar, M. S. and Akgul, M.A. 2023. Actual evapotranspiration estimation using METRIC model and landsat satellite images over an irrigated field in the Eastern Mediterranean Region of Turkey. *Mediterranean Geoscience Reviews*, 5(1):35-49. https://doi.org/ 10.1007/s42990-023-00099-y.
4. Asadi, M. and Kamran, K. V. 2022. Comparison of SEBAL, METRIC, and ALARM algorithms for estimating actual evapotranspiration of wheat crop. *Theoretical and Applied Climatology*, 149(1):327-337. https://doi.org/10.1007/s00704-022-04026-3.
5. Ayaz, A., Chandra, S., Mandlecha, P. and Shaik, R. 2021. Modelling of reference evapotranspiration for semi-arid climates using artificial neural network. In *Water and Energy Management in India: Artificial Neural Networks and Multi-Criteria Decision Making Approaches*, 141-160. https://doi.org/10.1007/978-3-030-66683-5_7.
6. Bhakar, S. R., Rajput, J., Lakhawat, S. S. and Kothari, M. 2020. Comparative evaluation of actual evapotranspiration of capsicum inside and outside of naturally ventilated polyhouse. *Agricultural Engineering Today*, 44(4):14-21. http://dx.doi.org/ 10.52151/aet2020444. 1526.
7. Dhawan, V. 2017. Water and agriculture in India. *Background paper for the South Asia expert panel during the Global Forum for Food and Agriculture*, 28(8):80-85. http://www. Yourarticle library.com/essay/essay-on-

water-scarcity-in-india-1113-words/20871/.

8. Madugundu, R., Al-Gaadi, K. A., Tola, E., Hassaballa, A. A. and Patil, V. C., 2017. Performance of the METRIC model in estimating evapotranspiration fluxes over an irrigated field in Saudi Arabia using Landsat-8 images. *Hydrology and Earth System Sciences*, 21(12):6135-6151. https://doi.org/10.5194/hess-21-6135-2017.
9. Mondal, I., Thakur, S., De, A. and De, T. K. 2022. Application of the METRIC model for mapping evapotranspiration over the Sundarban Biosphere Reserve, India. *Ecological Indicators*, 142:1-28. https://doi.org/10.1016/j.ecolind.2022.108553.
10. Numata, I., Khand, K., Kjaersgaard, J., Cochrane, M. A. and Silva, S. S. 2017. Evaluation of Landsat-based METRIC modeling to provide high-spatial resolution evapotranspiration estimates for Amazonian forests. *Remote Sensing*, 9(1):1-16. https://doi.org/10.3390/rs9010046.
11. Rajput, J., Singh, M., Lal, K., Khanna, M., Sarangi, A., Mukherjee, J. and Singh, S. 2023. Data-driven reference evapotranspiration ($ET_0$ ) estimation: A comparative study of regression and machine learning techniques. *Environment, Development and Sustainability*, 1-28. https://doi.org/10.1007/s10668-023-03978-4.
12. Reyes-González, A., Kjaersgaard, J., Trooien, T., Hay, C. and Ahiablame, L. 2017. Comparative analysis of METRIC model and atmometer methods for estimating actual evapotranspiration. *International Journal of Agronomy*, 2017(1):1-16. https://doi.org/10.1155/2017/3632501.
13. Reyes-González, A., Kjaersgaard, J., Trooien, T., Reta-Sánchez, D. G., Sánchez-Duarte, J. I., Preciado-Rangel, P. and Fortis-Hernández, M. 2019. Comparison of leaf area index, surface temperature, and actual evapotranspiration estimated using the METRIC model and in situ measurements. *Sensors*, 19(8):1-21. https://doi.org/10.3390/s19081857.
14. Rezaei, M., Ghasemieh, H. and Abdollahi K. 2021. Simplified version of the METRIC model for estimation of actual evapotranspiration. *International Journal of Remote Sensing*, 42(14):5568-5599. https://doi.org/10.1080/01431161.2021.1925991
15. Senay, G. B., Leake, S., Nagler, P. L., Artan, G., Dickinson, J., Cordova, J. T. and Glenn, E. P. 2011. Estimating basin scale evapotranspiration (ET) by water balance and remote sensing methods. *Hydrological Processes*, 25(26):4037-4049. https://doi.org/10.1002/hyp.8379.
16. Sharafi, S. and Ghaleni, M. M. 2021. Evaluation of multivariate linear regression for reference evapotranspiration modeling in different climates of Iran. *Theoretical and Applied Climatology*, 143:1409-1423. https://doi.org/10.1007/s00704-020-03473-0.

17. Silva Oliveira, B., Caria Moraes, E., Carrasco-Benavides, M., Bertani, G. and Augusto VerolaMataveli, G. 2018. Improved albedo estimates implemented in the METRIC model for modeling energy balance fluxes and evapotranspiration over agricultural and natural areas in the Brazilian Cerrado. *Remote Sensing*, 10(8):1-27. https://www.mdpi.com/2072-4292/10/8/1181/notes.
18. Sołtysiak, M. and Rakoczy, M. 2019. An overview of the experimental research use of lysimeters. *Agricultural Water Management*, 212:17-26. https://doi.org/ 10.2478/environ-2019-0012.
19. Tasumi, M. 2019. Estimating evapotranspiration using METRIC model and Landsat data for better understandings of regional hydrology in the western Urmia Lake Basin. *Agricultural Water Management*, 226:1-11. https://doi.org/10.1016/j.agwat. 2019.105805.

International Agricultural Engineering Journal ISSN 0858-2114

*September 2025, 34 (1-4) : 135-154*

# Impact of Check Dams on Groundwater Recharge and Quality in Upper Vaigai Sub-Basin, Tamil Nadu, India

**K. Keerthy[1,2], S.Chandran[1*], D.Sivakumar[3], V. Kumar[4]**

## ABSTRACT

Groundwater is essential for various sectors, including agriculture, domestic use, and industry. This study aims to assess the suitability of groundwater for different uses and understand the impact of check dams on groundwater quality in the Upper Vaigai Sub-basin in Theni district, Tamil Nadu, India. The water quality parameters analyzed included potential of hydrogen, total dissolved solids, electrical conductivity, major cations (calcium, magnesium, sodium, and potassium, and anions such as chloride, sulphate, carbonate, bicarbonate, and fluoride ion) to evaluate irrigation suitability. The groundwater quality before and after the construction of check dams at Mayiladumparai, Ambasamudram and Amachiyapuram was evaluated using electrical conductivity, sodium adsorption ratio, sodium percentage, and ion concentrations through Wilcox, United States Salinity Laboratory, and Piper plots. Results from these plots indicated that groundwater quality improved post-construction, making it suitable for irrigation. Groundwater within 5 km of the check dams was found to be suitable for drinking purposes. Additionally, the impact of the check dams on groundwater levels was analyzed using the Mann-Kendall, Sen Slope Estimator, and Innovative Trend Analysis methods. The results of this study reveal that in Ambasamudram, Mayiladumparai, and Amachiyapuram, the groundwater recharge rates increased by 47%, 44%, and 23%, respectively. Check dam construction has also improved groundwater quality and recharge, though the effectiveness varies based on site-specific factors such as geology, cropping patterns, and irrigation practices.

***Keywords:*** *Agricultural Water Use; Aquifer Response; Hydrochemical Assessment; Non-Parametric Trend Methods; Recharge Structures, Seasonal Variability.*

## 1. INTRODUCTION

Water is a fundamental component of the natural world, significantly influencing the viability of organisms and the socio-economic advancement of communities. Natural water resources serve humans as sources of potable drinking water and irrigation (da Silva *et al.*, 2020). The accessibility and quality of water have shaped daily life, but rapid population growth and agro-industrial expansion have increasingly challenged the maintenance of suitable water quality for diverse uses (Sinha Ray and Elango, 2019). Human, industrial, and agricultural activities pose serious threats to the ecological diversity of water resources. Numerous studies worldwide have analyzed groundwater quality using diverse methodologies.

[1] Department of Civil Engineering, Thiagarajar College of Engineering, Madurai.

[2] Presently Asst. Engineer, Tamil Nadu Pollution Control Board, Virudhunagar, Tamil Nadu, India.

[3] Dept. of Agrl. Engineering, Kalasalingam Academy of Research and Education, Krishnankoil, Tamil Nadu, India.

[4] Formerly Professor and Head, Agricultural Engineering Department, Tamil Nadu Agricultural University, Madurai, Tamil Nadu, India.

**Corresponding author -email: schandran@tce.edu*

Received: 29 November 2024; Revised: 19 August 2025; Accepted: 24 August 2025.

For instance, groundwater near the Rooppur Nuclear Power Plant in Bangladesh was assessed through 17 hydrogeochemical indicators from nine samples to determine drinking and irrigation suitability (Uddin *et al.,* 2023). In northern Karnataka, India, water samples from 68 wells collected quarterly (2013–2014) were analyzed for electrical conductivity (EC), pH, and dominant ions (Thirumurugan *et al.,* 2018). In Sheikhupura district, 195 groundwater samples mostly met WHO guidelines except for arsenic, which exceeded the recommended 10 µg/L limit for drinking water (Rehman *et al.,* 2023).

Groundwater quality in Nyamira County, Kenya, was evaluated through samples from three springs during the November 2018 rainy season (Rehman *et al*., 2023). The Upper Yellow River region in China showed groundwater quality influenced by rock dominance, evaporation, and cation exchange, with nitrogen and fluorine as major pollutants. Although 96.19% of samples were deemed good via Integrated Weight Matter-Element Extension Analysis, 57% posed unacceptable health risks to children, and 21% to adults (Wang *et al.,* 2022). In India's Tamsa River basin, groundwater exhibited higher major ion and silica concentrations than river water, which had greater alkalinity. Both were suitable for consumption, household use, and irrigation, with variations linked to rock weathering, ion interactions, and human activities (Siraj *et al.*, 2023). In Ilesha West, Nigeria, groundwater quality for irrigation was assessed by physicochemical properties and heavy metals, including sodium adsorption ratio (SAR). Sodium ($Na^+$), potassium ($K^+$), calcium ($Ca^{2+}$), bicarbonate ($HCO_3^-$), carbonate ($CO_3^{2-}$), and chloride ($Cl^-$) were dominant ions. The Irrigation Water Quality Index (IWQI) indicated many wells fell under high-to-severe irrigation restrictions. GIS-based zoning in Abu Dhabi highlighted limited irrigation-suitable areas, emphasizing the need for real-time monitoring and risk management to support sustainable agriculture (Siraj *et al.,* 2023). In the Jinghe River Basin, China, groundwater quality categories reflected human impacts, with unsuitable quality mainly in the north. Health risk assessments showed elevated carcinogenic arsenic risks, especially for children (Li *et al*., 2022).

Heavy metal contamination in surface water of Jamalpur Sadar, Bangladesh, posed significant health risks, while groundwater quality indices and pollution categorizations confirmed unsuitability for consumption (Yakovlev *et al.*, 2023). Groundwater quality for drinking in South Korea was modelled using a neural network with 95% predictive accuracy, supported by 2D spatial analysis, indicating the necessity for revised management policies (Ahn *et al.,* 2023). Groundwater quality assessment in Dayrout, Upper Egypt, using indices and diagrams, revealed seasonal fluctuations in borehole water levels (Gabr *et al.,* 2021). Long-term analyses have highlighted contrasting groundwater trends across regions. Mann–Kendall tests in Terengganu, Malaysia, indicated rising groundwater levels from 2000 to 2012 under a tropical monsoon climate (Shaharudin *et al.,* 2021). Declining trends were projected for Uttar Pradesh and Karnal district, India, through modified Mann–Kendall and Sen's slope estimators, extending to 2050 (Kumar *et al.,* 2018; Zakwan, 2021). Groundwater levels near agricultural lands in West Bengal declined according to Mann–Kendall and Standard Groundwater Level Index analyses (Halder *et al*., 2020). Ardabil Plain, Iran, experienced declines linked to human activity, prompting calls for additional hydrogeochemical studies (Daneshvar Vousoughi *et al.,* 2013). Sagar district, Madhya Pradesh, showed cyclical yet declining patterns identified through Kendall and regression tests (Thakur and Thomas, 2011).

Global case studies reveal further depletion concerns. Groundwater development in

Vietnam's Red River Delta from 1995 to 2009 was unsustainable in urban zones, with falling confined aquifer levels (Thakur and Thomas, 2011). The UAE, particularly Sharjah, experienced severe depletion and salinization over the past 15 years due to limited rainfall and population growth (Yilmaz *et al.,* 2020). Expanding reliance on groundwater in areas lacking surface water, combined with over-extraction, has accelerated depletion rates worldwide (Sinha Ray and Elango, 2019). Artificial recharge interventions have been implemented to address overuse. Check dams, small low-level structures built across rivers, streams, or channels, slow water flow, trap sediments, and create upstream reservoirs for irrigation, livestock, domestic supply, and aquifer recharge (Rao *et al.,* 2022). They also reduce sediment transport to downstream areas (Parimala Renganayaki and Elango, 2014).

The Upper Vaigai Sub-basin study in Theni aimed to assess groundwater suitability for agricultural, domestic, and industrial use through parameters such as pH, TDS, EC, and ion concentrations. It also aimed to evaluate the influence of multiple check dams (Mayiladumparai, Ambasamudram, Amachiyapuram) on groundwater quality using Wilcox, USSL, and Piper Trilinear plots; and analyze recharge trends within a 5 km radius using Mann–Kendall, Sen's Slope Estimator, and Innovative Trend Analysis. Findings confirmed the role of check dams in enhancing groundwater availability for irrigation and drinking purposes, contributing to sustainable water resource management.

## 2. MATERIALS AND METHODS

### 2.1. Study Area

The Upper Vaigai sub-basin, situated in the Theni district of Tamil Nadu, India, holds great ecological significance. It is home to the Vaigai River, one of Tamil Nadu's primary rivers, which originates in the Western Ghats and flows through the sub-basin, providing essential water resources for irrigation, drinking, and domestic purposes to surrounding communities (Keerthy *et al.,* 2024). This study covers the geographical area between latitudes 09°30'00" and 10°00'00"N and longitudes 77°15'10" and 77°45'00"E, spanning a total area of 725 square kilometres.

The Upper Vaigai sub-basin experiences a subtropical climate with annual precipitation ranging from 650 to 2000 mm and temperatures between 26 and 36°C. The northeast monsoon from October to December delivers substantial rainfall that enhances aquifer recharge more effectively than the southwest monsoon (Kaliraj *et al.,* 2015). Rapid population growth in recent years has intensified water scarcity, as monsoon failures and over-extraction drive declining groundwater levels (Kaliraj *et al.,* 2014). The undulating plain terrain, interspersed with irregular charnockitic hillocks and hornblende biotite gneissic rocks, influences soil composition, water retention, and vegetation distribution. The interplay of climatic, topographic, and geological features governs ecosystem dynamics and sustainability (Kaliraj *et al.,* 2015; Pothiraj and Rajagopalan, 2013). The sub-basin is notable for its biodiversity, cultural heritage, and agricultural significance, yet it faces sustainability challenges including deforestation, water over-extraction, agricultural and industrial pollution, and unsustainable farming practices (Sankar, 2002). Addressing these issues requires strategies such as forest and wetland preservation, promotion of sustainable agriculture, and adoption of water-saving technologies (Sankar, 2002). Check dams are investigated as a sustainable intervention to enhance groundwater quality and quantity, mitigating water scarcity and supporting ecological balance in the Upper Vaigai sub-basin.

### 2.2. Methodology

Fig. 1 illustrates the comprehensive methodology employed in the investigation, wherein the chosen study area encompasses the upper Vaigai sub-basin. This is followed by the collection of pertinent data, specifically related to groundwater levels and groundwater quality, which were subsequently utilized to examine the influence of

check dams on groundwater recharge and its quality through the application of trend analysis and groundwater plots, respectively.

The details of check dams obtained from the Public Works Department (Theni) are summarized in Table 1. Furthermore, information regarding groundwater levels and quality was obtained from the Central Ground and Surface Water Board **(**India Data Portal, 2024). Data on groundwater levels and quality were collected for the period spanning 2009 to 2019. The years of construction for the selected check dams were considered individually in the analysis. The check dam at Amachiyapuram was constructed during 2013 to 2014, while at Ambasamudram and Mayiladumparai were constructed during 2015 to 2016. Based on this, the pre-construction period was defined as 2009 to 2012 for Amachiyapuram, and 2009 to 2014 for Ambasamudram and Mayiladumparai. The post-construction period was considered as 2015 to 2019 for Amachiyapuram, and 2017 to 2019 for the other two sites. This distinction allowed for a comparative assessment of groundwater trends before and after the implementation of check dams.

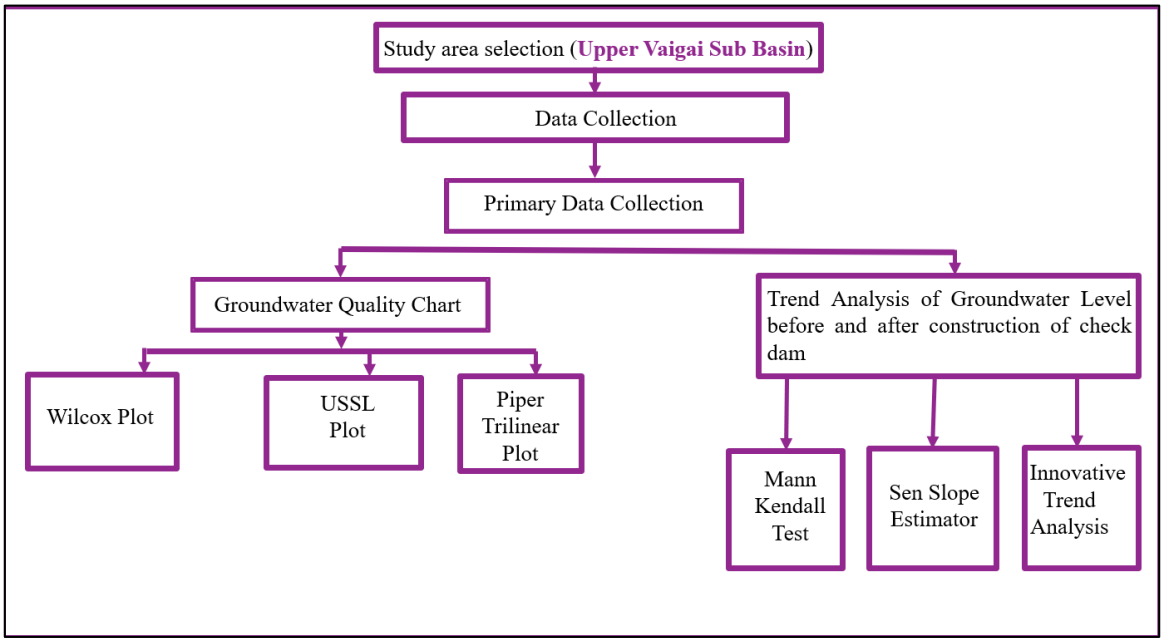


**Fig. 1. Flow chart showing the methodology of the study.**

### 2.3. Hydrogeochemical Characteristics of Groundwater

Hydrogeochemical investigation assesses water quality by measuring physicochemical parameters and comparing them with standards for drinking and irrigation. Groundwater samples were collected from selected bore wells and tube wells in the Upper Vaigai Sub-basin, with emphasis on areas influenced by check dams. On-site measurements of pH, electrical conductivity (EC), and temperature were conducted using calibrated multi-parameter probes. Samples were stored in acid-washed, high-density polyethylene (HDPE) bottles, preserved when necessary (e.g., acidified for metal analysis), and transported under refrigerated conditions (4°C) to authorized laboratories. Laboratory analyses determined major cations ($Ca^{2+}$, $Mg^{2+}$, $Na^{+}$, $K^{+}$), anions ($HCO_3^{-}$, $SO_4^{2-}$, $Cl^{-}$, $NO_3^{-}$), total dissolved solids (TDS), and hardness using flame photometry, atomic absorption spectroscopy (AAS), UV-visible spectrophotometry, gravimetric analysis, and titration, all in accordance with Standard Methods for the Examination of Water and

Wastewater (APHA, 2017). Groundwater samples were meticulously collected and analyzed to determine their physicochemical attributes and understand the hydrochemistry of the water. The study obtained groundwater data for 2009–2019 from the India Data Portal, which aggregates datasets published by official government agencies, including the Central Ground Water Board (CGWB) (India Data Portal, 2024).

**Table 1. Particulars of check dams**

| Sl. No. | Name of the check dam | Latitude | Longitude | Year of construction |
|---|---|---|---|---|
| 1 | Ambasamudram | 9° 55' 54"N | 77° 30' 44"E | 2015-2016 |
| 2 | Mayiladumparai | 9° 47' 10"N | 77° 30' 43"E | 2015-2016 |
| 3 | Amachiyapuram | 9° 57' 38"N | 77° 30' 28"E | 2013-2014 |

Additional supporting documentation and groundwater trend data were cross-referenced from the Ground Water Year Books published by the CGWB, Ministry of Jal Shakti, Government of India. These analyses provide a comprehensive understanding of hydrological processes, help identify potential contamination sources, assess groundwater suitability for drinking and irrigation, and inform effective water management strategies. Groundwater quality data collected over a decade from Ambasamudram, Mayiladumparai, and Amachiyapuram were analyzed using graphical tools such as the Wilcox diagram, United States Salinity Laboratory (USSL) diagram, and Piper trilinear plot, facilitating assessment of hydrochemical characteristics, water quality classification, and identification of dominant ions (Parimala Renganayaki and Elango, 2014; Mahammad *et al*., 2023).

Groundwater recharge is the process by which water from precipitation, surface water, or irrigation infiltrates the ground to replenish aquifers (Rajesh *et al.*, 2019). It is a vital component of the hydrological cycle, sustaining groundwater resources for drinking, irrigation, and industrial use. Recharge supports depleted aquifers, base flow in rivers, and ecosystem health, providing environmental improvement, enhanced agricultural productivity, sustained water supply, and improved water quality (Parimala Renganayaki and Elango, 2014).

### 2.4. Groundwater Quality Chart

A groundwater quality chart compiles key physico-chemical parameters measured at multiple sampling locations, offering a structured overview of groundwater characteristics across the study area. Visualization of this data allows comparison of spatial and seasonal variations, identification of patterns in water chemistry, and detection of zones with elevated contamination levels (da Silva *et al*., 2020). Such visual representation simplifies complex hydrogeo-chemical information, supporting assessment of groundwater suitability in relation to irrigation and drinking standards. Trends observed in the chart reflect underlying geological and anthropogenic influences, assisting in evaluating the effectiveness of groundwater recharge structures and identifying areas requiring management attention (Asomaku, 2023). Through integration of measured data and visual analysis, the chart enhances understanding of aquifer behaviour and supports decisions aimed at improving water quality and sustainability.

### 2.5. USSL Plot

The USSL diagram, also known as the USSL plot or USSL classification, is a visual depiction used to assess the appropriateness of water for irrigation based on its chemical composition (Rajesh *et al.*, 2019). It aids in the evaluation of groundwater quality by graphically representing the concentrations of

various ions or parameters. Water quality assessment for irrigation is commonly visualized using the USSL diagram, which plots groundwater samples based on EC and SAR. EC indicates salinity hazard, while SAR reflects sodium hazard. Each point on the USSL plot corresponds to a specific water sample and its placement depends on the EC and SAR values. The diagram is structured into interpretive zones ranging from C1 to C4 for salinity classification and from S1 to S4 for sodium hazard classification. Water is considered excellent when EC is less than 250 µS/cm, good between 250 and 750 µS/cm, doubtful from 750 to 2250 µS/cm, and unsuitable when EC exceeds 2250 µS/cm. Similarly, SAR values between 0 and 10 denote excellent water quality, 10 to 18 indicate good, 18 to 26 are classified as doubtful, and values greater than 26 are considered unsuitable. This combined EC and SAR framework enables accurate interpretation of groundwater suitability for irrigation and supports sustainable agricultural water management strategies.

### 2.6. Wilcox Plot

The Wilcox plot classifies irrigation water based on Na% and EC. Water with low Na% (0–20) and EC (<250 µS/cm) is considered excellent, while values up to 40% Na and 750 µS/cm EC are rated good. Water with moderate salinity and Na% (40–60; EC 750–2250 µS/cm) is permissible, mainly for salt-tolerant crops. Higher values (Na% 60–80; EC 2250–3000 µS/cm) are doubtful, and water exceeding these levels is unsuitable for irrigation. This classification aids in evaluating salinity and sodium hazards for effective water use in agriculture (Parimala Renganayaki and Elango, 2014; Aher *et al*., 2022; Ekbal and Khan, 2022). These zones indicate the potential impact of $Na^+$ concentration and salinity on soil permeability and crop health. Higher $Na^+$ levels can degrade soil structure, reduce infiltration, and impair plant growth over time. In this study, groundwater samples were evaluated using the Wilcox plot by graphing EC against Na%, enabling a quick visual classification of irrigation water quality. The interpretation focuses on the position of sample points within the defined zones, offering a practical basis for understanding spatial and temporal variations in groundwater suitability. Detailed theoretical background on the Wilcox method can be found in the original referenced works.

### 2.7. Piper Trilinear Plot

The Piper trilinear diagram is a graphical tool used to classify groundwater types based on the relative concentrations of major cations ($Ca^{2+}$, $Mg^{2+}$, $Na^+ + K^+$) and anions ($Cl^-$, $SO_4^{2-}$, $HCO_3^- + CO_3^{2-}$), expressed in milliequivalents per litre (meq/L) (Marghade *et al.,* 2021). Three dominant water types were observed: Ca-$HCO_3$, indicating recharge from carbonate rocks with $Ca^{2+}$ and $HCO_3^-$ values around 40–120 mg/L and 150–350 mg/L respectively (Dhakate *et al.,* 2021); Mg-$HCO_3$, showing similar recharge conditions but with higher $Mg^{2+}$ concentrations (Fu *et al.,* 2023); and Na-Cl, suggesting saline influence or anthropogenic sources where $Na^+$ and $Cl^-$ exceed 200 mg/L and 250 mg/L respectively (Dhakate *et al.,* 2021). Mixed water types were also noted, reflecting blending of recharge sources and varied geochemical processes (Fu *et al.,* 2023). Piper trilinear diagram enabled the interpretation of groundwater chemistry relevant to the study area.

### 2.8. Trend Analysis

Trend analysis holds critical value within hydrogeological studies. This approach reflects changes occurring within aquifer systems under varying influences such as climate variation, land modification, groundwater extraction, and recharge patterns. This study applied the Mann-Kendall (MK) test and Sen's slope estimator. These statistical methods support detection and quantification of long-term trends within groundwater level data. The MK test involves comparison between successive data points arranged in chronological order. Each comparison contributes to a cumulative score known as the S statistic. A positive S implies rising groundwater levels over time, while a negative S suggests declining levels. A value near zero indicates a stable trend without significant directional

change. To assess statistical significance, a standardized value Z is calculated from S and compared against a threshold. A p-value below 0.05 indicates a statistically significant trend, leading to the rejection of the null hypothesis and acceptance of an existing trend within the series.

Trend magnitude was estimated using Sen's slope method, which calculates the median slope between all data point pairs. Positive slopes indicate rising groundwater levels, while negative slopes reflect declines, with slope magnitude representing the rate of change. This non-parametric approach resists distortion from outliers or non-normal data, enhancing reliability. Analyses revealed spatial and temporal variations in groundwater, identifying vulnerable zones and emerging trends. Such trend-based evaluations inform policy design, resource allocation, and long-term planning, supporting sustainable groundwater management under climate variability and human pressure. Integration of innovative trend detection further strengthens understanding of groundwater dynamics across temporal and spatial scales.

## 3. RESULTS AND DISCUSSIONS

This study evaluates groundwater quality and availability in the Upper Vaigai sub-basin to determine its suitability for agricultural, domestic, and industrial use, with a focus on the impact of check dams. Key hydrochemical parameters, trend analyses, and graphical methods were employed to support sustainable water resource management.

### 3.1. USSL Plot

Figures 2-4 illustrate the groundwater quality during pre-monsoon and post-monsoon periods at Ambasamudram, Mayiladumparai, and Amachiyapuram, respectively, before and after the construction of check dams. At Ambasamudram, pre-monsoon samples showed 88% in C3–S2/C4–S2 classes, indicating high EC and unsuitability for irrigation (Batarseh *et al.*, 2021). Post-construction, 46% of samples shifted to C1–S1/C2–S1, with 52% EC < 750 µS/cm and 48% S1 (SAR < 10), reflecting significant improvement through enhanced recharge and reduced salinity (Verma *et al*., 2020; Alshehri *et al*., 2023). Mayiladumparai exhibited higher initial stress, with all five pre-construction locations in C4–S2/ C4–S3 (EC > 2250 µS/cm, SAR 10–18), restricting crop productivity (Uddin *et al*., 2023). Post-dam, 50% of samples improved to C2–S1/C3–S1 (moderate EC, SAR < 10), demonstrating the check dam's role in reducing salinity and sodium hazard via infiltration and dilution. Amachiyapuram showed intermediate pre-construction conditions, dominated by C3–S3/C3–S2/C3–S1 (EC > 2250 µS/cm, SAR > 13), indicating high risk to soil and salt-sensitive crops (Verma *et al*., 2020). Post-construction, SAR declined to S1–S2 (SAR < 13) and EC to C2–C3 (750–2250 µS/cm), improving suitability for moderately salt-tolerant crops, though salinity constraints remain.

Comparison reveals that Ambasamudram experienced the most pronounced improvement in EC and SAR, achieving "Excellent" irrigation suitability, while Mayiladumparai showed moderate recovery, and Amachiyapuram, though improved, still faces salinity constraints. Overall, check dam construction enhanced groundwater recharge, reduced sodium hazard, and improved irrigation suitability across all three stations, with site-specific variations highlighting the need for adaptive nutrient and irrigation management to optimize agricultural productivity.

### 3.2. Wilcox Plot

Groundwater quality at Ambasamudram, Mayiladumparai, and Amachiyapuram check dams was assessed before and after construction to evaluate irrigation suitability. At Ambasamudram (Fig. 5 a & b), 27 pre-construction samples showed 33% doubtful to unsuitable (Na% > 60, high EC) and 48% permissible (Na% 40–60); post-construction, 85% were excellent (Na% 0–20) and 15% good (Na% 20–40), indicating substantial improvement due to increased Vaigai River infiltration (Verma *et al*., 2020). Mayiladumparai (Fig. 6 a & b) initially had moderate suitability (Na% 40–60, medium EC)

across five sites, with post-construction sampling at ten locations showing 50% good to permissible (Na% 20–60), reflecting moderate gains limited by seasonal variations. Amachiyapuram (Fig. 7 a & b) pre-construction had 23% unsuitable (Na% > 60) and 77% permissible (Na% 40–60), improving post-construction to 30% excellent (Na% 0–20) and 50% good (Na% 20–40) due to enhanced recharge and dilution (Alshehri *et al*., 2023; Verma *et al*., 2020). Comparatively, Ambasamudram exhibited the most pronounced water quality enhancement, Amachiyapuram showed significant but partial improvement, while Mayiladumparai experienced moderate gains constrained by seasonal effects. These findings suggest that check dams effectively reduce sodium hazard and salinity, enhancing irrigation suitability, with site-specific factors and seasonal variability influencing the magnitude of improvement, highlighting the need for continued monitoring and adaptive management.

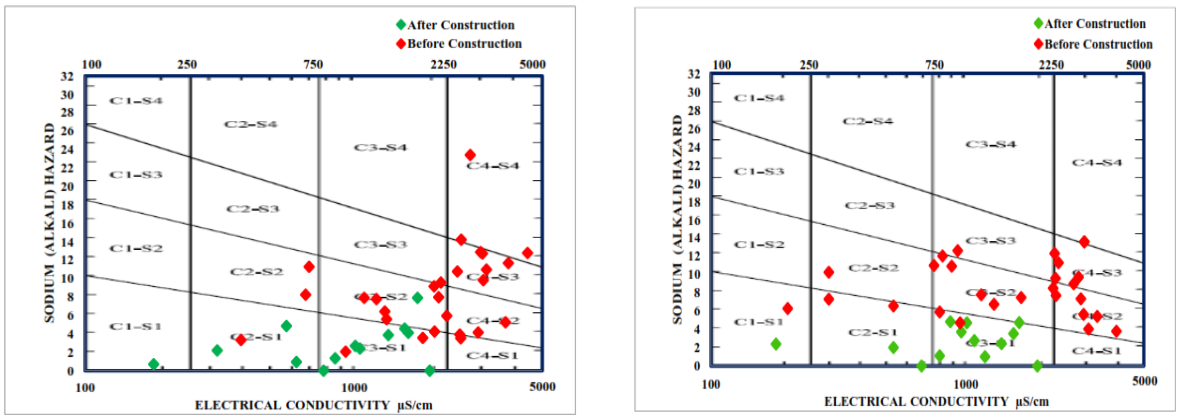


**a. Pre-monsoon** **b. Post - monsoon**

**Fig. 2. USSL plot: Ambasamudram check dam**

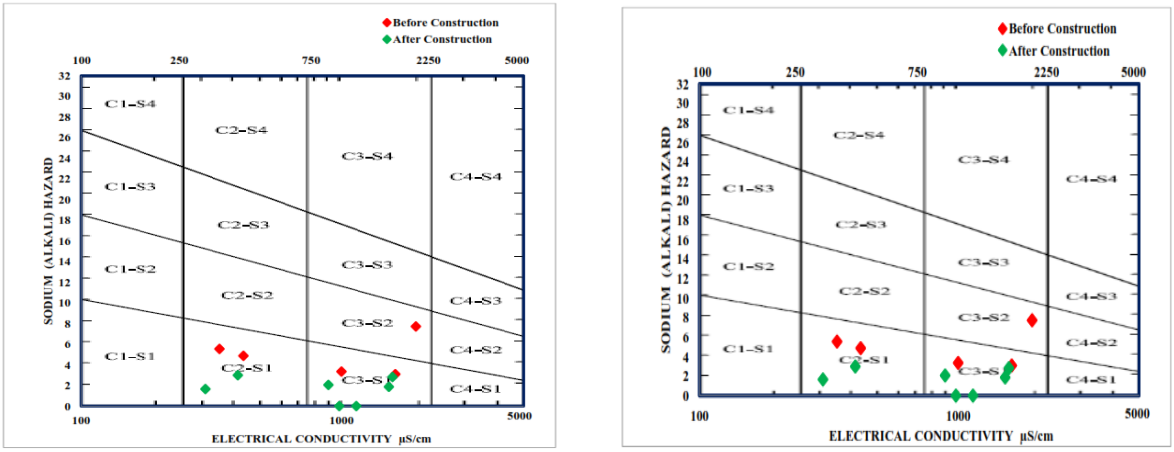


**a. Pre-monsoon** **b. Post - monsoon**

**Fig. 3. USSL plot: Mayiladumparai check dam**

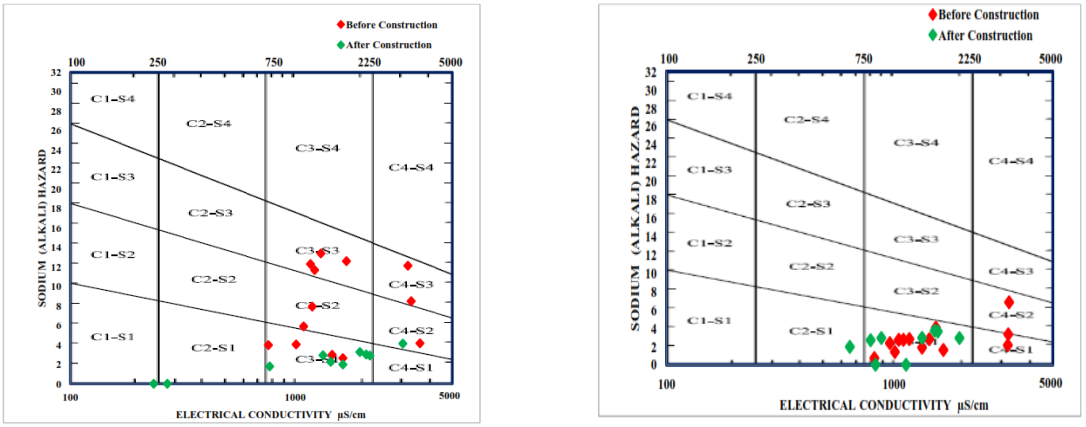


**a. Pre-monsoon** **b. Post - monsoon**

**Fig. 4. USSL plot: Amachiyapuram check dam**

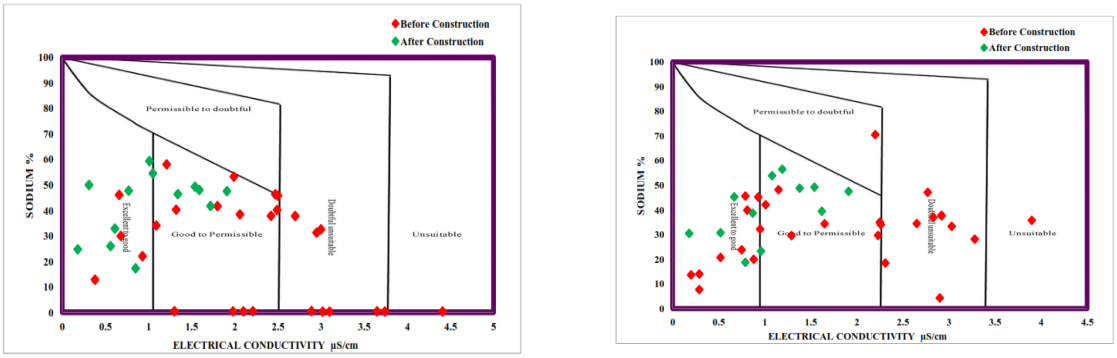


**a. Pre-monsoon** **b. Post - monsoon**

**Fig. 5. Wilcox plot: Ambasamudram check dam**

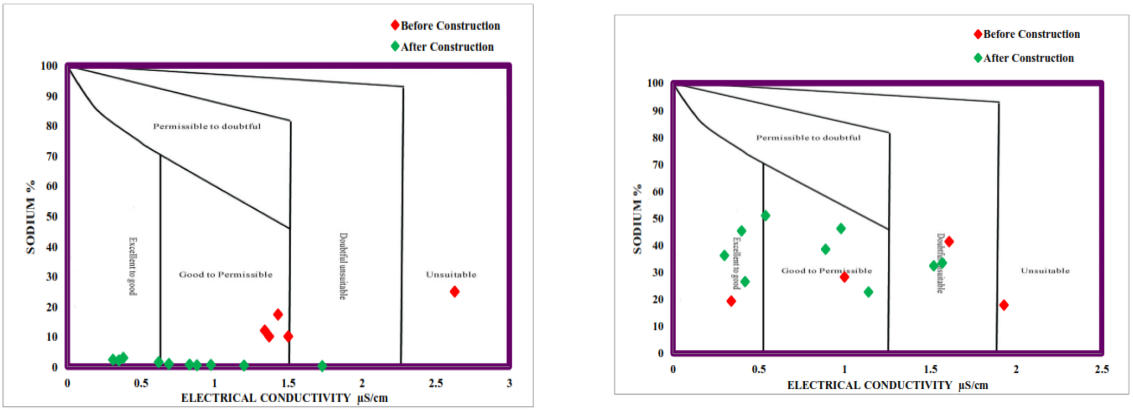


**a. Pre-monsoon** **b. Post - monsoon**

**Fig. 6. Wilcox plot: Mayiladumparai check dam**

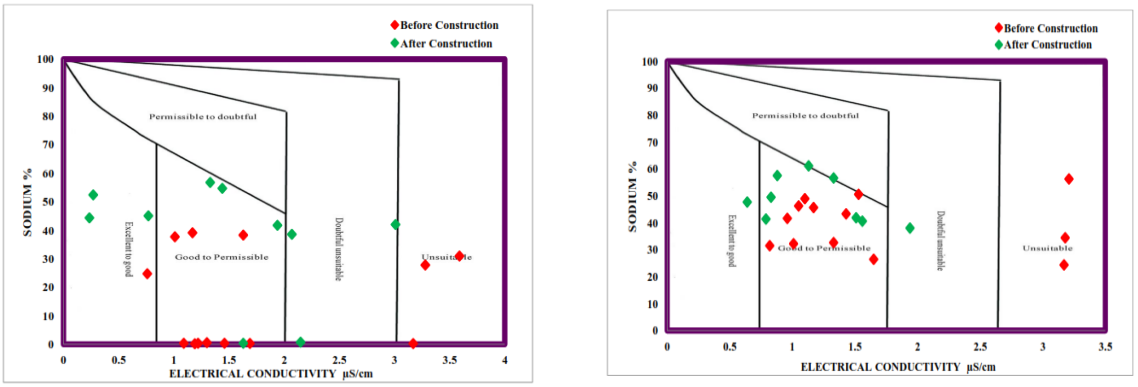


**a. Pre-monsoon** **b. Post - monsoon**

**Fig. 7. Wilcox plot: Amachiyapuram check dam**

### 3.3. Piper Trilinear Plot

Groundwater quality and hydrochemical composition were monitored at Ambasamudram, Mayiladumparai, and Amachiyapuram before and after check dam construction, revealing varying impacts across the sites. At Ambasamudram, pre-monsoon groundwater was largely unsuitable for irrigation, with 33% of samples doubtful to unsuitable (Na% > 60) and 48% permissible (Na% 40–60), while post-construction 85% of samples improved to excellent (Na% 0–20) and 15% good (Na% 20–40), reflecting reduced $Na^+$ and EC due to enhanced recharge (Verma *et al*., 2020); Piper plots (Fig. 8 a & b) indicated a shift from $Mg^{2+}$–$Ca^{2+}$ dominance to No Dominant Cation Type with increased $HCO_3^-$, showing balanced cation distribution and improved dilution, although post-monsoon 58% of samples fell into the doubtful to unsuitable category, highlighting seasonal effects.

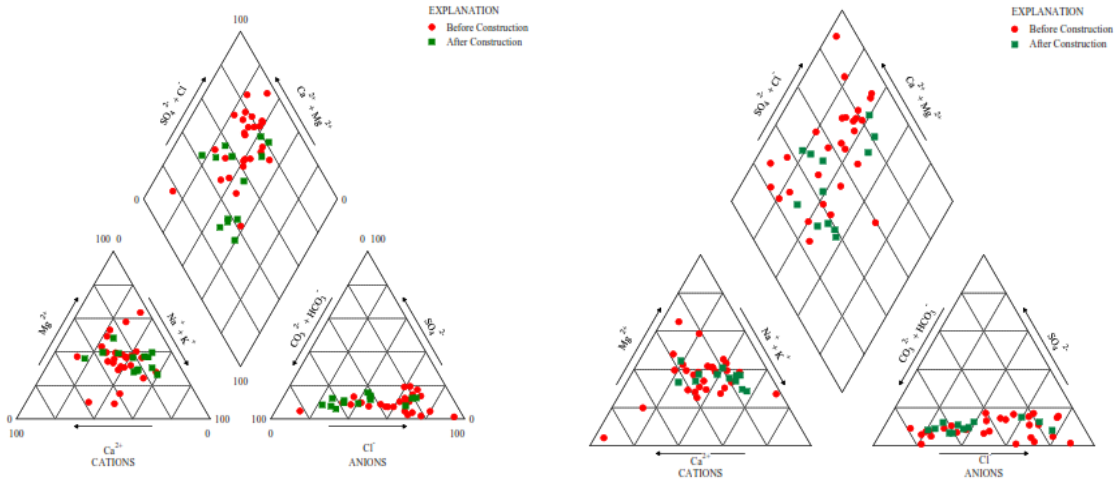


**a. Pre-monsoon** **b. Post - monsoon**

**Fig. 8. Piper trilinear plot: Ambasamudram check dam**

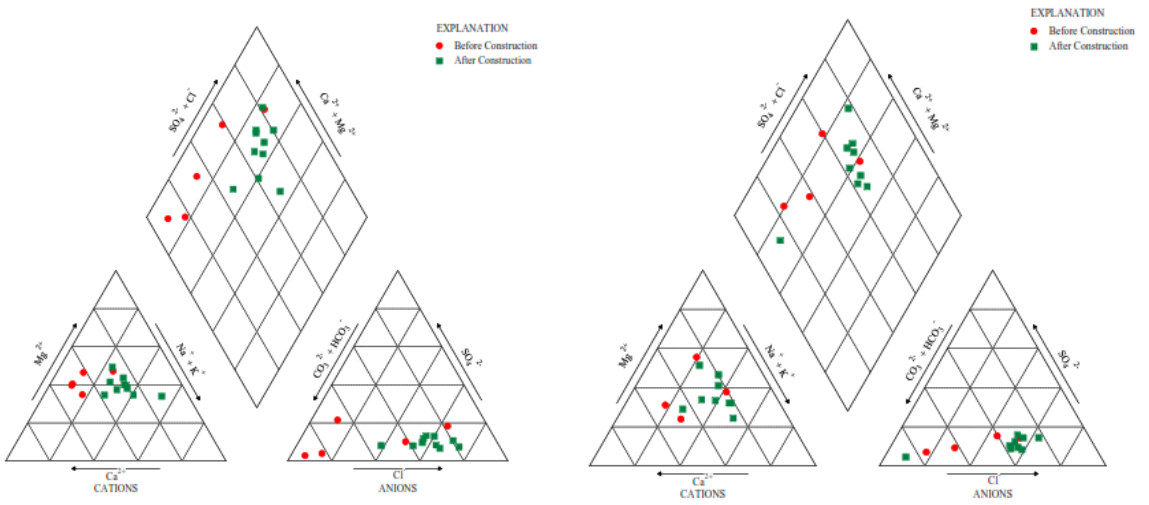


**a. Pre-monsoon** **b. Post - monsoon**

**Fig. 9. Piper trilinear plot: Mayiladumparai check dam.**

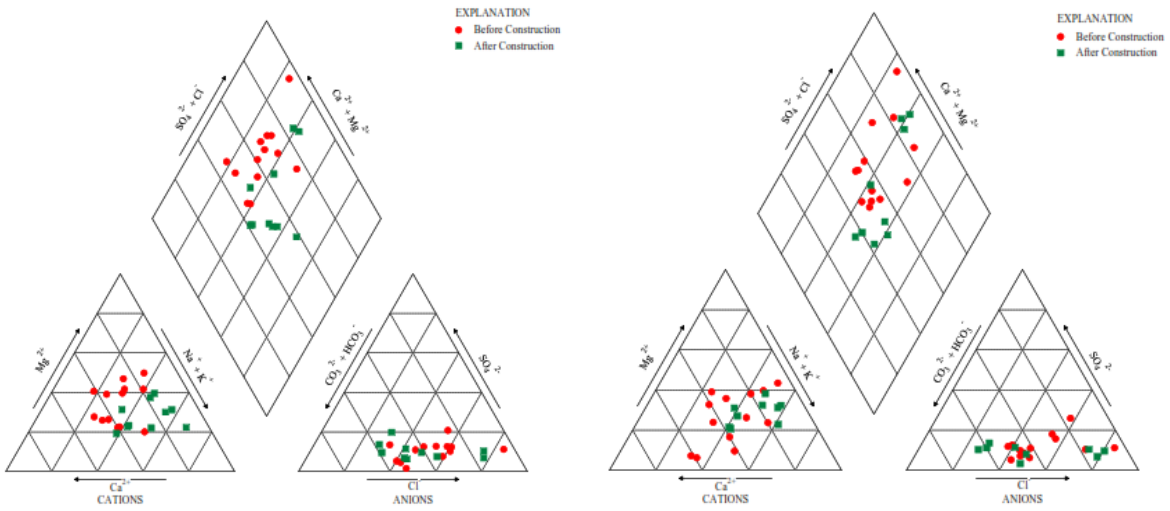


**a. Pre-monsoon** **b. Post - monsoon**

**Fig. 10. Piper trilinear plot: Amachiyapuram check dam.**

Mayiladumparai exhibited moderate pre-monsoon suitability, with 80% permissible (Na% 40–60) and 20% good (Na% 20–40), and post-construction improvements were modest, with 50% of samples good to permissible; Piper diagrams (Fig. 9 a and b) showed limited cation–anion changes, indicating stabilization rather than substantial enhancement. Amachiyapuram pre-monsoon samples were 23% unsuitable and 77% permissible, improving post-construction to 30% excellent and 50% good (Verma *et al*., 2020; Alshehri *et al*., 2023), with Piper plots (Fig. 10 a & b) showing 65% No Dominant Cation Type, 25% $Ca^{2+}$–$Mg^{2+}$, minor $Na^{+} + K^{+}$ dominance, and $Cl^{-}$ with emerging $SO_4^{2-}$, reflecting mixed hydrochemical sources and minimal seasonal influence. Overall, Ambasamudram experienced the greatest improvement, Amachiyapuram

moderate, and Mayiladumparai the least, indicating that check dams enhance groundwater recharge and reduce salinity hazards, but the magnitude of improvement varies with local hydrogeology, initial water quality, and seasonal factors, highlighting the need for continued monitoring to sustain irrigation potential.

### 3.4. Trend Analysis for Ambasamudram, Mayiladumparai, and Amachiyapuram

Data from 2009 to 2018 were analyzed to assess groundwater levels, measured as the depth from the ground surface to the water table, where a decrease in depth indicates a rise in groundwater. The methodologies employed provided insights into temporal variations and influencing factors (Batarseh *et al*., 2021). During the pre-monsoon season, Ambasamudram (Table 2) exhibited an average groundwater depth of 9.62 m, with a Kendall's Tau of -0.556 ($p = 0.048$) and a Sen's slope of -0.959 m/year, indicating a statistically significant steep decline, confirmed by ITA in the bottom triangle due to limited recharge and high groundwater dependency. Post-monsoon, the depth slightly improved to 9.31 m, with a slower, statistically insignificant decline (Kendall's Tau -0.333, $p = 0.108$; Sen's slope -0.723 m/year), although ITA still indicated a downward trend. Mayiladumparai (Table 2) showed more severe pre-monsoon depletion, with an average depth of 13.89 m, Kendall's Tau -0.643 ($p = 0.035$), and Sen's slope -1.470 m/year, placed in the ITA bottom triangle, likely due to over-extraction and limited recharge; post-monsoon levels improved to 13.45 m, but the decreasing trend persisted (Kendall's Tau -0.467, $p = 0.062$; Sen's slope -1.012 m/year). Amachiyapuram (Table 2) had a pre-monsoon depth of 7.01 m, Kendall's Tau -0.556 ($p = 0.002$), and Sen's slope -0.381 m/year, also in the ITA bottom triangle, reflecting strong depletion; post-monsoon, the decline weakened (Kendall's Tau -0.378, $p = 0.079$; Sen's slope -0.215 m/year) but persisted. Overall, all three sites exhibited pre-monsoon groundwater decline, partially alleviated post-monsoon, with Mayiladumparai experiencing the sharpest depletion, highlighting the need for targeted water management to sustain aquifer levels. Tables 2 summarize these trends using Kendall's Tau, Sen's slope, and ITA, providing a comprehensive understanding of temporal groundwater changes across the selected sites.

From Figs. 2 - 10 and Table 2, the study findings reveal significant improvements after check dam construction, with groundwater recharge increasing by 44% at Mayiladumparai, 23% at Amachiyapuram, and 47% at Ambasamudram. These results confirm the positive impact of check dams on enhancing groundwater availability. However, the observed spatial variability in recharge levels highlights the significant role played by localized hydrogeological factors.

### 3.5. Hydrological Processes, Water Quality Interpretation, and Management Implications

The integrated hydrochemical evaluation, spatial-temporal classification, and trend analyses provide a comprehensive understanding of groundwater dynamics across the three check dam locations: Ambasamudram, Mayiladumparai, and Amachiyapuram. These findings not only illustrate water quality variations but also offer insights into underlying hydrological processes, potential contamination sources, and implications for irrigation management and sustainable groundwater use.

#### 3.5.1. Hydrological processes and seasonal trends

USSL and Wilcox diagrams revealed significant spatial and seasonal variability in groundwater salinity and sodium hazard across the three check dam catchments. Ambasamudram exhibited persistently high EC (> 4000 µS/cm) and SAR (C3–S4, C4–S4) in both seasons, indicating limited dilution and recharge despite the check dam. Piper plots show $Na^+$ and $K^+$ dominance with $Cl^-$ anions, suggesting prolonged evapotranspiration, fertilizer use, and anthropogenic inputs. Mayiladumparai displayed moderate EC (~2800 µS/cm) and SAR (C2–S3), with post-monsoon improvements due to enhanced infiltration and reduced anthropogenic pressure. Its Piper diagram shows $Ca^{2+}$ and $Mg^{2+}$

dominance, reflecting recharge from less mineralized sources. Amachiyapuram showed the most improvement post-construction, with EC ~1250 µS/cm, SAR in safer categories (C1–S2, C2–S2), and a mixed water type in the Piper plot, indicating balanced ionic composition from improved recharge and reduced runoff.

**Table 2. Trend analysis of groundwater level fluctuations at selected check dams**

| Season & Station | Average Depth to Groundwater (m) | Kendall's Tau | Trend Direction | p - value | Sen's Slope (m/year) | ITA Interpretation |
|---|---|---|---|---|---|---|
| **Pre-monsoon** | | | | | | |
| (a) Ambasamudram | 9.62 | -0.556 | Decreasing | 0.048 | -0.959 | Significant Decreasing Trend |
| (b) Mayiladumparai | 13.89 | -0.643 | Decreasing | 0.035 | -1.470 | Significant Decreasing Trend |
| (c) Amachiyapuram | 7.01 | -0.556 | Decreasing | 0.002 | -0.381 | Significant Decreasing Trend |
| **Post-monsoon** | | | | | | |
| (a) Ambasamudram | 9.31 | -0.333 | Decreasing | 0.108 | -0.723 | Insignificant Decreasing Trend |
| (b) Mayiladumparai | 13.45 | -0.467 | Decreasing | 0.062 | -1.012 | Insignificant Decreasing Trend |
| (c) Amachiyapuram | 6.72 | -0.378 | Decreasing | 0.079 | -0.215 | Insignificant Decreasing Trend |

### 3.5.2. Influence of land use and cropping practices

Cropping patterns and irrigation practices directly affected groundwater quality. Ambasamudram's intensive rice–rice–pulse system with basin irrigation increases water demand and nutrient leaching, maintaining high salinity and sodium levels post-construction. Mayiladumparai, cultivating groundnut, millets, and pulses with furrow/ridge irrigation, promotes recharge and lowers leaching. Amachiyapuram, with diversified cropping and moderate irrigation, achieved noticeable post-monsoon water quality improvement.

### 3.5.3. Pollution sources and quality suitability

Ionic ratios and geochemical signatures indicate contamination sources. Elevated $Na^+$ and $Cl^-$ in Ambasamudram suggest fertilizer input, poor drainage, and over-irrigation, whereas Mayiladumparai and Amachiyapuram show mostly geogenic signatures. Wilcox and USSL classifications indicate Ambasamudram groundwater is unsuitable for most crops without treatment, while the other two sites support moderately salt-tolerant to salt-sensitive crops.

### 3.5.4. Trend analysis and long-term sustainability

Trend analysis using Kendall's Tau, Sen's slope, and ITA (Table 2) shows significant pre-monsoon groundwater decline at all sites, especially Ambasamudram (–0.412 m/year) and Amachiyapuram (-0.381 m/year). Post-monsoon trends remain negative but less severe, reflecting insufficient recharge and high extraction. ITA zones consistently in the bottom triangle highlight the need for adaptive water management.

### 3.5.5. Implications for water management

Site-specific strategies are critical: Ambasamudram requires controlled irrigation, improved drainage, and seasonal monitoring. Mayiladumparai benefits from expanded recharge structures and sustainable fertilization practices. Amachiyapuram illustrates effective water management through check dam construction, moderate cropping, and mixed irrigation. Overall, integrated hydrochemical, spatial, and temporal analyses underscore the need for sustainable irrigation, periodic monitoring, and recharge enhancement to ensure long-term groundwater sustainability.

## 3.6. Comparative Assessment of Irrigation Water Quality and Recharge Response across Selected Sites

Evaluation of irrigation water quality focused on electrical conductivity, sodium adsorption ratio, and sodium percentage using USSL and Wilcox plots. Distinct spatial variations emerged across sites, reflecting differential recharge effectiveness and hydrochemical response.

### 3.6.1. Irrigation suitability: USSL and Wilcox interpretations

Amachiyapuram showed EC reduction to ~1250 µS/cm pre-monsoon, SAR below 8, and Na% under 20 in nearly half the samples, indicating efficient ionic moderation post-recharge. This aligns with Ahn *et al.* (2023), where managed aquifer recharge reduced SAR from 11.2 to 7.6. Mayiladumparai recorded moderate values (EC ~2600 µS/cm, SAR ~13, Na% 20–60), reflecting marginal dilution, consistent with Fu *et al*. (2023) who reported EC 2300–2700 µS/cm and SAR >12 in coastal aquifers under seasonal recharge. Ambasamudram maintained high EC (2500–2800 µS/cm), SAR >13, and Na% >60, showing minimal improvement despite recharge, similar to trends observed by Alshehri *et al*. (2023) in arid inland zones.

### 3.6.2. Hydrochemical signature: Piper Plot Insights

Piper plots indicated clear hydrochemical evolution across sites. Amachiyapuram exhibited increased $Ca^{2+}$–$Mg^{2+}$ proportions and reduced $Na^{+}$ dominance, with diamond field samples trending toward balanced facies, supporting interpretations by Mahammad *et al.* (2023) for stable anthropogenic recharge. Mayiladumparai showed partial $SO_4^{2-}$ increase while $Cl^{-}$ remained dominant; cation balance was moderately unstable, consistent with Li *et al*. (2022) in irrigation-stressed aquifers. Ambasamudram retained $Na^{+}$–$Cl^{-}$ dominance, with Piper plots confirming persistent saline signatures, reflecting findings of Asomaku (2023) where seasonal recharge produced minimal ionic restructuring in landfill-adjacent aquifers.

### 3.6.3. Quality trend reflection across time

Amachiyapuram pattern displayed consistent SAR decline, EC reduction across multiple seasons, indicating long-term recharge impact. Similar hydrochemical behavior recorded in the Upper Vaigai sub-basin, documented through MIKE-HYDRO simulations (Keerthy *et al.*, 2024), projected declining salinity under effective structure placement. Mayiladumparai seasonal variation remained limited, SAR and EC fluctuations stayed minor. This aligned with Batarseh *et al.* (2021), who observed irrigation water index remained unchanged in low-permeability terrains despite structural interventions, reflecting comparable stagnation. Ambasamudram yielded near-static values through time. Climatological and lithological barriers possibly restricted percolation. Findings matched Ekbal and Khan (2022), where similar granitic formations exhibited stable high-salinity zones due to weak recharge response.

This study concluded that Amachiyapuram recorded significant hydrochemical improvement, aligning with recharge-responsive aquifers reported under managed conditions. Mayiladumparai revealed limited changes,

reflecting transitional behaviour under restricted hydraulic conductivity. Ambasamudram remained chemically static, resembling earlier documented non-responsive aquifers under confined or fractured geological settings.

### 3.7. Implication of the Study

This study demonstrates the effectiveness of check dams supporting sustainable groundwater management within semi-arid regions. The observed increase in recharge levels across all three sites confirms their value in enhancing groundwater availability. However, variation in performance between locations highlights the influence of site-specific conditions such as soil permeability, aquifer properties, and land use patterns. Achieving more reliable outcomes requires incorporating detailed hydrogeological assessments that inform the placement, design, and construction of check dams. A uniform approach may not yield consistent results; instead, adopting a location-sensitive, data-informed methodology helps optimize performance. These findings provide a scientific basis supporting the development of adaptive and resilient groundwater management strategies amid growing water stress from climate variability, rising population, and agricultural expansion.

## 4. CONCLUSIONS

The Upper Vaigai sub-basin was selected for the current study because of its importance as the primary water source and irrigation source for Theni district and the surrounding areas. Groundwater plays a critical role as an additional water resource for the area due to the Vaigai River not being perennial. To enhance ground potential, three check dams were built along the Vaigai River. It is essential to assess the impact of these check dams on groundwater quality and recharge to determine their effectiveness. The quality of groundwater for irrigation suitability was evaluated using irrigation indices and hydrochemical diagrams like the USSL plot, Wilcox plot, and Piper trilinear plot. The USSL plot indicated a shift from C3–S4 and C4–S4 to C1–S2 and C2–S2 zones at Amachiyapuram, and from C3–S4 to C2–S3 at Mayiladumparai showing improved conditions post-construction, except for minimal improvement observed in Mayiladumparai. The Wilcox plot showed water moving from “unsuitable” to “permissible” zones in Amachiyapuram and from “doubtful” to “permissible” in Mayiladumparai, while Ambasamudram remained in the “unsuitable” range. The Piper plot displayed a shift from $Na^{+}$–$Cl^{-}$ dominance to mixed $Ca^{2+}$–$Mg^{2+}$ types in Amachiyapuram, indicating balanced recharge. These variations are likely due to differences in geology, cropping systems, and soil characteristics. Groundwater quantity trends analyzed using Mann-Kendall, Sen slope, and ITA indicated a significant pre-monsoon decline in Amachiyapuram (Sen: –0.381 m/year), Ambasamudram (- 0.412 m/year), and Mayiladumparai (- 1.470 m/year), with all ITA zones located in the bottom triangle, indicating continued depletion despite seasonal recharge. The analysis revealed that groundwater recharge rates increased by 47%, 44%, and 23% in Ambasamudram, Mayiladumparai, and Amachiyapuram, respectively. Check dam construction has contributed to improved groundwater quality and recharge, although the effectiveness varies based on site-specific factors such as geology, cropping patterns, and irrigation practices.

## ACKNOWLEDGEMENT

Authors sincerely thank the Departments of Civil Engineering, Thiagarajar College of Engineering, Madurai; Agricultural Engineering, Kalasalingam Academy of Research and Education, Krishnankoil; and Agricultural Engineering, ACRI-TNAU Campus, Madurai, for their support, and resources that greatly contributed to this work.

## REFERENCES


1. Aher, S., Deshmukh, K., Gawali, P., Zolekar, R. and Deshmukh, P. 2022. Hydrogeochemical characteristics and groundwater quality investigation along the basinal cross-section of Pravara River, Maharashtra, India. *Journal of Asian Earth Sciences*, X(7):1-13. https://doi.org/10.1016/ j.jaesx.2022.100082.
2. Ahn, S. H., Jeong, D. H., Kim, M., Lee, T. K. and Kim, H. K. 2023. Prediction of groundwater quality index to assess suitability for drinking purpose using averaged neural network and geospatial analysis. *Ecotoxicology and Environmental Safety*, 265:1-9. https://doi.org/ 10.1016/j.ecoenv.2023.115485.
3. Alshehri, F., El-Sorogy, A. S., Almadani, S. and Aldossari, M. 2023. Groundwater quality assessment in western Saudi Arabia using GIS and multivariate analysis. *Journal of King Saud University-Science*, 35(4):1-10. https: //doi.org/10.1016/j.jksus.2023.102586.
4. APHA (American Public Health Association). 2017. *Standard Methods for the Examination of Water and Wastewater*, 23rd ed. Washington, DC: American Public Health Association. https://www.standardmethods.org.
5. Asomaku, S. O. 2023. Quality assessment of groundwater sourced from nearby abandoned landfills from industrial city in Nigeria: Water pollution indices approach. *HydroResearch*, 6:130-137. https://doi.org/10.1016/j.hydres.2023.0 3.002.
6. Batarseh, M., Imreizeeq, E., Tilev, S., Al Alaween, M., Suleiman, W., Al Remeithi, A. M., Al Tamimi, M. K. and Al Alawneh, M. 2021. Assessment of groundwater quality for irrigation in the arid regions using irrigation water quality index (IWQI) and GIS-Zoning maps: Case study from Abu Dhabi Emirate, UAE. *Groundwater for Sustainable Development*, 14:1-17. https://doi.org/10.1016/j.gsd.2021.100611.
7. Central Ground Water Board (CGWB). Various years. *Ground Water Year Book*. Ministry of Jal Shakti, Department of Water Resources, Government of India. http://cgwb.gov.in/Ground-Water/ Year-Book.html.
8. Da Silva, J., Fernandes, V., Limont, M., Dziedzic, M., Andreoli, C. V. and Rauen, W. B. 2020. Water sustainability assessment from the perspective of sustainable development capitals: Conceptual model and index based on literature review. *Journal of Environmental Management*, 254: 109750. https://doi.org/10.1016/j.jenvman. 2019.109750.
9. Daneshvar Vousoughi, F., Dinpashoh, Y., Aalami, M. T. and Jhajharia, D. 2013. Trend analysis of groundwater using non-parametric methods (case study: Ardabil plain). *Stochastic Environmental Research and Risk Assessment*, 27:547-559. https://doi. org/10.1007/s00477-012-0599-4.
10. Dhakate, R., Guguloth, S. and Srinivas, B. 2021. Hydrochemical appraisal of groundwater quality for drinking and agricultural utility in a granitic terrain of Maheshwaram area of Ranga Reddy district, Telangana State, India. *Hydro Research*, 4:11-23. https://doi.org/ 10.1016/ j.hydres.2021.02.002.
11. Ekbal, E. and Khan, T. A. 2022. Hydrogeochemical characterization of groundwater quality in parts of amroha district, western Uttar Pradesh, India. *HydroResearch*, 5:54-70. https:// doi.org/10.1016/j.hydres.2022.07.002.

12. Fu, T., Li, C., Wang, Z., Qi, C., Chen, G., Fu, Y., Su, Q., Xu, X., Liu, W. and Yu, H. 2023. Hydrochemical characteristics and quality assessment of groundwater in Guangxi coastal areas, China. *Marine Pollution Bulletin*, 188:114564. https://doi.org /10.1016/j.marpolbul. 2022.114564.

13. Gabr, M. E., Soussa, H. and Fattouh, E. 2021. Groundwater quality evaluation for drinking and irrigation uses in Dayrout city Upper Egypt. *Ain Shams Engineering Journal*, 12(1):327-340. https://doi.org/10.1016/j.asej.2020.05. 010.

14. Halder, S., Roy, M. B. and Roy, P. K. 2020. Analysis of groundwater level trend and groundwater drought using standard groundwater level index: a case study of an eastern river basin of West Bengal, India. *SN Applied Sciences*, 2(3):1-24. https://doi.org/ 10.1007/s42452-020-2302-6.

15. India Data Portal. 2024. *Groundwater levels and quality dataset (2009–2018)*. CKAN India Data Portal. https://ckandev.indiadataportal.com/dataset/groundwater/resource/580a8f6e-3d86-4ca7-ac7d-cd5df12b443c.

16. Kaliraj, S., Chandrasekar, N. and Magesh, N. S. 2014. Identification of potential groundwater recharge zones in Vaigai upper basin, Tamil Nadu, using GIS-based analytical hierarchical process (AHP) technique. *Arabian Journal of Geosciences*, 7:1385-1401. https://doi. org/10.1007/s12517-013-0849-x.

17. Kaliraj, S., Chandrasekar, N. and Magesh, N.S. 2015. Evaluation of multiple environmental factors for site-specific groundwater recharge structures in the Vaigai River upper basin, Tamil Nadu, India, using GIS-based weighted overlay analysis. *Environmental Earth Sciences*, 74:4355-4380.https://doi.org/ 10.1007/s12665-015-4384-9.

18. Keerthy, K., Chandran, S., Dhanasekarapandian, M. and Kumar, V. 2024. MIKE HYDRO River model's performance in simulating rainfall-runoff for Upper Vaigai sub-basin, Southern India. *Arabian Journal of Geosciences*, 17(4):125. https://doi. org/ 10.1007/s12517-024-11930-7.

19. Kumar, P. R., Gowd, S. S. and Krupavathi, C. 2024. Groundwater quality evaluation using water quality index and geospatial techniques in parts of Anantapur District, Andhra Pradesh, South India. *HydroResearch*, 7:86-98. https://doi.org/10.1016/j.hydres.2024.0 1.001.

20. Kumar, P., Chandniha, S. K., Lohani, A. K., Krishan, G. and Nema, A. K. 2018. Trend analysis of groundwater level using non-parametric tests in alluvial aquifers of Uttar Pradesh, India. *Current World Environment*, 13 (1):1-12. http://dx.doi.org/10.12944/ CWE.13.1.05.

21. Li, Z., Yang, Q., Xie, C., Wang, H. and Wang, Y. 2022. Spatiotemporal characteristics of groundwater quality and health risk assessment in Jinghe River Basin, Chinese Loess Plateau. *Ecotoxicology and Environmental Safety*, 248:1-12. https://doi.org/10.1016/ j.ecoenv. 2022. 114278.

22. Mahammad, S., Islam, A. and Shit, P. K. 2023. Geospatial assessment of groundwater quality using entropy-based irrigation water quality index and heavy metal pollution indices. *Environmental Science and Pollution Research*, 30 (55): 116498-116521. https://doi.org/10.1007/ s11356-022-20665-5.

23. Marghade, D., Malpe, D. B. and Subba Rao, N. 2021. Applications of geochemical and multivariate statistical approaches for the evaluation of groundwater quality and human health risks in a semi-arid region of eastern Maharashtra, India. *Environmental Geochemistry and Health*, 43:683-703. https://doi.org/10.1007/s10653-019-00478-1.

24. Parimala Renganayaki, S. and Elango, L. 2014. Impact of recharge from a check dam on groundwater quality and assessment of suitability for drinking and irrigation purposes. *Arabian Journal of Geosciences*, 7:3119-3129. https://doi.org/10.1007/s12517-013-0989-z.

25. Pothiraj, P. and Rajagopalan, B. 2013. A GIS and remote sensing based evaluation of groundwater potential zones in a hard rock terrain of Vaigai sub-basin, India. *Arabian Journal of Geosciences*, 6:2391-2407. https://doi.org/10.1007/s12517-011-0512-3.

26. Rajesh, R., Elango, L. and Brindha, K. 2019. Methods for assessing the groundwater quality. *GIS and Geostatistical Techniques for Groundwater Science*, 57-78. https://doi.org/10.1016/B978-0-12-815413-7.00006-7.

27. Rao, N. S., Gugulothu, S. and Das, R. 2022. Deciphering artificial groundwater recharge suitability zones in the agricultural area of a river basin in Andhra Pradesh, India using geospatial techniques and analytical hierarchical process method. *Catena*, 212:106085. https://doi.org/10.1016/j.catena.2022.106085

28. Rehman, F., Azeem, T., Hashmi, R. A., Siddique, J., Shahab, A. and Mustafa, S. 2023. Drinking and irrigation quality of groundwater and health risk assessment due to arsenic exposure in Sheikhupura district, Punjab, Pakistan. *Kuwait Journal of Science*, 50(3):368-375. https://doi.org/10.1016/j.kjs.2022. 12.001.

29. Sankar, K. 2002. Evaluation of groundwater potential zones using remote sensing data in Upper Vaigai river basin, Tamil Nadu, India. *Journal of the Indian Society of Remote Sensing*, 30:119-129. https://doi.org/10.1007/BF02990644.

30. Shaharudin, S. M., Ismail, S., Samsudin, M. S., Azid, A., Tan, M. L. and Basri, M. A. A. 2021. Prediction of epidemic trends in COVID-19 with mann-kendall and recurrent forecasting-singular spectrum analysis. *Sains Malays*, 50(4):1131-1142. http://doi.org/10.17576/jsm-2021-5004-23.

31. Sinha Ray, S. P. and Elango, L. 2019. Deterioration of groundwater quality: Implications and management. *Water governance: Challenges and prospects*, 87-101. https://doi.org/10.1007/978-981-13-2700-1_5.

32. Siraj, G., Khan, H. H. and Khan, A. 2023. Dynamics of surface water and groundwater quality using water quality indices and GIS in river Tamsa (Tons), Jalalpur, India. *Hydro Research*, 6: 89-107. https://doi.org/10.1016/j.hydres.2023.02.002.

33. Thakur, G. S. and Thomas, T. 2011. Analysis of groundwater levels for detection of trend in Sagar district, Madhya Pradesh. *Journal of the Geological Society of India*, 77(4):303-308. https://doi.org/10.1007/s12594-011-0038-z.

34. Thirumurugan, M., Manoj, S., Gowrisankar, G. and Elango, L. 2018. Hydrogeochemical characteristics and groundwater quality in a weathered rock aquifer in northern Karnataka,

India. *Geochemistry International*, 56: 950-960. https:// doi.org /10.1134/ S001670 2918090100.

35. Uddin, M. G., Diganta, M. T. M., Sajib, A. M., Hasan, M. A., Moniruzzaman, M., Rahman, A., Olbert, A. I. and Moniruzzaman, M. 2023. Assessment of hydrogeochemistry in groundwater using water quality index model and indices approaches. *Heliyon*, 9(9):1-22. doi: 10.1016/j.heliyon.2023.e19668.
36. Verma, A., Yadav, B. K. and Singh, N. B. 2020. Data on the assessment of groundwater quality in Gomti-Ganga alluvial plain of Northern India. *Data in Brief*, 30:1-11. https://doi.org/10.1016/ j.dib.2020.105660.
37. Wang, X., Zheng, W., Tian, W., Gao, Y., Wang, X., Tian, Y., Li, J. and Zhang, X., 2022. Groundwater hydrogeochemical characterization and quality assessment based on integrated weight matter-element extension analysis in Ningxia, upper Yellow River, Northwest China. *Ecological Indicators*, 135:1-14. https://doi.org/ 10.1016/j.ecolind.2021. 108525.
38. Yakovlev, E., Druzhinin, S., Druzhinina, A., Zykov, S. and Ivanchenko, N. 2023. Trace metals in surface water of the Pechora River and its tributaries: Content, water quality and risks assessment (Arctic Ocean basin). *Marine Pollution Bulletin*, 194: 115317. https://doi.org/10.1016/ j.marpolbul. 2023.115317.
39. Yilmaz, A. G., Shanableh, A., Al-Ruzouq, R. I. and Kayemah, N. 2020. Spatio-temporal trend analysis of groundwater levels in Sharjah, UAE. *International Journal of Environmental Science and Development*, 11(1):9-14. https://doi.org/ 10.18178/ijesd.2020.11.1.1218.
40. Zakwan, M. 2021. Trend analysis of groundwater level using innovative trend analysis. In *Groundwater resources development and planning in the Semi-Arid Region.* Cham: Springer International Publishing, 389-405. https://doi.org/ 10.1007/ 978-3-030-68124-1_20.

International Agricultural Engineering Journal ISSN 0858-2114

*September 2025, 34 (1-4) : 155-170*

# Climatic Variability and Groundnut Crop Yield: Unveiling the Scenario in Anantapur, India

**Fawaz Parapurath[1], Kumar Veluswamy[2]**

## ABSTRACT

Groundnut (*Arachis hypogaea*) cultivation in India relies solely on rainfed conditions and prevailing climatic conditions. The faster rate of change in climate variables combined with the occurrences of extreme weather events have a significant impact on agriculture. In this study, the trend in yield of groundnut at Anantapur, India is computed with respect to the variation in climatic parameters over 2000 to 2019. Indices namely the Soil Moisture Index (SMI), Moisture Availability Index (MAI), Aridity Index (AI), and Normalized Difference Moisture Index (NDMI) were utilized to elucidate the relationship between yield variations and climate variability. The findings reveal a slight hike in groundnut yield, with an increase of 1.1 kg/ha annually, corresponding to augmented wetness (manifested through rainfall and MAI) and diminished dryness (reflected by AI and consecutive dry days for 2D, 3D, & 4D). Notably, wetness indices such as SMI and MAI exhibited strong positive correlations (0.604** and 0.56*, respectively) with yield, while AI displayed a negative correlation (0.557*). Furthermore, NDMI peaks escalated from 0.76 to 0.81, indicating progressive soil moisture levels. These results suggest that climatic fluctuations in Anantapur have positively impacted groundnut yield (77.9% of the variability is explained by the selected predictors) with a discernible prevalence of wet conditions throughout the study period. This study employs both statistical and geospatial component (GEE – Java scripting) to analyse the relationship between groundnut yield and climatic variables, providing insights into the dynamics of agricultural productivity in the Anantapur region.

***Keywords:*** *Aridity Index (AI); Moisture Availability Index (MAI); Normalized Difference Moisture Index (NDMI): Soil Moisture Index (SMI).*

## 1. INTRODUCTION

Groundnut (*Arachis hypogaea*) stands among the top five crucial oilseed crops globally, holding significant importance for its nutritional content and economic value. It provides a major source of edible oil, protein, and income for millions of smallholder farmers, particularly in tropical and subtropical regions (Virmani and Shurapli, 1999). The productivity of groundnut varies worldwide due to diverse farming conditions, including differences in agro-climatic zones, soil fertility status, and cultivation practices. In India, factors such as abiotic stresses, inadequate soil fertility, pest and disease incidence, and limited access to quality inputs contribute to low groundnut productivity.

[1]Agro Climate Research Centre, Tamil Nadu Agricultural University, Coimbatore, India

[2]Formerly Professor and Head, Agrl. Engineering Dept., Agrl. College and Res. Institute, TNAU, Madurai, India.

**Corresponding author- email: faazzz96here@gmail.com*

Received: 07 December 2024; Revised: 14 August 2025; Accepted: 18 August 2025.

Additionally, a considerable proportion of groundnut cultivation occurs on marginal and submarginal lands, which further reduces yield potential under rainfed farming systems. Climatic fluctuations have emerged as a pivotal factor influencing crop production in arid and semi-arid regions, generating significant meteorological variations across seasons and years (Rao *et al.,* 2015). The magnitude and frequency of changes in climate that might impact crop productivity appear to be increasing, with projections indicating further escalation at both regional and global scales (Greve *et al.,* 2019; Subba Rao *et al.,* 2024). Even rapid increases in the frequency of extreme weather events pose significant challenges (Senapati *et al.,* 2024). Since, agriculture accounts for around 14% of India's GDP, a 4.5 - 9% decline productivity implies that the yearly cost of climate change could reach 1.5% of GDP (Subba Rao *et al.,* 2024).

From an agricultural perspective, crop response to changing climate can be evaluated by examining variability in thermal and moisture regimes using real-time crop data (Ong, 1984). For instance, rainfed crop production in the semi-arid tropics, including groundnut, exhibits substantial variation in response to seasonal rainfall anomalies and moisture availability (Gadgil *et al.,* 2002). Therefore, climate data analysis plays a critical role in lowering vulnerability to climate change through adaptation and mitigation strategies (Singh *et al.,* 2013). Several indices have been developed and applied in earlier studies to quantify moisture and climate variability, which are essential for understanding crop–climate interactions. The Aridity Index (AI), developed by Thornthwaite (1948) and further refined by Greve *et al.* (2019), served as a key indicator of dryness and water deficit conditions. The Moisture Availability Index (MAI), introduced by Hargreaves (1975), is used to evaluate the sufficiency of available moisture for crops during their growth cycle. Moreover, remote sensing based indices such as the Normalized Difference Moisture Index (NDMI) are also used to detect changes in vegetation water content and soil moisture over time (Gao, 1996; Nasiłowska and Kubiak, 2016). Although some studies employ machine learning (ML) techniques for remote sensing data analysis, this study does not use any ML models. NDMI data were obtained through standard processing algorithms in Google Earth Engine (GEE) without ML involvement. These indices have d been successfully applied in various agro-ecological contexts to assess the impacts of climate variability on agricultural systems. However, limited studies existed that integrate multiple wetness and dryness indices to examine their combined influence on groundnut yield in arid and semi-arid regions of India.

Research gaps remain in understanding how different climatic indices, particularly when used in combination, could explain variations in groundnut yield in regions like Anantapur, which is characterized by low and erratic rainfall. Most previous studies either focused on single climate parameters or broader regional analyses without detailed local-scale index-based assessments (Banik, 1996; Meng and Qian, 2024). Addressing this gap could provide more precise insights into climate–yield relationships and improve agricultural planning under changing climatic conditions. In this study, an analytical approach is attempted to assess variations in the productivity of groundnut grown under the arid climate of the Anantapur region in Peninsular India over 2000–2019 with two specific objectives. Firstly, to analyze the trend in climatic variables alongside yield patterns to discern any notable shifts or consistencies. Secondly, to calculate and assess the Aridity Index (AI), Moisture Availability Index (MAI), and Soil Moisture Index (SMI) along with NDMI, with the aim of determining their respective correlations with groundnut yield. This integrated analysis aims to address the lack of multi-index studies on groundnut - climate

interactions in arid regions of India has left to a need for a comprehensive investigation was considered imperative to identify the key factors influencing climate variability on seasonal scales in this context.

## 2. MATERIALS AND METHODS

### 2.1. Study Area

Data on groundnut (*kharif*) yields and weather variables in Anantapur from 2000 to 2019 were collected, with *kharif* seasonal data including weather variables for June, July, August, and September. Anantapur district, located in the drought-prone Rayalaseema region of Andhra Pradesh, India, is recognized as one of the country's top groundnut-producing areas. The district lies between 13º 41′ N & 15º 14' N latitude and 76º 47′ E & 78º 26' E longitude.

It has a hot semi-arid climate, with an average annual rainfall of 550 to 600 mm, mostly of which is received during the southwest monsoon. Groundnut cultivation in the region is primarily rainfed, making it highly vulnerable to inter-annual rainfall variability and extended dry periods. The predominant soils are red sandy loams classified as Alfisols, well-drained and suitable for groundnut growth but with low water-holding capacity, requiring careful rainfall management for successful yields. The warm temperatures during the glowing season, combined with the soil properties, create a favourable environment for groundnut production, although frequent droughts and erratic precipitation patterns often limit productivity. Major crops grown in the area include groundnut, red gram, sunflower, and maize.

### 2.2. Detrending of Yield

In general, crop yield time series can be divided into parts influenced by climatic factors and those that are not. The former, related s to the short-term yield volatility mostly caused by meteorological conditions, is known as meteorological yield. The long-term yield variance due to non-meteorological factors, like improved farm management (e.g., fertilizers, high-yielding varieties, irrigation practices, and crop management techniques) is called trend yield (Meng and Qian, 2024).

Trend yield ($Y_{tr}$) was estimated using the FAO approach, where the observed annual groundnut yield series ($Y_{ob}$) from 2000–2019 was smoothed using a centered 5-year moving average and fitted with a linear regression on year.

$$Y_{ob}(t) = \text{Total Production } (t) / \text{Area Sown } (t) \quad \ldots (1)$$

The fitted values represented $Y_{tr}$, capturing long-term, non-meteorological influences (e.g., improved varieties, fertilizers, irrigation). Meteorological yield ($Y_{met}$) was then calculated as:

$$Y_{tr}(t) = \alpha + \beta t \quad \ldots (2)$$

$$Y_{met}(t) = Y_{ob}(t) - Y_{tr}(t) \quad \ldots (3)$$

Where, $t$ is the year; α is the intercept and $\beta$ is the slope of the trend line.

### 2.3. Mann-Kendall trend test

The Mann-Kendall test statistic $S$ is calculated as (Mann, 1945; Kendall, 1975):

$$S = \sum_{i=1}^{n-1} \sum_{j=i+1}^{n} sgn(x_j - x_i) \quad \ldots (4)$$

Where, $n$ is the number of data points; $x_i$ and $x_j$ are the data values in time series $i$ and $j$ ($j>i$), respectively and $sgn\ (x_j - x_i)$ is the sign function as:

$$+1, if\ x_j - x_i > 0 \quad \ldots (5)$$

$$sgn(x_j - x_i) = 0, if\ x_j - x_i = 0 \quad \ldots (6)$$

$$-1, if\ x_j - x_i < 0 \quad \ldots (7)$$

The variance is computed as:

$$Var(S) = \frac{n(n-1)(2n+5) - \sum_{i=1}^{m} t_i(t_i-1)(2t_i+5)}{18} \quad \ldots (8)$$

Where, $n$ is the number of data points; $m$ is the number of tied groups; $t_i$ denotes the number of ties of extent $i$, and 18 is a constant. Testing of trends is done at the specific α significance level. In this study, α = 0.05 is used (5% significance level). When $|Z_S| > Z_{1-\alpha/2}$, the null hypothesis is

rejected, meaning the existing trend is significant ($Z_{1-\alpha/2}$ is obtained from the standard normal distribution table).

### 2.4. Sen's Slope estimator

Sen (1968) developed a non-parametric procedure for estimating the slope of trend (magnitude) in a sample of N pairs of data. The Sen's slope is computed as:

$$Q_{i=\frac{x_j - x_k}{j-k}} \quad \ldots (9)$$

The median of all $Q_i$ values is taken as the Sen's slope estimate. This method is robust against outliers and does not assume a normal distribution of residuals. If the calculated autocorrelation coefficient ($r_1$) is not significant at the 5% level, then the Mann–Kendall test and Sen's slope estimator are applied directly to the original time series.

### 2.5. Aridity Index (AI)

Since PET represents a theoretical maximum evapotranspiration under unlimited water availability, it needs to be estimated using data from climate models or meteorological observations (Table 1). The most widely used PET parameterizations come from various models designed to calculate evapotranspiration over open water or well-irrigated land areas (Greve *et al.*, 2019). The Thornthwaite method is used in this study to estimate *AI*, and the resulting equation is as follows:

$$\text{Aridity Index } (AI) = \frac{\text{Deficit}}{\text{Potential Evapotranspiration}} \text{x10} \quad \ldots (10)$$

Where, Deficit = *PET* – Actual Evapotranspiration (*AET*) or, if *AET* is not directly available, it can be estimated as:

$$\text{Deficit} = PET - \text{Precipitation } (P) \quad \ldots \quad (11)$$

If *PET* > P, the deficit is positive (moisture shortage), whereas if $PET \leq P$, the deficit is zero (no shortage).

According to UNEP (1992), AI classification, the $AI_{Thornthwaite}$ is related to $AI_{UNEP}$ as:

$$AI_{Thornthwaite} = (1 - AI_{UNEP}) * 100 \quad \ldots (12)$$

Here, *PET* was estimated using the Thornthwaite (1948) temperature-based method, while AET was derived from the Thornthwaite and Mather (1955) water balance approach, which incorporates precipitation, temperature, and soil water holding capacity for the study region.

**Table 1. Classification of Aridity Index (AI)**

| Classification | $AI_{Thornthwaite}$ | $AI_{UNEP}$ |
|---|---|---|
| Extremely arid | >95 % | <0.05 |
| Arid | 80-95 % | 0.05-0.2 |
| Semi-arid | 50-80 % | 0.2-0.5 |
| Dry sub-humid | 35-50 % | 0.5-0.65 |
| Humid | <35 % | >0.65 |

### 2.6. Soil Moisture Index (SMI)

The Moisture Index (MI) is a climatic indicator representing the net water balance over a specified time period, reflecting the relative dominance of wetting and drying processes in an agro-climatic system. Wetting processes (source functions) include precipitation, irrigation, and upward capillary movement of groundwater, while drying processes (sink functions) involve evapotranspiration, surface runoff, and deep percolation losses (Cornick *et al.*, 2003). In this study, MI was calculated using the Thornthwaite and Mather (1955) water balance model:

$$MI = \frac{(P-PET)}{PET} \text{ x } 100 \quad \ldots (13)$$

Where, *P* is precipitation, mm during the crop season and *PET* is potential evapotranspiration (mm), estimated using the Thornthwaite (1948) method. Soil moisture storage and actual evapotranspiration (*AET*) were computed by iteratively updating a soil water balance, assuming an available water-holding capacity of approximately 150 mm for Anantapur's dominant red sandy loam soils. The *MI* classifications (UNESCO, 1979) are Humid (>100), Moist sub-humid (50 to 100), Dry sub-humid (0 to 50), Semi-arid (-33.3 to 0), and Arid (<-33.3).

In this study, the Soil Moisture Index (SMI) was estimated following the climatic water balance approach of Thornthwaite and Mather (1955):

$$\text{Soil moisture index } (SMI) = \frac{\text{Surplus} - \text{Deficit}}{\text{Potential Evapotranspiration}} \text{X100} \quad \ldots (14)$$

The term surplus in mm is the amount of water available after meeting the crop's potential evapotranspiration (*PET*) demand, occurring when precipitation (*P*) plus stored soil moisture exceeds *PET*. This surplus represents potential runoff or groundwater recharge. A positive SMI value indicates net water gain (moisture surplus), whereas negative values reflect water stress (moisture deficit). For interpretation, values above +20 generally indicate favourable moisture conditions, values between 0 and -20 indicate mild stress, and values below -20 indicate severe drought conditions (UNESCO, 1977).

### 2.7 Moisture Availability Index (MAI)

MAI is defined as the ratio of weekly rainfall at different confidence levels to PET of the corresponding period (Hargreaves, 1971).

$$\text{Moisture availability Index (MAI)} = \frac{\text{Rainfall at different confidence interval}}{\text{Potential Evapotranspiration}} \text{ x } 100 \quad \ldots (15)$$

In this study, the 50% probability level was used, representing the median rainfall expected under normal climatic conditions. The MAI is typically computed for 30%, 50%, and 70% probability levels, where lower probability values (e.g., 30%) correspond to wetter-than-normal years, and higher probability values (e.g., 70%) represent dry years. According to Banik (1996), threshold MAI values can guide agricultural operations, such as scheduling transplanting or irrigation for rice cultivation.

### 2.8. Normalized Difference Moisture Index (NDMI)

The Normalized Difference Moisture Index (NDMI) was computed to quantify vegetation moisture content and assess drought stress conditions. NDMI is expressed as:

$$\text{Normalized Difference Moisture Index (NDMI)} = \frac{\text{NIR} - \text{SWIR}}{\text{NIR} + \text{SWIR}} \text{X100} \quad \ldots (16)$$

Where, NIR and SWIR represent the near-infrared and short-wave infrared reflectance values, respectively.

In this study, NDMI was derived from Landsat 5 TM, Landsat 7 ETM+, and Landsat 8 OLI satellite imagery accessed through the Google Earth Engine (GEE) platform covering the period 2000–2019. Landsat 5 and 7 utilized Band 4 (NIR) and Band 5 (SWIR), while Landsat 8 utilised Band 5 (NIR) and Band 6 (SWIR). Cloud-contaminated pixels were removed using the CFMask algorithm, and NDMI values corresponding to the peak crop growth months of August and September were extracted annually. This index has been recognised as an effective tool for monitoring vegetation water status (Gao, 1996; Wilson and Sader, 2002; Nasiłowska and Kubiak, 2016).

### 2.9. Correlation and Regression analysis

Correlation analysis was employed to quantify the strength and direction of the linear association between pairs of variables. The Pearson correlation coefficient (r) ranges from –1 to +1, where values closer to ±1 indicate stronger linear relationships, and values near 0 indicate weak or no linear relationship.

In this study, Multiple Linear Regression (MLR) analysis was conducted to assess the combined and individual effects of several independent variables on the dependent variable, Yield. In this approach, the dependent variable is modelled as a linear function of the predictors, allowing estimation of regression coefficients that quantify the expected change in Yield for a one-unit change in each predictor, holding all other variables constant.

## 3. RESULTS AND DISCUSSION

### 3.1. Climatological Outlook

The climatological summary reveals that the average percentage rainfall deviation over the South-west monsoon season coinciding with *kharif* (June, July, August, and September) from 2000 to 2019 was + 0.72%. The average absolute deviation in maximum temperature and minimum temperature were 0.05°C and 0.09°C, respectively. The normal seasonal (*kharif*) rainfall, maximum temperature and minimum temperature for Anantapur are 336.79 mm, 31.33°C, and 22.21°C, respectively (Table 2). During the study period, the maximum positive and negative rainfall deviation was observed in 2007 (69.72%) and 2002 (-49.08%), respectively. Similarly, the highest positive and negative deviation of maximum temperature were reported in 2015 (+0.97°C) and 2013 (-0.93°C). The highest positive deviation in minimum temperature was observed in 2019 (0.59°C) and negative deviations in 2000, 2008, 2010 equally (-0.31°C). Further, the fluctuations in yield with respect to the rainfall and temperature variation are represented in Fig. 2 and Fig. 3, respectively.

### 3.2. Yield dynamics with respect to Dry Days, Dryness Indicators and Wetness Indicators

The seasonal fluctuation of detrended yield along with the weather variables and indicators (wet and dry) are represented in Table 3. The results unveiled that the highest yield (1231.4 kg/ha) was reported in 2007 because of the occurrence of maximum rainfall (571.6 mm), which had also contributed to highest Moisture Availability Index (3.5) and Soil Moisture Index (1.41) over the study period. Conversely, the Potential Evapotranspiration (549.5 mm) and AI (12.94) recorded the lowest in 2017. However, the dryness indicators were substantially evident in the year 2001, with 10 consecutive two dry days (2D), 8 consecutive three dry days (3D) and 6 consecutive four dry days (4D).

### 3.3. Mann-Kendall Trend Test

The yield data and observed weather condition over the study period is tabulated (Table 4). It was observed that the yield shows a marginal increase of about 1.1 kg/ha per year over the period 2001–2019. The year-wise trends of weather variables and derived indices during the southwest monsoon revealed that the dryness in Anantapur is retarding slightly. However, the indices selected for trend analysis primarily serve as significant indicators of drought. Notably, AI (dryness parameter) displayed a small declining trend of about 0.28% per year. Conversely, rainfall and MAI (wetness parameter) showed slight upward tendencies, with yearly increases of about 2.5 mm/year and 0.01% per year, respectively. Furthermore, there was a modest reduction in consecutive dry days (two, three, and four days) during the southwest monsoon. From Table 4, it could be noted that all parameters, including rainfall, maximum temperature, minimum temperature, MAI, and yield, displayed positive but negligible trends, while consecutive dry days, AI, and SMI showed small negative trends. Importantly, none of these changes were statistically significant ($p > 0.05$), indicating that no conclusive trend can be established over the study period.

### 3.4. Karl Pearson's Coefficient of Correlation

From Fig. 4(a) and 4(b), the correlation matrix reveals significant interrelationships among the ten variables (var 1 to var 10) and their influence on yield. The wetness-related indices (SMI and MAI) tended to have positive relationships with groundnut yield, whereas dryness-related indices (AI and consecutive dry days) were negatively related. The highest positive association was observed between SMI (var 10) and yield ($r = 0.604$), followed by rainfall (var 1) and yield ($r = 0.59$). Conversely, AI (var 9) showed a moderate negative correlation with yield ($r = –0.557$). Rainfall (var 1) is strongly correlated

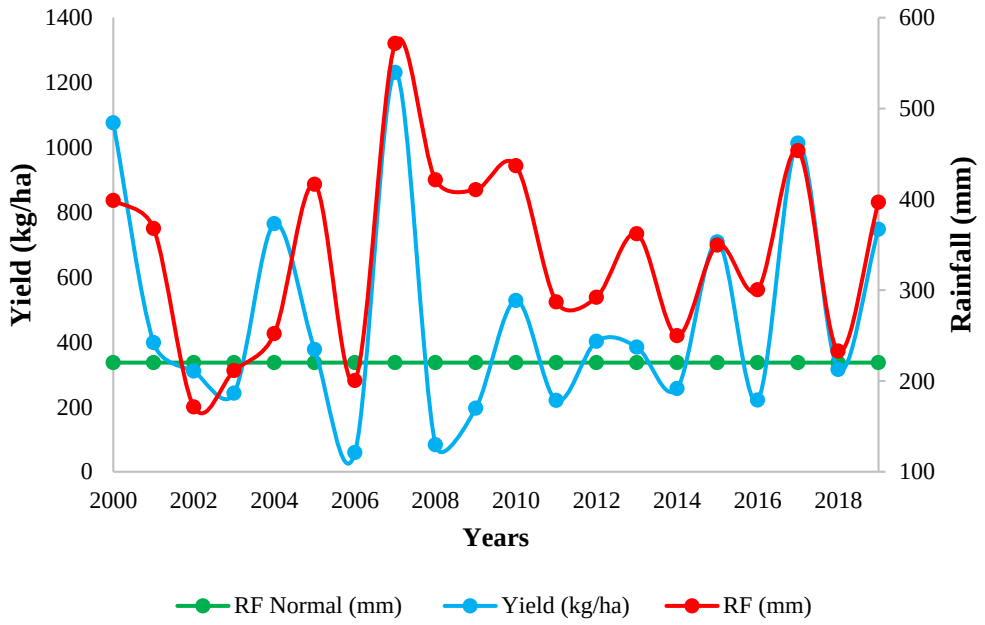


**Fig. 2. Yield variations with respect to rainfall fluctuations over the study period**

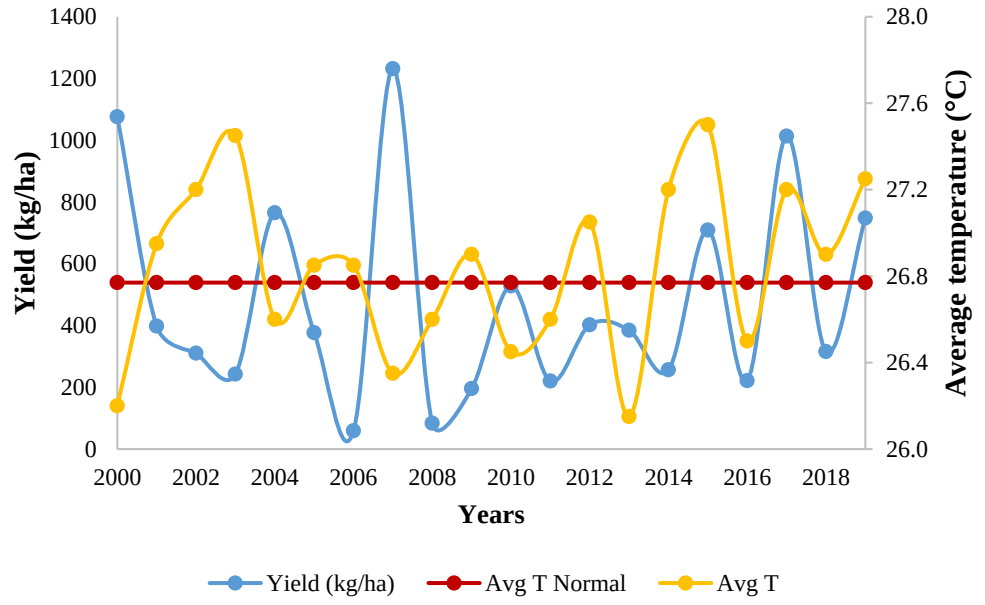


**Fig. 3. Yield variations with respect to temperature fluctuations over the study period**

**Table 2. Weather data and their deviation from the normal (2000 to 2019 - *kharif* season Anantapur)**

| Year | Rainfall, mm | Rainfall normal, mm | Rainfall deviation, % | Maximum temperature, °C | Maximum temperature normal, °C | Maximum temperature deviation, °C | Minimum temperature, T °C | Minimum temperature normal, °C | Minimum temperature deviation, °C |
|---|---|---|---|---|---|---|---|---|---|
| 2000 | 398.8 | 336.8 | 18.41 | 30.5 | 31.3 | –0.83 | 21.9 | 22.2 | –0.31 |
| 2001 | 368.0 | 336.8 | 9.27 | 31.4 | 31.3 | 0.07 | 22.5 | 22.2 | 0.29 |
| 2002 | 171.5 | 336.8 | –49.08 | 32.0 | 31.3 | 0.67 | 22.4 | 22.2 | 0.19 |
| 2003 | 211.4 | 336.8 | –37.23 | 32.2 | 31.3 | 0.87 | 22.7 | 22.2 | 0.49 |
| 2004 | 252.2 | 336.8 | –25.12 | 31.1 | 31.3 | –0.23 | 22.1 | 22.2 | –0.11 |
| 2005 | 416.5 | 336.8 | 23.67 | 31.3 | 31.3 | -0.03 | 22.4 | 22.2 | 0.19 |
| 2006 | 200.5 | 336.8 | –40.47 | 31.5 | 31.3 | 0.17 | 22.2 | 22.2 | –0.01 |
| 2007 | 571.6 | 336.8 | 69.72 | 30.5 | 31.3 | –0.83 | 22.2 | 22.2 | –0.01 |
| 2008 | 421.5 | 336.8 | 25.15 | 31.3 | 31.3 | –0.03 | 21.9 | 22.2 | –0.31 |
| 2009 | 410.6 | 336.8 | 21.91 | 31.6 | 31.3 | 0.27 | 22.2 | 22.2 | –0.01 |
| 2010 | 437.0 | 336.8 | 29.75 | 31.0 | 31.3 | –0.33 | 21.9 | 22.2 | –0.31 |
| 2011 | 287.0 | 336.8 | –14.78 | 31.2 | 31.3 | –0.13 | 22.0 | 22.2 | –0.21 |
| 2012 | 292.2 | 336.8 | –13.24 | 31.9 | 31.3 | 0.57 | 22.2 | 22.2 | –0.01 |
| 2013 | 362.1 | 336.8 | 7.51 | 30.4 | 31.3 | –0.93 | 21.9 | 22.2 | –0.31 |
| 2014 | 249.9 | 336.8 | –25.80 | 31.8 | 31.3 | 0.47 | 22.6 | 22.2 | 0.39 |
| 2015 | 349.6 | 336.8 | 3.80 | 32.3 | 31.3 | 0.97 | 22.7 | 22.2 | 0.49 |
| 2016 | 300.4 | 336.8 | –10.81 | 30.8 | 31.3 | –0.53 | 22.2 | 22.2 | –0.01 |
| 2017 | 453.6 | 336.8 | 34.68 | 31.7 | 31.3 | 0.37 | 22.7 | 22.2 | 0.49 |
| 2018 | 232.9 | 336.8 | –30.85 | 31.4 | 31.3 | 0.07 | 22.4 | 22.2 | 0.19 |
| 2019 | 396.9 | 336.8 | 17.85 | 31.7 | 31.3 | 0.37 | 22.8 | 22.2 | 0.59 |

**Table 3. Weather data, wetness and dryness indicators on the yield of groundnut (2000 to 2019 - *kharif* season - Anantapur)**

| Year | Yield, kg/ha | Rainfall, mm | Maximum temperature, ˚C | Minimum temperature, ˚C | Consecutive two dry days, 2D | Consecutive three dry days, 3D | Consecutive four dry days, 4D | PET, mm | Wetness and Dryness Indicators | | |
|---|---|---|---|---|---|---|---|---|---|---|---|
| | | | | | | | | | MAI | AI | SMI |
| 2000 | 1076.0 | 398.8 | 30.5 | 21.9 | 4 | 2 | 0 | 555.1 | 2.70 | 32.62 | 0.76 |
| 2001 | 398.2 | 368.0 | 31.4 | 22.5 | 10 | 8 | 6 | 578.5 | 1.84 | 55.00 | 1.00 |
| 2002 | 310.4 | 171.5 | 32.0 | 22.4 | 6 | 3 | 1 | 599.3 | 1.16 | 71.37 | 0.00 |
| 2003 | 242.6 | 211.4 | 32.2 | 22.7 | 5 | 3 | 1 | 604.0 | 1.43 | 65.00 | 0.00 |
| 2004 | 764.8 | 252.2 | 31.1 | 22.1 | 7 | 5 | 3 | 575.7 | 1.78 | 56.19 | 0.00 |
| 2005 | 377.0 | 416.5 | 31.3 | 22.4 | 5 | 3 | 1 | 577.6 | 2.96 | 28.00 | 0.01 |
| 2006 | 59.2 | 200.5 | 31.5 | 22.2 | 4 | 1 | 0 | 589.4 | 1.36 | 65.97 | 0.00 |
| 2007 | 1231.4 | 571.6 | 30.5 | 22.2 | 2 | 0 | 0 | 549.5 | 3.50 | 12.94 | 1.41 |
| 2008 | 83.6 | 421.5 | 31.3 | 21.9 | 5 | 3 | 1 | 586.3 | 2.66 | 34.61 | 0.38 |
| 2009 | 195.8 | 410.6 | 31.6 | 22.2 | 5 | 4 | 3 | 591.2 | 2.41 | 40.65 | 0.60 |
| 2010 | 528.0 | 437.0 | 31.0 | 21.9 | 1 | 0 | 0 | 576.3 | 3.01 | 25.21 | 0.16 |
| 2011 | 220.2 | 287.0 | 31.2 | 22.0 | 5 | 1 | 0 | 583.9 | 1.99 | 50.83 | 0.00 |
| 2012 | 402.4 | 292.2 | 31.9 | 22.2 | 9 | 6 | 4 | 600.8 | 1.98 | 51.36 | 0.00 |
| 2013 | 384.6 | 362.1 | 30.4 | 21.9 | 3 | 1 | 0 | 551.6 | 2.11 | 47.88 | 0.75 |
| 2014 | 256.8 | 249.9 | 31.8 | 22.6 | 6 | 3 | 1 | 590.9 | 1.69 | 57.71 | 0.00 |
| 2015 | 709.0 | 349.6 | 32.3 | 22.7 | 2 | 1 | 0 | 606.1 | 2.29 | 44.22 | 0.12 |
| 2016 | 221.2 | 300.4 | 30.8 | 22.2 | 3 | 1 | 0 | 560.9 | 2.13 | 46.44 | 0.00 |
| 2017 | 1013.4 | 453.6 | 31.7 | 22.7 | 3 | 1 | 0 | 581.7 | 2.70 | 33.73 | 0.68 |
| 2018 | 315.6 | 232.9 | 31.4 | 22.4 | 8 | 5 | 2 | 578.8 | 1.59 | 59.76 | 0.00 |
| 2019 | 747.8 | 396.9 | 31.7 | 22.8 | 7 | 4 | 2 | 581.5 | 2.11 | 49.58 | 1.00 |

**Table 4. Trends in weather parameters, moisture indices, and yield (2001–2019)**

| Particulars | $Z_c$ value | *P* value | Sen's slope | Significance | Remarks | Inference |
|---|---|---|---|---|---|---|
| RF, mm | 0.85 | 0.39 | 2.52 | Non-significant | Positive | Increasing Trend |
| Max T, °C | 1.67 | 0.09 | 0.01 | Non-significant | Positive | Increasing Trend |
| Min T, °C | 1.71 | 0.08 | 0.01 | Non-significant | Positive | Increasing Trend |
| Consecutive dry days, 2D | –1.17 | 0.24 | –0.03 | Non-significant | Negative | Decreasing Trend |
| Consecutive dry days, 3D | -0.86 | 0.38 | 0.00 | Non-significant | Negative | Decreasing Trend |
| Consecutive dry days, 4D | –1.12 | 0.26 | 0.00 | Non-significant | Negative | Decreasing Trend |
| AI, % | –0.34 | 0.72 | –0.28 | Non-significant | Negative | Decreasing Trend |
| SMI, % | –0.19 | 0.85 | 0.00 | Non-significant | Negative | Decreasing Trend |
| MAI, % | 0.63 | 0.52 | 0.01 | Non-significant | Positive | Increasing Trend |
| Yield, kg/ha | 0.62 | 0.53 | 1.12 | Non-significant | Positive | Increasing Trend |

$Z_c$ value – Mann–Kendall test statistic; *P* value – Probability value; Sen’s slope – Magnitude of change per year; Positive / Negative – Direction of trend.

with MAI (var 8) and SMI (var 10), reinforcing its central role in the system. Conversely, var 7 (Consecutive dry days (4D)) consistently shows negative correlations with most other variables and yield (r = −0.50 to −0.56), implying it may act as a suppressor or stressor within the system. Therefore, variables 1, 8, and 9 emerge as strong candidates for predictive modelling and yield optimization.

In contrast, maximum temperature (MaxT, var 2), minimum temperature (MinT, var 3), potential evapotranspiration (PET, var 4), and consecutive dry days at 2 day and 3 day thresholds (var 5 and 6) show non-significant correlations, suggesting limited or indirect impact under the prevailing conditions. These results emphasize the dominant role of rainfall and soil moisture in driving yield variability, while moisture stress indices capture sub-seasonal drought effects. However, these correlations only indicate associations and do not establish causation.

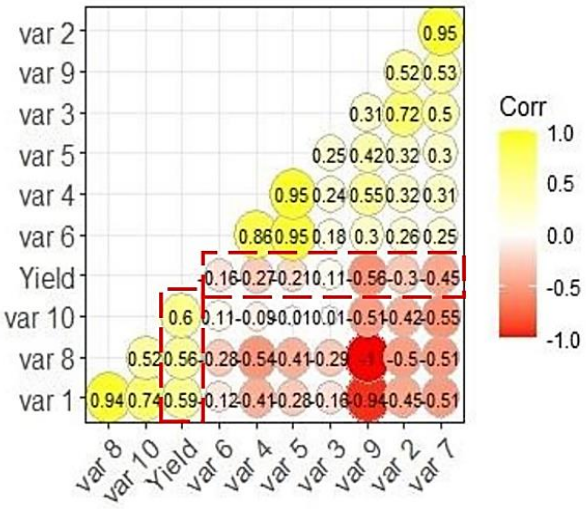


(a)

| Correlation | Remarks |
|---|---|
| (var 1) RF v/s Yield | Significant*** |
| (var 2) MaxT v/s Yield | Non-Significant |
| (var 3) MinT v/s Yield | Non-Significant |
| (var 4) PET v/s Yield | Non-Significant |
| (var 5) Consecutive dry days-2D v/s Yield | Non-Significant |
| (var 6) Consecutive dry days-3D v/s Yield | Non-Significant |
| (var 7) Consecutive dry days-4D v/s Yield | Significant** |
| (var 8) MAI v/s Yield | Significant** |
| (var 9) AI v/s Yield | Significant** |
| (var 10) SMI v/s Yield | Significant*** |

*95% confidence interval - ***
*99% confidence interval - ****

(b)

**Fig. 4 (a) Correlogram (b) Test of significance**

### 3.5. Regression Analysis – Multiple Linear Regression (MLR)

Fig. 5 represents the relationship between the actual and predicted yields obtained from a multiple linear regression model using ten independent variables: rainfall (RF), maximum temperature (MAX_T), minimum temperature (MIN_T), consecutive two dry days (2D), consecutive three dry days (3D), consecutive four dry days (4D), Potential evapotranspiration (PET), Moisture adequacy index (MAI), Aridity index (AI), and Soil moisture index (SMI). The regression equation, prominently displays MAX_T, 2D, 4D, MAI, AI, and SMI have positive coefficients, suggesting a direct association with yield, whereas RF, MIN_T, 3D, and PET exhibit negative coefficients, indicating an inverse relationship. The coefficient of determination ($R^2$) is 0.779, signifying that approximately 77.9% of the variability in yield can be explained by the selected predictors, reflecting a strong model fit.

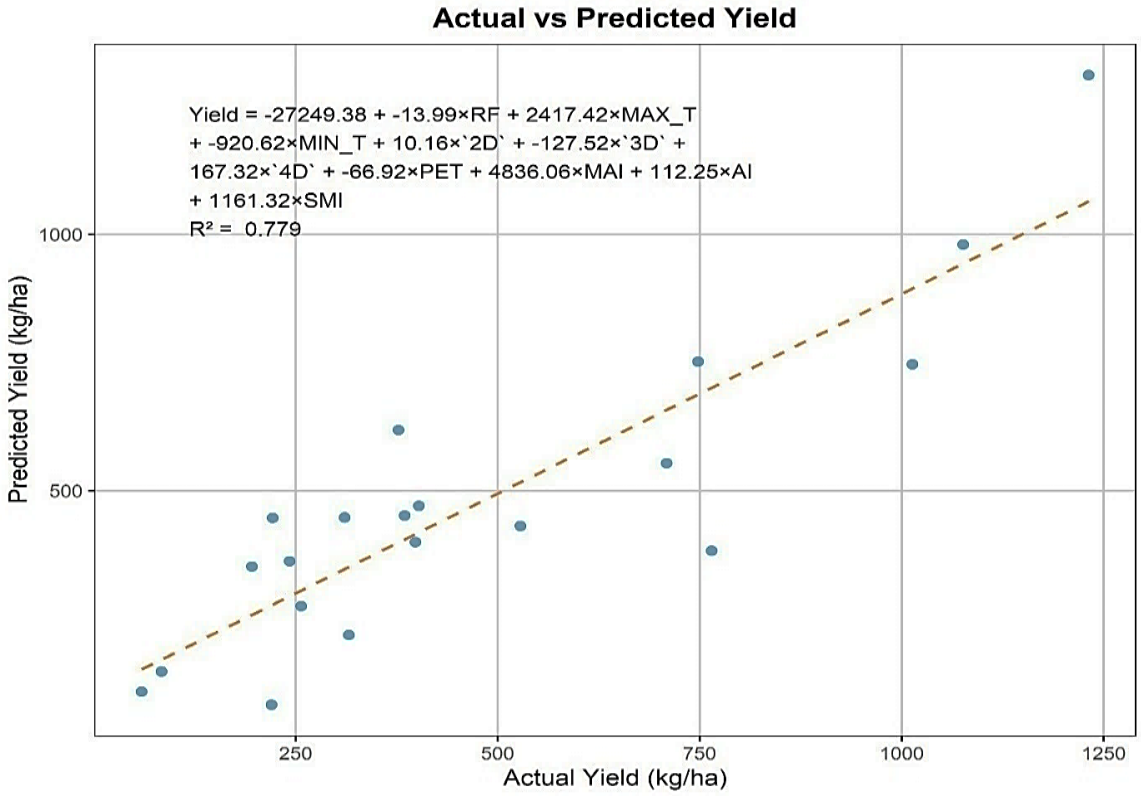


**Fig. 5 Multiple Linear Regression Plot**

### 3.6. Normalized Difference Moisture Index (NDMI)

Since NDMI index is an indication of surface soil wetness, the spatial and temporal dynamics of the land surface moisture can be computed based on the NDMI thresholds (ranging from low to high). From Fig. 6, it can be seen that, between 2000 and 2019, the spatial distribution of values exhibited a pronounced shift toward increased variability and polarization. In 2000, moderate values (−0.36 to 0.76) dominated the landscape, covering approximately 68.4% of the area, while high-value zones (≥0.6) and low-value zones (≤−0.2) were limited to 7.2% and 4.8%, respectively, indicating relatively stable baseline conditions. By 2009, high-value areas expanded to 11.6%, and low-value regions increased to 6.3%, suggesting a gradual intensification of spatial heterogeneity, potentially driven by land use transitions or climatic influences. In 2019, the area covered by high values rose sharply to 18.9%, representing an overall increase of 11.7% since 2000, while low-value zones more than doubled to 12.4%. This pronounced shift reflects significant environmental changes across the region, possibly linked to anthropogenic pressures, hydrological alterations, or localized remediation efforts. The contraction of moderate zones to 56.2% further underscores the growing spatial disparity, highlighting the need for targeted, site-specific management strategies. The observed trends suggest that the region is undergoing a dynamic transformation, with increasing spatial contrasts that may signal both degradation in vulnerable zones and improvement in areas benefiting from intervention. Continuous monitoring and adaptive planning are essential to mitigate emerging risks and sustain positive developments.

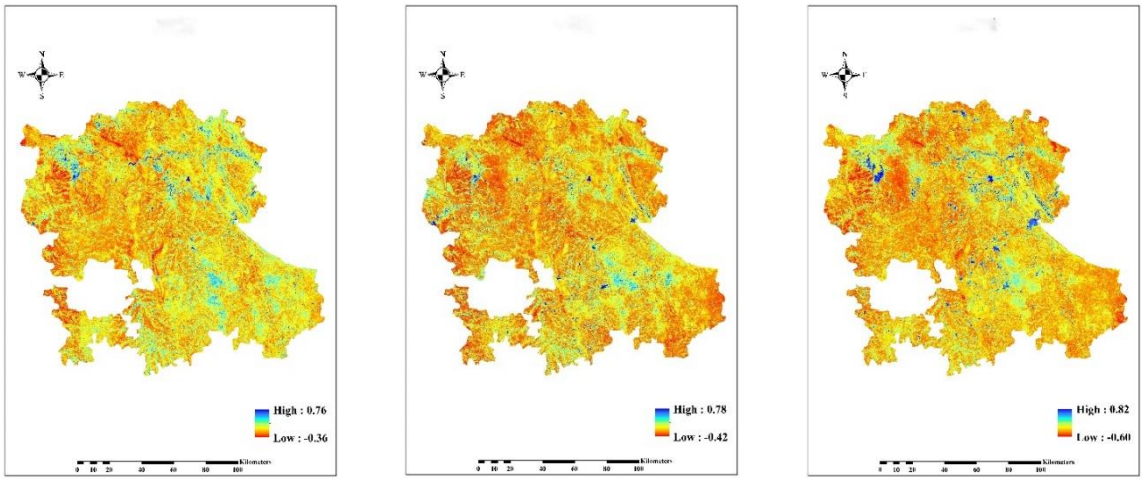


**Fig. 6. NDMI dynamics over 2000 to 2019**

### 3.7. Comparison with Previous Studies

The study of groundnut yield and weather variables in Anantapur district from 2000 to 2019 shows results both consistent with and distinct from earlier research. Unlike Rao *et al.* (2015) who reported pronounced yield fluctuations influenced by droughts, this study reveals a marginal but statistically insignificant increase in groundnut yield. Virmani and Shurapli (1999) emphasized rainfed groundnuts' vulnerability to erratic rainfall, often causing yield declines, whereas here, the yield trend remains relatively stable. This suggests that agronomic improvements may have mitigated climatic stresses more effectively than in previous decades.

#### 3.7.1. Rainfall and moisture trends

Climatic variables showed non-significant upward trends, with rainfall increasing by 2.52 mm/year and the Moisture Availability Index (MAI) rising slightly by 0.01% per year. Dryness indicators such as the Aridity Index (AI) declined marginally by 0.28% annually, though none were statistically significant. These results align with Singh *et al.* (2013), who underscored the importance of moisture availability over absolute rainfall for crop performance in the Semi-Arid Tropics. Overall, integrating rainfall and moisture indices into predictive models could enhance yield forecasting accuracy, while monitoring consecutive dry days beyond critical thresholds may support early warning systems and adaptive planning. Halder *et al.* (2020) reported that moisture availability strongly influences peanut yields under future climate variability scenarios in eastern India, consistent with the significant positive correlations observed here for rainfall, SMI, and MAI in Fig. 4.

#### 3.7.2. Relationship between yield and moisture indices

Correlation analyses highlighted strong positive associations between yield and moisture-related indices. The Soil Moisture Index (SMI) correlated most strongly with yield ($r = 0.604$, $p < 0.01$), followed by the Moisture Availability Index (MAI) ($r = 0.560$, $p < 0.05$). The Aridity Index (AI) showed a significant negative correlation ($r = – 0.557$, $p < 0.05$), while rainfall also had a significant positive relationship with yield ($r = 0.59$, $p < 0.01$). In contrast, temperature and evapotranspiration showed no significant correlation, reinforcing earlier findings (Ong, 1984; Virmani and Shurapli, 1999) that moisture availability is the key factor governing groundnut productivity in drought-prone environments. Arumugam *et al.* (2015) emphasized climate-

driven yield variability in rainfed crops in Tamil Nadu, with moisture stress as a primary factor, reinforcing the strong moisture-yield linkages and the tightly coupled subsystem involving variables 1, 6, 8, and 9 shown in Fig. 4(a). Further analysis revealed that groundnut yield fluctuations are closely linked to climatic variability associated with El Niño and La Niña events. Specifically, El Niño years tend to coincide with below-average rainfall and higher temperatures, resulting in reduced groundnut yields (Rao *et al.*, 2007; Aggarwal, 2008). Understanding this relationship is crucial for local farmers and policymakers, as it underscores the need for climate-resilient agricultural practices and timely forecasting. However, limitations such as variability in soil conditions and farming techniques must be considered when interpreting these results. Future research should focus on integrating climate models with crop simulation to improve yield predictions under different climatic scenarios.

### 3.7.3 NDMI and Surface moisture conditions

Normalized Difference Moisture Index (NDMI) analysis revealed a substantial 19.16% increase in areas with high NDMI values over the study period, indicating improved surface moisture conditions. The coverage of high NDMI zones expanded from 7.2% in 2000 to 18.9% in 2019, while low NDMI areas more than doubled, signaling increased spatial variability in soil moisture. This heterogeneity may reflect localized water conservation efforts, cropping changes, or land management practices, consistent with previous remote sensing studies (Nasiłowska and Kubiak, 2016; Cornick *et al.*, 2003). Kadiyala *et al.* (2015) demonstrated how integrating crop models with GIS tools helps capture and manage spatial variability in agricultural landscapes, emphasizing that rising spatial contrasts call for more precise, location-specific agronomic decisions.

## 4. CONCLUSIONS

In the context of climate change, the hypothesis is that the dry area becomes drier and the wet area becomes wetter. Nevertheless, the analysis for Anantapur during 2000–2019 reveals that wetness indicators, including SMI, MAI, and NDMI, exhibited significant increasing trends attributable to climatic variability, despite the region's arid classification. The increased wetness and decreased dryness components (decrease in AI and Consecutive dry days for 2D, 3D and 4D) attributed to a positive trend in yield. Although wetness indices like SMI and MAI correlated positively with yield, whereas AI depicted a negative relationship, NDMI indicated improved soil moisture levels over the study period. The variations in wetness indices (SMI and MAI) and dryness indicators (*AI*, consecutive dry days) showed clear associations with groundnut yield, although the overall annual increase of 1.12 kg/ha was small, indicating a weak yield response to climate variability. This lack of significance may be due to adaptive management by farmers, inherent crop resilience, and unaccounted non-climatic factors like soil fertility and pest pressure. Future research should focus on weather fluctuations during critical crop growth phases, including El Niño and La Niña years. Adaptive measures such as drought-resistant varieties, improved irrigation, and climate-smart planning can help mitigate these impacts. These findings enhance understanding of climate effects on groundnut and support efforts to improve farming resilience.

## DATA AVAILABILITY

Manuscript data may be available upon reasonable request.

## DECLARATION OF COMPETING INTEREST

The authors of this manuscript declare that they do not have any competing financial interests or personal relationships that could have appeared to influence the work reported in this paper.

## AUTHOR CONTRIBUTIONS

**Fawaz Parapurath:** Conceptualization, Data Curation, Methodology, Review & Editing, and Writing - Original Draft; **Kumar Veluswamy:** Review & Supervision, writing in revision.

## REFERENCES


1. Aggarwal, P. K. 2008. Implications of global climate change for Indian agriculture. In *ISPRS Archives XXXVIII-8/W3 Workshop Proceedings: Impact of Climate Change on Agriculture*.
2. Arumugam, S., K. R., A., Kulshreshtha, S. N., Vellangany, I. and Govindasamy, R. 2015. Yield variability in rainfed crops as influenced by climate variables: A micro level investigation into agro-climatic zones of Tamil Nadu, India. *International Journal of Climate Change Strategies and Management,* 7: 442–459.
3. Banik, P. 1996. *Studies on paddy based cropping system under different agronomical practices in eastern plateau area.* Unpublished Ph.D. thesis, University of Calcutta, West Bengal, pp. 267.
4. Cornick, S., Djebbar, R. and Dalgliesh, W. A. 2003. Selecting moisture reference years using a Moisture Index approach. *Building and Environment*, 38(12): 1367-1379.
5. Gadgil, S., Rao, P. S. and Rao, K. N. 2002. Use of climate information for farm-level decision making: rainfed groundnut in southern India. *Agricultural Systems*, 74(3): 431-457.
6. Gao, B.C. 1996. NDWI - A normalized difference water index for remote sensing of vegetation liquid water from space. *Remote Sensing of Environment*, 58(3): 257–266.
7. Greve, P., Roderick, M. L., Ukkola, A. M. and Wada, Y. 2019. The aridity index under global warming. *Environmental Research Letters*, 14(12): 124006.
8. Halder, D., Kheroar, S., Srivastava, R. K. and Panda, R. K. 2020. Assessment of future climate variability and potential adaptation strategies on yield of peanut and *kharif* rice in eastern India. *Theoretical and Applied Climatology*, 140: 823–838.
9. Hargreaves, G. H. 1975. Moisture availability and crop production, *Transactions of the ASAE*. 18(5): 980-984.
10. Hargreaves, G.H. 1971. Precipitation dependability and potential for agricultural production in north-east Brazil. *EMBRAPA and Utah State University Publication No.74-D 159.* pp.123.
11. Kadiyala, M. D. M., Nedumaran, S., Padmanabhan, J., Gumma, M. K., Gummadi, S., Srigiri, S. R., Robertson, R. and Whitbread, A. 2021. Modeling the potential impacts of climate change and adaptation strategies on groundnut production in India. *Science of the Total Environment*, 776: 145996.
12. Kadiyala, M. D. M., Nedumaran, S., Singh, P., Irshad, M. A. and Bantilan, M. C. S. 2015. An integrated crop model and GIS decision support system for assisting agronomic decision making under climate change. *Science of the Total Environment*, 521: 123–134.
13. Kendall, M. G. 1948. *Rank correlation methods*. 5th edition. Oxford University Press, *USA*. pp 272. ISBN: 978-0195208375.
14. Mann, H. B. 1945. Nonparametric tests against trend. *Econometrica*, 13: 245-259.

15. Meng, H. and Qian, L. 2024. Performances of different yield-detrending methods in assessing the impacts of agricultural drought and flooding: A case study in the middle-and-lower reach of the Yangtze River, China. *Agricultural Water Management*, 296, 108812.

16. Nasiłowska S. and Kubiak, K. 2016. Volatility NDVI and NDMI indicators on an example analysis of maize cultivation in Ethiopia. *Remote sensing Environments*, 55: 15–26.

17. Ong, C.K. 1984. The influence of temperature and water deficit on the partitioning of dry matter in groundnut (*Arachis hypogaea* L.). *Journal of Experimental Botany*, 35: 746-755.

18. Rao, B. B., Manikandan, N. and Rao, V. U. M. 2015. Assessing the climate variability impacts using real time groundnut (*Arachis hypogaea* L.) yield data from an arid region of Peninsular India. *Legume Research-An International Journal*, 38(3): 334-340.

19. Rao, V. N., Singh, P., Hansen, J., Giridhara Krishna, T., and Krishna Murthy, S. K. 2007. Use of ENSO-based seasonal rainfall forecasting for informed cropping decisions by farmers in the SAT India. In *Climate Prediction and Agriculture: Advances and Challenges* (pp. 165-180). Berlin, Heidelberg: Springer Berlin Heidelberg.

20. Sen, P. K. 1968. Estimates of the regression coefficient based on Kendall's tau. *J. Am. Stat. Assoc.*, 63: 1379-1389.

21. Senapati, R., Rath, B. S., Parapurath, F., Mahanty, M., Ghosh, A., Meena, A. K., Pandit, R. 2024. Forest Cover Change Detection Over North Eastern Ghat Zone of Odisha, India Using Multi-Year Landsat Data. *International Journal of Environment and Climate Change*, 14(9), 787–795.

22. Singh, N. P., Byjesh, K., Bantilan, C., Murthy, M. V. R., Rao, V. U. M., Rao, G. G. S. N., Manikandan, M. and Harini, D. 2013. *Vulnerability to Climate Change: Adaptation Strategies and Layers of Resilience-Agro-climatic analysis of Climatic Trends in Semi-Arid Tropics of India (Andhra Pradesh and Maharashtra).* Research Report No. 22. *ICRISAT, Patancheru,* Andhra Pradesh, India. 152 pp.

23. Subba Rao, A. V. M., Parapurath, F., Sarath Chandran, M. A., Bal, S. K., Manikandan, N., and Singh, V. K., 2025. Spatiotemporal variability and trends of hailstorms over India. *Natural Hazards*, *121*(2), 1687-1710.

24. Thornthwaite, C. W. 1948. An approach toward a rational classification of climate. *Geographical review*, 38(1): 55-94.

25. Thornthwaite, C. W. and Mather, J. R. 1955. *The Water Balance*. Publications in Climatology. Laboratory of Climatology, Drexel Institute of Technology, Centerton, New Jersey.

26. UNEP. 1992. *World Atlas of Desertification*. Arnold, London, pp. 69.

27. UNESCO. 1977. *Map of the World Distribution of Arid Regions*, MAB Technical Notes, 7(18). Document No. SC.78/XXIX.7/A, p 54, UNESCO, Paris.

28. Virmani, S. M. and Shurapli, J. N. 1999. *Climate Prediction for Sustainable Production of Rainfed Groundnuts in SAT Crop Establishment Risks in the Anantapur Region*. International Crops Research Institute for the Semi-Arid Tropics, Technical Manual #4. *ICRISAT, Patancheru,* Andhra Pradesh, India: ISBN 92-9066-409-6.

29. Wilson, E. H. and Sader, S. A. 2002. Detection of forest harvest type using multiple dates of Landsat TM imagery. *Remote Sensing of Environment*, 80: 385–3.

International Agricultural Engineering Journal ISSN 0858-2114

*September 2025, 34 (1-4) : 171-186*

# Comparison Study on Removal of Fluoride in Groundwater using Boron-doped and Non-doped Activated Carbon Prepared from Indian Kino tree (*Pterocarpus marsupium*)

**D. Sivakumar[1*], V. Kumar[2], B. Baranitharan[1]**

## ABSTRACT

Elevated fluoride concentrations in drinking water are recognized as a public health concern due to their potential to cause a range of dental disorders upon prolonged ingestion. The objective of this study was to assess the amount of fluoride removed from groundwater using activated carbon made from Indian Kino tree or Malabar Kino tree (*Pterocarpus marsupium*) sawdust, both doped and non-doped with boron. The adsorbents were investigated under varying experimental conditions including temperature, agitation speed, adsorbent dosage, and particle size. The non-doped *Pterocarpus marsupium* activated carbon served as the control group in this study, with 20 samples, and boron-doped *Pterocarpus marsupium* activated carbon represented the experimental group, also with 20 samples. The results indicated that the boron-doped *Pterocarpus marsupium* activated carbon achieved a maximum fluoride removal efficiency of 97.5%. In comparison, the non-doped activated carbon reached a slightly lower efficiency of 94% under optimized conditions (Run 4), which involved a particle size of 600 µm, an adsorbent dosage of 4 g, an agitation speed of 450 rpm, and a temperature of 50 °C. These results confirmed the efficacy of both materials, with boron doping providing an enhanced fluoride adsorption capability. Statistical analysis yielded a significant p-value of 0.013 ($p < 0.05$), indicating that the difference in removal efficiency between the two groups was statistically significant. Overall, the findings indicated that boron-doped *Pterocarpus marsupium*-derived activated carbon offered improved fluoride remediation potential, making it a promising candidate for addressing fluoride contamination in groundwater and reducing associated dental health risks.

***Keywords:*** *Adsorption Efficiency; Biomass-Derived Adsorbents; Boron Modification; Defluoridation; Water Purification.*

## 1. INTRODUCTION

Fluoride contamination in groundwater is a significant global environmental and public health issue. While fluoride is essential for dental and skeletal health in trace amounts, excessive intake can lead to detrimental health effects such as dental and skeletal fluorosis. The World Health Organization (WHO) recommends a fluoride concentration limit of 1.5 mg/L in drinking water.

[1] Department of Agrl. Engineering, Kalasalingam Academy of Research and Education, Krishnankoil, India.

[2] Formerly Professor & Head, Agrl. Engineering Department, Tamil Nadu Agrl. University, Madurai, India.

[*] *Corresponding author - email: shri.sivakumar0307@gmail.com*

Received: 22 January 2025; Revised: 17 July 2025; Accepted: 19 August 2025.

However, in many regions, especially in arid and semi-arid areas, fluoride levels exceed this limit due to natural and anthropogenic factors, necessitating effective fluoride removal techniques (Damtie *et al*., 2019; Wan *et al*., 2021). Fluoride pollution can be brought on by both natural and artificial sources, much like any other type of pollution (Shaji *et al*., 2024). Fluoride is considered one of the most hazardous elements since fluoride ions are prevalent in groundwater and leach from fluorspar rock resources (Lubojanski *et al*., 2023). The concentration of fluoride ions determines their dangerous effects. If the fluoride content is higher than 1.5 mg/L, young children typically experience dental problems and discoloured teeth (Tiwari *et al*., 2023). If the groundwater has more fluoride than this, it must be treated to below the 1.5 mg/L level before consumption (Tanwer *et al*., 2023). Skeletal fluorosis has been linked to groundwater fluoride concentrations greater than 3.2 mg/L (Keesari *et al*., 2021). Treating groundwater with activated carbon reduced the fluoride concentration to 0.3 mg/L (Bakhta *et al*., 2022); however, excessively low fluoride levels below the optimal range of around 0.7 mg/L are also undesirable, as they may increase the risk of dental caries (O'Malley *et al.*, 2025).

Paikaray and Chander (2022) examined groundwater geochemistry in Fazilka, a predominantly agricultural district located in the south-western part of Punjab, India, near the India–Pakistan border, where serious fluorosis concerns were reported due to high fluoride contamination of groundwater used for drinking water purposes Fluoride concentrations in Fazilka's groundwater are much higher than those found in surface water and range from 6 to 12 mg/L, significantly exceeding both national and international permissible limits (Paikaray and Chander, 2022). Prolonged exposure to such high fluoride levels has led to a dental decay rate of approximately 70% among the local population, underscoring the urgent need for implementing effective defluoridation strategies in the area. Fluoride is removed from groundwater using a wide range of treatment methods, including coagulation, membrane filtering, ion exchange, electrochemical oxidation, and electrocoagulation. The adsorption process is regarded as the most practical, long-lasting, and environmentally benign of these techniques. Activated carbon filtration, which is generally believed to combine ion exchange and physical adsorption, is considered the most effective method for removing fluoride (Panhwar *et al.*, 2024). Neutral and acidic sulfate-containing solutions reduce activated carbon capacity regarding fluoride adsorption (Turki *et al*., 2023). Activated carbon adsorption recently gained prominence with regards to groundwater defluoridation, due to rapid equilibrium attainment (approximately 20 minutes) (Thomas *et al*., 2023). This study adopts methodological approaches established by previous investigations (Turki *et al*., 2023; Thomas *et al*., 2023; Sivakumar *et al*., 2018), ensuring comparability and validity of results. According to Google Scholar, approximately 225 studies, and as per Science Direct, 80 studies have examined the removal of fluoride using different adsorbents in the past five years. This indicates a growing global research interest in developing efficient, low-cost, and sustainable adsorbent-based technologies for fluoride removal, highlighting the urgency and relevance of addressing fluoride contamination in drinking water.

Extensive research has explored various materials and techniques for fluoride removal. Advanced cellulose-, polymer-, and graphene-based membranes have shown promise, with hydrophilicity and ion selectivity being critical to performance (Tolkou *et al*., 2021a). Graphene-enhanced membranes further improved efficiency due to superior mechanical strength and chemical stability (Tolkou *et al*., 2021a). Zeolites modified with metal ions significantly increased fluoride adsorption, as supported by kinetic and isotherm analyses (Turki *et al*., 2023). Nanomaterials such as graphene oxide and composite adsorbents

supported on activated carbon exhibited high fluoride removal due to their reactive surfaces and tunable structures (Chufa *et al*., 2022; Patel and Bhasin, 2023). Other techniques include electrocoagulation and photocatalysis, which offer innovative fluoride removal mechanisms. Electrocoagulation has been evaluated for cost-effective drinking water treatment (Castañeda *et al*., 2021), and visible-light photocatalysis has emerged as a novel oxidative process (Lin *et al*., 2021). Natural and modified low-cost adsorbents also show potential: diatomite modified with aluminium hydroxide and hydroxyapatite-modified shell powder performed effectively in fluoride removal, particularly in resource-limited settings (Akafu *et al*., 2019; Yapo *et al*., 2022). Additionally, zirconium-impregnated anion exchange resins and composite adsorbents synthesized from various materials displayed notable adsorption capabilities (Singh *et al*., 2020; Wei *et al*., 2022).

Several studies have explored the use of activated carbon and its modifications for effective fluoride removal from water. Previous research has utilized various bio-adsorbents for fluoride removal from groundwater and alleviating dental symptoms. However, these studies did not utilize activated carbon doped or non-doped with boron derived from *Pterocarpus marsupium* sawdust (Akafu *et al*., 2019; Ogata *et al*., 2020). The main objective of this research is to discover new materials that can remove contaminants, including fluoride from groundwater. Previous treatment techniques showed a lower proportion of fluoride removal from groundwater. Another goal of this study is to incorporate boron into activated carbon made from *Pterocarpus marsupium* sawdust to enhance bio sites, with both forms targeting fluoride removal. Activated carbon, a commonly used adsorbent, has shown promise in contaminant removal due to its high surface area, porous structure, and customizable properties. Recent advancements include doping activated carbon with elements like boron to enhance adsorption capacity and selectivity towards fluoride ions (Pillai *et al*., 2020; Patel and Bhasin, 2023).

This study aims to investigate and compare the efficiency of boron-doped and non-doped activated carbon derived from *Pterocarpus marsupium* in removing fluoride from groundwater. The choice of *Pterocarpus marsupium*, a sustainable and readily available biomass, aligns with the growing emphasis on environmentally friendly and cost-effective water treatment solutions. Modifying activated carbon with boron introduces new adsorption mechanisms that could potentially enhance fluoride uptake capacity and provide a competitive edge over traditional adsorbents (Ogata *et al*., 2020; Akafu *et al*., 2019). Bakhta *et al*. (2022) synthesized functional activated carbon and demonstrated its efficacy in reducing groundwater fluoride concentrations, showcasing high adsorption capacity and practical applicability. Patel and Bhasin (2023) developed a graphene/cerium (Ce) composite supported on activated carbon, exhibiting enhanced fluoride adsorption performance due to the synergistic effects of the composite materials. Thomas *et al*. (2023) investigated aluminum-modified activated carbon, reporting efficient fluoride removal and favorable adsorption behavior, supporting its use in groundwater remediation. Sivakumar *et al*. (2018) focused on nickel removal from industrial wastewater using bamboo-based activated carbon contributing valuable knowledge on activated carbon development and its potential in heavy metal and ion removal, including fluoride. These studies collectively confirm that activated carbon, especially when modified or composited with other materials, remains a promising and effective adsorbent for fluoride removal from aqueous systems.

While various modified adsorbents and nanocomposites have shown improved fluoride removal efficiency, such as aluminium hydroxide-coated diatomite (Akafu *et al*., 2019), hydroxyapatite-modified shell powder (Yapo *et al*., 2022), and zirconium-based resins (Singh *et al*., 2020), none of these studies focused on boron-doped activated carbon derived from *Pterocarpus marsupium* sawdust. Additionally, while recent

studies (Bakhta *et al*., 2022; Patel and Bhasin, 2023; Thomas *et al*., 2023) reported success using advanced carbon-based materials, a direct comparison between boron-doped and non-doped forms of activated carbon from this specific biomass under controlled conditions has not been conducted. The statistical significance of such a comparison also remains underexplored. This study uniquely develops and compares boron-doped and non-doped activated carbon synthesized from *Pterocarpus marsupium* sawdust for fluoride remediation. It introduces boron doping as a strategy to enhance adsorption efficiency through improved surface properties and affinity toward fluoride ions. The use of a sustainable, underutilized biomass source, along with a controlled experimental design and statistical evaluation, distinguishes this work from prior research and supports the development of cost-effective, eco-friendly water treatment technologies. Therefore, this study aims to evaluate the efficiency of fluoride removal from groundwater using activated carbon derived from *Pterocarpus marsupium* sawdust, both doped and non-doped with boron.

## 2. MATERIALS AND METHODS

### 2.1. Study Area

This study was conducted in Thiruvallur, located in Thiruvallur District, Tamil Nadu, India (13.14°N latitude and 79.91°E longitude). The region has a tropical climate, with an average annual temperature of 28°C and mean annual precipitation of approximately 1,200 mm, primarily during the northeast monsoon. In Thiruvallur district, fluoride concentrations in several groundwater sources exceeded permissible limits, with levels reaching up to 2.7 mg/L in Thiruvallur town, likely due to leaching from mineral-rich rocks (Muththamizh *et al*., 2023). As a result, five representative groundwater samples from different locations within Thiruvallur town were collected and assessed for fluoride concentration levels, following the procedures of the American Public Health Association (APHA Standard Methods, 2017). The results indicated an average fluoride concentration of 3.6 mg/L, significantly exceeding the Bureau of Indian Standards (BIS) permissible limit of 1.5 mg/L for drinking water (IS 10500:2012), highlighting the urgent need for efficient fluoride removal interventions in the region.

Various characteristics of groundwater from different sites were examined to determine its suitability for drinking (Sivakumar *et al*., 2018). However, this analysis focused more on fluoride in groundwater than other ions. The groundwater samples were collected in airtight bottles, transported to the environmental laboratory for storage at a temperature of 5°C to avoid contamination, and later used for testing.

### 2.2. Preparation and Chemical Activation of Activated Carbon

Indian Kino tree or Malabar Kino tree (*Pterocarpus marsupium*) grows upto a height of 31 m and is locally referred to as *Vengai*. This the starting material needed to extract fluoride. From the wood chips of *Pterocarpus marsupium*, saw dust was prepared for the production of non-doped activated carbon. The saw dust was sieved to obtain the desired particle size and then dried for 16 hours at 400°C in a hot air oven to produce activated carbon. After cooling to room temperature, this non-doped activated carbon was collected and stored for use in experiments.

Chemical activation was carried out using boric acid with a portion of this non-doped activated carbon by mixing 10 g of dried activated carbon with 100 ml of boric acid and heating at 85°C for three hours in a hot air oven, followed by drying at 110°C to produce boron-doped activated carbon. After cooling to room temperature, the boron-doped samples were stored in sealed plastic containers and used in experiments.

### 2.3. Adsorption Study

In the adsorption study, two groups were involved, the control group (group 1 – N=20) consisted of non-doped boron novel *Pterocarpus marsupium* activated carbon as the control group (group 1 - Number of samples, N=20) and boron-doped novel *Pterocarpus marsupium* activated carbon. Instead of conducting 625 trials for each group using a full factorial design with 4 parameters at 5 levels, this study adopted the Box–Behnken experimental design, which reduced the experiment runs to 20 per group for both non-doped and boron-doped *Pterocarpus marsupium* activated carbon powders (Sivakumar, 2021). In this study, fluoride is removed from groundwater against various process parameters: particle size of 600, 500, 425, 300 and 150 µm, adsorbent dosage of 1, 2, 3, 4 and 5 g per liter, agitation speed of 150, 250, 350, 450 and 550 rpm, and groundwater temperature of 35°C, 40°C, 45°C, 50°C and 55°C. For the experiments, one litre of ground water was taken in a glass container along with the adsorbent and heated to the required temperature by placing it on a magnetic stirrer provided with hot plate at the agitation speed as per the experimental plan. The flow diagram of the experiment is given in Fig.1. The average fluoride ion concentration in groundwater was found to be 3.6 mg/L with a pH of 6.4. Table 1 summarizes the design of experimental runs (20) for removing fluoride ions in groundwater using non-doped and doped *Pterocarpus marsupium* activated carbon. The fluoride removed from groundwater was calculated using Eq. 1.

$$\text{Fluoride percentage removal, } F = \frac{C_1 - C_2}{C_1} \times 100 \quad \ldots (1)$$

Where, $C_1$ is the initial value of fluoride concentration in mg/L before treatment and $C_2$ is the final value of fluoride concentration in mg/L, after treatment with both non-doped and doped boron *Pterocarpus marsupium* activated carbon prepared from sawdust.

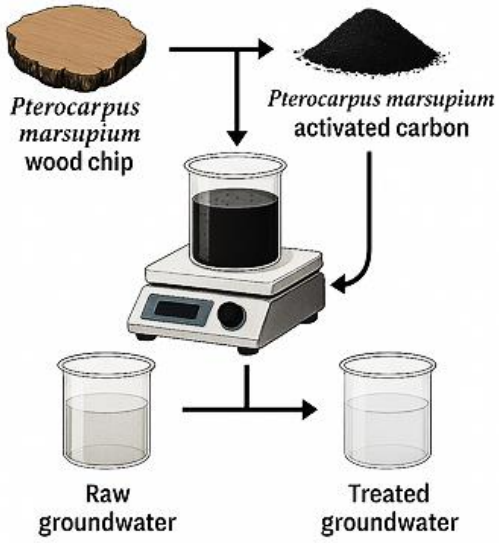


**Fig. 1. Treatment of groundwater using *Pterocarpus marsupium* activated carbon**

### 2.4. Surface Characteristics of Activated Carbon

Scanning Electron Microscopy (SEM) was employed to examine the surface morphology and pore network of non-doped and boron-doped activated carbon produced from sawdust of *Pterocarpus marsupium*. Prior to imaging, samples were dried, mounted on conductive stubs, and sputter-coated with a thin metal layer to prevent charging. Imaging was done at multiple magnifications to capture both overall particle texture and finer pore features. SEM provides detailed visualization of morphological characteristics such as pore opening size, distribution uniformity, surface roughness, network connectivity, and structural integrity.

**Table 1. Design of experimental runs**

| Runs | Particle size, µm | Adsorbent dosage, g/l | Agitation speed, rpm | Temperature, °C |
|---|---|---|---|---|
| 1 | 600 | 1 | 150 | 35 |
| 2 | 600 | 2 | 250 | 40 |
| 3 | 600 | 3 | 350 | 45 |
| 4 | 600 | 4 | 450 | 50 |
| 5 | 500 | 5 | 550 | 55 |
| 6 | 500 | 1 | 250 | 35 |
| 7 | 500 | 2 | 150 | 40 |
| 8 | 500 | 3 | 450 | 45 |
| 9 | 425 | 4 | 350 | 50 |
| 10 | 425 | 5 | 550 | 55 |
| 11 | 425 | 1 | 350 | 35 |
| 12 | 425 | 2 | 450 | 40 |
| 13 | 300 | 3 | 550 | 45 |
| 14 | 300 | 4 | 150 | 50 |
| 15 | 300 | 5 | 250 | 55 |
| 16 | 300 | 1 | 550 | 35 |
| 17 | 150 | 2 | 450 | 40 |
| 18 | 150 | 3 | 350 | 45 |
| 19 | 150 | 4 | 250 | 50 |
| 20 | 150 | 5 | 150 | 55 |

Observations of the non-doped carbon reveal a baseline structure with irregular, less interconnected pores. Boron-doped samples display more uniformly distributed micropores and mesopores, indicating enhanced accessible surface and improved diffusion pathways. SEM micrographs also allow assessment of structural integrity, including the absence of collapsed walls or fractures, and reveal surface heterogeneities introduced by boron incorporation. These observations explain differences in adsorption performance between the non-doped and boron-doped materials.

### 2.5. Statistical Analysis

Descriptive statistics (mean and standard deviation) of fluoride removal percentages for non-doped and boron-doped *Pterocarpus marsupium* activated carbon were computed from 20 runs per group at 95% confidence level using Statistical Package for the Social Sciences (SPSS) (Sivakumar *et al*., 2018). An independent-sample t-test compared mean removal efficiencies between the two adsorbent types, with a two-tailed significance level set at $p < 0.05$. The T-test yielded the mean difference, standard error, and 95% confidence interval for the difference, providing both statistical significance and optimal

parameter value. These results demonstrate whether boron incorporation produces a reliably higher fluoride removal performance under the specified experimental conditions.

## 3. RESULTS AND DISCUSSION

### 3.1. Surface Morphology Analysis of Non-Doped and Boron-Doped Carbon Structures

Experiments were conducted to study the percentage of fluoride removal in groundwater using non-doped and boron-doped activated carbon produced from *Pterocarpus marsupium* sawdust. The SEM offers comprehensive details such as pores, fissures, and cracks regarding the surface morphology of active carbon prepared from *Pterocarpus marsupium* sawdust. Fig. 2a and 2b show the SEM image of non-doped and boron-doped *Pterocarpus marsupium* sawdust-activated carbon, respectively. These images were captured with an Electron High Tension (EHT) of 20.00 kV, a Working Distance (WD) of 10.5 mm, and using the secondary electrons of type 1 (SE1) signal with the scale bar indicating a length of 20 µm**.**

The SEM images present a comparative analysis of non-boron-doped and boron-doped activated carbon. The SEM image provides a detailed view of a sample at a magnification of 500 times (500X), revealing a heterogeneous mixture of irregularly shaped particles. Fig. 2a, depicting non-boron-doped activated carbon, shows a heterogeneous microstructure characterized by irregularly shaped particles and a limited number of pores. This irregular distribution and smaller pore quantity indicate potential variability in material performance, affecting properties like adsorption capacity and structural strength. In contrast, Fig. 2b, featuring boron-doped activated carbon, reveals a more homogeneous microstructure with a significantly higher number of well-defined pores. The boron doping process appears to enhance the uniformity and porosity of the material, potentially increasing its surface area and improving its adsorption efficiency. This comparison highlights the impact of boron doping on the microstructural properties of activated carbon, demonstrating how the introduction of boron atoms can create a more uniform and porous material, which is advantageous for applications requiring high adsorption capacity and consistent material performance.

### 3.2. Fluoride Removal Efficiency Assessment

Fig. 3 presents the fluoride percentage removal in groundwater using non-doped activated carbon prepared from *Pterocarpus marsupium* sawdust. Accordingly, Fig. 4 presents fluoride ion percentage removal in groundwater using boron-doped activated carbon prepared from novel *Pterocarpus marsupium* activated carbon. The results of Fig. 3 demonstrate a consistent and significant reduction in fluoride concentration using non-doped activated carbon, with removal efficiencies ranging from 75% to 93.8%. The mean removal efficiency was 82.4%, with a standard deviation of 3.4%, indicating moderate variability across experimental trials. These findings confirm the effectiveness of non-doped *Pterocarpus marsupium*-derived activated carbon in fluoride adsorption under varying operational parameters. The results of Fig. 4 demonstrate a consistent and significant reduction in fluoride concentration using boron-doped activated carbon, with removal efficiencies ranging from 88.1% to 97.5%. The mean removal efficiency was 92.3%, with a standard deviation of 2.1%, indicating high performance and low variability across the experimental trials. These findings validate the enhanced adsorption capability of boron-doped *Pterocarpus marsupium*-based activated carbon in removing fluoride from groundwater.

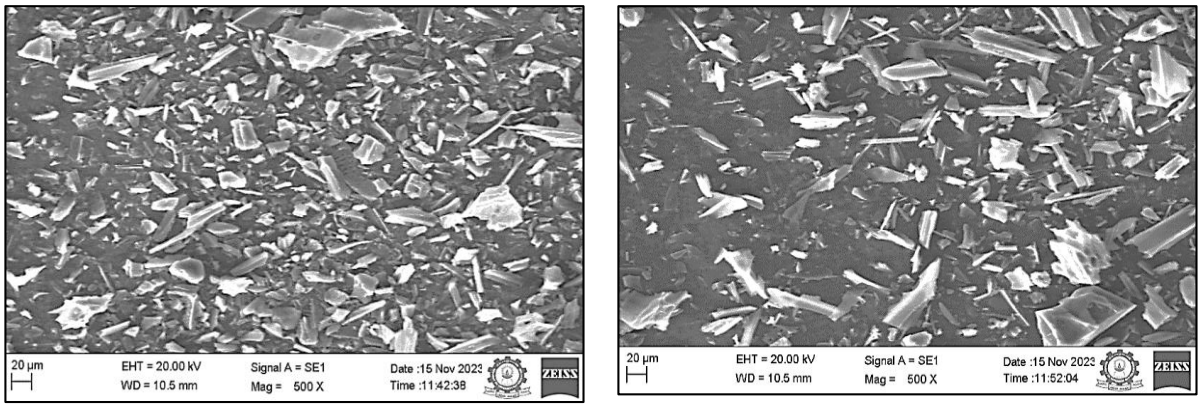


**a. Non-doped activated carbon** **b. Boron-doped activated carbon**

**Fig. 2. Micro images of activated carbon produced from *Pterocarpus marsupium* sawdust**

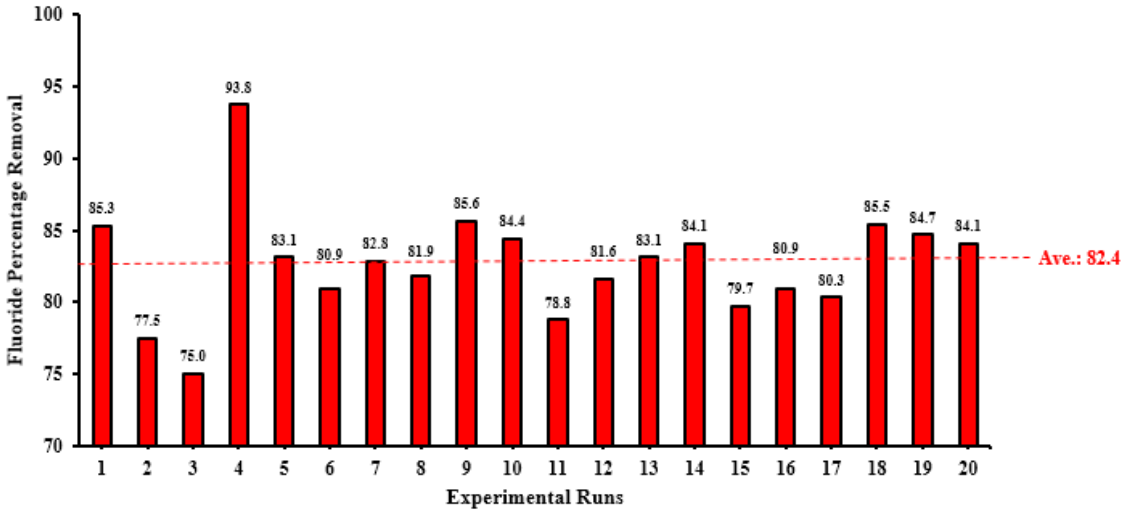


**Fig. 3. Fluoride removal percentage in groundwater using non-doped *Pterocarpus marsupium* activated carbon**

As shown in Figs. 3 and 4, the fluoride percentage removal in groundwater was higher in boron-doped activated carbon compared to non-doped activated carbon prepared from novel *Pterocarpus marsupium*. The highest percentage of fluoride removal in groundwater was greater (97.5%) with the boron-doped activated carbon prepared from *Pterocarpus marsupium* sawdust than non-doped activated carbon (93.8%), both at optimum process values of 600 µm, 4 g, 450 rpm, and 50°C for particle size, dosage, speed, and temperature with a contact time of 60 min (Run 4). For the statistical analysis, the sample data were taken from the optimized parameters.

The comparative analysis of Fig. 3 and Fig. 4 illustrates the superior fluoride removal performance of boron-doped *Pterocarpus marsupium*-based activated carbon over the non-doped variant, attributed to improvements in multiple physicochemical properties.

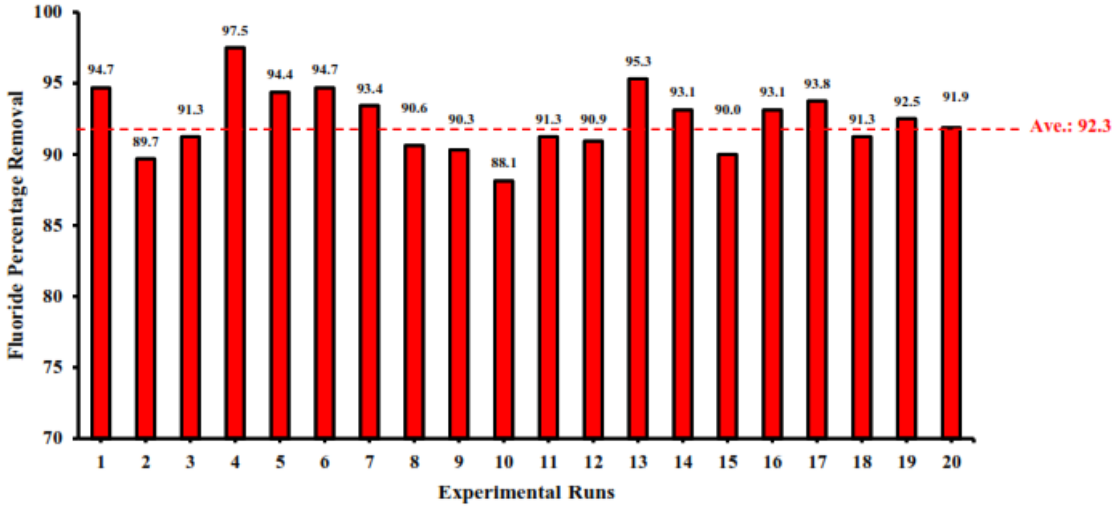


**Fig. 4. Fluoride removal percentage in groundwater using boron-doped *Pterocarpus marsupium* activated carbon**

Boron doping enhances the surface area of the activated carbon, providing more accessible sites for fluoride interaction and increasing overall adsorption efficiency compared to the relatively lower surface availability in the non-doped material. The pore structure of the boron-doped adsorbent is more uniform and better developed, with increased micropore and mesopore volumes that facilitate efficient diffusion and entrapment of fluoride ions. In contrast, the non-doped carbon exhibits a less organized pore distribution, limiting fluoride accessibility and retention. Additionally, boron incorporation introduces electron-deficient sites that create stronger electrostatic attractions with negatively charged fluoride ions, resulting in a greater number of reactive adsorption sites and higher selectivity. The non-doped form, lacking these modifications, shows reduced affinity for fluoride and increased variability in performance. The enhanced stability and reproducibility observed in the boron-doped adsorbent, reflected in its higher mean removal efficiency and lower standard deviation, can also be linked to its improved interaction with key operational parameters, such as contact time, adsorbent dosage, agitation speed, and temperature, as outlined in the experimental design (Table 1). These combined effects demonstrate that boron doping significantly improves the adsorptive characteristics and operational reliability of activated carbon for fluoride remediation in groundwater.

### 3.3. Effect of Process Parameters on Fluoride Adsorption

In this study, when the activated carbon material is used for treatment to remove fluoride at different process parameters, such as different particle sizes (600, 500, 425, 300, and 150 µm), adsorbent dosages (1, 2, 3, 4, and 5 g), agitation speeds (150, 250, 350, 450, and 550 rpm), and temperatures (35, 40, 45, 50, and 55°C), the boron-doped activated carbon appears to perform significantly better than non-doped activated carbon (Fig. 4). Understanding the surface morphology is crucial, as it impacts the total adsorption capacity of activated carbon and the surface area that may be used for adsorption. From Figs. 2a and 2b, it could be noted that the pore area is higher in the case of boron-doped *Pterocarpus marsupium* sawdust-activated carbon than in the case of non-doped *Pterocarpus marsupium*

sawdust-activated carbon. This result also coincides with the fluoride removal efficiency from groundwater using both doped (Fig. 4) and non-doped *Pterocarpus marsupium* sawdust activated carbon (Fig. 4). From Fig. 3, it may be found that there could be not much difference among various experimental runs from 1 to 20, except experimental run 4, in which this study obtained the maximum removal of fluoride using non-doped *Pterocarpus marsupium* sawdust activated carbon. Whereas, from Fig. 4, it could be found that there was a fluoride removal percentage change among the various experimental runs, except for experimental run 4. The reason for the variation in fluoride removal percentage using *Pterocarpus marsupium* sawdust-activated carbon is due to the increased active sites on *Pterocarpus marsupium*-activated carbon by boron ions. From Figs. 2a and 2b, it may be noted that the fluoride ion removal percentage depends on the usage of process parameters. The study's Fisher value, which is 3.15 at a significant p-value of 0.0001, shows that the fluoride percentage removal using non-doped and boron-doped novel *Pterocarpus marsupium* activated carbon differs significantly from one another.

### 3.4. Statistical Evaluation of Adsorption Performance

Table 2 summarizes and compares the descriptive statistics of fluoride removal efficiencies for non-doped and boron-doped *Pterocarpus marsupium* activated carbon, providing the basis for statistical inference regarding their performance differences. From Table 2, it can be observed that the boron-doped activated carbon derived from *Pterocarpus marsupium* sawdust exhibits a higher mean fluoride removal efficiency along with a lower standard deviation and standard error of the mean compared to the non-doped variant. These statistical indicators suggest not only improved performance but also greater consistency and reliability in adsorption behavior. The results of the independent samples T-test further confirm that the differences between the two groups are statistically significant ($p < 0.05$). This highlights the beneficial effect of boron doping, which likely enhances the surface functionality and structural properties of the activated carbon, thereby increasing its affinity for fluoride ions. Consequently, boron-doped *Pterocarpus marsupium* activated carbon emerges as a promising and efficient material for fluoride remediation in groundwater treatment.

**Table 2. Statistical comparison of performance of activated carbon**

| Group | Total Samples | Mean (%) | SD | SE to Mean |
|---|---|---|---|---|
| Boron Non-doped | 20 | 82.4 | 3.4 | 0.66 |
| Boron- doped | 20 | 92.3 | 2.1 | 0.37 |

The results of independent sample T-test between non-doped and boron-doped *Pterocarpus marsupium* activated carbon for the removal of fluoride in groundwater are presented in Table 3. From Table 3, it may be noted that the lower and higher 95% confidence interval of the mean difference is between -11.782 and -7.704 with the dF value is 38 when equal variances are assumed between the two groups. The p-value between non-doped and boron-doped *Pterocarpus marsupium* activated carbon is 0.0001 ($p < 0.05$).

### 3.5. Comparison with Previous Studies

This comparative study demonstrates the transformative effects of boron doping on microstructural and adsorption properties. Prior research underscores the efficacy of modified materials in enhancing fluoride removal from aqueous solutions, a trend supported by the results of this study. Boron-doped activated carbon achieved fluoride removal efficiencies of 88.1% to 97.5%, significantly outperforming non-doped activated carbon, which achieved 75% to 93.8%. Following each contact period, the treated water, which contained non-doped and boron-doped *Pterocarpus marsupium* activated carbon, was preserved for a full day without being altered and then filtered with filter paper. Previous studies

also observed that the maximum removal of fluoride ions in groundwater depends on the contact time (Bakhta *et al.*, 2022), and the largest amount of fluoride removed from filtered groundwater occurred at a contact duration of 60 minutes (Sivakumar *et al.*, 2018). Additionally, a 9% increase in the percentage of fluoride removed from groundwater on boron-doped activated carbon is evident; in contrast, the percentage of fluoride removed from non-doped activated carbon was determined to be 97.5% (Sivakumar *et al.*, 2018). In line with research results, the mean accuracy of boron-doped activated carbon is higher than that of non-doped activated carbon, although the boron-doped activated carbon's standard deviation is somewhat higher.

**Table 3. Independent sample T-test between non-doped and boron-doped activated carbon produced from *Pterocarpus marsupium***

| Particulars | Levene's Test for Equality of Variances | | T-test for Equality of Means | | | | 95% Confidence Interval of the Difference | |
|---|---|---|---|---|---|---|---|---|
| | F | P | T | dF | Mean Difference | SE Difference | Lower | Upper |
| Equal variances assumed | 3.15 | 0.0001 | -9.76 | 38 | -9.743 | 0.9985 | -11.782 | -7.704 |

Note: F – Levene's test statistic for equality of variances; P – Significance level (p-value); T – t-test statistic; dF – Degrees of freedom; SE Difference – Standard Error of the Difference; Lower and Upper – Lower and Upper bounds of the 95% Confidence Interval for the Mean Difference; All values are calculated at a 95% confidence level and a p-value less than 0.05 indicates statistical significance.

This study demonstrated that boron-doped activated carbon achieved higher percentages of fluoride removal from groundwater, while non-doped activated carbon resulted in lower removal efficiencies. Similar results were reported in other studies, indicating that the percentage of fluoride removed from groundwater can be controlled by using different types of adsorbents. However, applying temperatures and extending the fluoride removal periods may lead to longer removal times or increased costs. Therefore, this study recommends further research to determine the efficacy of prepared activated carbon, by examining its characteristics. Consistent with these findings, Tolkou *et al.* (2021a) and Turki *et al.* (2023) reported that polymer- and zeolite-modified membranes exhibit enhanced adsorption kinetics and capacity, achieving fluoride removal efficiencies exceeding 90%. Similarly, Chufa *et al.* (2022) observed that graphene oxide nano adsorbents achieved fluoride removal rates of 93–97.5%, attributed to their increased surface area and functional adsorption sites. Patel and Bhasin (2023) support these findings, highlighting a 98.2% fluoride removal efficiency for graphene/Ce composites supported on activated carbon.

Material modifications are crucial for maintaining consistent performance under varying environmental conditions, as reviewed by Damtie *et al.* (2019). For example, advanced materials like iron oxide nanoparticles modified with ionic liquids achieved 91.6% fluoride removal (Pillai *et al.*, 2020), while zirconium-impregnated anion exchange resins demonstrated efficiencies exceeding 90% (Singh *et al.*, 2020). Akafu *et al.* (2019) achieved over 89% fluoride removal using aluminium hydroxide-modified diatomite, and Yapo *et al.* (2022) demonstrated efficiencies of 95.6% with hydroxyapatite-modified materials. Furthermore, Wei *et al.* (2022) and Wan *et al.* (2021) reviewed composite

adsorbents and their synergistic interactions, which could be extended to boron doping. This study's high fluoride removal efficiency aligns with their findings on enhanced functional site formation and adsorption capacity. For example, Lin *et al.* (2021) observed fluoride degradation efficiencies of 94% using photocatalytic systems, while Ogata *et al.* (2020) demonstrated hydroxide-based materials removing fluoride at rates of 90–95%. Affordable and scalable methods like electrocoagulation reported by Castañeda *et al.* (2021), achieving fluoride removal efficiencies of 85–92.0%, and cellulose-based adsorbents discussed by Tolkou *et al.* (2021b), with removal rates exceeding 88%, could complement high-performing materials such as boron-doped activated carbon. These synergies could enable broader accessibility and sustainability in addressing fluoride contamination in drinking water.

### 3.6. Optimizing Fluoride Removal using Boron-Doped Carbon

This study investigates the impact of boron doping on the fluoride adsorption performance of *Pterocarpus marsupium* activated carbon. Through a detailed analysis of key operational factors, it highlights the enhanced efficiency and stability of the doped material.

#### 3.6.1. Effect of particle size

Particle size plays a critical role in determining the external surface area and diffusion path length available for fluoride ions. Across a wide particle size range, boron-doped *Pterocarpus marsupium* activated carbon consistently demonstrated superior removal efficiency compared to its non-doped counterpart. This enhanced performance is attributed to the optimized pore structure and greater density of active sites in the doped material, which reduce diffusion constraints. The ability of boron-doped carbon to maintain high efficiency even with coarser particle sizes indicates its reduced dependence on precise size control.

#### 3.6.2. Effect of adsorbent dosage

The dosage of activated carbon affects the total number of available adsorption sites. Both adsorbents showed improved fluoride removal with increasing dosage; however, boron-doped carbon achieved high performance at relatively lower dosages. This implies a stronger inherent affinity for fluoride ions, leading to more efficient usage of material. Moreover, the doped carbon demonstrated more consistent results across different dosages, confirming its reliability and economic advantage in practical applications.

#### 3.6.3. Effect of Agitation Speed

Agitation speed influences the rate of mass transfer between the aqueous phase and the adsorbent surface. Boron-doped carbon maintained high fluoride removal even at moderate agitation levels, while the performance of non-doped carbon was more sensitive to increased mixing. This difference suggests that the doped variant possesses improved pore connectivity and more accessible active sites, allowing it to function effectively under less intensive mixing conditions.

#### 3.6.4. Effect of Temperature

Temperature affects both diffusion kinetics and adsorption equilibrium. Both materials showed enhanced performance with moderate temperature increases. However, boron-doped carbon exhibited greater thermal stability and less variability in removal efficiency across the tested temperature range. This indicates that the fluoride binding on the doped surface is more thermodynamically favourable, making it more robust under varying environmental temperatures.

This study presents a comprehensive evaluation of boron-doped versus non-doped *Pterocarpus marsupium* activated carbon for fluoride removal from groundwater. Key operational parameters, including particle size, dosage, agitation speed, and temperature, were systematically assessed. Morphological analysis using SEM, combined with statistical validation, confirmed that boron

doping significantly enhances the adsorption performance. The doped carbon demonstrated superior fluoride removal efficiency, improved consistency across varying environmental conditions, and outperformed many advanced modified materials reported in the literature. These findings highlight the novelty and potential of boron-doped activated carbon as a cost-effective, robust, and scalable solution for groundwater defluoridation with promising applicability in hybrid treatment systems.

## 4. CONCLUSIONS

From the comparison of non-boron-doped and boron-doped activated carbon produced from *Pterocarpus marsupium* saw dust, it is found that boron doping significantly enhanced both structural and adsorption performances. SEM imaging revealed that non-boron-doped activated carbon exhibited irregularly shaped particles with limited pores, contributing to higher fluoride removal efficiencies ranging from 75% to 93.8%, with variability likely caused by inconsistent binding sites. In contrast, boron-doped activated carbon displayed a uniform microstructure with increased porosity, achieving consistently higher fluoride removal efficiencies between 88.1% and 97.5%. The enhanced performance of the boron-doped variant is attributed to the introduction of additional functional sites, improved surface area, and increased affinity for fluoride ions. Even under less optimal conditions, the boron-doped material maintained superior efficiency, with its lowest removal rate surpassing the highest achieved by the non-doped variant. These findings affirm that boron doping of activated carbon produced from *Pterocarpus marsupium* saw dust, makes it a highly effective and reliable material for water treatment applications for fluoride removal. Future research should focus on optimizing the boron doping process and exploring its scalability for practical implementation.

## ACKNOWLEDGMENT

The authors sincerely thank Kalasalingam Academy of Research and Education, Krishnankoil, Tamil Nadu, India, and the Agricultural Engineering Department, Tamil Nadu Agricultural University, Madurai campus, India, for their support throughout this research.

## REFERENCES

1. Akafu, T., Chimdi, A. and Gomoro, K. 2019. Removal of fluoride from drinking water by sorption using diatomite modified with aluminium hydroxide. *Journal of Analytical Methods in Chemistry*, 2019:1–11. https://doi.org/10.1155/2019/4831926
2. APHA Standard Methods. 2017. *Standard Methods for the Examination of Water and Wastewater*. 23rd ed. American Public Health Association (APHA), American Water Works Association (AWWA) & Water Environment Federation (WEF), Washington, D.C. https://www.standardmethods.org.
3. Bakhta, S., Sadaoui, Z., Bouazizi, N., Samir, B., Allalou, O., Devouge-Boyer, C., Mignot, M. and Vieillard, J. 2022. *Functional activated carbon: from synthesis to groundwater fluoride removal*. RSC advances, 12(4): 2332-2348. https://doi.org/10.1039/D1RA08209D.
4. Castañeda, L. F., Rodríguez, J. F. and Nava, J. L. 2021. Electrocoagulation as an affordable technology for decontamination of drinking water containing fluoride: A critical review. *Chemical Engineering Journal*, 413:127529. https://doi.org/10.1016/j.cej.2020.127529.
5. Chufa, B. M., Gonfa, B. A. and Anshebo, T. Y. 2022. Graphene oxide nanoadsorbent for the removal of fluoride ion from groundwater:

Adsorbent performance and adsorption mechanism. *Journal of Nanotechnology*, 2022:1–12. https://doi.org/10.1155/2022/7371227.

6. Damtie, M. M., Woo, Y. C., Kim, B., Hailemariam, R. H., Park, K. D., Shon, H. K., Park, C. and Choi, J. S. 2019. Removal of fluoride in membrane-based water and wastewater treatment technologies: Performance review. *Journal of Environmental Management*, 251:1-25. https://doi.org/10.1016/j.jenvman.2019.109524.
7. IS 10500:2012. 2012. *Drinking Water – Specification.* Bureau of Indian Standards (BIS), New Delhi.
8. Keesari, T., Pant, D., Roy, A., Sinha, U. K., Jaryal, A., Singh, M. and Jain, S. K. 2021. Fluoride geochemistry and exposure risk through groundwater sources in north-eastern parts of Rajasthan, India. *Archives of Environmental Contamination and Toxicology*, 80:294-307. https://doi.org/10.1007/s00244-020-00794-z.
9. Lin, C., Liu, B., Pu, L., Sun, Y., Xue, Y., Chang, M., Li, X., Lu, X., Chen, R. and Zhang, J. 2021. Photocatalytic oxidation removal of fluoride ion in wastewater by $gC_3N_4/TiO_2$ under simulated visible light. *Advanced Composites and Hybrid Materials*, 4:339–349. https://doi.org/10.1007/s42114-021-00228-x.
10. Lubojanski, A., Piesiak-Panczyszyn, D., Zakrzewski, W., Dobrzynski, W., Szymonowicz, M., Rybak, Z., Mielan, B., Wiglusz, R. J., Watras, A. and Dobrzynski, M. 2023. The safety of fluoride compounds and their effect on the human body - A narrative review. *Materials*, 16(3):1-20. https://doi.org/10.3390/ma16031242.
11. Muththamizh, B., Sowmya, A., Prabhakar, S., Muthamilselvi, P., Kapoor, A. and Rajesh, M., 2023. Spatial distribution of nitrate and fluoride pollution and risk assessment in drinking water resources of Chennai, Kancheepuram, and Tiruvallur districts of Tamil Nadu, India. *Desalination and Water Treatment*, 316, 1–21. https://doi.org/10.5004/dwt.2023.30096.
12. Ogata, F., Nagai, N., Nagahashi, E., Kadowaki, N., Saenjum, C. and Nakamura, T. 2020. Removal of fluoride using magnesium and iron complex hydroxides. *Water Supply*, 20:2815–2825. https://doi.org/10.2166/ws.2020.177.
13. O'Malley, L., Clarkson, J., Lewis, S., Walsh, T. and Glenny, A.M., 2025. Water fluoridation for the prevention of dental caries. *British Dental Journal*. 238: 241-242. https://doi.org/10.1038/s41415-025-8412-1.
14. Paikaray, S. and Chander, S. 2022. Geochemical variations in uranium and fluoride enriched saline groundwater around a semi-arid region of SW Punjab, India. *Applied Geochemistry*, 136: 105167. https://doi.org/10.1016/j.apgeochem.2021.105167.
15. Panhwar, S., Keerio, H. A., Khokhar, N. H., Muqeet, M., Ali, Z., Bilal, M. and UlRehman, A. 2024. Magnetic nanomaterials as an effective absorbent material for removal of fluoride concentration in water: a review. *Journal of Water and Health*, 22(1):123-137. https://doi.org/10.2166/wh.2023.116.
16. Patel, R. V. and Bhasin, C. P. 2023. Efficient fluoride removal from aqueous solution using graphene/Ce composite supported on activated carbon. *Current*

*Nanomaterials*, 8:374–384. https://doi.org/10.2174/2405461508666230110164054.

17. Pillai, P., Dharaskar, S., Sinha, M. K., Sillanpää, M. and Khalid, M. 2020. Iron oxide nanoparticles modified with ionic liquid as an efficient adsorbent for fluoride removal from groundwater. *Environmental Technology and Innovation*, 19:100842. https://doi.org/10.1016/j.eti.2020. 100842.
18. Shaji, E., Sarath, K.V., Santosh, M., Krishnaprasad, P. K., Arya, B. K. and Babu, M.S. 2024. Fluoride contamination in groundwater: A global review of the status, processes, challenges, and remedial measures. *Geoscience Frontiers*, 15(2): 1-29. https://doi.org/ 10.1016/j.gsf.2023. 101734.
19. Singh, S., German, M., Chaudhari, S. and Sengupta, A. K. 2020. Fluoride removal from groundwater using zirconium impregnated anion exchange resin. *Journal of Environmental Management*, 263:1-8. https://doi.org/10.1016/j.jenvman.2020.110415.
20. Sivakumar, D. 2021. Wastewater treatment and bioelectricity production in microbial fuel cell: salt bridge configurations. *International Journal of Environmental Science and Technology*, 18:1379-1394. https://doi.org/10.1007/s13762-020-02864-0
21. Sivakumar, D., Nouri, J., Modhini, T.M. and Deepalakshmi, K. 2018. Nickel removal from electroplating industry wastewater: A bamboo activated carbon. *Global Journal of Environmental Science and Management*, 4(3):1-14. https://doi.org/10.22034/ GJESM.2018. 03.006.
22. Tanwer, N., Deswal, M., Khyalia, P., Laura, J. S. and Khosla, B. 2023. Fluoride and nitrate in groundwater: a comprehensive analysis of health risk and potability of groundwater of Jhunjhunu district of Rajasthan, India. *Environmental Monitoring and Assessment*, 195(2):1-17. https://doi.org/10.1007/s10661-022-10886-z.
23. Thomas, A. M., Kuntaiah, K., Korra, M. R. and Nandakishore, S. S. 2023. Efficient removal of fluoride on aluminium modified activated carbon: an adsorption behavioural study and application to remediation of ground water. *Journal of Environmental Science and Health, Part A*, 58(1):69-80. https://doi.org/10.1080/ 10934529. 2023.2177059.
24. Tiwari, K. K., Raghav, R. and Pandey, R. 2023. Recent advancements in fluoride impact on human health: A critical review. *Environmental and Sustainability Indicators*, 1-11. https://doi.org/10.1016/j.indic.2023.100305.
25. Tolkou, A. K., Meez, E., Kyzas, G. Z., Torretta, V., Collivignarelli, M. C., Caccamo, F. M., Deliyanni, E. A. and Katsoyiannis, I.A. 2021a. A mini review of recent findings in cellulose-, polymer-, and graphene - based membranes for fluoride removal from drinking water. *C Journal of Carbon Research*, 7(74): 1-16. https://doi.org/10.3390/c7040074.
26. Tolkou, A. K., Manousi, N., Zachariadis, G. A., Katsoyiannis, I. A. and Deliyanni, E. A. 2021b. Recently developed adsorbing materials for fluoride removal from water and fluoride analytical determination techniques: A review. Sustainability, 13: 1-26. https://doi.org/10.3390/su13137061

27. Turki, T., Hamdouni, A. and Enesca, A. 2023. Fluoride Adsorption from aqueous solution by modified Zeolite—Kinetic and Isotherm studies. *Molecules*, 28 (10): 1-23. https://doi.org/10.3390/molecules28104076

28. Wan, K., Huang, L., Yan, J., Ma, B., Huang, X., Luo, Z., Zhang, H. and Xiao, T. 2021. Removal of fluoride from industrial wastewater by using different adsorbents: A review. *Science of the Total Environment*, 773, 1-20. https://doi.org/10.1016/j.scitotenv.2021.145535

29. Wei, Y., Wang, L., Li, H., Yan, W. and Feng, J. 2022. Synergistic fluoride adsorption by composite adsorbents synthesized from different types of materials - A review. *Frontiers in Chemistry*, 10:1-23. https://doi.org/10.3389/fchem.2022.900660

30. Yapo, N. S., Aw, S., Briton, B. G. H., Drogui, P., Yao, K. B. and Adouby, K. 2022. Removal of fluoride in groundwater by adsorption using hydroxyapatite modified corbulatrigona shell powder. *Chemical Engineering Journal Advances*, 12: 1-12. https://doi.org/10.1016/j.ceja.2022.100386

# Author Guidelines

International Agricultural Engineering Journal (IAEJ) accepts only original research manuscripts, and submission of a manuscript will be considered to imply that no similar manuscript has been or is being submitted elsewhere. The following three types of manuscripts are considered.

**Original research manuscript:** Report results of original research, significant findings of original research, and materials not previously published elsewhere. Research manuscripts are the normal type of papers published and make up the main content of the journal. They should not normally exceed 15 journal pages.

**Review manuscript:** Intended to be in-depth studies of the state-of-the-art in a chosen subject that provide new insights or interpretation of the subject through thorough and systematic evaluation of available evidences. They should not normally exceed 20 journal pages.

**Research Note:** Reports a concise, but complete, description of a limited or preliminary investigation, enabling important scientifically proven findings to be speedily communicated, and facilitate the reporting of work not meriting a full-length research manuscript. They should not exceed 8 journal pages.

**Submission of Manuscript**

Soft copy of the manuscript in Microsoft (MS) Word, along with a cover letter and a list of potential reviewers of this manuscript with designation, correspondence address, email, *etc.* should be submitted to the Editor-in-Chief through IAEJ online journal management system at ***https://iaejournal.org/index.php/IAEJ***. Corresponding author will create a login account and can have all the roles (Authour, Reviewer and Reader). The official language of publication is English and the manuscripts written in English only will be considered. The manuscript is to be typed in double space in single column on A-4 size page. The e-mail address and mobile number of the corresponding author must be mentioned therein.

**Preparation of Manuscript**

Soft copy of the manuscript, not exceeding 5 MB size, should be prepared in MS Word using Times New Roman Font using the font size specified below.

**Font size: Manuscript Title:** 15 pt. bold first letter capital in each word; **Author name(s):** 11 pt., bold, first letter capital in name and surname; **Authors' affiliation(s):** 11 pt. normal; **Abstract heading:** 12 pt. bold capital; **Abstract text:** 11 pt. normal; **Manuscript text:** 11 pt. normal; **Main -heading (FIRST LEVEL HEADING):** 11 pt. bold each letter and word in uppercase (**INTRODUCTION, MATERIALS AND METHODS, CONCLUSIONS, *etc*.**); **First Sub-heading (Second Level Heading):** 11 pt. bold first letter capital in each word; **Second Sub-heading (Third level heading):** 11 pt. bold sentence case; Headings should not be at more than three levels; **Figure caption/Table title:** 12 pt. bold sentence case; **Acknowledgements, Author contribution, Conflict of Interest and References:** 11 pt. normal, **Footnote:** 9 pt. italics.

**Section numbering**: Provide numbering to main section (1, 2, …) and sub-sections (1.1, 1.2, …) up to three levels such as **1. INTRODUCTION** (main heading), **2. MATERIALS AND METHODS** (main heading), **2.1. Description of Study Area** (first sub-heading), **2.2.1. Soil and geology** (second sub-heading), *etc*.

- **Length of manuscript:** A Research Paper should not exceed 8000 words limit. However, a more elaborated Review Paper may contain 12000-15000 words
- Use the **equation editor** or Math Type for equations
- Use the **table function**, not spreadsheets to make tables
- Use **tab stops** or other commands for indents, not the space bar
- Always use internationally accepted signs and symbols for units (**SI units**). All derived units should be written in exponent form ($m^3/s$; $kg/m^3$).
- **Title:** The title should be concise and informative. Avoid abbreviations and formulae in the Title.
- **Short title** of not more than 80 characters
- **Author name(s):** Provide name, designation, affiliation, full postal and email addresses for each author. Please also indicate the corresponding author along with e-mail address.
- **Abstract:** The Abstract of not more than 200 words should state the problem investigated specifying the aims of the work, outline the methods used, and summarize the main results obtained and the conclusions drawn. Up to 6 keywords in alphabetical order with each word stating in uppercase and separated by semicolon (;) should be given to enable subsequent abstracting or information retrieval systems to locate the paper. Words used in title should be avoided as keywords.
- **Acknowledgment:** Optional, depending upon the cases.

- **Conflict of Interest -** Authors must declare all such interests (or their absence) in writing upon submission of a manuscript. This conflict declaration includes conflicts or potential conflicts of all listed authors. If any conflicts are declared, the journal will publish them with the paper. In cases of doubt, the circumstance should be disclosed so that the editors may assess its significance.
- **Author contribution:** Authors are expected to provide a short description of the contributions made by each listed author. This too will be published in a separate section after the Conflict of Interest statement.
- **References:** Authors are encouraged to **cite latest references (preferably of last ten years)** as far as possible, except for some basic/fundamental research papers/books, *etc*. Citations of references in the text should be in the format of surnames of authors, followed by the year of publication of the appropriate reference, separated by a comma.

**In the text**: "Harms and Campbell (1967) employed multiple …",

"… multiple models were employed (Harms and Campbell, 1967)".

If a work has more than two authors, cite first author followed by "*et al.*" and the year.

Example: Lin *et al.* (2019), (Lin *et al.*,2019).

In the references list (to journals):

**Journal Paper:** Silva, T. P., Bressiani, D., Ebling, É. D. and Reichert, J. M. 2023. Best management practices to reduce soil erosion and change water balance components in watersheds under grain and dairy production. *International Soil and Water Conservation Research*, 12(1):121-136. https://doi.org/10.1016/j.iswcr.2023.06.003

**Books:** Kepner, R.A., Bainer, R. and Barger, E.L. 1971. *Principles of Farm Machinery*. Second Edition, The AVI Publishing Company Inc., USA, 527p

**Edited Book:** Varzakas, T. and Tzia, C. (ed.) 2015. *Handbook of Food Processing*. CRC Press, Boca Raton, 741p. https://doi.org/10.1201/b19397

**Book Chapter:** Mosley, M.P. and McKerchar, A.I. 1993. Streamflow. In: D.R. Maidment (ed.), *Handbook of Hydrology*. McGraw-Hill, Inc., New York, p. 8.1-8.35.

**Report:** CGWB. 2014. *Concept Note on Geogenic Contamination of Ground Water in India (with a Special Note on Nitrate)*. Report of the Central Ground Water Board (CGWB). Ministry of Water Resources, Government of India, pp. 78. https://cgwb.gov.in/cgwbpnm/public/uploads/documents/ 16860557107485313 99file.pdf (accessed on 03 January 2024)

**Manual:** Šejna, M., Šimůnek, J. and van Genuchten, M. 2018. *The HYDRUS Software Package for Simulating Two- and Three-Dimensional Movement of Water, Heat, and Multiple Solutes in Variably-Saturated Media*. User Manual, Version 3.01. PC-Progress, Prague, Czech Republic, 322p.

**Dissertation:** Ajia, F.O. 2020. *Water efficiency engagement in the UK: barriers and opportunities*. Unpublished Ph.D. Thesis, The University of Sheffield, United Kingdom.

***Web references:*** As a minimum, the full URL and the date when the reference was last accessed should be given.

USEPA. 2002. *Persistent Organic Pollutants: A Global Issue, A Global Response*. United States Environmental Protection Agency (USEPA). https://www.epa.gov/international-cooperation/persistent-organic-pollutants-global-issue-global-response (accessed on 25 May 2018).

**Appendices:** It may be appropriate to place detailed mathematical derivations in appendices, rather than in the main body of the text.

**Figures:** All figures are to be numbered using Arabic numerals; Figures should always be cited in text in consecutive numerical order (cite as Fig. 1); Figure parts should be denoted by lowercase letters (a, b, c, *etc*.). Each figure should have a concise caption describing accurately what the figure depicts. Figure captions begin with the term **Fig.** in bold type, followed by the figure number, also in bold type. Figure captions should be placed beneath each figure (**Fig. 1. Moisture ratio and drying time of onion slices under fluidized drying**).

**Tables:** Each table must be placed on a separate page after References, and numbered consecutively throughout the text (with Arabic numerals), and referred to as Table 1, Table 2, *etc.* There must be a caption explaining the components of the table (**Table 1. Performance parameters of bullock drawn sprayer**) at the top of each Table.

**Copyright Information:** Upon acceptance of a manuscript for publication in the International Agricultural Engineering Journal (IAEJ), authors will be advised to complete a "**Copyright Transfer Agreement Form**".

**Print proof:** The corresponding author will be notified via email when proofs are ready. The corresponding author is responsible to download the copy edited manuscript and carryout proof reading very carefully within given time frame to avoid errors in the final published article. Any corrections marked with annotations must be returned within given time and should only cover typesetting errors/minor corrections. No new additions of text / major changes are allowed at this stage.